



HAL
open science

Quantum-dot lasers on silicon: nonlinear properties, dynamics, and applications

Bozhang Dong

► **To cite this version:**

Bozhang Dong. Quantum-dot lasers on silicon: nonlinear properties, dynamics, and applications. Physics [physics]. Institut Polytechnique de Paris, 2021. English. NNT: 2021IPPAT047. tel-03741827

HAL Id: tel-03741827

<https://theses.hal.science/tel-03741827v1>

Submitted on 2 Aug 2022

HAL is a multi-disciplinary open access archive for the deposit and dissemination of scientific research documents, whether they are published or not. The documents may come from teaching and research institutions in France or abroad, or from public or private research centers.

L'archive ouverte pluridisciplinaire **HAL**, est destinée au dépôt et à la diffusion de documents scientifiques de niveau recherche, publiés ou non, émanant des établissements d'enseignement et de recherche français ou étrangers, des laboratoires publics ou privés.



INSTITUT
POLYTECHNIQUE
DE PARIS

NNT : 2021IPPAT047

Thèse de doctorat



Quantum-dot lasers on silicon: nonlinear properties, dynamics, and applications

Thèse de doctorat de l'Institut Polytechnique de Paris
préparée à Télécom Paris

École doctorale n°626 École doctorale de l'Institut Polytechnique de Paris (EDIPP)
Spécialité de doctorat : Électronique et optoélectronique

Thèse présentée et soutenue à Palaiseau, le 16 Décembre 2021, par

BOZHANG DONG

Composition du Jury :

Yves Jaouen Professeur, Institut Polytechnique de Paris (Télécom Paris), France	Président
Alexei Baranov Directeur de Recherches, Université de Montpellier (Institute of Electronics and Systems), France	Rapporteur
Angelique Rissons Professeur, ISAE-Supaero (Department of Electronics, Optronics and Signal Processing), France	Rapporteur
John Bowers Professor, University of California, Santa Barbara (Institute for Energy Efficiency), USA	Examineur
Fan-Yi Lin Professor, National Tsing Hua University (Institute of Photonics Technologies), Taiwan	Examineur
Gaëlle Lucas-Leclin Maitrice de Conference, Institut d'Optique Graduate School (Charles Fabry Laboratory), France	Examineur
Damien Rontani Maitre de Conference, CentraleSupélec Metz (Optical Materials, Photonics and Systems Laboratory), France	Examineur
Frédéric Grillot Professeur, Institut Polytechnique de Paris (Télécom Paris), France	Directeur de thèse
Di Liang Distinguished Technologist, Hewlett Packard Labs, USA	Invité

ACKNOWLEDGEMENTS

First and foremost, I would like to express my most sincere gratitude to my PhD advisor Prof. Frédéric Grillot, who has been extremely supportive of my PhD studies and academic goals. I truly appreciate his scientific guidance, continuous motivation, tremendous scientific and technological knowledge that he shared with me. I also thank him for supporting me on various scientific trainings, exchange programs, and international conferences that enabled me to develop myself and to complete my thesis.

Special thanks to Prof. John E. Bowers from University of California Santa Barbara, USA and Dr. Di Liang from Hewlett Packard Labs, USA for providing me high-quality laser samples that allowed me to access a rich variety of results sustaining the comprehension of underlying physics. I would also thank Prof. Fan-Yi Lin from National Tsing Hua University, Taiwan for hosting me in his youthful and vigorous group for more than three months. Their scientific rigors along with their deep insights in laser physics and applications granted me important guidance on my researches.

I am extremely grateful to all who in one way or another contributed to the completion of this thesis. In particular, many thanks to Dr. Jianan Duan from Harbin Institute of Technology Shenzhen, China, Dr. Heming Huang from Télécom Paris, France, Dr. Jun-Da Chen and Han-Ling Tsay from National Tsing Hua University, Taiwan, who provided me a great amount of assistance and invaluable contribution to my work. I also appreciate the work of my collaborators: Dr. Weng W. Chow from Sandia National Laboratories, USA, Dr. Justin C. Norman from Quintessent, Inc., USA, Dr. Songtao Liu from Inter, Inc., USA, Dr. Geza Kurczveil from Hewlett Packard Labs, USA, Xavier Champagne de Labriolle from Institut polaire français Paul Emile Victor, France, Prof. Kathy Lüdge and Felix Köster from Technische Universität Berlin, Germany, Dr. Yating Wan, Chen Shang, and Mario Dumont from University of California Santa Barbara, USA, Prof. Cheng Wang from ShanghaiTech University, China, Yueguang Zhou from Technical University of Denmark, Denmark, Dr. Kenichi Nishi, Dr. Keizo Takemasa, and Dr. Mitsuru Sugawara from QD Laser, Inc., Japan, Shiyuan Zhao, Shihao Ding, and Jingtian Liu from Télécom Paris, France for fruitful scientific discussions.

I would like to thank all the professors, all my colleagues and all the friends in GTO

group, Télécom Paris, and in Laser Dynamics Lab, National Tsing Hua University, who aid me in work and in life.

I also want to thank my undergraduate classmates from Huazhong University of Science and Technology, China, for their support and all the memorable moments we had together in France.

I acknowledge the Institut Mines-Telecom for funding my PhD work.

Last but not least, I deeply appreciate the unwavering support and encouragement from my parents. My special thanks to my love Jiayi Hong for her love, support, and understanding. This work would have not been possible without them.

ABSTRACT

Silicon photonics is promising for high-speed communication systems, short-reach optical interconnects, and quantum technologies. Direct epitaxial growth of III-V materials on silicon is also an ideal solution for the next generation of photonic integrated circuits (PICs). In this context, quantum-dots (QD) lasers with atom-like density of states are promising to serve as the on-chip laser sources, owing to their high thermal stability and strong tolerance for the defects that arise during the epitaxial growth. The purpose of this dissertation is to investigate the nonlinear properties and dynamics of QD lasers on Si for PIC applications. The first part of this thesis investigates the dynamics of epitaxial QD lasers on Si subject to external optical feedback (EOF). In the short-cavity regime, the QD laser exhibits a strong robustness against parasitic reflections hence giving further insights for developing isolator-free PICs. In particular, a near-zero linewidth enhancement factor is crucial to achieve this goal. The second part is devoted to studying the static properties and dynamics of a single-frequency QD distributed feedback (DFB) laser for uncooled and isolator-free applications. The design of a temperature-controlled mismatch between the optical gain peak and the DFB wavelength contributes to improving the laser performance with the increase of temperature. The third part of this dissertation investigates the QD-based optical frequency comb (OFC). External control techniques including EOF and optical injection are used to improve the noise properties, the timing-jitter, and the frequency comb bandwidth. In the last part, an investigation of the optical nonlinearities of the QD laser on Si is carried out by the four-wave mixing (FWM) effect. This study demonstrates that the FWM efficiency of QD laser is more than one order of magnitude higher than that of a commercial quantum-well laser, which gives insights for developing self-mode-locked OFC based on QD. All these results allow for a better understanding of the nonlinear dynamics of QD lasers and pave the way for developing high-performance classical and quantum PICs on Si.

TABLE OF CONTENTS

Acknowledgements	iii
Abstract	v
Table of Contents	vi
List of Illustrations	viii
List of Tables	xxi
Chapter I: Introduction	1
1.1 Booming optical network and data centers	1
1.2 Photonic integrated circuits	5
1.3 Quantum technologies	7
1.4 Quantum-Dot laser	11
1.5 Motivations of the dissertation	15
1.6 Organization of the dissertation	20
Chapter II: Physics and properties of quantum dot lasers	23
2.1 Electronic structure of QD	23
2.2 Carrier scattering process	25
2.3 Gain broadening mechanisms	27
2.4 Linewidth enhancement factor	30
2.5 Relaxation oscillations and damping	34
2.6 Gain compression	38
2.7 Noise properties	40
2.8 Nonlinear optical susceptibility	45
2.9 Summary	48
Chapter III: Dynamics of quantum-dot lasers subject to external optical feedback	50
3.1 Principle of optical feedback	50
3.2 Lang & Kobayashi equations	55
3.3 Light-current characteristics under optical feedback	57
3.4 Phase conditions	58
3.5 Critical feedback level for coherence collapse	62
3.6 Towards a reflection-resistant optical transmitter	64
3.7 Dynamics of QD laser in long-delay optical feedback operation	67
3.8 QD lasers studied	69
3.9 Optical feedback apparatus in experiments	75
3.10 Dynamics of QD laser subject to external optical feedback	78
3.11 Route to periodic oscillations in QD laser	81
3.12 Impact of the p-doping on the feedback dynamics	83
3.13 Impact of the dash orientation on the feedback insensitivity	83
3.14 Summary	85
Chapter IV: Quantum-dot distributed feedback laser with large optical mismatch	87
4.1 Introduction to distributed feedback laser	87

4.2	Coupled wave equations	90
4.3	Stopband of a DFB laser	93
4.4	Coupling coefficient of the DFB grating	93
4.5	Description of the InAs/GaAs QD-DFB laser studied	97
4.6	Extraction of linewidth enhancement factor	100
4.7	Characterization of relative intensity noise and modulation properties	108
4.8	Dynamics in long-delay optical feedback operation	112
4.9	Impact of the optical wavelength detuning on the feedback insensitivity	115
4.10	Impact of the feedback dynamics on transmission properties	117
4.11	Summary	120
Chapter V: Design and optimization of quantum-dot optical frequency comb .		122
5.1	Introduction to optical frequency comb	122
5.2	Frequency comb technologies	125
5.3	Applications of optical frequency combs	131
5.4	Towards an optical frequency comb for silicon photonic integrated circuits	132
5.5	Delay-differential equation model	135
5.6	QD-OFC studied	137
5.7	Impact of the saturable absorber reverse bias on the linewidth en- hancement factor	142
5.8	Impact of the linewidth enhancement factor on the mode-locking dynamics	145
5.9	Impact of the saturable absorber section length ratio on the mode- locking dynamics	150
5.10	Stabilization of quantum-dot mode-locked laser by external optical feedback	152
5.11	Frequency comb bandwidth improvement by optical injection	157
5.12	Summary	161
Chapter VI: Nonlinear frequency conversion in epitaxial quantum-dot laser on silicon		163
6.1	Introduction to four-wave mixing	163
6.2	Four-wave mixing in quantum-dots	165
6.3	Towards QD-based self-mode-locked optical frequency comb and quantum light generator	167
6.4	Theory of nondegenerate four-wave mixing	170
6.5	Devices studied and input parameters for the model	175
6.6	Low group velocity dispersion in quantum-dot laser	176
6.7	Nondegenerate four-wave mixing apparatus in experiments	178
6.8	Enhanced four-wave mixing efficiency in quantum-dot lasers	179
6.9	Summary	182
Chapter VII: Conclusions and perspectives		184
Bibliography		189
Appendix A: Published contents		218
Appendix B: Résumé de thèse en Français		222

LIST OF ILLUSTRATIONS

<i>Number</i>	<i>Page</i>
1.1 Global mobile data traffic forecast by ITU. Overall mobile data traffic is estimated to grow at an annual rate of around 55 percent in 2020–2030 to reach 607 exabytes (EB) in 2025 and 5,016 EB in 2030. M2M, machine-to-machine. (Source: Cisco).	2
1.2 Global optical transceiver market forecast. Annual revenue in 2026 is estimated to increase to US \$ 20.9 billion. (Source: Yole Développement).	3
1.3 Anatomy of different link architectures: (a) single-wavelength point-to-point photonic link; (b) WDM photonic link based on individual single-wavelength lasers and broadband modulators; (c) photonic link based on comb laser, parallel broadband modulators, and DeMux/Mux. (d) WDM photonic link based on comb laser, cascaded microring resonators, and cascaded drop filters. MOD, modulator; Det, detector; TIA, trans-impedance amplifier; CLK, clock; Mux, multiplexer; DeMux, demultiplexer. From Ref. (Cheng et al., 2018).	4
1.4 Trend of the components number on PICs based on three major platforms over the last three decades. Native indium phosphide (blue), silicon photonic (green), and hybrid silicon (red). From Ref. (Hänsel and Heck, 2020)	6
1.5 Quantum computer roadmap. Quantum annealer, the noisy version (with rather poor quality qubits) of adiabatic quantum computing. NISQ, Noisy Intermediate-Scale Quantum. Quantum-gate, simple unitary operations on qubits. (Source: Yole Développement).	9
1.6 Quantum light generation in a nonlinear medium that relies on $\chi^{(2)}$ (spontaneous parametric down-conversion) or $\chi^{(3)}$ (spontaneous four-wave mixing) process, in which one or two pump photons (ω_p) are converted into correlated signal (ω_s) and idler (ω_i) photons, respectively.	10

1.7	Structure and evolution of the density of states (DOS) for semiconductor structures with different degrees of dimensionality. (a-1, a-2) bulk, (b-1, b-2) quantum-well (QW), (c-1, c-2) quantum-dash (QDash), and (d-1, d-2) quantum-dot (QD). From Ref. (Frédéric Grillot, Jianan Duan, et al., 2021).	11
1.8	Threshold current density versus publication year for semiconductor lasers starting with double-heterostructure (DH) and then moving to quantum confined devices. Results for QW and QD lasers are shown for growth on native substrates and Si with the most recent results moving to CMOS-standard on-axis Si as opposed to the miscut substrates used previously. From Ref. (J. C. Norman, R. P. Mirin, and John E Bowers, 2021)	13
1.9	Comparison of the room-temperature Photoluminescence of (a) single InAs QD layer and (b) single 8 nm InGaAs QW grown on either GaAs (blue) or silicon (green) substrates. From Ref. (A. Y. Liu, Srinivasan, et al., 2015).	14
1.10	Estimated power consumption of DFB laser-based optical transceivers at different bit-rates with different signaling interfaces. From Ref. (K.-L. Lee et al., 2012)	16
2.1	Schematic of a QD laser electronic band structure of electrons and holes.	24
2.2	Illustration of the carrier capture and relaxation processes: (a) multiphonon processes under low excitation density, (b) single Auger process, and (c) sequential Auger processes under high injection current density. Reproduced from Ref. (Ohnesorge et al., 1996)	26
2.3	Schematic diagram of QDs (a) with and (b) without inhomogeneous broadening and their corresponding photon modes. GS, ground state ; ES, excited state. The QD size uniformity in the left inset are described by the Gaussian-shaped energy bandwidth Γ_{in} . From Ref. (Jungho Kim et al., 2010)	28
2.4	Photoluminescence spectrum as a function of temperature from a single InAs/GaAs dot. From Ref. (Bayer and Forchel, 2002)	29
2.5	Lasing and electroluminescence spectra under pulsed injection mode for different bias level at two different temperatures: (a) 110K and (b) 253 K. From Ref. (Veselinov et al., 2007)	30

2.6	Schematic of the gain g_m and the refractive index n profiles variation with the carrier density changes for QD and QW. From Ref. (Rosencher and Vinter, 2002)	32
2.7	Frequency response of a membrane laser (and is valid for semiconductor lasers as well) for several different bias current. The oscillation peaks represent the relaxation oscillation frequency. The modulation bandwidth that is represented by the black dashed line is determined by the 3 dB down cutoff frequency. From Ref. (Yamaoka et al., 2021).	36
2.8	Relaxation oscillation frequency (continuous lines, left axis) and damping rate (dashed lines, right axis) as a function of current. Calculated curves are derived from three different homogeneous broadening bandwidth Γ_{homo} : single-mode (blue squares), multimode with $\Gamma_{homo} = 10$ meV (red dots), and multimode with $\Gamma_{homo} = 1$ meV (green triangles). The inhomogeneous broadening bandwidth Γ_{ih} is fixed at 35 meV. From Ref. (Fiore and Markus, 2007)	37
2.9	GS α_H -factor versus the bias current in simulation (black dots) and in experiment (red stars). From Ref. (Frédéric Grillot, Béatrice Dagens, et al., 2008)	39
2.10	Noise in modulated laser signals for both analog and digital applications. From Ref. (Coldren, Corzine, and Mashanovitch, 2012)	41
2.11	Noise in modulated laser signals for both analog and digital applications. From Ref. (Coldren, Corzine, and Mashanovitch, 2012)	44
2.12	Directions of the third-order nonlinear susceptibilities of carrier density pulsation (CDP) and spatial hole burning (SHB) for bulk, QW and QD. From Ref. (Akiyama, Kuwatsuka, et al., 2002).	48
3.1	(a) Schematic of a semiconductor laser that is subject to optical feedback. (b) Polar plot of equivalent reflectivity r_{re} from output side of laser. Δr_1 represents feedback that changes both the amplitude and phase of r_{re}	51
3.2	Schematic representation of the physical processes involved in a semiconductor laser under optical feedback. From Ref. (H. Huang et al., 2020)	53

3.3	Feedback regimes in a semiconductor DFB laser. Regime I, stable regime in which the linewidth is either broadened or narrowed. Regime II, line splitting. Regime III, linewidth narrowing. Regime IV, unstable oscillations. Regime V, strong linewidth narrowing. From Ref. (Tkach and Chraplyvy, 1986)	54
3.4	(a) L-I curves of a QD FP laser in free-running operation (black) and for three different amounts of feedback ($\eta_F = 1.7\%$, 3.4% and 6.7%). The external cavity length L_{ext} is fixed. From Ref. (Heming Huang, 2017). (b) L-I curves of a semiconductor laser in free-running operation (solid black line), and with identical η_F but different L_{ext} at 15 cm (dotted red line) or at 150 cm (broken blue line). From Ref. (Ohtsubo, 2012).	59
3.5	Relationship between the laser cavity modes and external cavity modes, in (a) integer resonant condition ($\tau_{ext}/\tau_{in} \in N$, N is integer), and in (b) non-resonant condition ($\tau_{ext}/\tau_{in} \notin N$). From Ref. (Lang and K. Kobayashi, 1980).	59
3.6	Number of solutions for Eq. (3.18) in (C, ϕ_0) space. The roman numbers represent the number of solutions. From Ref. (Ohtsubo, 2012).	60
3.7	Number of solutions for Eq. (3.18) for (a) a QW laser with $\alpha_H = 4$, and for (b) a QD laser with $\alpha_H = 1$. In both cases, the external cavity length is fixed to 10 cm, while the feedback strength is -35 dB (green), -25 dB (red), and -20 dB (blue). The black dashed line corresponds to the free-running operation. From Ref. (Frédéric Grillot, J. C. Norman, et al., 2020).	61
3.8	Optical spectral linewidth as a function of the feedback strength. The markers represent different feedback phase conditions. roman numbers represent the feedback regimes. From Ref. (Klaus Petermann, 1995).	62
3.9	The critical feedback level r_{crit} as a function of the delay time τ_{ext} (solid line). The dashed line marks $C = 1$, and the vertical line indicates $f_{RO} \times \tau_{ext} = 1$. From Ref. (Schunk and Petermann, 1989).	63

3.10	(a) Feedback strength η_F and (b) relaxation oscillation frequency f_{RO} as a function of the external cavity length L_{ext} (solid line). The black vertical line at 3.25 GHz in (b) represents the f_{RO} in free-running operation. P1, period-one; P2, period-two; QP, quasi-period. From Ref. (Ohtsubo, 2012).	65
3.11	Optical and RF spectral mappings as a function of the feedback strength η_F for the QD laser on Si [(a) and (c)] and for the QW laser [(b) and (d)] at $3 \times I_{th}$. The vertical axis is in logarithmic scale. 100% η_F means -7.4 dB. From Ref. (Jianan Duan, Heming Huang, et al., 2019)	67
3.12	BER plots versus received optical power for (a) the QD laser and for (b) the QW laser. From Ref. (Jianan Duan, Heming Huang, et al., 2019)	68
3.13	(a) $1 \times 1 \mu\text{m}^2$ AFM image of the QD morphology. (b) Cross-section scanning transmission electron micrograph displays five layers of InAs quantum dots within the active region. (c) Schematic of the laser epi-structure. (a) and (b) are from Ref. (J. C. Norman, Daehwan Jung, Z. Zhang, et al., 2019)	70
3.14	Light-current characteristics and optical spectra measured at $5 \times I_{th}$ for undoped [(a) and (b)] and p-doped [(c) and (d)] QD laser.	71
3.15	The above-threshold α_H -factor of the p-doped (burgundy) and the undoped (blue) QD laser with the bias current ranging from $1 \times I_{th}$ to $3 \times I_{th}$ at 20°C. The dashed lines are for guiding eyes only. From Ref. (H. Huang et al., 2020).	72
3.16	(a) $1 \times 1 \mu\text{m}^2$ AFM image of the QDash morphology. The QDashes are elongated in the $[1 \bar{1} 0]$ direction. The average height and width is about 7 nm and 20 nm, respectively. (b) Cross-section TEM image of the $[1 \bar{1} 0]$ surface at $9000 \times$ magnification highlights the 5 layers of QDash. The electron beam energy was 200 keV. (c) Schematic of the laser epi-structure.	73
3.17	(a) Light-current characteristics and (b) optical spectra measured at $1.5 \times I_{th}$ for QDash oriented parallel (gold) and perpendicular (burgundy) to the cavity axis. Insets in (a) illustrate the dashes orientation with respect to the wave propagation direction \vec{k}	74

3.18	Spectral dependence of (a) net modal gain in different bias conditions from below to threshold and (b) threshold α_H -factor for QDash laser with dashes parallel (gold) or perpendicular (burgundy) to the cavity axis.	75
3.19	Experimental setup for the short-delay coherent external optical feedback measurement. VOA, variable optical attenuator; PD, 12 GHz photodiode; ESA, electrical spectrum analyzer; OSC, oscilloscope.	76
3.20	Experimental setup used for the long-delay coherent external optical feedback measurement. ISO, optical isolator; PD, photodiode; PC, polarization controller; VOA, variable optical attenuator.	77
3.21	Electrical spectra (left), time series (middle), and phase portraits (right) of the p-doped QD laser with $(\eta_F, L_{ext}) =$ (a) (68.2%, 4 cm), (b) (68.2%, 6.5 cm), (c) (68.2%, 15 cm), (d) (33%, 15 cm), and (e) solitary, when it is biased to 160 mA. f_{ext} , frequency of the external cavity; f_{sp} , self-pulsation frequency.	79
3.22	Mappings of the dynamic states and the oscillation frequencies of the p-doped QD laser in different feedback conditions at 125 mA [(a) and (b)] and at 160 mA [(c) and (d)]. The vertical red dashed lines depict the boundaries of the SCR and the LCR. The horizontal dotted black lines illustrate the free-running f_{RO}	82
3.23	The onset of periodic oscillations $r_{ext,p}$ associated with L_{ext} of the p-doped (burgundy) and undoped (gold) QD laser. Both devices operate at $\sim 3 \times I_{th}$. The vertical dashed burgundy and dotted gold lines depict the boundaries of the SCR and the LCR of the p-doped and the undoped device, respectively.	84
3.24	RF power mapping and the optical power mapping as a function of the feedback strength for the QDash laser whose dashes are oriented parallel [(a) and (c)] or perpendicular [(b) and (d)] to the cavity axis. Both devices operate at $1.5 \times I_{th}$ at 20°C	84
4.1	(a) Schematic of a corrugated Bragg grating with a periodicity of Λ . (b) Bragg reflection characteristic of the subsequent reflectivities. (c) Phases corresponding to each wave propagation after a distance of $\Lambda/2$. From Ref. (Morthier and Vankwikelberge, 2013).	88
4.2	Schematic diagram of (a) DFB laser and (b) DBR laser. From Ref. (Morthier and Vankwikelberge, 2013).	90

4.3	Dispersion diagram for an infinite index grating in a waveguide without loss or gain. From Ref. (Morthier and Vankwikelberge, 2013). . .	93
4.4	Relationship between the amplitude threshold gain and the detuning coefficient of a mirrorless index-coupled DFB Laser. From Ref. (Ghafouri-Shiraz, 2003).	94
4.5	Relationship between the amplitude threshold gain and the detuning coefficient of an index-coupled DFB Laser with asymmetric facet reflectivities. The corrugation phase Ψ_1 is fixed while the other Ψ_2 varies. From Ref. (Ghafouri-Shiraz, 2003).	95
4.6	Experimental (solid line) and calculated (dashed line) yield of as-cleaved DFB lasers as a function of κL . From Ref. (David et al., 1991).	96
4.7	(a) $0.5\mu\text{m} \times 0.5\mu\text{m}$ Atomic force microscopy image of InAs QDs grown on GaAs substrate. (b) Photoluminescence spectrum of the active region of the laser studied after the improved growth sequence (red). From Ref. (Kenichi Nishi, Takemasa, et al., 2017).	97
4.8	(a) Light-current characteristics with temperature ranging from 15 to 55°C. (b) Threshold current (burgundy) and external efficiency (jade) as a function of temperature.	98
4.9	(a) Optical spectra of the QD-DFB laser from 15°C to 55°C ($2 \times I_{th}$). Temperature dependent (b) DFB wavelength (burgundy), optical gain peak (jade), (c) optical wavelength detuning (gray) and side-mode suppression ratio (emerald).	99
4.10	Sub-threshold optical spectra of QD laser for different bias currents. .	102
4.11	Spectral net modal gain of QD laser in various bias current conditions below threshold.	103
4.12	The net modal gain and modal wavelength as a function of bias current for the mode located at gain peak at around 1305 nm. Burgundy solid lines: linear fitting below threshold; emerald solid lines: linear fitting above threshold.	103
4.13	Spectral dependence of α_H -factor for InAs QD laser on GaAs substrate measured at threshold. The vertical black dashed represents the wavelength of the optical gain peak at threshold.	104

4.14	Schematics of the experimental set-up for the sinusoidal optical phase modulation method. EOS: External Optical Source; DUT: Device Under Test; ODL: Optical Delay Line; PM: Phase Modulator; OSA Optical Spectrum Analyzer; BT: Bias Tee; RFPS: RF Power Splitter. From Ref. (Provost et al., 2011)	105
4.15	(a) Optical spectra around the DFB mode and the modulation sidebands of the QD-DFB laser measured at $2 \times I_{th}$ under 55°C . The spectra obtained for 4 different optical delays are normalized to the main lobes. (b) Effective α_H -factor in different operating conditions. .	108
4.16	Experimental setup used for characterizing the RIN of QD lasers. From Ref. (Jianan Duan, Y. Zhou, et al., 2020).	109
4.17	(a) Measured RIN spectra at several bias currents at 20°C . (b) Extracted damping factor γ as a function of the squared relaxation oscillation frequency f_{RO}^2 at 20°C (jade) and at 55°C (burgundy). (c) Tendency of K-factor versus the temperature, T_m is marked by the black dashed line.	111
4.18	RF spectra and optical spectra in different r_{ext} conditions at 25°C , when the QD-DFB laser operates at $2 \times I_{th}$ [(a) and (e)] and $6 \times I_{th}$ [(b) and (f)]. Corresponding power mapping of the RF and optical spectra as a function of η_F at $2 \times I_{th}$ [(c) and (g)] and at $6 \times I_{th}$ [(d) and (h)].	113
4.19	RF spectra and optical spectra in different r_{ext} conditions at 55°C , when the QD-DFB laser operates at $2 \times I_{th}$ [(a) and (e)] and $6 \times I_{th}$ [(b) and (f)]. Corresponding power mapping of the RF and optical spectra as a function of η_F at $2 \times I_{th}$ [(c) and (g)] and at $6 \times I_{th}$ [(d) and (h)].	116
4.20	(a) Critical feedback level associated with the onset of regime IV r_{crit} and (b) the feedback level associated with the onset of periodic oscillations $r_{ext,p}$ in different operating conditions.	117
4.21	Experimental setup used for the PAM4 transmission with coherent external optical feedback. PRBS, pseudo-random bit sequence; ISO, optical isolator; SMF, single-mode fibre; PD, photodiode; PC, polarization controller; VOA, variable optical attenuator.	118

4.22	BER versus received optical power of the QD-DFB laser in the back-to-back PAM4 configuration with the feedback strength increasing from 3.2% (gold) to 6.3% (emerald) and further to 31.6% (burgundy). The BER plot in free-running operation (black) is performed as a reference. The laser operates at $6 \times I_{th}$ at 55°C.	119
4.23	BER versus received optical power in the PAM4 configuration for back-to-back or after 12 km transmission when the QD-DFB laser is in free-running (black) or with the feedback strength at 3.2% (burgundy). The laser operates at $6 \times I_{th}$ at 55°C.	120
5.1	Sketch of a frequency comb that functions in a manner analogous to a light gear. It links the radio frequencies f_r and f_0 to a vast array of optical frequencies f_n . From Ref. (Diddams, Vahala, and Thomas Udem, 2020).	123
5.2	Time-domain spectrum of a frequency comb pulse train along with the corresponding frequency-domain response, which illustrates the equally spaced comb lines. The FWHM of the optical pulse and the optical bandwidth are represented by Δt and Δf , respectively. From Ref. (Schliesser, Picqué, and Hänsch, 2012).	124
5.3	Sketch for (a) active mode-locking, with an intra-cavity modulator driven at the repetition rate; and (b) passive mode-locking, with the repetition rate determined by the laser cavity length. SA, saturable absorber.	127
5.4	Sketch for electro-optic modulated frequency comb, with the repetition rate determined by the modulation frequency.	129
5.5	Sketch for microresonator frequency comb. The dielectric resonator made of a $\chi^{(3)}$ nonlinear material is pumped by a single-frequency CW laser. Signal and idler sidebands are generated by a parametric frequency conversion through both degenerate and nondegenerate FWM.	130

5.6	Optical frequency comb technologies as a function of their mode spacing and fractional bandwidth. The frequency combs with high-repetition-rate and large-bandwidth (gold regime) is required for a variety of applications including astrophysical spectrometer calibration, telecommunications, optical arbitrary waveform generation, and spectroscopy. The stars represent the cases of microresonator-based frequency combs made from different materials. From Ref. (Kippenberg, Holzwarth, and Diddams, 2011).	131
5.7	Characterizations of an epitaxial QD-MLL on Si: (a) autocorrelation traced pulse duration; (b) RF spectrum in a span of 50 GHz; (c) narrow span RF linewidth of the repetition frequency; (d) single-sideband phase noise plot in the narrowest pulse width condition. From Ref. (Songtao Liu, X. Wu, et al., 2019).	133
5.8	Transmission characterizations of a QD-based comb laser on Si: eye diagrams of its 15 channels with corresponding extinction ratio (ER) and bit-error-rate (BER) values. Each channel is modulated by an external optical modulator with 10 Gbit/s pseudo-random bit sequence. From Ref. (Kurczveil, C. Zhang, et al., 2018).	134
5.9	Sketch of (a) the QD-MLL on Si (not to scale). (b) Corresponding epitaxial structure of the device. SA, saturable absorber.	138
5.10	SA reverse bias dependent light-current characteristics and optical spectra measured at $2 \times I_{th}$ for the QD-MLL whose SA length ratio is 8% [(a) and (c)] and 5% [(b) and (d)] at 20°C.	139
5.11	(a) Sketch of the hybrid-silicon QD comb laser. SOA, semiconductor optical amplifier; SA, saturable absorber; FM, front mirror; BM, back mirror; GC, grating coupler. (b) SEM image of the cross section of the device.	140
5.12	(a) Mapping of the coupled power of the QD-OFC in different bias conditions on the SA and on the SOAs. The evolution of the threshold current with the SA reverse voltage is marked by the white dashed line. Optical spectra measured with $(I_{gain}, V_{SA}) =$ (b) $(5 \times I_{th}, 0 \text{ V})$, (c) $(3 \times I_{th}, -6 \text{ V})$, (d) $(5 \times I_{th}, -6 \text{ V})$	142

5.13	(a) Characterization of the QD-MLL whose r_{SA} is 5%: the differential gain (emerald) and the differential wavelength (burgundy) as a function of SA reverse voltage for a longitudinal mode near gain peak. (b) Threshold α_H -factor as a function of SA reverse voltage for the same mode of the QD-MLL (burgundy) and for a longitudinal mode near gain peak of the QD-OFC (emerald). Measurements at threshold are performed by ASE method.	144
5.14	Calculated dynamics of the QD-MLL performed by time traces and inset the RF spectra in different operating conditions: (a) Q-switched mode-locking (QSML) with $(g_{mod}, \alpha_q) = (9.1 \text{ cm}^{-1}, 2)$; (b) unstable fundamental mode-locking (uFML) with $(g_{mod}, \alpha_q) = (14.6 \text{ cm}^{-1}, 2)$; (c) fundamental mode-locking (FML) with $(g_{mod}, \alpha_q) = (11.8 \text{ cm}^{-1}, 2)$; and (d) FML with $(g_{mod}, \alpha_q) = (11.8 \text{ cm}^{-1}, 5)$. Recorded experimental RF response: (e) QSML with $(I_{gain}, V_{SA}) = (95 \text{ mA}, -2 \text{ V})$ and (f) FML with $(I_{gain}, V_{SA}) = (160 \text{ mA}, -2 \text{ V})$	147
5.15	Calculated mappings of (a) the pulse width and (b) the RF peak intensity as a function of the modal gain and α_q of the QD-MLL. (c) Experimental mapping of the RF peak signal-to-noise ratio (SNR) as a function of the gain current and SA reverse voltage obtained from the same device.	149
5.16	Calculated mappings of (a) the pulse width and (b) the RF peak intensity as a function of the modal gain and the SA section length ratio r_{SA} . (c) Recorded experimental RF response of of the QD-MLL whose r_{SA} is 5% (black) and 8% (burgundy) in the optimum conditions.	151
5.17	Calculated mappings of (a) the RF peak intensity and (b) the pulse width as a function of the feedback strength η_F and α_q	153
5.18	(a) Experimental mapping of the RF peak SNR as a function of the η_F and V_{SA} , when the device operates at 167 mA. (b) Experimental RF spectra in free-running operation (burgundy) and in optical feedback operation (gold) with $(I_{gain}, V_{SA}, \eta_F) = (167 \text{ mA}, -1 \text{ V}, -34 \text{ dB})$	154
5.19	Variation of the repetition frequency (gold) and the RF linewidth (burgundy) as a function of the external cavity length change in experiment, when the device operates with $(I_{gain}, V_{SA}, \eta_F) =$ (a) (167 mA, 0 V, -34 dB) and (b) (167 mA, -3 V, -34 dB).	156
5.20	Experimental setup for optical injection operation. PC, fibre-based polarization controller.	158

5.21	Characterization of the inter-mode optical injection: (a) wavelength of the master laser as a function of the voltage of the slave QD-OFC. (b) Spectral power of the comb laser as a function of its wavelength and the master laser wavelength. OIB, optical injection broadening regime. FR, free-running regime.	159
5.22	Characterization of the intra-mode optical injection: (a) optical spectra of the QD-OFC in free-running (black) and in optical injection (gold) operation. (b) Spectral power of the comb laser as a function of its wavelength and the master laser wavelength. OIB, optical injection broadening regime. FR, free-running regime.	160
6.1	Illustration of the nondegenerate FWM process, the interaction of the drive and probe photons leads to the generation of signal and idler. . .	164
6.2	Contributions from carrier-density pulsation (navy), carrier heating (blue), and spectral-hole burning (purple) to the FWM efficiency. The cases for stokes and antistokes are represented by All (+) and All (-), respectively. From Ref. (D. Nielsen and S. L. Chuang, 2010). . .	166
6.3	FWM efficiency as a function of frequency detuning for (a) and (b) bulk. The stokes case is defined as $\Delta f > 0$ in this paper. From Ref. (Akiyama, Kuwatsuka, et al., 2002).	167
6.4	Characterizations of an epitaxial self-mode-locked QD laser on Si: (a) sech^2 -shape optical pulse and (b) RF response. From Ref. (Liu, Jung, et al., 2018).	168
6.5	Experimental schematic for light squeezing in microresonators. From Ref. (Y. Zhao et al., 2020).	169
6.6	(a) Light-current characteristics of the QD (burgundy) and QW (jade) laser. Measured and calculated curves are performed by solid and dashed lines, respectively. Experimental optical spectrum of (b) QD and (c) QW laser at $2 \times I_{th}$. Calculated mode powers are performed by the black points. Measurements are taken at 25°C	177
6.7	Optical spectrum (jade) and corresponding free spectral range (FSR) as a function of longitudinal mode frequency (burgundy) for (a) QD and (b) QW laser at $2 \times I_{th}$. The burgundy solid lines are guiding lines for the variation of FSR.	178
6.8	Experimental setup for nondegenerate four-wave mixing experiments. From Ref. (Jianan Duan, Weng W Chow, et al., 2021).	179

- 6.9 Optical spectra in stokes FWM operation for (a) QD laser with frequency detuning of 30 GHz and (b) QW laser with frequency detuning of 110 GHz (probe-drive mode number difference $\Delta m = 1$). The spectra with the increase of probe power are marked in different colors. 180
- 6.10 (a) Mapping of the calculated signal power versus drive power $lg(r_{sd})$ as a function of the probe power versus drive power $lg(r_{pd})$ and the frequency detuning $\Delta\nu$ for the QD laser. (b) r_{sd} versus r_{pd} for QD laser with different $\Delta\nu$ 181
- 6.11 (a) r_{sd} versus r_{pd} with $\Delta\nu \approx 110$ GHz for QD (dotted line) and QW (dashed line) laser. (b) r_{sd} versus $\Delta\nu$ with $r_{pd} = 0.02$ for QD (dotted line) and QW (dashed line) laser. Experimental results are shown by the symbols. 182

LIST OF TABLES

<i>Number</i>	<i>Page</i>
1.1 Comparison of the price and wafer diameter for various III-V substrates and Si and SOI substrates. From Ref. (J. C. Norman, Daehwan Jung, Wan, et al., 2018)	6
4.1 Main parameters of the QD-DFB laser in different operating conditions.	120
5.1 Parameter values used in numerical simulations.	146
6.1 Device parameters. [†] Computed for QW embedding QDs.	175
6.2 Model input parameters. [†] Calculated from $C_{2d} = C_{3d}/d_{qw}^2$ with $C_{3d} = 1.7 \times 10^{-38} m^6 s^{-1}$	175

Chapter 1

INTRODUCTION

The introduction sets the context and the motivations of this thesis. First, key-features and current challenges of fibre-optics communication networks, photonic integrated circuits and quantum technologies are described. Then, a brief history of quantum-dot (QD) lasers is recalled as well as their potentials for the aforementioned applications. The well developed GaAs-, InP- and Si-based InAs QD lasers are introduced along with the main breakthroughs. Exploiting the nonlinear properties of QDs is the central point of the dissertation. To this end, QD lasers operating with external control are introduced with the view to propose novel solutions for photonic integration to realize isolator-free transmitters, optical frequency combs, all-optical wavelength converters, self-mode-locked source and light squeezing. Finally, the overall organization of the manuscript will be detailed at the end of this introduction chapter.

1.1 Booming optical network and data centers

During the past decades, our modern society is being reshaped by the emergence of new technologies. Examples as internet of things (IOT) constitute a network of physical objects including wearables, vehicles, buildings, and machinery that are embedded with sensors, software, and network connectivity (M. Chang, 2016). The International Telecommunication Union (ITU) predicted that the overall mobile data traffic will reach 5 zettabytes (ZB) per month (see Fig. 1.1). In this context, high-speed and low-latency communication network based on the fifth generation (5G) is regarded as an essential solution for the interconnections and data transmission over the internet by providing a sufficient transmission capacity. Nowadays, the modern communication society is based on the long-haul fibre-optic networks in which the generated data are transported. Depending on the nature of optical fibres, three principal wavelength windows are widely exploited. The first C-band (1530-1565 nm) window in which the optical loss below 0.2 dB/km is the preferred option for long-haul optical communication. The whole network thus benefits from a reduced number of optical amplifiers with light propagating in this low-loss window. The chromatic dispersion is another important parameter of optical fibre, which is the origin of pulse broadening during the propagation

of light. The second O-band (1260-1360 nm) window in which the chromatic dispersion being null is therefore suitable for short-reach communications including the supercomputers and data centers. Third, the L-band (1565-1625 nm) has been another popular low-loss transmission window for wavelength-division multiplexing (WDM) and erbium-doped fibre amplifier (EDFA) technologies, owing to its much larger optical bandwidth than the conventional C-band. The exponential growth of data traffic expands the markets for Telecom and Datacom. In 2026, the global optical transceiver market is estimated to be doubled to 20.9 billion US dollars (see Fig. 1.2).

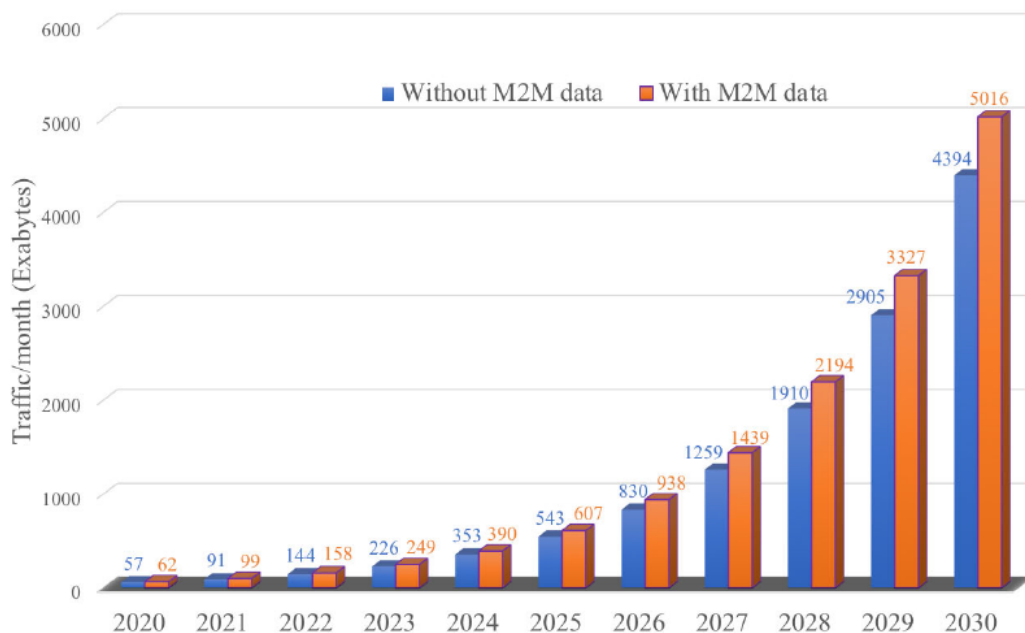


Figure 1.1: Global mobile data traffic forecast by ITU. Overall mobile data traffic is estimated to grow at an annual rate of around 55 percent in 2020–2030 to reach 607 exabytes (EB) in 2025 and 5,016 EB in 2030. M2M, machine-to-machine. (Source: Cisco).

Driven by the huge demand for Artificial Intelligence (AI) algorithms, consumer applications, such as social networks and media applications, and the digitalization of companies during the on-going worldwide COVID-19 pandemic, the data center server market has been boosted. To meet the requirement of transmission capacity and improve the performance of data center, the high-bandwidth communication link is solution of low-cost and energy-efficiency. At present, the optical transceivers for data centers include laser light source, modulator, (de)multiplexer, and photodetector (Cheng et al., 2018). Especially, the laser source is of significant

2020-2026 optical transceiver revenue growth forecast by market segment

(Source: Optical Transceivers for Datacom & Telecom Market 2021 report, Yole Développement, 2021)

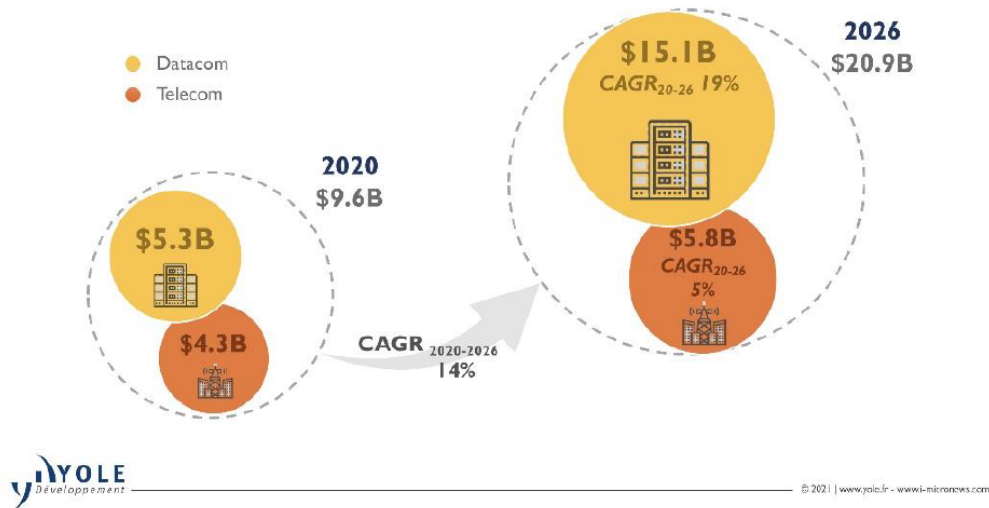


Figure 1.2: Global optical transceiver market forecast. Annual revenue in 2026 is estimated to increase to US \$ 20.9 billion. (Source: Yole Développement).

importance to determine the modulation bandwidth and optical link architectures. Figure 1.3 schematically depicts the anatomy of different optical link architectures. The conventional transceiver design for a single channel link is shown in Fig. 1.3(a). In this case, the single-wavelength laser source is directly modulated; its output signal is then sent into optical fibre for transmission until it is finally captured by the photodiode to be demodulated. Nevertheless, driven by the huge demand to utilize the vast amount of bandwidth offered by optical fibres, wavelength-division multiplexing (WDM) solutions have evolved quickly, which allows different data streams at different frequencies to be sent over a single optical fibre while ensuring the independence of each channel (Brackett, 1990). To this end, one of the commonly used link architecture is based on distributed feedback (DFB) laser arrays, as depicted in Fig. 1.3(b). All modulated signals from each channel need to be combined by a multiplexer (Mux) before they are sent into optical fibre. At the receiver side, a demultiplexer (DeMux) is utilized to retrieve the signal from each channel. Nevertheless, this architecture still suffers from strong inconvenience once the transmission rate is improved to the Tbps regime, since a large number of individual lasers must be deployed. In this case, the foot-print of the whole system will be greatly increased towards monolithic integration. To overcome this issue, the generation of optical frequency combs that emit over 100 individual channel becomes promis-

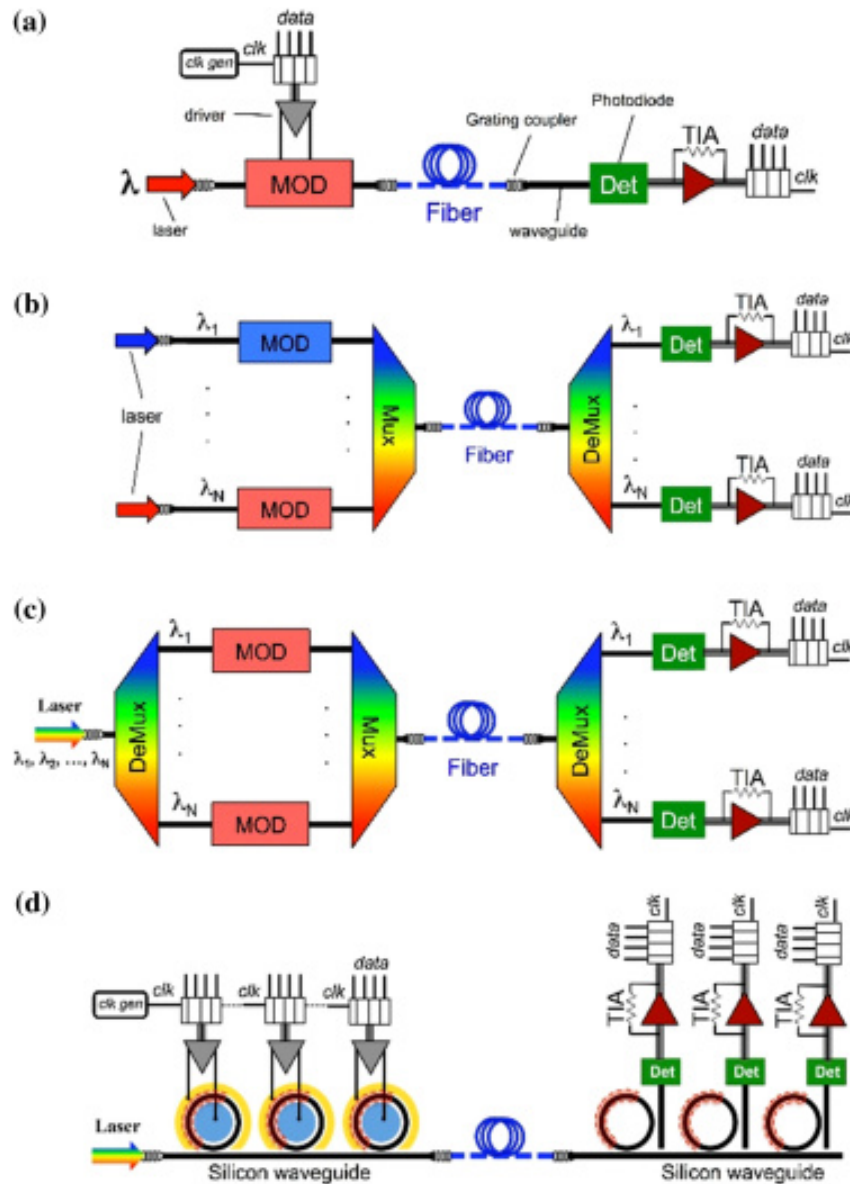


Figure 1.3: Anatomy of different link architectures: (a) single-wavelength point-to-point photonic link; (b) WDM photonic link based on individual single-wavelength lasers and broadband modulators; (c) photonic link based on comb laser, parallel broadband modulators, and DeMux/Mux. (d) WDM photonic link based on comb laser, cascaded microring resonators, and cascaded drop filters. MOD, modulator; Det, detector; TIA, trans-impedance amplifier; CLK, clock; Mux, multiplexer; DeMux, demultiplexer. From Ref. (Cheng et al., 2018).

ing. Figure 1.3(c) illustrates a potential architecture based on multi-wavelength comb source. The only difference from the aforementioned Mux/DeMux system is the participation of a supplement DeMux placed after the laser emission, whose presence contributes to separating and modulating each channel of the output light. On the other hand, breakthrough in wavelength-selective microring modulators is another solution for Mux/DeMux system. Corresponding architecture based on the frequency comb lasers and microring modulators is shown in Fig. 1.3(d).

1.2 Photonic integrated circuits

For decades, the exponential growth of computing capacity in supercomputers and data centers is based on the increased volume of silicon (Si) microelectronics, which is guided by Moore's Law. Since 2010, the advancement of microelectronics integration has slowed industry-wide. In this context, the closely interlocked tie between microelectronics and photonics becomes more crucial, given that the optical interconnects keep their exponential traffic growth. In the upcoming years, the rapidly increasing market demands for high-speed, energy-efficiency, and low-cost solutions for both digital integrated circuits (ICs) and photonic integrated circuits (PICs).

Photonic integration was once a challenge due to the fact that different optical functionalities are inherently dependent on a variety of materials, which not only limits the scalability of PICs, but also makes the PICs very expensive. From mid-2020, the commercialized 5 nm process technology (N5) of TSMC, Taiwan features a transistor density of around 170 million transistors per square millimeter, thanks to the mature complementary metal-oxide semiconductor (CMOS) foundry with a standard 300 mm Si wafer production line. However, the most sophisticated III-V compound semiconductor PICs contains only over one thousand components per chip (Hänsel and Heck, 2020), with most of them being produced in 75 mm III-V wafer production lines. It is worth stressing that the chip cost is highly dependent on the size of wafer, III-V substrates are thus orders of magnitude more expensive than Si due to their much smaller wafer sizes that limit scalability. Table 1.1 displays a comparison of III-V wafer costs and sizes with Si (J. C. Norman, Daehwan Jung, Wan, et al., 2018). In this context, silicon photonics exhibits its potential to create photonic components with high integration densities and low cost, by taking advantage of the CMOS foundry. In particular, the high-quality interfaces and refractive index contrasts between Si, Ge, SiO₂, Si₃N₄ and other dielectrics make silicon photonics an ideal solution for on-chip waveguide with strong light

confinement. Figure 1.4 shows the historical evolution of PIC integration densities based on three major platforms. The rapid growth of silicon PICs has surpassed their counterparts on native InP substrate. In 2019, it was reported that the number of components on a Si-based PIC approached one hundred thousand (Seok et al., 2019).

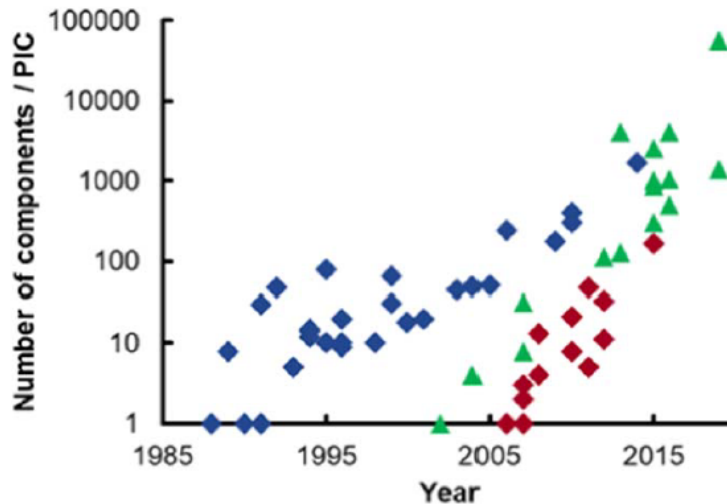


Figure 1.4: Trend of the components number on PICs based on three major platforms over the last three decades. Native indium phosphide (blue), silicon photonic (green), and hybrid silicon (red). From Ref. (Hänsel and Heck, 2020)

	InAs	InP	GaAs	SOI	Si
Substrate cost (US \$ / cm ²)	18.25	4.55	1.65	1.30	0.20
Maximum size (mm)	76	150	200	450	450

Table 1.1: Comparison of the price and wafer diameter for various III-V substrates and Si and SOI substrates. From Ref. (J. C. Norman, Daehwan Jung, Wan, et al., 2018)

It is used to be a challenge to integrate the direct-gap III-V materials on silicon substrate, due to the high densities of crystalline defects. Those undesired defects cause mismatches in their crystalline lattice constant and in their coefficients of thermal expansion (J. C. Norman, Daehwan Jung, Wan, et al., 2018), which degrade the performance of photonic components relative to their counterparts grown on native substrates. For instance, the threading dislocations induced by the mismatched interfaces raise up the nonradiative recombinations that decrease the internal efficiencies and device lifetimes. Those inconveniences become more critical when epitaxially

growing lasers on silicon. To address those issues, both heterogeneous and heteroepitaxy research has been focused on fabricating efficient sources on Si. Both approaches take advantage of the high-performance III-V materials and large-scale Si wafers, allowing for reducing packaging complexity and cost, and improving module assembly as well as higher levels of integration (Jones et al., 2019). The heterogeneous integration approach has been widely adopted in industry by Juniper Networks (B. R. Koch et al., 2013), Hewlett Packard Enterprise (Liang et al., 2016), and Intel (Jones et al., 2019).

For the purpose of achieving broader commercial viability of silicon PICs, the cost of heterogeneous integration is still too high. Such an issue is caused by its fabrication process. Based on such an approach, all III-V devices are firstly grown on a native substrate. Then the native wafer is bonded to Si. Finally, the III-V substrate will be removed and discarded. This approach would be analogous to the case of PIC on native substrate. Despite the progress, the expensive native wafers are still required. In this context, integrating III-V materials on silicon by epitaxial growth that avoids the cost of III-V substrate becomes very promising for photonic integration (A. Y. Liu and John Bowers, 2018). This approach is now pursued both within academia and commercially by AIM, IMEC, IBM, and NTT, among others. In addition, the direct epitaxy growth of III-V on Si can be considered to utilize the template assisted selective epitaxy technique which allows for minimizing the threading dislocations and defects (Wirths et al., 2018).

Since the first demonstration of high-performance quantum-dot (QD) laser that was epitaxially grown on Si (T. Wang et al., 2011), huge breakthrough in silicon photonics greatly improves the performance of both the active components such as lasers, modulators, photodetectors, and non-reciprocal components such as isolators and circulators. Today, the epitaxial III-V/Si process is regarded as the first solution for the next generation of high-speed and low-cost PICs.

1.3 Quantum technologies

Since the demonstration of quantum mechanism, including test of entanglement (Freedman and Clauser, 1972), violation of Bell's inequalities (Aspect, Grangier, and Gérard Roger, 1982), generation of squeezed light (L.-A. Wu et al., 1986), single-photon generation (Grangier, Gerard Roger, and Aspect, 1986), quantum teleportation (Bouwmeester et al., 1997) and loophole-free tests of Bell nonlocality (Shalm et al., 2015), quantum technologies are on the way to reshape the future of

internet. Indeed, interests in quantum computing from both academia and industry have been boomed up during the past years. A quantum computer (QC) is said to have n quantum bits (qubits) if it has a Hilbert space of 2^n dimensions and so has available 2^n mutually orthogonal quantum states (Steane, 1998). In theory, a QC is expected to perform tasks which surpass the capabilities of today's classical digital computers, as long as it has a large number of qubits, an efficient quantum algorithm and a well controlled quantum error correction (Preskill, 2018). Despite the fact that QCs will not be commercially available in the near future due to their high sensitivity to environmental noise, on-going researches are pursuing this goal. Pioneering studies revealed that photons are the ideal carriers of quantum information, owing to their distinguished features such as low-noise and high degree of coherence which enable stable operations at room temperature. During the past decades, extensive studies revealed that quantum states of light such as single photons, entangled-photon pairs, and quadrature-squeezed light play crucial roles in versatile applications. For instance, optical solitons are robust waveforms that preserve their shape upon propagation in dispersive media and can be found in a variety of nonlinear systems. In engineering, they are known from their high optical bandwidth in theory and are regarded as potential solutions for terabit optical coherent communications, atomic clocks, ultrafast distance measurements, dual-comb spectroscopy, and the calibration of astrophysical spectrometers. Driven by the growing demand for a high secure communication system, quantum key distribution (QKD) that is based on quantum laws is regarded as an essential element of the future quantum safe infrastructure including quantum-resistant classical algorithms and quantum cryptographic solutions (Diamanti et al., 2016). Firstly proposed by Ekert, 1991 and Bennett, Brassard, and Mermin, 1992, entangled photon source is a promising solution for QKD owing to its high tolerance for channel loss and high robustness to environmental fluctuations (Yin et al., 2017). In 2018, the first intercontinental quantum-secured communication based on QKD was realized with Chinese satellite Micius (S.-K. Liao et al., 2018), efficient entangled photon source is thus crucial in the upcoming era of satellite QKD. Last, squeezed light is also interesting from both fundamental and practical points of view. Its definition comes from the mechanism that fluctuations in one quadrature of the optical amplitude drop below the level of vacuum noise. Such a ultra-low noise source can thus be utilized to improve the measurement sensitivity in applications ranging from gravitational wave detection (Aasi et al., 2013) to biology (Taylor et al., 2013). Moreover, light squeezing is regarded as a potential technique to develop the laser

source for continuous variable information processing in the future QCs (Braunstein and Van Loock, 2005).

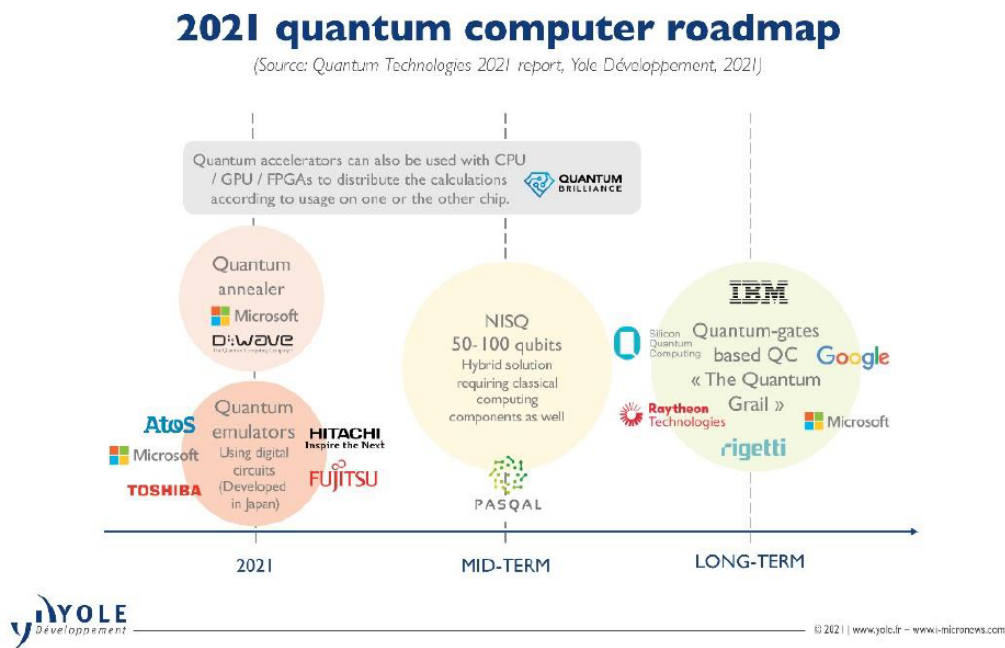


Figure 1.5: Quantum computer roadmap. Quantum annealer, the noisy version (with rather poor quality qubits) of adiabatic quantum computing. NISQ, Noisy Intermediate-Scale Quantum. Quantum-gate, simple unitary operations on qubits. (Source: Yole Développement).

Figure 1.5 depicts the roadmap for developing a QC. In 2021, only D-Wave from Canada is manufacturing and shipping quantum annealers, which is the noisy version of adiabatic QC. Those using machines are restricted to optimization problems due to the poor quality qubits. Meanwhile, Japanese companies are developing quantum emulators that are based on classical digital ICs. On the way to develop a real QC, highly scalable and energy-efficiency ICs and PICs will play essential roles in quantum computing. To meet the requirement of quantum information processing as well as reach a high level of component integration, integrated quantum photonics (IQP) that takes advantage of mature CMOS industry is a compelling platform for the future of quantum technologies (Jianwei Wang et al., 2020). A quantum light source that is IQP available is thus of significant importance, given that photons provide the only viable technology to connect distributed quantum systems, or for quantum communication systems (Gisin et al., 2002). Generation of single photon and entangled photon pairs were available in 1970s, however, the quality of such sources were not satisfactory enough at that time. Until 1995, the first high-quality, intense

source of polarization-entangled photon pairs became available with table-top type-II spontaneous parametric down conversion (SPDC), which enabled the production of all four EPR-Bell states (Kwiat et al., 1995). Today, the most widely used approach for generating quantum states of light is based on optical conversion processes in nonlinear materials. Figure 1.6 illustrates two well developed techniques. The first approach that is SPDC relies on the nonlinear light-matter interaction between a pump field and a medium with second-order nonlinear susceptibility $\chi^{(2)}$, in which the pump photon is destroyed to create two correlated photons, signal and idler, respectively. The second approach is to utilize a nonlinear medium with third-order susceptibility $\chi^{(3)}$. The entangled-photon pairs are created by converting two pump photons, which is known as spontaneous four wave mixing (SFWM) process. Prior studies demonstrate that all the aforementioned three quantum states of light can be generated through SPDC and SFWM (Spring et al., 2013; Samara et al., 2019; Lvovsky, 2015). In this context, a platform that is rich in optical nonlinearities becomes crucial to efficiently generate, transmit, and detect those non-classical states of light. Depending on the nature of material, silicon, silicon nitride (SiN), Lithium niobate (LN), and III–V semiconductors such as InP, InAs, $\text{Al}_x\text{Ga}_{1-x}\text{As}$, GaN, AlN, and InSb are commonly used nonlinear materials and platforms for IQP.

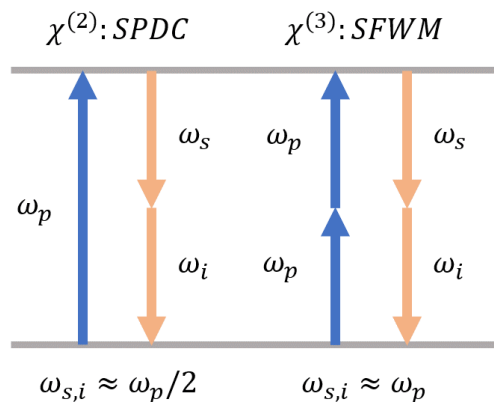


Figure 1.6: Quantum light generation in a nonlinear medium that relies on $\chi^{(2)}$ (spontaneous parametric down-conversion) or $\chi^{(3)}$ (spontaneous four-wave mixing) process, in which one or two pump photons (ω_p) are converted into correlated signal (ω_s) and idler (ω_i) photons, respectively.

1.4 Quantum-Dot laser

Quantum confined hererostructure

Since the first demonstration of semiconductor laser in 1960, huge progress has taken place. Figure 1.7 displays the evolution of the heterostructure and the density of states for different active region of laser. Significant performance including room temperature operation and continuous wave lasing was firstly reported with a device whose gain medium was made of bulk heterostructure (Kroemer, 1963; Alferov et al., 1971), as shown in Fig. 1.7(a-1) and (a-2).

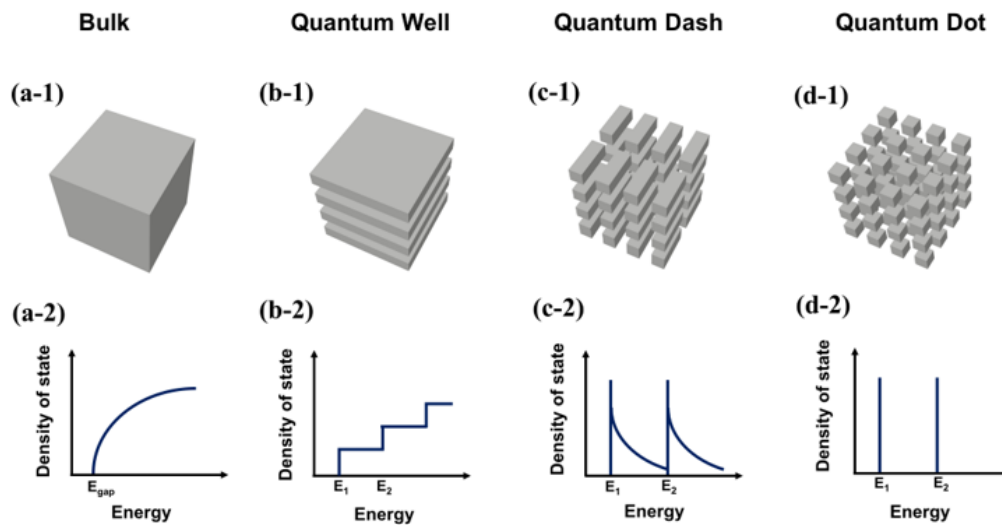


Figure 1.7: Structure and evolution of the density of states (DOS) for semiconductor structures with different degrees of dimensionality. (a-1, a-2) bulk, (b-1, b-2) quantum-well (QW), (c-1, c-2) quantum-dash (QDash), and (d-1, d-2) quantum-dot (QD). From Ref. (Frédéric Grillot, Jianan Duan, et al., 2021).

Then, benefiting from the developments of the molecular beam epitaxy (MBE) technique, ultra-thin film with a thickness of a few nanometer (nm) was available in earlier 1970s (Cho, 1971). Such a breakthrough allowed for confining the carriers within one dimension thus improving the injection efficiency; the first quantum confined laser whose active region was made of quantum-well (QW) heterostructure was reported in 1975 (Van der Ziel et al., 1975). As depicted in Fig. 1.7(b-1) and (b-2), by reducing the spatial dimensions of the nanocrystal that approaches de Broglie wavelength of carrier (~ 10 nm), the quantum confinement of electrical carriers occurs and leads to a quantization of the density of states. Compared to

the bulk heterostructure that has a continuous electron energy band, the discrete energy levels offered by QW gives the laser a superior performance such as a much lower threshold current. If we go a step further by reducing the freedom of carriers within three spatial dimensions, we have another type of heterostructure named as quantum-dot (QD). As shown in Fig. 1.7(d-1) and (d-2), this kind of complete spatial quantization that exhibits an atom-like density of states in theory leads to an ultimate carrier confinement, which is a benefit to develop high-performance photonic devices. The concept of QD laser was firstly proposed by Arakawa and Sakaki, 1982. Twelve years later, Kirstaedter et al., 1994 reported the first QD laser operating at 77 K, which was followed by R. Mirin, A. Gossard, and Bowers, 1996 who demonstrated the first clear evidence of the atom-like density of states. Owing to the complete spatial quantization, QD lasers exhibit superior performances to bulk and QW devices, including a lower threshold current density (G. Liu, Stintz, et al., 1999), a higher thermal stability (Mikhrin et al., 2005), and a higher material gain as well as differential gain (Bhattacharyya et al., 1999; Pallab Bhattacharya et al., 2000). Last, the quantum-dash (QDash) is also a commonly used gain medium of laser, which looks like an elongated QD whose electronic properties are rather intermediary between the QD and the QW, as depicted in Fig. 1.7(c-1) and (c-2). This kind of nanostructure is usually caused by the complex strain distribution along with the small lattice mismatch at the interface between the active region and the substrate, which is discussed hereinafter.

Quantum-Dot laser for photonic integrated circuits

Despite the advantages in theory, it was once a challenge to epitaxially grow QDs. One initial approach was to grow arrays of QDs in a patterned mesa-etched QW, which was a dot-in-well (DWELL) structure (Miyamoto et al., 1987). Nevertheless, the etched QW layer not only induces some radiative recombinations but also gives rise to the nonradiative defects, which alter the material quality of the matrix of nanostructure. Therefore, a new approach that allows for growing self-assembled QDs in absence of the QW layer became a preferred option. In mid-1980s, it was reported that MBE growth of thin InAs layers on GaAs substrate led to the formation of QDs (Goldstein et al., 1985). Such a finding led to the first demonstration of self-assembled InAs QDs on GaAs (Leonard et al., 1993; Moison et al., 1994) and then the first InAs/GaAs QD laser in mid-1990s (Kirstaedter et al., 1994). In the same timeframe, the atom-like density of states was first verified in single QDs via photo- and cathodo-luminescence techniques (Marzin et al., 1994; Grundmann et al.,

1995). Soon after that, room temperature lasing from QDs was achieved in 1996 (R. Mirin, A. Gossard, and Bowers, 1996; Kamath et al., 1996; Shoji et al., 1996). These lasers first operated between 1000 and 1100 nm and then exhibited room temperature lasing at 1310 nm (Huffaker et al., 1998), which was highly desired by fibre-optic communication society. More recently, InAs QDs that are facilitated by the direct bandgap of GaAs are regarded as an ideal solution for single-photon generation owing to their high probability to be channeled into a desired waveguide mode (Arcari et al., 2014). Today, GaAs wafer has been a well-known, mature material platform for both classical and quantum photonic integration. Huge progress in GaAs-based photonic devices including waveguides, modulators (Walker, Bennion, and Carter, 1989), and single-photon detectors (Sprengers et al., 2011) paves the way for future high-performance quantum simulation and computing (Collins et al., 2013).

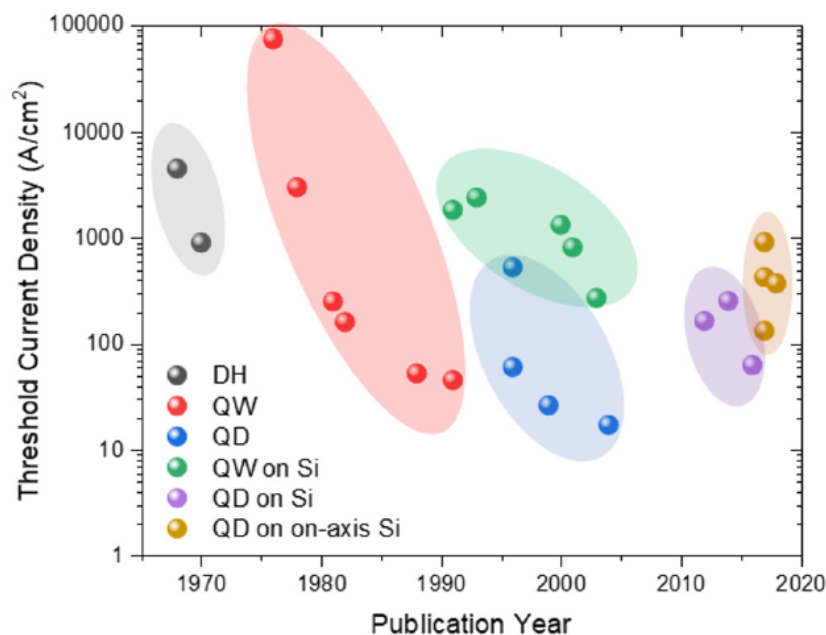


Figure 1.8: Threshold current density versus publication year for semiconductor lasers starting with double-heterostructure (DH) and then moving to quantum confined devices. Results for QW and QD lasers are shown for growth on native substrates and Si with the most recent results moving to CMOS-standard on-axis Si as opposed to the miscut substrates used previously. From Ref. (J. C. Norman, R. P. Mirin, and John E Bowers, 2021)

InP is also a well developed platform for photonic integration. InAs QDs grown on InP substrate is a commonly used approach for light generation at 1550 nm (C-band).

Nevertheless, the formation of QDs on InP is much more challenging than on the GaAs substrate. Until 1998, the first InAs/InP QD laser emitting at $\sim 1.84 \mu\text{m}$ at 77 K was reported by Ustinov et al., 1998. In the same year, room temperature lasing from QD on InP substrate was realized (Kenichi Nishi, Yamada, et al., 1998). The differences between the InAs/GaAs and the InAs/InP systems come from three aspects. First, the lattice mismatch for InAs/InP (3%) is smaller than that for InAs/GaAs (7%). Second, InAs/InP QDs exhibit less confinement potential for electrons, but a stronger confinement for holes. Third, the InAs/InP material shares the same cation (In), whereas the InAs/GaAs shares the same anion (As) at the interface (M. Gong et al., 2008). The small lattice mismatch and the complex strain distribution easily result in the formation of the self-assembled QDashes instead of QDs. To address this issue, employing special InP wafers such as miscut (100) and misoriented (311) along with various innovations in the growth process can be considered (Khan, T. K. Ng, and Ooi, 2014). Benefiting from the mature active and passive components, InP-based optical transceivers still dominates the commercial sales of PICs over this time period (Arafin and Coldren, 2017).

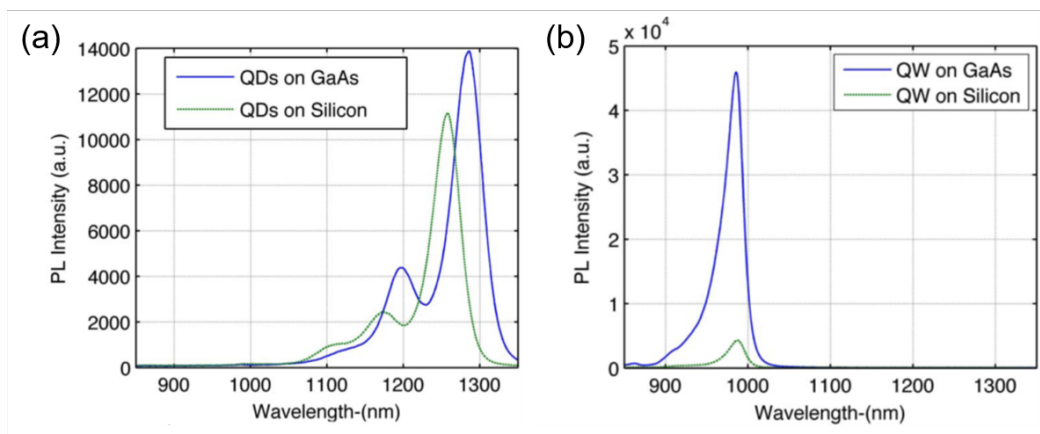


Figure 1.9: Comparison of the room-temperature Photoluminescence of (a) single InAs QD layer and (b) single 8 nm InGaAs QW grown on either GaAs (blue) or silicon (green) substrates. From Ref. (A. Y. Liu, Srinivasan, et al., 2015).

As discussed in Sec. 1.2, epitaxially growing III-V laser on Si substrate has been an interesting topic in the past years, since it paves the way for a much cheaper PIC solution for optical transceivers. A good news is that the QDs exhibit a high degree of tolerance for the defects that arise when III-V materials are directly grown on Si (A. Y. Liu, Srinivasan, et al., 2015). Figure 1.9(a) displays the photoluminescence (PL) of a single InAs QD layer either grown on GaAs (blue) or Si (green) substrate.

Same measurements for a single 8 nm InGaAs QW are shown in (b) for comparison. A large degradation of PL intensity by a factor of 10 takes place by moving the QW from the native substrate to the Si. In contrary, the PL intensity of the QD on Si is comparable with that of the QD on GaAs. Such an important property is attributed to the reduced ambipolar diffusion of injected carriers in QD layers (JK Kim et al., 1999). The first InGaAs/GaAs QD laser on silicon operating at 80 K was reported in Linder et al., 1999. In 2005, the first room temperature InGaAs/AlGaAs QD laser on silicon was available (Mi, Bhattacharya, J. Yang, et al., 2005). Then, the well-studied 1.3 μm InAs/GaAs QD lasers could be grown on Si by either wafer bonding (Tanabe, Watanabe, and Yasuhiko Arakawa, 2012) or direct growth (T. Wang et al., 2011). In contrary, QWs are much more sensitive to those defects than QDs, hence it is a challenge to fabricate a Si-based QW laser which is able to rival those on native substrate. Figure 1.8 illustrates the effects of defect tolerance of QD and QW lasers on different substrate. The performance in term of the threshold current density of the QD lasers on silicon is comparable with those on native substrate, whereas the huge discrepancy between the QW lasers on silicon and those on native substrate remains to be minimized. Recent studies reveal that QD lasers on silicon are sources of high thermal stability (Shang et al., 2021), very long device lifetime (J. C. Norman, R. P. Mirin, and John E Bowers, 2021), low noise properties (Jianan Duan, Y. Zhou, et al., 2020), low linewidth enhancement factor (α_H -factor) (Duan, Huang, Jung, et al., 2018), high tolerances for back-reflection (Jianan Duan, Heming Huang, et al., 2019; H. Huang et al., 2020), and rich optical nonlinearities (Jianan Duan, Weng W Chow, et al., 2021). All these properties make QD lasers promising for low-cost, energy-efficiency, isolator-free and small-footprint photonic integration. Last but not least, it is more challenging to directly grow 1.5 μm InAs/InP QDash laser on Si than InAs/GaAs on Si system, due to the large lattice mismatch between InP and Si being 8%. In contrary, the lattice mismatch between GaAs and Si is cut to 4%. Such an issue can be partially addressed by utilizing V-grooved silicon substrate (Zhu et al., 2018). Recently, the first C-band room-temperature continuous-wave electrically pumped QDash lasers on CMOS standard (001) silicon substrates are available (Xue et al., 2020; Luo et al., 2020).

1.5 Motivations of the dissertation

As aforementioned, the recent evolution of optical communication systems is towards short-reach applications that require high data throughputs. Examples as consumer applications, digitalization of companies, data center servers and IOT have

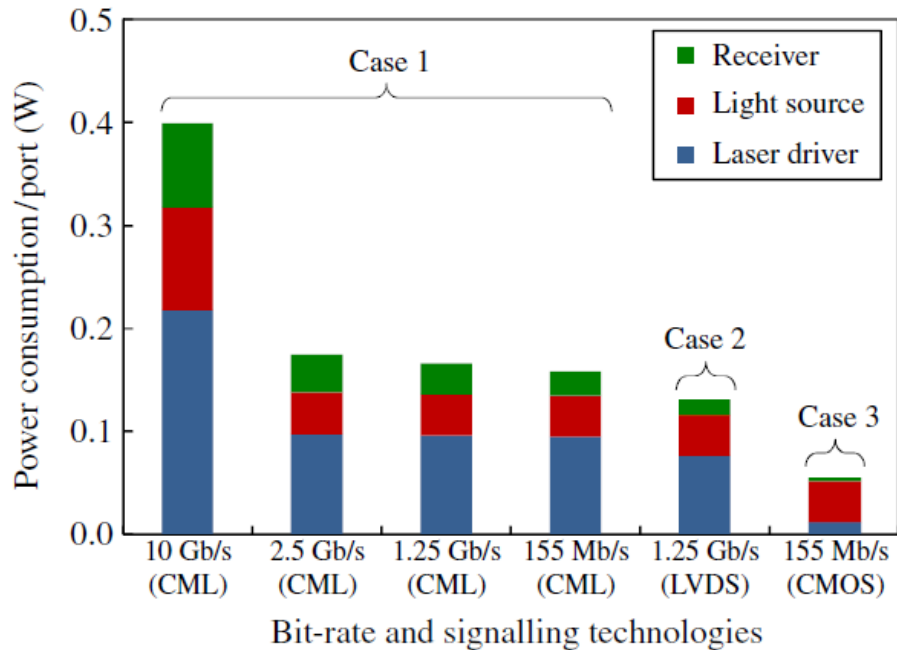


Figure 1.10: Estimated power consumption of DFB laser-based optical transceivers at different bit-rates with different signaling interfaces. From Ref. (K.-L. Lee et al., 2012)

emerged and been boosted. The new requirements in terms of cost and energy consumption set by novel short-reach applications therefore need to be considered in the design and operation of a new generation of on-chip laser sources, which is the main topic of the present dissertation. The evolution of the requirements on new optical transmitters takes two forms. First, with the exponential growth of data transmission supported by data center servers, their power consumption is also a matter of significant importance. Activities must be conducted to address the increased public concerns about climate change and environmental issues (Cook, 2011). Figure 1.10 depicts the total per-port power consumption of optical transceivers in various bit-rates operations. With the increase of bit-rates, the total power consumption is largely increased. Compared to the receiver (green), it is shown that the majority of power is consumed by the light sources (red) and their drivers (blue). In this context, QD laser is a promising solution for energy-efficient applications. In 2017 and 2018, researchers at the University of California Santa Barbara reported QD lasers on silicon with threshold currents as low as 9.5 mA, single-facet output powers of 175 mW, ground state lasing up to 80 °C, wall-plug-efficiencies of 38.4%, and extrapolated lifetimes in excess of 10,000,000 h (Daehwan

Jung, J. Norman, et al., 2017; Daehwan Jung, Z. Zhang, et al., 2017; Daehwan Jung, R. Herrick, et al., 2018). Second, the central point of this thesis is to exploit the nonlinear properties of QDs, aiming at developing novel optical functionalities including reflection-resistant transmitters, high-bandwidth as well as low-noise optical frequency combs, all-optical wavelength-converters with improved efficiency, self-mode-locking (SML) and generation of squeezed light. Based on both theoretical analysis and experimental results, we believe that QD laser is an ideal solution for overcoming the challenges for those applications, which are introduced hereinafter.

Reflection-resistant quantum-dot laser

In photonic integration, one of the major challenges comes from the parasitic reflections that emerge from the various active and passive transitions and regrowth interfaces. Prior studies on the laser dynamics subject to external optical feedback revealed that those unwanted reflections can easily lead to strong destabilization of laser. Examples as mode-hopping, low-frequency fluctuations, and coherence collapse (Tkach and Chraplyvy, 1986; Mørk, Mark, and Tromborg, 1990; Klaus Petermann, 1995) are observed to largely degrade the power penalty and transmission performance of lasers (Lenstra, Verbeek, and Den Boef, 1985; Heming Huang, Jianan Duan, et al., 2018). To overcome these issues, on-chip optical isolator is one solution. However, reliable optical isolators with high isolation performance and low cost remain to be developed (Lenstra, Schaijk, and Williams, 2019). Besides, the integration of an optical isolator also increases the footprint of PICs. Other approaches to improve the reflection resistance include reducing the threshold current by taking advantage of the fano laser configuration (Rasmussen and Mork, 2021) or optimizing the phase shift between the gain and loss gratings in the case of complex-coupled DFB laser (Perrière et al., 2021). Nevertheless, their improvements of reflection insensitivity remains limited. In this context, QD laser is regarded as an ideal source for isolator-free PICs, owing to its much higher degree of tolerance for optical feedback than its counterparts (Jianan Duan, Heming Huang, et al., 2019).

To further improve the reflection resistance of QD/QDash lasers, approaches that decrease the linewidth enhancement factor, which is also named as α_H -factor, or that increase the damping are worth to be considered (A. Y. Liu, Komljenovic, et al., 2017). In the case of QDash laser, the strong anisotropy of QDash makes the laser properties determined by the dash polarization with respect to the laser cavity axis. A prior study revealed that the α_H -factor changes with different QDash

orientation (Ukhanov et al., 2002). The feedback insensitivity of laser can thus be improved by well controlling the dash polarization. For QD laser that has a Fabry-Perot (FP) cavity, p-modulation doping that brings more holes in the active region is a commonly used approach to improve the laser performance. Recent studies reveal that the p-doping technique is beneficial for improving modal gain, differential gain, and thermal stability (J. C. Norman, Z. Zhang, et al., 2019). How does it impact the feedback insensitivity through the α_H -factor becomes interesting. In the case of single-frequency DFB laser, a positive optical detuning between the Bragg wavelength and the optical gain peak allows the laser to operate at a high temperature (Katsuyama, 2009), however, its influence on the nonlinear properties of QD laser remains to be studied. In this dissertation, the author tries to answer those questions by performing experimental results.

Quantum-dot-based optical frequency comb

The optical frequency comb (OFC) is a series of equally spaced spikes in the frequency domain. In 1999, the OFC based on a mode-locked laser was utilized as a revolutionary new approach for optical frequency measurements (Th Udem et al., 1999). Today, the OFC provides an approach for reliably and accurately counting optical cycles on the femtosecond time scale, which is required for realizing optical clocks (Diddams, Th Udem, et al., 2001). Beyond their initial purpose in precision spectroscopy and optical clocks, frequency combs also exhibit their potential for various emerging applications, including WDM in massively parallel coherent telecommunications (Marin-Palomo et al., 2017; Songtao Liu, X. Wu, et al., 2019), LIDAR (Trocha et al., 2018), dual-comb spectroscopy (Suh, Q.-F. Yang, et al., 2016), low-noise microwave generation (Papp et al., 2014), optical frequency synthesizers (Spencer et al., 2018), and astrophysical spectrometer calibration (Suh, Yi, et al., 2019). Generation of frequency combs are based on three commonly used approaches. The first one is mode-locking that utilizes a saturable absorber (SA) or another nonlinear element to provide a net increase in gain for pulsed operation (Thompson et al., 2009; Fermann and Hartl, 2013). The second one is to employ an electro-optical (EO) modulator driven by a microwave signal to impose a grid of sidebands on a continuous-wave laser (Carlson et al., 2018). The third approach relies on the Kerr nonlinearity that arises from resonant enhancement of light in whispering-gallery microresonators (Armani et al., 2003) or in ring-like resonators (Q. Li et al., 2017).

QDs is regarded as a promising material to be the active region for a mode-locked

laser (MLL). The major benefit comes from the inherent inhomogeneously broadened gain spectrum, which bringing both a broad emission spectrum and a low mode-partition noise leads to a high-bandwidth and flat-top frequency comb (ZG Lu, JR Liu, C. Song, et al., 2018). Not limit by that, the ultrafast gain/absorption recovery (Malins et al., 2006) and low amplified spontaneous emission (ASE) noise level (Yvind et al., 2008) in QDs allows for generating optical pulses with ultra-short duration, high repetition rates, and low timing-jitter. In this context, growing QD-based frequency comb lasers on Si by either wafer-bonding or direct growth gives insights for developing high-performance and low-cost PICs. Recently, mode-locking or frequency comb generation by utilizing QD on Si exhibits sub-picosecond pulse duration, kilohertz RF linewidth and 10 terahertz optical bandwidth (Liu, Jung, et al., 2018; Songtao Liu, X. Wu, et al., 2019; Kurczveil, C. Zhang, et al., 2018). In mode-locking, the reverse bias on the SA plays an important role to influence the dynamics of MLLs. Exploration of the mechanism behind it is thus interesting. To further improve the performance of frequency comb laser in terms of optical bandwidth and noise properties, investigations of the optical injection and the optical feedback operation are performed in this dissertation.

Quantum-dot-based quantum photonic integrated circuits

QDs play crucial roles in quantum technologies. To generate single-photon, commonly used approaches include SPDC mechanism and spontaneous emission from a two-level system (Senellart, Solomon, and White, 2017). In the latter case, epitaxial QDs made from various materials successfully realize single-photon generation from near infrared to ultraviolet spectral range, and from cryogenic to room temperature (Yasuhiko Arakawa and Holmes, 2020). Not limit by that, the generation of polarization-entangled photon pairs can also be realized from QDs with appropriate symmetry (Kuroda et al., 2013; Huber et al., 2018).

The control of optical nonlinearities in QDs is also meaningful for both classical optical communications and quantum photonic applications. Owing to their large optical nonlinearities with fast response speed (Akiyama, Ekawa, et al., 2005), QDs exhibit a high four-wave mixing (FWM) based nonlinear conversion efficiency (Sadeev et al., 2015; Heming Huang, Schires, et al., 2015). The advantages offered by FWM can be applied to WDM system, optical clock distribution and optical wavelengths converters (Cheng et al., 2018). More recently, single-section QD/QDash lasers that exclude the SA section demonstrate self-mode-locking effect by showing sub-picosecond pulse duration and kHz frequency-comb linewidth (Rosales, Mur-

doch, et al., 2012; Liu, Jung, et al., 2018). Sometimes it originates from unaccounted saturable absorption such as from uneven current injection. Nevertheless, SML can also result from the inhomogeneously-broadened bandwidth offered by QDs along with the FWM mechanism that causes the locking of beat frequencies among lasing modes (Weng W Chow, Songtao Liu, et al., 2020). Last, it is possible to broaden the scope of FWM to quantum technologies such as quantum frequency translators and light squeezing (Y. Zhao et al., 2020). In this context, investigations of the FWM of on-chip QD lasers as well as the nonlinear properties behind it become crucial for developing the next generation of both classical and quantum PICs.

1.6 Organization of the dissertation

This dissertation is organized as follows:

Chapter 2 reminds the fundamentals of QD lasers including the electronic structure, the gain broadening mechanisms, the relaxation oscillations and damping, the linewidth enhancement factor (α_H -factor), the optical spectral linewidth, and the nonlinear susceptibility. This introduction constitutes a substrate for the understanding of the various experimental and theoretical investigations conducted throughout the thesis.

Chapter 3 is devoted to studying the optical feedback dynamics of QD/QDash lasers that are grown on either native or Si substrate. Investigations of how the feedback dynamics is influenced by the laser configurations such as the p-doping in QDs and the different dash polarization are performed. To further explore the potential optimization of such transmitters in terms of the tolerance for inter-chip and intra-chip back reflections, the laser dynamics are analyzed in both short- and long-cavity feedback regimes. As a consequence, an optimum p-modulation doping level in QDs enables the laser a 16 dB improvement of the feedback insensitivity; rotating the dashes orientation from parallel to perpendicular to the cavity axis allows for increasing the critical feedback level by 11 dB. In addition, the epitaxial QD laser on Si exhibits a remarkable tolerance for chip-scale back-reflections without showing any chaos behavior. This study is of first importance for developing feedback resistant optical transmitters for isolator-free integration technologies.

Chapter 4 describes a single-frequency QD-DFB laser with a design of optical wavelength detuning (OWD) that denotes the mismatch between the Bragg wavelength and the optical gain peak. The OWD can be controlled by temperature variation. The impacts of the OWD on the lasing properties are investigated by the static

characteristics, the modulation properties and the dynamics under external optical feedback. Descriptions of two different methods (Amplified Spontaneous Emission and phase modulation) for extracting the α_H -factor are performed. On one hand, the QD laser exhibits a low intrinsic α_H -factor below 1, which gives insights for developing chirp-free optical transmitter. On the other hand, the laser performance improves with temperature, which is attributed to the reduction of the OWD. For the device studied, an increase of temperature from 15 to 55°C results in a decrease of the OWD from 30 to 10 nm. As a consequence of the OWD reduction, the threshold current and the α_H -factor show a 45% and a 43% decrease, respectively. Meanwhile, the modulation performance of laser improves in presence of the K-factor decreasing from 2.87 to 1.72 ns. In particular, the laser's tolerance for back-reflections exhibits an improvement of 9 dB with the reduction of OWD. This study paves the way for developing high-performance single-frequency lasers for uncooled and isolator-free applications.

In Chapter 5, the author investigate the dynamics of a 20 GHz epitaxial passively QD-MLL and a 102 GHz QD-OFC. Both devices are either direct-grown or wafer-bonded on Si substrate. With a view to understanding the dynamics of the QD-MLL and optimizing the cavity design to improve the laser performance, theoretical analysis based on a delay-differential equation (DDE) model by using measured parameters are performed. First, both calculated and experimental results suggest that QD is an ideal solution for ensuring a highly stable frequency comb generation owing to its near-zero α_H -factor. Second, a reasonable large SA length to total cavity length ratio is beneficial for reducing the pulse duration and improving the phase noise simultaneously. With the increase of SA section length ratio from 5% to 8%, a 15 dB increase of signal-to-noise ratio (SNR) along with 4-fold reduction of the RF linewidth is identified. Third, optical feedback operation is an efficient approach to improve the phase noise. In the optimum feedback condition, the QD-MLL exhibits a 13 dB increase of SNR along with a 40-fold reduction of the RF linewidth. Fourth, the optical injection operation is a reliable approach to improve the optical bandwidth. A 3.5-fold increase of the 3-dB optical bandwidth is achieved on the QD-OFC in the optimum injection condition.

In Chapter 6, investigations of the FWM mechanism in epitaxial QD laser on Si are performed. Another commercial QW laser is analyzed for comparison. Both theoretical analysis and experiments reveal that the FWM efficiency is improved by more than one order of magnitude by utilizing QD as the active region of laser rather

than QW. Besides, the FWM bandwidth of QD laser that exceeds terahertz is also twice larger than that of the QW one. These remarkable nonlinear properties of QD laser is attributed to its high $\chi^{(3)}$ nonlinear coefficient. This last study gives insights for developing compact, small-footprint, energy-efficient and low-cost self-mode-locked optical frequency combs and quantum light generators by taking advantage of the QD, which is of significant importance for the integrated WDM technologies on silicon and for the possible application in future quantum photonic integrated circuits.

Finally, Chapter 7 gives a general conclusion and the perspectives to this work.

Chapter 2

PHYSICS AND PROPERTIES OF QUANTUM DOT LASERS

The objective of this chapter is to recall the basic features of quantum-dot (QD) lasers. First, the electronic structure and carrier scattering processes are presented. The latter includes the capture and relaxation processes. Second, fundamental properties of QD lasers such as gain broadening mechanisms, linewidth enhancement factor, gain compression, relaxation oscillation frequency, damping factor, noise properties as well as nonlinear optical susceptibility are introduced.

2.1 Electronic structure of QD

Figure 2.1 schematically illustrates the electronic structure of the gain medium of QD laser. The whole active region consists of a three-dimensional separate confinement heterostructure (SCH or barrier), a two-dimensional carrier reservoir (RS or roughly the wetting layer) and QDs that are three dimensional confined. The quantum confinement of electrical carriers takes place once the crystal dimension is reduced below the de Broglie wavelength of carriers, which is about 10 nm. In this process, the critical diameter D_{min} that allows for carrier quantification is related to the material band offset ΔE_c , which is expressed as follows (Dieter Bimberg, Marius Grundmann, and Nikolai N Ledentsov, 1999):

$$D_{min} = \frac{\pi\hbar}{\sqrt{2m_e^*\Delta E_c}} \quad (2.1)$$

where m_e^* and $\hbar = h/2\pi$ account for the effective mass of electron and the reduced Plank constant, respectively. In the case of self-assembled QDs, a typical value of D_{min} varies from 3 to 5 nm, which is at the same order of magnitude of the dot dimension. Thus, the electronic structure of QDs can be approximately represented in the form of a three-dimensional potential well with discretized energy levels.

In the concept of QDs, carriers are usually treated as quasi-free particles within the SCH and the RS. In effective mass theory, the densities of states (DOS) for the SCH (per volume) and for the RS (per area) can be expressed as follows (Gioannini,

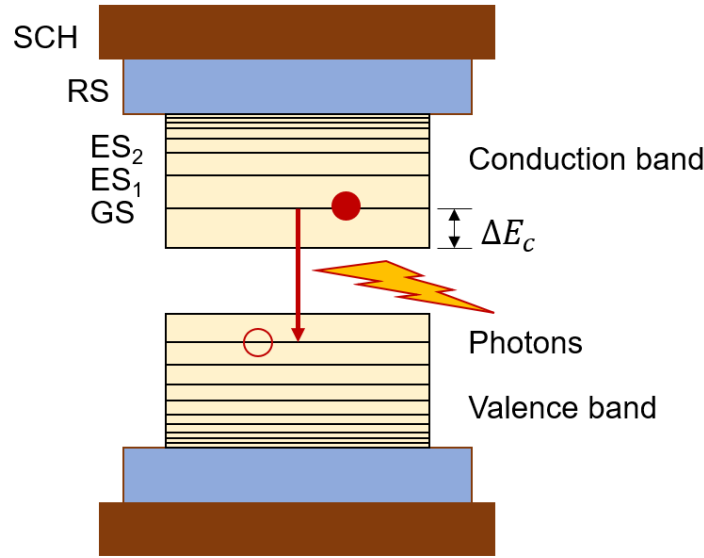


Figure 2.1: Schematic of a QD laser electronic band structure of electrons and holes.

2006):

$$\rho_{SCH} = d_{SCH} \left(\frac{2m_{SCH}^*}{2\pi^2\hbar} \right)^{2/3} \sqrt{E - E_{SCH}} \quad (2.2)$$

$$\rho_{RS}(E) = \frac{m_{RS}^*}{\pi\hbar^2 d_{RS}} u(E - E_{RS}) \quad (2.3)$$

where m_{SCH}^* and m_{RS}^* account for the effective mass of electrons in the conduction band (CB) or of holes in the valence band (VB) that are located in the SCH and RS, respectively. d_{SCH} and d_{RS} denote the thickness of the SCH and the RS, respectively. E_{SCH} and E_{RS} are the recombination energy from the SCH and the RS, and $u(E - E_{RS})$ denotes the step-like function. The quantized energy solutions that represent the ground state (GS) and the higher excited state (ES) transitions can be solved by using a 3D finite box approximation. The quasi-continuum carrier reservoir incorporating the localized energy states of the dots results in smaller energy separations and thus states overlapping at higher energies. In the CB, the discrete states are separated by a few tens of meV at lower energies. However, such a separation is reduced in the VB due to the heavier effective hole masses (Cornet et al., 2005).

In Coulomb interaction theory, electrons and holes in the semiconductor active region are bounded into excitons, in other word, electron-hole pairs. The Bohr radius of exciton is defined as the distance between the electron and the hole within

an exciton, whose length is of a few nanometers (Nozik, 2008). The exciton nature that can be modified by the confinement structure plays an important role in optical properties. Through the excitonic approach, semi-empirical models have been developed with a great success to reproduce the time resolved photoluminescence (TRPL) experiments, to reproduce the noise properties and to predict the modulation dynamics of QD semiconductor lasers (C. Wang, Zhuang, et al., 2016; T. Chen and Y. Liu, 2016). In this model, the vertical coupling is taken into account from two discrete states in QDs: a two-fold degenerate GS and a four-fold degenerate first ES. The lateral coupling among the QDs is involved in the RS. Despite the advantage, the excitonic approach has some limitations in predicting nonlinear behaviors such as the GS quenching effect and the impact of p- or n-type modulation doping. The former that occurs when QD lasers exhibit simultaneous GS and ES lasing is attributed to the asymmetry between electrons and holes (Virte, 2014). In the latter case, a step beyond by considering the electrons and holes separately is necessary (Sanaee and Zarifkar, 2015).

2.2 Carrier scattering process

The carrier dynamics in QDs is driven by the capture and the relaxation processes. With a current injected into a QD device, a high density carrier plasma is activated in the SCH (T. R. Nielsen, Gartner, and Jahnke, 2004). The carriers firstly traverse across the SCH before they reach the 2D RS. The carrier transportation time that is determined by the thickness of SCH is in the range of 1~5 ps. In general, the carrier transport in the SCH is a very fast process and has a minor influence on the overall carrier scattering process in the QDs. When the carriers are captured by the QDs, there are two carrier capture processes. In the first case, the carriers will relax through the higher energy levels of ES and eventually down to the GS. At this stage, the recombination between electrons and holes leads to the onset of lasing. The mechanisms that mainly contribute to the carrier capture and relaxation are carrier-phonon and carrier-carrier scatterings involving Auger effect, respectively, as illustrated in Fig. 2.2. In the second case, the carriers can directly move from the RS to the GS. This direct relaxation channel contributes to accelerating the carrier dynamics. In addition, this direct capture process also leads to a dual-state lasing operation in the presence of simultaneous emissions from GS and ES (Veselinov et al., 2007). Last but not least, the lateral coupling among the QDs and defects assistance are also alternative ways for increasing the carrier dynamics through carrier scattering (Sercel, Efros, and Rosen, 1999; Cornet et al., 2005).

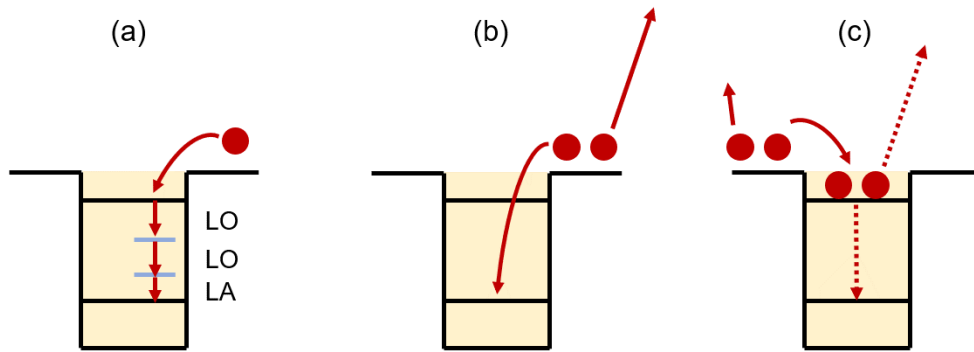


Figure 2.2: Illustration of the carrier capture and relaxation processes: (a) multi-phonon processes under low excitation density, (b) single Auger process, and (c) sequential Auger processes under high injection current density. Reproduced from Ref. (Ohnesorge et al., 1996)

Carrier capture in QD is driven by both Auger process and longitudinal optical (LO) phonon-carrier scattering (Ohnesorge et al., 1996). Different from the capture process in QW in which the carrier capture is dominated by the LO phonon-carrier scattering, that in QDs is more complicated. It is shown that the carrier scattering is dependent on the carrier density. At a high carrier density, the carrier-carrier scattering (e-e and h-e) from the RS into the QDs plays a dominant role in the carrier capture. However, the LO phonon-assisted capture that is temperature dependent becomes the most efficient process at a low carrier density. It is shown that scattering by electrons is more efficient than scattering by holes, owing to their smaller effective mass. In addition, it is worth stressing that the energy separation between the RS and the QD states strongly influences the capture rate. A larger energy separation decreases the Auger coefficients for all types of Auger process (ee, e-h, h-h, h-e), which means that carrier capture into the highest excited states is the most efficient process in QDs (Magnúsdóttir et al., 2002).

On the other hand, relaxation process in zero-dimensional QDs mainly relies on carrier-phonon interactions (Bockelmann and Bastard, 1990; Marcinkevičius, 2008), in which the carriers interact with multi-phonons including LO phonons and longitudinal acoustic (LA) phonons. In theory, this phonon-assisted relaxation process will slow down the relaxation rate in QDs, due to the enlarged energy level spacings compared to QW (H. Jiang and Singh, 1998; Urayama et al., 2001). Nevertheless, the observations of such a "phonon bottleneck" effect in self-assembled QDs have

always been circumvented. Prior studies revealed that other processes such as Auger processes (Morris, Perret, and Fafard, 1999; Ohnesorge et al., 1996), multi-phonon processes (Inoshita and Sakaki, 1992; Farfad et al., 1995) or defect-assisted phonon emission (X.-Q. Li and Yasuhiko Arakawa, 1997) could compensate for the effect of phonon bottleneck, and the relaxation rate could be even accelerated. All these peculiar properties offered by QDs result in the ultrafast carrier dynamics in presence of the capture and relaxation time on the order of picosecond. Such behaviors make QD promising for ultrafast optics. Last, modulation doping is an efficient approach to further increase the overall carrier scattering rate, owing to the doping-induced carriers that implement a much faster carrier-carrier scattering-assisted relaxation (Siegert, Marcinkevičius, and Q. X. Zhao, 2005).

2.3 Gain broadening mechanisms

In theory, ideal QDs exhibit atom-like discrete energy levels. Nevertheless, it is a challenge to grow these ideal QDs from a technical view, since all the dots need to be identical and have the same single energy level. In a real case, the QD laser have both homogeneous and inhomogeneous gain broadening mechanisms.

The nonuniformity QD size dispersion is the origin of the inhomogeneous gain broadening. Figure 2.3 display a comparison between the energy states of a self-assembled QDs (a) with and (b) without inhomogeneous broadening. In the former case, each dot has its own energy level, thus the combination of QDs results in the fluctuations in energy states and the gain spectrum is inhomogeneously broadened with a Gaussian-shaped energy bandwidth Γ_{in} . In the latter case, however, the high uniformly self-assembled QDs with identical energy levels do not suffer from this inconvenience and emit an ideal δ -function-like optical gain. From a technical view, it is a challenge to largely increase the number of dots while maintaining a high lasing performance in terms of the optical gain (Dery and Eisenstein, 2005). As a consequence of that, the full width at half maximum (FWHM) Γ_{in} of the inhomogeneously broadened gain spectrum is an approach to evaluate the uniformity of the QD size dispersion, and the typical values for GaAs-, InP- and Si-based QD lasers are in the range of 20 to 60 meV (Akahane, N. Yamamoto, and Tsuchiya, 2008; Kenichi Nishi, Takemasa, et al., 2017; Duan, Huang, Jung, et al., 2018). Evidently, a low inhomogeneous broadening assisted QD active region is beneficial for improving the current injection efficiency hence developing a single-mode laser with low threshold. Nevertheless, the inhomogeneous broadening is not always a drawback, since it provides an additional tunability to the gain profile. Taking

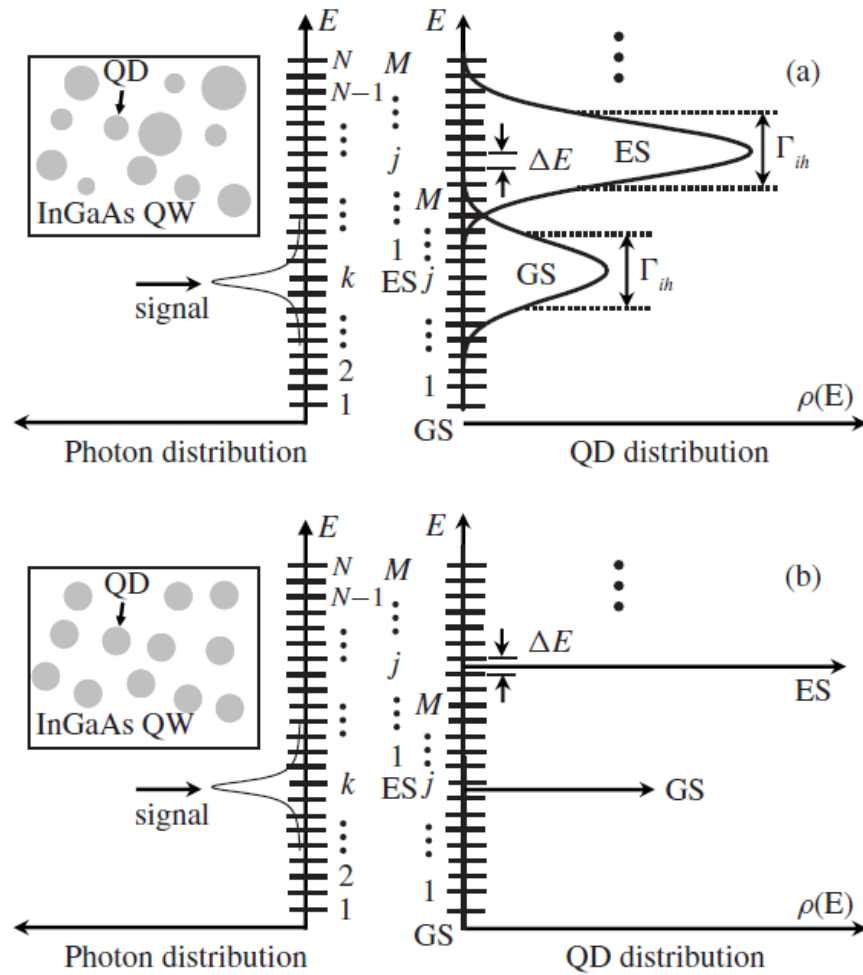


Figure 2.3: Schematic diagram of QDs (a) with and (b) without inhomogeneous broadening and their corresponding photon modes. GS, ground state ; ES, excited state. The QD size uniformity in the left inset are described by the Gaussian-shaped energy bandwidth Γ_{in} . From Ref. (Jungho Kim et al., 2010)

advantage of its ability to enlarge the optical bandwidth, such a mechanism is favorable for amplifiers, tunable lasers and optical frequency combs (Songtao Liu, X. Wu, et al., 2019).

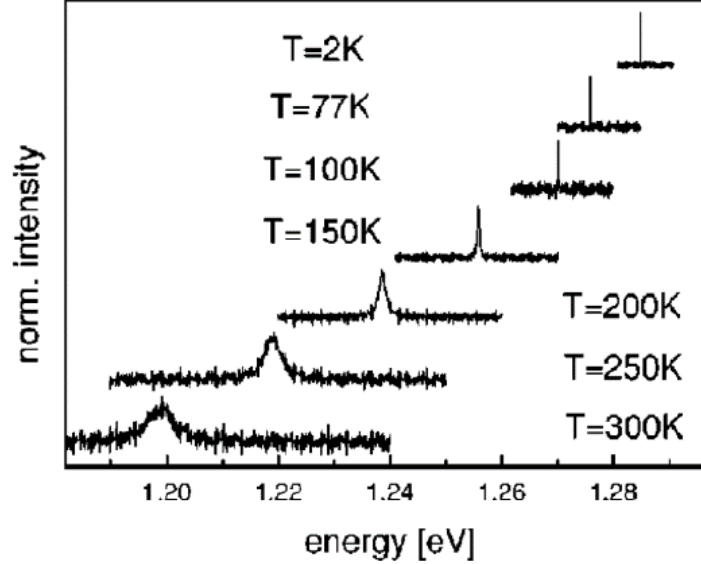


Figure 2.4: Photoluminescence spectrum as a function of temperature from a single InAs/GaAs dot. From Ref. (Bayer and Forchel, 2002)

The homogeneous broadening is determined and is proportional to the polarization dephasing rate, which corresponds to the decay time of the optical polarization associated with an interband transition (Schneider, Weng Wah Chow, and S. W. Koch, 2004). For a quasi-equilibrium carrier system, the dephasing time T_2 is approximated to twice the total carrier scattering time constant (Haug and S. W. Koch, 2009), and the FWHM of the homogeneously broadened spectrum for a confined QD lasing state can be expressed as (Nilsson, J.-Z. Zhang, and Galbraith, 2005):

$$2\hbar\Gamma_{hom} = \frac{2\hbar}{T_2} = \hbar\left(\frac{1}{\tau_{hh}} + \frac{1}{\tau_{he}} + \frac{1}{\tau_{ee}} + \frac{1}{\tau_{eh}}\right) + \hbar\frac{1}{\tau_{phon}} + \hbar\frac{1}{\tau_{recom}} \quad (2.4)$$

where the first term on the right-hand side accounts for the contribution of the Auger scattering process among electrons and holes (hh,he,ee,eh). The second term denotes the carrier-phonon interaction and carrier-carrier scatterings. The radiative recombination is described by the last term (Sakamoto and Sugawara, 2000; Borri et al., 2001; Matsuda et al., 2001). Compared to the Auger scattering process, the contributions of the other two mechanisms are much lower and negligible

(Nilsson, J.-Z. Zhang, and Galbraith, 2005). It is worth stressing that the homogeneous broadening exhibits an evident dependence of the temperature. Figure 2.4 depicts the photoluminescence (PL) spectra as a function of temperature of a single InAs/GaAs QD. By increasing the temperature from 2 to 300 K, the energy level exhibits an evident trend of decrease, while the PL bandwidth enlarges from a few micro-eV to a few meV (Bayer and Forchel, 2002). The former behavior illustrates how the lasing wavelength of QD laser increases with temperature, while the latter one along with the inhomogeneous broadening strongly affect the lasing behavior in terms of the optical bandwidth (Sugawara et al., 2000). At a low temperature when the homogeneous broadening is negligible, the dots that are spatially isolated and have different energies are independent with each other. In this case, a drive current above threshold allows all dots to lase independently, which results in the broad-band optical bandwidth, as shown in Fig. 2.5(a). Nevertheless, once the homogeneous broadening gets amplified and becomes comparable with inhomogeneous broadening at a high temperature, both the energetically resonant dots and other nonresonant dots within the scope of the homogeneous broadening are ready for emission. In this case, the incorporation of the spatially isolated and energetically QDs leads to the collective lasing from all QDs thus largely reducing the optical bandwidth, as shown in Fig. 2.5(b).

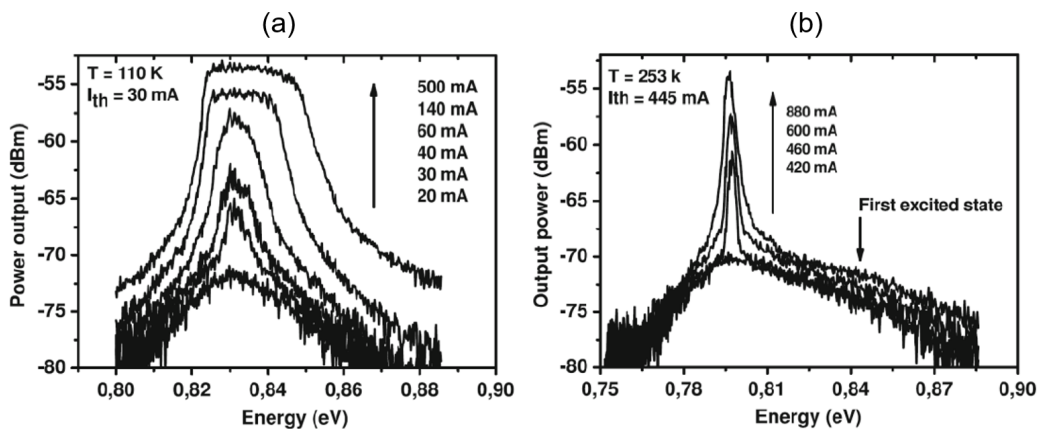


Figure 2.5: Lasing and electroluminescence spectra under pulsed injection mode for different bias level at two different temperatures: (a) 110K and (b) 253 K. From Ref. (Veselinov et al., 2007)

2.4 Linewidth enhancement factor

The linewidth enhancement factor (also named as Henry factor, α_H -factor) is a well-known gain medium parameter in semiconductor lasers that influences many

lasing characteristics and performances. Examples as the optical spectral linewidth (Charles Henry, 1982), the frequency chirp (G. Duan, Philippe Gallion, and Debarge, 1987), the mode stability (G. P. Agrawal, 1989) as well as the nonlinear dynamics under optical injection (Wieczorek, Krauskopf, and Lenstra, 2002) or optical feedback (Haegeman et al., 2002) have been extensively studied. The determination of α_H -factor relies on the gain and the refractive index that are coupled via the Kramers-Kronig relations (Charles Henry, 1982) through the carrier injection. In theory, the Kramers-Kronig relations require the use of microscopic equations in which the Hamiltonian of the system takes into account the contributions from various effects. Examples as the kinetic energies, the many-body Coulomb interactions, the electric-dipole interaction between the carriers and the laser field, the carrier-phonon interactions, and the effects of the injection current (Weng W Chow and S. W. Koch, 1999) have been discussed. From a general viewpoint, the macroscopic polarization P can be expressed as the sum of the microscopic polarizations p_i related to all interband transitions:

$$P = \frac{1}{V} \sum_{i=1}^n \mu_i p_i \quad (2.5)$$

with V the volume of active region, μ_i the dipole matrix element for the GS, ES and RS transitions in QDs. Assuming the gain medium is isotropic, the complex optical susceptibility can be written as:

$$\chi = \frac{1}{\epsilon_0 n_0^2} \frac{P}{E} \quad (2.6)$$

where ϵ_0 is the vacuum permittivity and E the electric field amplitude. The electric field that propagates in the active region of laser E is then coupled via the material gain g_m and the carrier-induced refractive index δn in the following relationship:

$$\frac{d}{dt} E(t) = \Gamma \frac{c g_m}{2 n_0} E(t) + j \frac{\omega \delta n}{n_0} E(t) \quad (2.7)$$

With Γ the confinement factor of the gain medium, c the velocity of light in vacuum, and ω the lasing angular frequency. Then, the material gain and the carrier-induced refractive index is written as:

$$g_m = -\frac{\omega n_0}{c} \text{Im}\{\chi\} = -\frac{\omega}{\epsilon_0 n_0 c} \frac{\text{Im}\{P\}}{E} \quad (2.8)$$

$$\delta n = \frac{n_0}{2} \text{Re}\{\chi\} = \frac{1}{2 \epsilon_0 n_0} \frac{\text{Re}\{P\}}{E} \quad (2.9)$$

Deriving from Eq. (2.8) and (2.9), the α_H -factor that describes the coupling between the gain and the refractive index is expressed as follows (Charles Henry, 1982; Osinski and Jens Buus, 1987):

$$\alpha_H = \frac{\partial \text{Re}\{\chi\}/\partial N}{\partial \text{Im}\{\chi\}/\partial N} = -2 \frac{\omega}{c} \frac{d\delta n/dN}{dg_m/dN} = -\frac{4\pi}{\lambda} \frac{d\delta n/dN}{dg_m/dN} \quad (2.10)$$

with N the carrier density injected into the laser, λ the lasing wavelength, $d\delta n/dN$ the differential refractive index, and dg_m/dN the differential gain.

In a laser system, the modal gain g is defined as the residual gain after deducting the internal loss, which can be described by assuming a linear carrier density dependence such as:

$$g = a(N - N_{tr}) \quad (2.11)$$

where N_{tr} is the carrier density at the transparency where the gain compensates totally the absorption, and a is the differential gain (i.e. dynamic gain). In general, $a = \partial g_m / \partial N$.

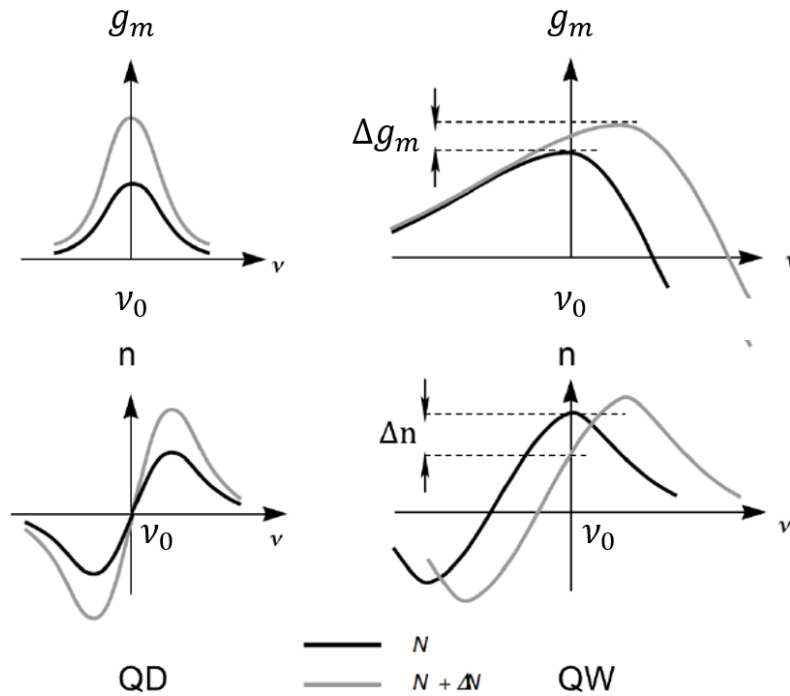


Figure 2.6: Schematic of the gain g_m and the refractive index n profiles variation with the carrier density changes for QD and QW. From Ref. (Rosencher and Vinter, 2002)

Figure 2.6 depicts the carrier density dependent material Kramer-Kronig related gain and refractive index versus the lasing photon energy in QD (left column) and

QW (right column) laser. The different gain profiles observed from the two devices give insight for the α_H -factors in these two materials. In QW laser, the zero point of the refractive index and the optical gain peak are mismatched for all carrier density conditions. With the increase of carrier density, the increase of material gain along with the decrease of refractive index result in a α_H -factor always positive (Coldren, Corzine, and Mashanovitch, 2012). However, in an ideal QD laser that has a symmetric gain profile with respect to the photon energy of the GS level $h\nu_0$, its gain arises from the carrier population in the resonant GS while its differential refractive index change located at $h\nu_0$ is kept at zero. According to Eq. (2.10), the α_H -factor of an ideal QD laser could be zero at the lasing frequency.

Nevertheless, a zero α_H -factor is used to be far from observation in experiment. This unexpected behavior is attributed to several mechanisms such as the large inhomogeneous broadening, the off-resonant states (i.e. higher energy levels like ES) as well as the free carrier plasma. As aforementioned, the first effect origins from the QD size fluctuations. The second mechanism generally takes place at a high injection current. Due to the discrete energy levels located in the conduction-band (CB) and valence-band (VB) of QDs, the large number of carriers brought by the amplified injection current firstly relax into the lower energy states like GS, and then enter into the higher energy levels such as ES after the GS is filled. The emission from ES significantly alters the symmetry of the gain spectrum hence ballooning the α_H -factor to larger values (Newell et al., 1999; Dagens et al., 2005; Mi, Bhattacharya, and Fathpour, 2005). Prior studies revealed that the off-resonant states affect the α_H -factor by mainly changing the refractive index variation (Lingnau, Lüdge, et al., 2012; Lingnau, Weng W Chow, et al., 2013) thus desynchronizing the $Re\{\chi\}$ and the $Im\{\chi\}$. Last, the carrier plasma effect in QDs originates from intraband transitions (Uskov et al., 2004). The carrier plasma effect in QW based on Drude formula is described as follows (Hegarty et al., 2005):

$$\delta n_{fc} = -\frac{\Gamma_p e^2 n}{2n_b \epsilon_0 m^* \omega^2} \quad (2.12)$$

where δn_{fc} is the carrier plasma induced refractive index change, e is the electron charge. In QD lasers, these analog transitions exist between the bound states and the continuum levels of the RS and the barrier. Despite its originality in QW, the Drude formula can also be applied to QD lasers when carriers are not tightly confined in the QDs and for photon energies within 0.8-1.0 eV (Uskov et al., 2004). Prior studies revealed that carrier plasma effect contributes to almost half of the overall refractive index changes (Uskov et al., 2004; Hegarty et al., 2005).

2.5 Relaxation oscillations and damping

Relaxation oscillations are inherent to class B semiconductor lasers including bulk, QW and QD lasers in which the photon lifetime τ_p is much smaller than the carrier lifetime τ_c (McCumber, 1966). In a semiconductor laser, the lasing field $\tilde{E}(t)$ can be described as (Uchida, 2012):

$$\frac{d\tilde{E}(t)}{dt} = \left\{ \frac{1 + i\alpha_H}{2} \left[\Gamma G_N(N(t) - N_{tr}) - \frac{1}{\tau_p} \right] + i\omega \right\} \tilde{E}(t) \quad (2.13)$$

with G_N the linear gain which is expressed as:

$$G_N = v_g dg/dN \quad (2.14)$$

where $N(t)$ is the carrier density, v_g and g are the group velocity and the optical gain, respectively. N_{tr} is the transparency carrier intensity, and ω is the lasing angular frequency.

Assuming the lasing field is in the form $\tilde{E}(t) = A(t) \exp(i\omega t + i\phi(t))$ thus by separating the real part and the imaginary part of Eq. (2.13), we obtain the following rate equations:

$$\frac{dA(t)}{dt} = \frac{1}{2} \left[\Gamma G_N(N(t) - N_{tr}) - \frac{1}{\tau_p} \right] A(t) \quad (2.15)$$

$$\frac{d\phi(t)}{dt} = \frac{\alpha_H}{2} \left[\Gamma G_N(N(t) - N_{tr}) - \frac{1}{\tau_p} \right] \quad (2.16)$$

In addition, the rate equation for $N(t)$ is expressed as (Uchida, 2012):

$$\frac{dN(t)}{dt} = \frac{\eta_i I}{qV} - \frac{N(t)}{\tau_c} - G_N[N(t) - N_{tr}] A^2(t) \quad (2.17)$$

with η_i the injection efficiency characterizing the fraction of carriers generated by the bias current in the active region, I the injection current, q the electron charge, V the volume of active region, and τ_c the carrier lifetime. Eq. (2.17) summarizes the mechanisms that occur during current injection. The first term on the right hand side accounts for the injected carriers into the laser active region; the carrier decay and photon generation are described by the second and last terms, respectively.

The solutions at the steady-state A_s , ϕ_s and N_s are then written as:

$$A_s^2 = \frac{\eta_i I / qV - N_s / \tau_c}{G_N(N_s - N_{th})} \quad (2.18)$$

$$\phi_s = 0 \text{ with } \omega_s = \omega \quad (2.19)$$

$$N_s = N_{tr} + \frac{1}{\Gamma G_N \tau_p} = N_{th} \quad (2.20)$$

with N_{th} the carrier density at threshold.

The small perturbations around the steady-state solutions are expressed as follows:

$$A(t) = A_s + \delta A(t) \quad (2.21)$$

$$\phi(t) = (\omega_s - \omega_0)t + \delta\phi(t) \quad (2.22)$$

$$N(t) = N_s + \delta N(t) \quad (2.23)$$

One can then obtain the following relationships by substituting Eqs. (2.18) - (2.23) into Eqs. (2.15) - (2.17):

$$\frac{d\delta A(t)}{dt} = \frac{1}{2}\Gamma G_N A_s \delta N(t) \quad (2.24)$$

$$\frac{d\delta\phi(t)}{dt} = \frac{\alpha_H}{2}\Gamma G_N \delta N(t) \quad (2.25)$$

$$\frac{d\delta N(t)}{dt} = -\frac{2A_s}{\Gamma\tau_p}\delta A(t) - \frac{1}{\tau_c}\delta N(t) - G_N A_s^2 \delta N(t) \quad (2.26)$$

Eqs. (2.24) - (2.26) can also be re-expressed as follows:

$$\begin{bmatrix} \frac{d\delta A(t)}{dt} \\ \frac{d\delta\phi(t)}{dt} \\ \frac{d\delta N(t)}{dt} \end{bmatrix} = \begin{bmatrix} 0 & 0 & \frac{1}{2}\Gamma G_N A_s \\ 0 & 0 & \frac{\alpha_H}{2}\Gamma G_N \\ -\frac{2A_s}{\Gamma\tau_p} & 0 & -\frac{1}{\tau_c} - G_N A_s^2 \end{bmatrix} \begin{bmatrix} \delta A(t) \\ \delta\phi(t) \\ \delta N(t) \end{bmatrix} = M_J \begin{bmatrix} \delta A(t) \\ \delta\phi(t) \\ \delta N(t) \end{bmatrix} \quad (2.27)$$

By solving the Jacobian Matrix M_J , one gets the solutions of Eqs. (2.24) - (2.26) through the eigenvalue ξ of M_J as follows:

$$|M_J - \lambda I| = -\xi[\xi^2 + (\frac{1}{\tau_c} + G_N A_s^2)\xi + \frac{G_N A_s^2}{\tau_p}] = 0 \quad (2.28)$$

Apart from the trivial value $\xi = 0$, the other two solutions are written as:

$$\xi = -\frac{1}{2}(\frac{1}{\tau_c} + G_N A_s^2) \pm i\sqrt{\frac{1}{4}(\frac{1}{\tau_c} + G_N A_s^2)^2} = Re\{\xi\} + iIm\{\xi\} \quad (2.29)$$

The relaxation oscillation frequency f_{RO} and the damping factor γ are defined as the real part $Re\{\xi\}$ and the imaginary part $Im\{\xi\}$ of ξ , respectively, such as:

$$f_{RO} = \frac{1}{2\pi}\sqrt{\frac{G_N A_s^2}{\tau_p}} \quad (2.30)$$

$$\gamma = \frac{1}{2}(\frac{1}{\tau_c} + G_N A_s^2) \quad (2.31)$$

The positive τ_c , G_N and A_s result in a negative $Re\{\xi\}$, which means the steady solutions of Eq. (2.29) are always stable. According to the definitions in Eqs. (2.30)

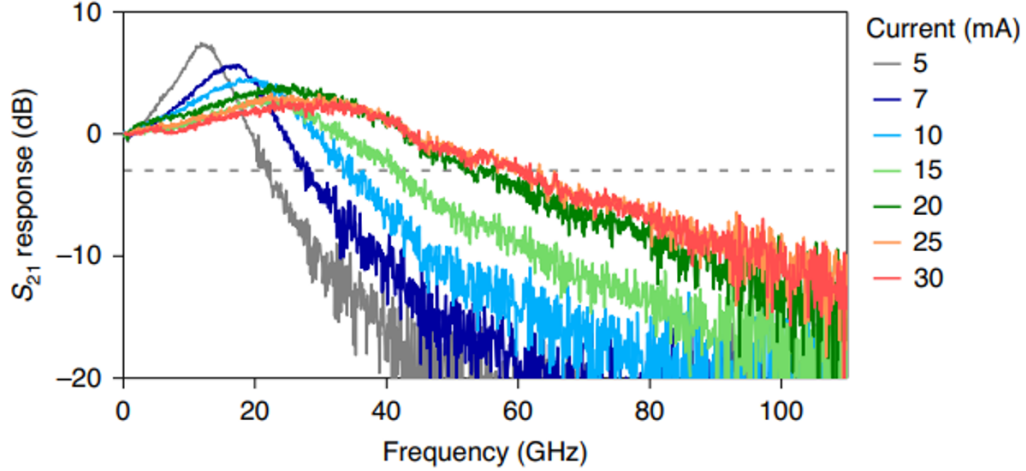


Figure 2.7: Frequency response of a membrane laser (and is valid for semiconductor lasers as well) for several different bias current. The oscillation peaks represent the relaxation oscillation frequency. The modulation bandwidth that is represented by the black dashed line is determined by the 3 dB down cutoff frequency. From Ref. (Yamaoka et al., 2021).

and (2.31), the increase of output power contributes to increasing the relaxation oscillation frequency and the damping via the steady-state field amplitude A_s , which have been widely observed in experiment.

Both the relaxation oscillation frequency and the damping rate of a semiconductor laser can be analyzed from its modulation response. To do so, a small signal analysis of the rate equations is an approach. For instance, a time-varying current $I(t)=I_0+\delta I \exp(i\omega t)$ can be deployed, where I_0 is the bias current and δI is the modulation current that should satisfy $\delta I \ll I_0$. Figure 2.7 shows the evolution of the modulation response of the laser with the increase of bias current of a membrane laser. The resonant peak with a magnitude of $\sim (f_{RO}/\gamma)^2$ is determined by the relaxation oscillation, while the small-signal modulation bandwidth of the laser is determined by the -3 dB down cutoff frequency f_{-3dB} .

In addition, the K -factor is also a well-known parameter in small-signal frequency response that describes the damping, which is directly determined by the relaxation oscillation frequency and the damping factor through the following relationship:

$$\gamma = K f_{RO}^2 + \gamma_0 \quad (2.32)$$

with γ_0 the damping factor offset. The maximum possible bandwidth can thus be

written as follows:

$$f_{3dB|max} = \sqrt{2} \frac{2\pi}{K} \quad (2.33)$$

In contrast to QW lasers, the direct modulation performance in terms of the modulation rate is not satisfactory enough in QD lasers, due to the strongly limited carrier capture and relaxation processes as well as the Pauli blocking (direct consequence of Pauli exclusion principle) that lead to a large damping factor (Malic et al., 2007). In general, the K -factor of QD laser is ≈ 0.9 ns (Arsenijević and Dieter Bimberg, 2016; Inoue et al., 2018), whereas that of QW laser is below 0.2 ns (Keating et al., 1999). It is worth stressing that the gain broadening mechanisms in QDs play a crucial role in affecting the relaxation oscillation frequency and the damping (Fiore and Markus, 2007). Such a statement is based on the results shown in Fig. 2.8. By fixing the inhomogeneous broadening bandwidth Γ_{in} at 35 meV, both the f_{RO} and the γ increase with the homogeneous broadening bandwidth Γ_{homo} enlarging from 1 meV (green triangles) to 10 meV (red dots) that approaches the Γ_{in} . As discussed in Sec. 2.3, a Γ_{homo} that is comparable with Γ_{in} leads to a reduction of the optical bandwidth, hence both the f_{RO} and the γ are at the same level of those taken from single-mode (SM, blue squares) emission.

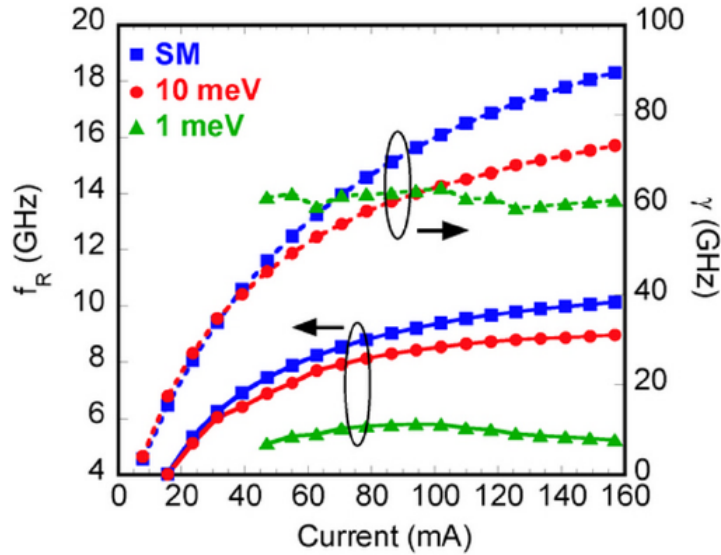


Figure 2.8: Relaxation oscillation frequency (continuous lines, left axis) and damping rate (dashed lines, right axis) as a function of current. Calculated curves are derived from three different homogeneous broadening bandwidth Γ_{homo} : single-mode (blue squares), multimode with $\Gamma_{homo} = 10$ meV (red dots), and multimode with $\Gamma_{homo} = 1$ meV (green triangles). The inhomogeneous broadening bandwidth Γ_{ih} is fixed at 35 meV. From Ref. (Fiore and Markus, 2007)

Last but not least, the high gain compression effects in QDs are also responsible for the reduction of relaxation oscillation frequency as well as the 3-dB modulation bandwidth (Coldren, Corzine, and Mashanovitch, 2012). Corresponding discussions are performed hereinafter.

2.6 Gain compression

The gain compression in interband semiconductor lasers originates from the decrease of gain coefficient with optical field intensity. Processes such as carrier heating, spectral hole burning, as well as spatial hole burning (Willatzen et al., 1991; J. Huang and Casperson, 1993; Klotzkin, 2020) contribute to the gain compression in semiconductors. The last one comes from the spatial dependence of photon and carrier densities along the cavity (Duan, Philippe Gallion, and G. P. Agrawal, 1992).

The material gain $g_{m,nl}$ and differential gain a_{nl} at GS that include the gain compression are expressed as follows (Coldren, Corzine, and Mashanovitch, 2012):

$$g_{m,nl} = \frac{g_{m,th}}{1 + \epsilon_s N_p} \ln\left(\frac{N + N_s}{N_{tr} + N_s}\right) \quad (2.34)$$

$$a_{nl} = dg_m/dN = \frac{g_{m,th}}{(N + N_s)(1 + \epsilon_s N_p)} \equiv \frac{a_{m,th}}{1 + \epsilon_s N_p} = \frac{a_{m,th}}{1 + \epsilon_P P} \quad (2.35)$$

with $g_{m,th}$ and $a_{m,th}$ the material gain and differential gain at threshold, respectively, ϵ_s the gain compression factor related to the photon density, N_p the photon density, and P the output power. N and N_s denote the carrier density and a linearity fitting parameter, respectively. According to Eqs. (2.34) and (2.35), with the increase of photon density above threshold, the material gain approaches its maximum while the differential gain decreases in presence of the gain compression until the material gain saturates. QD lasers are known from their large gain compression, i.e., a ϵ_P typically on the order of 0.2 mW^{-1} . Corresponding gain compression factor related to the photon density ϵ_s is in the range of 10^{-16} to $5 \times 10^{-16} \text{ cm}^3$. In contrary, the gain compression in QW lasers is in general one or two order of magnitude lower (Frédéric Grillot, Béatrice Dagens, et al., 2008).

Then, the saturation of gain above threshold is responsible for the variation of α_H -factor. In QW lasers whose gain medium is homogeneously-broadened, the carrier density is clamped at threshold. In this case, the above-threshold α_H -factor that takes into account the gain compression is written as follows:

$$\alpha_H(P) = \alpha_{H,th}(1 + \epsilon_P P) \quad (2.36)$$

with $\alpha_{H,th}$ the α_H -factor at threshold.

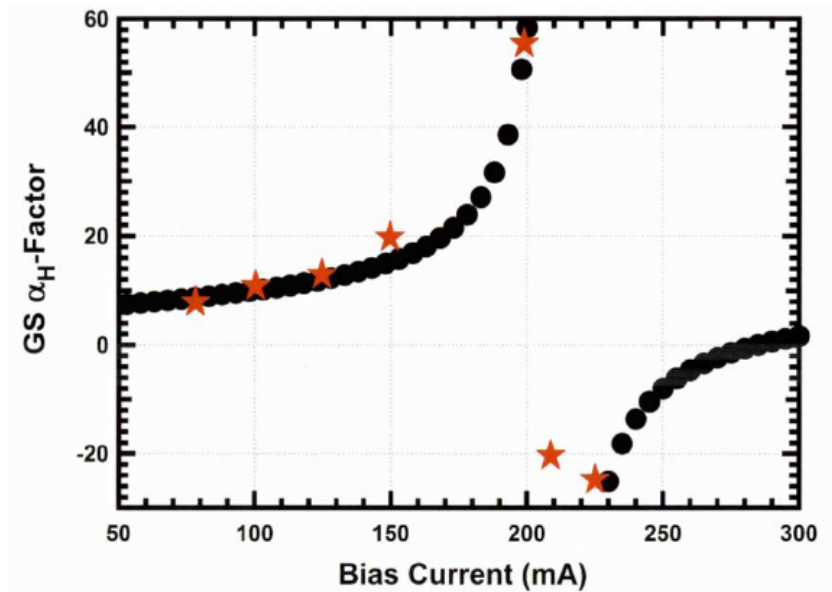


Figure 2.9: GS α_H -factor versus the bias current in simulation (black dots) and in experiment (red stars). From Ref. (Frédéric Grillot, Béatrice Dagens, et al., 2008)

In QD lasers, however, the α_H -factor is determined by the dual-state emission behavior, which is described analytically by the following equation (Frédéric Grillot, Béatrice Dagens, et al., 2008):

$$\alpha_H(P) = a_{GS}(1 + \epsilon_P P) + \frac{a_{ES}}{1 - \frac{g_{m,th}}{g_{GS,max} - g_{m,th}} \epsilon_P P} \quad (2.37)$$

where $g_{GS,max}$ denote the maximum material gain for sole GS emission. a_{GS} and a_{ES} are the differential gains for GS and ES lasing, respectively. The first term at the right hand side denotes the gain compression effect at the GS while the second term accounts for the carrier filling the ES after the gain saturation in the GS. Figure 2.9 depicts the α_H -factors that are calculated (black dots) or experimental observed (red stars) as a function of bias current in presence of dual-state emission. With the increase of bias current above threshold, the carrier filling into the excited states and the higher level nonlasing states such as the RS leads to a decrease of differential gain at GS, which results in the slight increase of α_H -factor. Nevertheless, once the bias current approaches the threshold of ES emission at 200 mA, the gain compression becomes significant and a sharp rising of α_H -factor before collapsing to negative values is observed. At the beginning of ES lasing, a number of carriers escape from GS to ES results in a crash of carrier density in GS hence the collapse of α_H -factor (Frédéric Grillot, Béatrice Dagens, et al., 2008). As a consequence, a

high bias current applied to QDs generally leads to an increase of frequency chirp in direct modulation operation, which limits the applications of QD laser in high-speed modulation operation.

Besides, the inconveniences of gain compression also include the decrease of damping rate and the reduction of 3-dB bandwidth. By substituting Eq. (2.35) into Eq. (2.14), one gets a nonlinear gain $G_{N,nl}$ expressed as:

$$G_{N,nl} = v_g \frac{\alpha_{m,th}}{1 + \epsilon_P P} = \frac{G_N}{1 + \epsilon_P P} \quad (2.38)$$

Thus, Eqs. (2.30) and (2.31) can be re-expressed as follows:

$$f_{RO} = \frac{1}{2\pi} \sqrt{\frac{G_N A_s^2}{\tau_p (1 + \epsilon_P P)}} \quad (2.39)$$

$$\gamma = \frac{1}{2} \left(\frac{1}{\tau_c} + \frac{G_N A_s^2}{1 + \epsilon_P P} \right) \quad (2.40)$$

2.7 Noise properties

In modulation operation, the noise properties of laser need to be taken into account. The noise of laser comes from the random carrier and photon recombination and generation events that produce instantaneous time variations of the carrier and photon densities, even though no modulation current is applied. As a consequence, two types of noise are commonly produced by the variations of photon density. First, the variations in the magnitude of the output power induced by the photon density variations can be described by the relative intensity noise (RIN). Second, the variations in the output wavelength induced by the carrier density variations can be described by the spectral linewidth of the lasing mode. In this section, the mechanisms of these two noise are introduced.

Relative intensity noise

The level relative intensity noise (RIN) has a tight relationship with the signal-to-noise ratio (SNR) and the bit-error rate (BER) in analog and digital signal transmission, respectively. Figure 2.10 illustrates a noisy modulated laser output signals for both analog and digital applications. In both cases, a false recording might happen if the noisy term $|\delta P(t)|$ exceeds half of the signal power $P_0/2$.

To analyze the level of such an intensity noise, the RIN is defined as follows (Coldren, Corzine, and Mashanovitch, 2012):

$$RIN = \frac{\langle \delta P(t)^2 \rangle}{P_0^2} \quad (2.41)$$

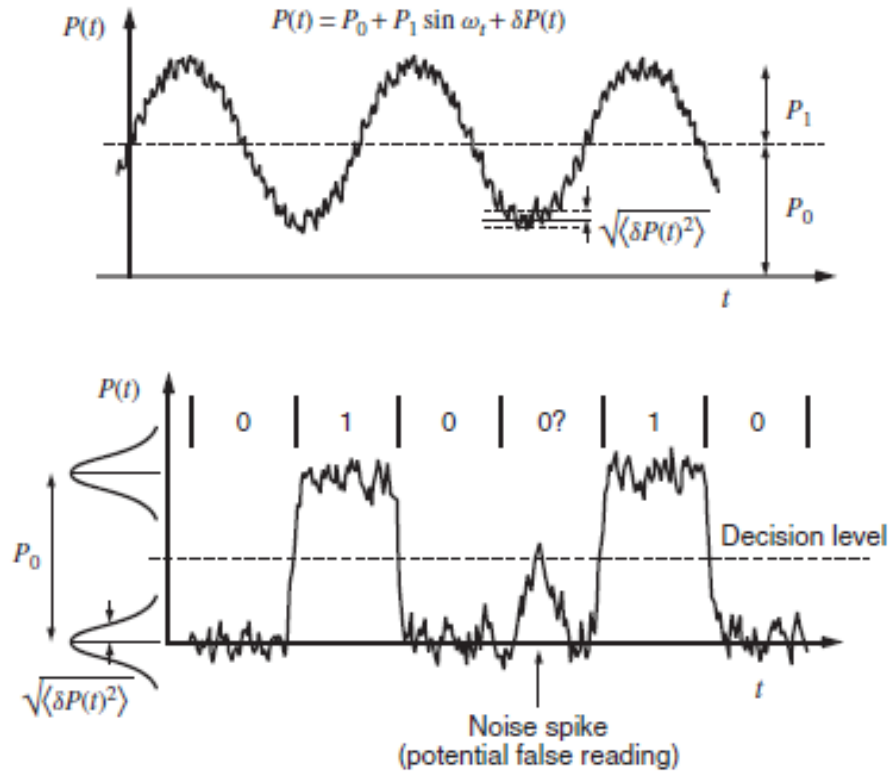


Figure 2.10: Noise in modulated laser signals for both analog and digital applications. From Ref. (Coldren, Corzine, and Mashanovitch, 2012)

with $\langle \rangle$ the time average. In general, the RIN is described in decibels. To quantify the output power fluctuations (and hence the RIN), it is meaningful for expressing the RIN in frequency domain. To do so, a first step is to make use of the Fourier transform as follows:

$$\langle \delta P(t)^2 \rangle = \frac{1}{2\pi} \int_{-\infty}^{+\infty} S_{\delta P}(\omega) |F(\omega)|^2 d\omega \quad (2.42)$$

where $S_{\delta P}(\omega)$ is the spectral density of $|\delta P(t)|$ and $F(\omega)$ denotes the filter passband of the spectrum analyzer. Assuming that the measurement filter is centered at ω_0 and is narrowband relative to variations in the spectral density, then with $F(\omega_0) = 1$ one obtains:

$$\langle \delta P(t)^2 \rangle \approx S_{\delta P}(\omega_0) \int_{-\infty}^{+\infty} |F(\omega)|^2 df = S_{\delta P}(\omega_0) 2\Delta f \quad (2.43)$$

with Δf the filter bandwidth of the measurement apparatus. Finally, a RIN in frequency domain that includes the measurement bandwidth is defined as follows:

$$\frac{RIN}{\Delta f} (dB/Hz) = \frac{2S_{\delta P}(\omega)}{P_0^2} \quad (2.44)$$

Following the definition in Eq. (2.44), the spectral density of the output power and carrier noise fluctuations is required to determine the RIN of laser. The spectral density of laser is dependent on both the Langevin noise sources for the carrier and photon densities, which are assumed to be white noise source. Therefore, their noise spectral densities are uniformly distributed over the whole frequency range. As a result, the output power spectral density is expressed as follows (Coldren, Corzine, and Mashanovitch, 2012):

$$S_{\delta P}(\omega) = h\nu P_0 \left[\frac{a + b\omega^2}{\omega_R^4} |H(\omega)|^2 + 1 \right] \quad (2.45)$$

where

$$a = \frac{8\pi(\Delta\nu)_{ST}P_0}{h\nu} \frac{1}{\tau_{\Delta N}^2} + \eta_0 \omega_R^4 \left[\frac{\eta_i(I + I_{th})}{I_{st}} - 1 \right] \quad (2.46)$$

$$b = \frac{8\pi(\Delta\nu)_{ST}P_0}{h\nu} \frac{1}{\tau_{\Delta N}^2} - 2\eta_0 \omega_R^2 \frac{\Gamma a_p}{a} \quad (2.47)$$

$$H(\omega) = \frac{\omega_{RO}^2}{\omega_{RO}^2 - \omega^2 - i\omega\gamma} \quad (2.48)$$

and $I_{st} = \eta_i(I - I_{th})$. $(\Delta\nu)_{ST}$ denotes the Schawlow-Towns linewidth of laser, which is introduced in the next subsection. $h\nu$ and $\tau_{\Delta N}$ accounts for the photon energy and the differential carrier lifetime, respectively. η_0 and η_i denotes the optical efficiency and the injection efficiency, respectively. Γ denote the gain confinement factor. a and a_p is the differential gain and the gain compression, respectively. ω_{RO} and γ denote the angular relaxation oscillation frequency and the damping factor, respectively. As a consequence, Eq. (2.44) can be re-expressed as:

$$\frac{RIN}{\Delta f} (dB/Hz) = \frac{2h\nu}{P_0} \left[\frac{a + b\omega^2}{\omega_R^4} |H(\omega)|^2 + 1 \right] \quad (2.49)$$

Eqs. (2.45)-(2.48) demonstrate that the RIN level is dependent on the laser configuration. In general, RIN levels ranging from -150 to -160 dB/Hz in both QW and QD lasers have been reported, which are reliable for data transmission in optical network (Tan et al., 2012; Capua et al., 2007; Francois Lelarge et al., 2007). A good news is that the QD lasers epitaxially grown on Si substrate have comparable performances in terms of RIN with those grown on native substrate (M. Liao et al., 2018; Jianan Duan, Y. Zhou, et al., 2020), which is beneficial for developing high-performance and low-cost optical interconnects. In particular, the RIN of QD laser is also dependent on mechanisms such as p-modulation doping and ES emission (G. Lin et al., 2011; Jianan Duan, Y. Zhou, et al., 2020), which originate from the change of optical gain. Corresponding discussions is performed in the next subsection.

Frequency noise

In addition to the intensity noise, the frequency noise of laser also affects the lasing spectrum. A well-known parameter that reflects the frequency noise level is the lasing mode spectral linewidth. The linewidth of a laser results from phase fluctuations in its output, which are induced by two basic mechanisms: the spontaneous emission and the carrier density fluctuations. The former results from the the random addition of spontaneously emitted photons to the quasi-coherent resonant cavity mode. However, the latter comes from the carrier density variation induced change in refractive index, which is known as the frequency chirp in modulation operation.

The first kind of linewidth caused by spontaneous emission is named as Schawlow-Towns linewidth $(\Delta\nu)_{ST}$. In this linewidth broadening process, the full-width half-maximum (FWHM) linewidth of the cold cavity is inversely proportional to photon lifetime τ_p . However, with the optical field traverses within the gain medium, the effective photon lifetime τ'_p is prolonged and is written as follows (Coldren, Corzine, and Mashanovitch, 2012):

$$\frac{1}{\tau'_p} = \frac{1}{\tau_p} - \Gamma v_g g \quad (2.50)$$

where v_g and g accounts for the group velocity in the gain medium and the gain, respectively. As a consequence, the photon density at steady-state N_p is amplified thanks to the increase of photon lifetime and can be expressed as:

$$N_p = \frac{\Gamma R'_{sp}}{1/\tau_p - \Gamma v_g g} \quad (2.51)$$

with R'_{sp} the effective spontaneous emission factor. Thus, the correlated Schawlow-Towns linewidth $(\Delta\nu)_{ST}$ is determined by the following relationship:

$$(\Delta\nu)_{ST} = \frac{\Gamma R'_{sp}}{4\pi N_p} \quad (2.52)$$

To provide guidelines for designing laser with low frequency noise, another definition of the Schawlow-Towns linewidth that includes laser configurations is expressed as follows (Yariv, 1989):

$$(\Delta\nu)_{ST} = \frac{\Gamma g_{m,th} v_g^2 \alpha_m h\nu}{4\pi P_0} n_{sp} \quad (2.53)$$

where α_m and n_{sp} account for the mirror loss and the population inversion factor, respectively.

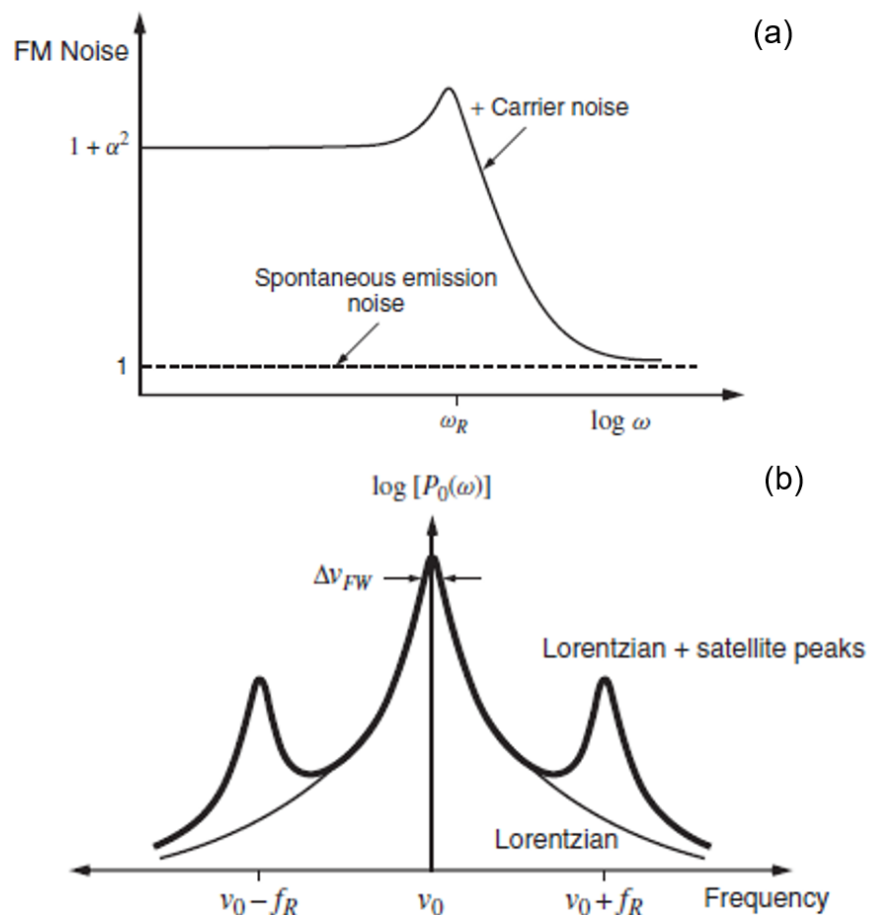


Figure 2.11: Noise in modulated laser signals for both analog and digital applications. From Ref. (Coldren, Corzine, and Mashanovitch, 2012)

On the other hand, the linewidth broadening effect that results from the frequency chirp can be explained by the α_H -factor in Eq. (2.10). To clarify, the frequency shift in response to carrier density change is expressed as (Coldren, Corzine, and Mashanovitch, 2012):

$$\Delta\nu = \nu - \nu_0 = \frac{\alpha_H}{4\pi} \gamma G_N \Delta N \quad (2.54)$$

where ν_0 denotes the initial frequency. $G_N = v_g dg/dN$ and γ are again used to define the linear gain and the damping factor, respectively. As a consequence, the frequency noise spectral density (double-sided) of laser becomes:

$$S_\nu(\omega) = \frac{1}{2\pi} (\Delta\nu)_{ST} (1 + \alpha_H^2 |H(\omega)|^2) \quad (2.55)$$

with $H(\omega)$ again a frequency domain transfer function whose definition is given

in Eq. (2.48). Figure 2.11(a) sketches a typical frequency modulated (FM) noise spectrum. The carrier noise plays a dominant role in low-frequency regime, until it progressively decreases when the modulation frequency is beyond the relaxation resonance frequency. In high-frequency regime, the carrier noise becomes negligible, reducing the FM noise to the white noise background provided by spontaneous emission phase noise. In addition, thermal noise from the pumping source can also contribute to the FM noise at low frequencies (Cox et al., 2006).

Then, the FWHM linewidth that includes both the broadening effects is expressed as follows:

$$\Delta\nu_{FW} = (\Delta\nu)_{ST}(1 + \alpha_H^2) \quad (2.56)$$

In experiment, the FWHM linewidth of laser can be retrieved from self-heterodyne method. To do so, the optical field needs to be time-delayed before it is correlated with itself. A typical Lorentzian-shaped frequency line is shown in Fig. 2.11(b). A series of satellite peaks spaced by the resonance frequency f_{RO} are identified. Similar with the oscillation peak at f_{RO} in RIN spectrum, the magnitude of the satellite peaks depends on the damping factor of the laser. A stronger damping is beneficial for suppressing these satellite oscillations. However, the relaxation oscillations do not affect the FWHM linewidth of laser.

According to Eqs. (2.49), (2.53) and (2.56), both the intensity noise and the frequency noise of laser can be minimized by increasing the quality-factor (Q-factor) of cavity; by optimizing the reflectivities of the coated facets; by enhancing the output power; and by utilizing a gain medium whose α_H -factor is low. Compared to QW devices, the QD lasers exhibit superior performances in terms of noise properties. While the linewidth of QW lasers is generally on the order of MHz (P. F. Liao and Kelley, 2012), that of QD lasers is observed below 200 kHz (Becker et al., 2017; Duan, Huang, ZG Lu, et al., 2018; Septon et al., 2019).

2.8 Nonlinear optical susceptibility

In Sec. 1.3, the author gives a brief introduction to the optical nonlinear processes that are required by quantum light generation. These nonlinear processes are realized by the modification of optical properties of a material system in the presence of light. The definition of “nonlinear” results from the fact that the response of a material system to an applied optical field is in a nonlinear manner on the strength of the optical field.

To describe the optical nonlinearity, the polarization $\tilde{P}(t)$ of a material system under

external optical injection is expressed as follows:

$$\begin{aligned}\tilde{P}(t) &= \epsilon_0(\chi^{(1)}\tilde{E}(t) + \chi^{(2)}\tilde{E}^2(t) + \chi^{(3)}\tilde{E}^3(t) + \dots) \\ &\equiv \tilde{P}^{(1)}(t) + \tilde{P}^{(2)}(t) + \tilde{P}^{(3)}(t) + \dots\end{aligned}\quad (2.57)$$

where $\tilde{E}(t)$ is the intensity of the applied optical field. The constant of proportionality $\chi^{(1)}$ is known as the linear susceptibility and ϵ_0 denotes the permittivity of free space. $\chi^{(2)}$ and $\chi^{(3)}$ account for the second- and third-order nonlinear optical susceptibilities, respectively. In $\chi^{(2)}$ and $\chi^{(3)}$ process, the optical nonlinearities are performed by the presence of a converted field whose intensity tends to increase as the square or the cube of the intensity of the injected field. In addition, the generated fields generally have frequencies different from those brought by the injected fields, owing to the nonlinear process. Assuming that the applied fields consist of two distinct frequencies, the real part of the field is expressed in the following form:

$$\tilde{E}(t) = E_1 e^{-i\Omega_1 t} + E_2 e^{-i\Omega_2 t} + c.c. \quad (2.58)$$

with

$$\Omega_1 = \omega_1 t + \phi_1 \quad (2.59)$$

$$\Omega_2 = \omega_2 t + \phi_2 \quad (2.60)$$

where $E_{1,2}$, $\omega_{1,2}$ and $\phi_{1,2}$ denote the amplitude, angular frequency and phase of those two injected fields, respectively. *c.c.* accounts for the complex conjugate of the field. Thus, the nonlinear polarization induced by $\chi^{(2)}$ processes is expressed as follows (Boyd, 2020):

$$\begin{aligned}\tilde{P}^{(2)}(t) &= \epsilon_0 \chi^{(2)} \tilde{E}^2(t) = \epsilon_0 \chi^{(2)} [E_1^2 e^{-2i\Omega_1} + E_2^2 e^{-2i\Omega_2} \\ &\quad + 2E_1 E_2 e^{-i(\Omega_1 + \Omega_2)} + 2E_1 E_2^* e^{-i(\Omega_1 - \Omega_2)} + c.c.] \\ &\quad + 2\epsilon_0 \chi^{(2)} [E_1 E_1^* + E_2 E_2^*]\end{aligned}\quad (2.61)$$

where $E_{1,2}^*$ is the complex conjugate of $E_{1,2}$. Four novel frequencies such as $2\Omega_{1,2}$, $\Omega_1 + \Omega_2$ and $\Omega_1 - \Omega_2$ are in turn the products of second-harmonic generation (SHG), sum-frequency generation (SFG) and difference-frequency generation (DFG). The last process has been shown in Fig. 1.6. After $\chi^{(2)}$ nonlinear process, the two injected photons will be destroyed while four novel photons are generated. Such an approach has been utilized for optical parametric oscillations and quantum states of light generation. It is worth stressing that the $\chi^{(2)}$ nonlinear optical interactions occur only in noncentrosymmetric crystals in which no inversion symmetry appears.

In the case of crystals like QDs that display inversion symmetry, the $\chi^{(2)}$ process vanishes.

The $\chi^{(3)}$ process is much more complicated than the $\chi^{(2)}$ one. Utilizing the same injected field in Eq. (2.58), the nonlinear polarization induced by $\chi^{(3)}$ processes is expressed as follows (Roncin, 2004):

$$\begin{aligned}
\tilde{P}^{(3)}(t) &= \epsilon_0 \chi^{(3)} \tilde{E}^3(t) \\
&= \epsilon_0 \chi^{(3)} [E_1^3 e^{-3i\Omega_1} + E_2^3 e^{-3i\Omega_2} \\
&\quad + E_1(3E_1^2 + 6E_2^2) e^{-i\Omega_1} + E_2(6E_1^2 + 3E_2^2) e^{-i\Omega_2} \\
&\quad + 3E_1^2 E_2 (e^{-i(2\Omega_1+\Omega_2)} + e^{-i(2\Omega_1-\Omega_2)}) \\
&\quad + 3E_2^2 E_1 (e^{-i(2\Omega_2+\Omega_1)} + e^{-i(2\Omega_2-\Omega_1)}) + c.c.] \tag{2.62}
\end{aligned}$$

In contrast to the $\chi^{(2)}$ process, the injected two photons will be maintained in the $\chi^{(3)}$ process while 6 novel photons are generated. Importantly, the $\chi^{(3)}$ is a well-known nonlinear optical interactions in QDs, given that its generation is much easier compared to $\chi^{(2)}$ since it occurs in both centrosymmetric and noncentrosymmetric materials (Boyd, 2020). The $\chi^{(3)}$ coefficient is responsible for the four-wave mixing (FWM) mechanism, which is another major approach to generate quantum states of light, as shown in Fig. 1.6. As a consequence, the frequency conversion efficiency is highly dependent on the $\chi^{(2)}$ and $\chi^{(3)}$ susceptibility.

The $\chi^{(3)}$ susceptibility in QDs is dependent on the carrier density pulsation (CDP), the spatial hole burning (SHB) and the carrier heating (CH), which can be extracted from the nondegenerate FWM operation (Akiyama, Kuwatsuka, et al., 2002). Assuming that the power of the pump field E_1 is higher than that of the other pump field E_2 , the frequency detuning is defined as $\Delta\Omega = \Omega_2 - \Omega_1$. The $\chi^{(3)}$ coefficient that is dependent on the frequency detuning is expressed as follows:

$$\chi^{(3)} = \sum_m \chi_m^{(3)} = \sum_m \chi_{m,\Delta\Omega=0}^{(3)} (1 - i\Delta\Omega\tau_m)^{-1} \tag{2.63}$$

where m accounts for the aforementioned three nonlinear processes that contribute to the $\chi^{(3)}$. $\chi_m^{(3)}$ and τ_m are thus the $\chi^{(3)}$ and the time constant for those processes. $\chi_{m,\Delta\Omega=0}^{(3)}$ denotes the $\chi_m^{(3)}$ in zero-detuning condition. Figure 2.12 schematically illustrates the complex plane representation of $\chi_m^{(3)}$ directions varies with the frequency detuning in the bulk, QW and QD materials. In the case of bulk and QW as shown in the first column, the direction of the $\chi_{SHB}^{(3)}$ is different from that of

	Bulk, QW ($\alpha \sim 4$)		QD ($\alpha \sim 0$)	
(a) $\Delta f = 0$				
(b) $f_{CDP} < \Delta f < f_{SHB}$	$\Delta f > 0$	$\Delta f < 0$	$\Delta f > 0$	$\Delta f < 0$
	<p>In Phase</p>	<p>Out of Phase</p>		
(c) $f_{SHB} < \Delta f $				

Figure 2.12: Directions of the third-order nonlinear susceptibilities of carrier density pulsation (CDP) and spatial hole burning (SHB) for bulk, QW and QD. From Ref. (Akiyama, Kuwatsuka, et al., 2002).

the $\chi_{CDP}^{(3)}$ in the zero-detuning condition due to the large α_H -factor. As a result, a large discrepancy between the $\chi^{(3)}$ in the positive and in the negative frequency detuning conditions takes place. In contrary, the theoretical zero α_H in QDs results in the directions of $\chi_m^{(3)}$ coincident with each other in the zero-detuning condition, as shown in the second column. This property leads to the symmetric $\chi^{(3)}$ with respect to the sign of frequency detuning. This peculiar property offered by QDs is beneficial for improving the FWM efficiency along with the FWM bandwidth. Corresponding discussions will be performed in Chap. 6.

2.9 Summary

In summary, this chapter introduces the fundamental features of QD lasers, including the electronic structure, the carrier dynamics, the gain broadening mechanisms, the linewidth broadening factor, the gain properties such as the linewidth enhancement factor, the small-signal modulation dynamics and gain compression, as well as the noise properties and optical nonlinearities. All these elements are essential

for understanding the results presented in the following chapters. For instance, the linewidth enhancement factor plays a crucial role in determining the laser's tolerance for optical feedback and laser dynamics under optical injection. The analysis of the gain properties of QDs is also important for understanding their improved optical nonlinearities compared to QW, which give insights for developing high-performance sources for both classical and quantum PICs.

DYNAMICS OF QUANTUM-DOT LASERS SUBJECT TO EXTERNAL OPTICAL FEEDBACK

External optical feedback (EOF) is a well-known mechanism that reshapes the laser dynamics. In several laser systems, a feedback strength below 1% is able to trigger complex nonlinear dynamics such as periodic or chaotic oscillations. Those complex dynamics are highly desired for some applications such as secure communication (Uchida, 2012), LIDAR system (F.-Y. Lin and J.-M. Liu, 2004), microwave photonics (Chan, Hwang, and J.-M. Liu, 2006), parallel random number generation (Sciamanna and Shore, 2015), compressive sensing (Damien Rontani et al., 2016) and speckle-free imaging (H. Cao et al., 2019). However, for applications like photonic integrated circuits (PICs) based high-speed optical interconnects, those dynamics are usually detrimental to their operational stability. In this chapter, experimental investigations are performed to study the dynamics of quantum-dot (QD) and quantum-dash (QDash) lasers subject to EOF, peculiar to give some design rules for developing reflection-resistant source for PICs.

3.1 Principle of optical feedback

In general, the EOF operation on a laser diode is realized by sending part of its emitted field back to the laser cavity. Figure 5.1 depicts the EOF process, in which a delayed field returns to the cavity through a mirror that is aligned on the beam's path. Therefore, two important parameters are related to this process. First, the distance between the laser and the mirror is defined as the external cavity length L_{ext} that corresponds to the external round-trip time τ_{ext} , which is expressed as:

$$\tau_{ext} = \frac{2L_{ext}}{v_g} \quad (3.1)$$

where v_g denotes the group velocity in the external cavity. Another parameter in the EOF process is the feedback strength, which is defined as the ratio of the returned power P_{return} to the output power P_{out} from the facet that is subjected to the EOF such as:

$$\eta_F = \frac{P_{return}}{P_{out}} \quad (3.2)$$

In practical, the equivalent reflectivity of the reinjecting facet will be changed by the EOF. Assuming that the multiple round-trips of the returning light within the external

cavity is negligible, and the light is reinjected to the front facet, the equivalent facet reflectivity r_{re} is written as follows (Coldren, Corzine, and Mashanovitch, 2012):

$$r_{re} = r_1 \left(1 + \frac{1 - |r_1|^2}{\sqrt{r_1}} \sqrt{\eta_F} \exp(-i\phi_{re}) \right) \quad (3.3)$$

with r_1 the reflectivity of the front facet and η_F the feedback strength. $\phi_{re} = \omega\tau_{ext}$ is the round-trip phase induced by the external cavity, where ω denotes the angular frequency of the laser emission. All these parameters are schematically shown in Fig. 3.1. This approach assumes that the external cavity resonance can be neglected when the feedback strength is relatively weak (Coldren, Corzine, and Mashanovitch, 2012). Thus, Eq. (3.3) accounts for the power of the returned field but excludes its periodicity.

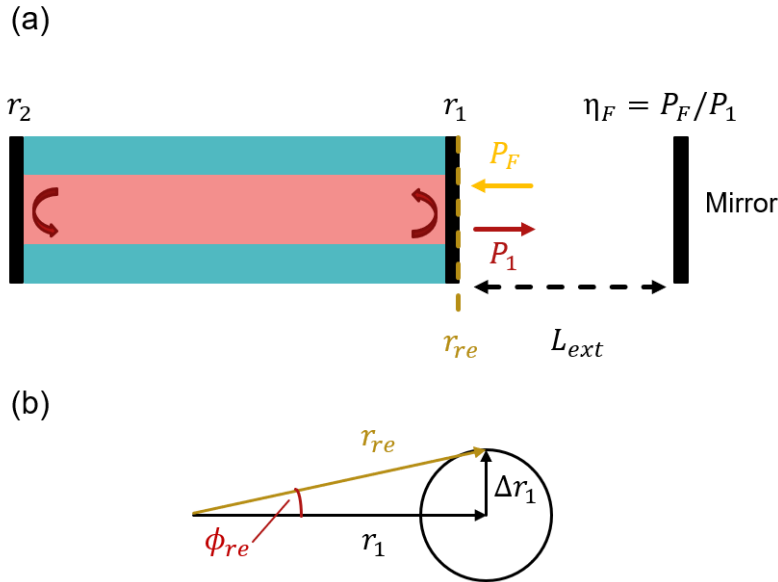


Figure 3.1: (a) Schematic of a semiconductor laser that is subject to optical feedback. (b) Polar plot of equivalent reflectivity r_{re} from output side of laser. Δr_1 represents feedback that changes both the amplitude and phase of r_{re} .

In this thesis, the investigations are focused on the aforementioned conventional optical feedback. It is worth stressing that there are also other architectures such as optoelectronics feedback (F. Lin and JM Liu, 2003), filtered optical feedback (Yousefi and Lenstra, 1999), phase conjugate feedback (Rontani et al., 2016) and tilted optical feedback (X.-G. Wang et al., 2021) are well developed over the past decades. Those techniques provide promising solutions for overcoming the damped

relaxation oscillations and generating more complex nonlinear dynamics. The reader is invited to consult Ref. (Kane and Shore, 2005) for further information.

The occurrence of oscillation dynamics from a laser system is not only dependent on the EOF conditions, but also determined by the laser itself. According to Arecchi, Lippi, et al., 1984, the classification of a laser system depends on the photon lifetime τ_p , the carrier lifetime τ_c and the polarization lifetime τ_{pol} . The class A lasers such as gas laser exhibits a high degree of stability that prevents them to generate chaotic oscillations except for two additional degrees of freedom are well controlled (Weiss, Godone, and Olafsson, 1983), since their photon lifetime is much longer than their carrier lifetime and polarization lifetime ($\tau_p \gg \tau_c \sim \tau_{pol}$). Therefore, a single electric field E equation is enough to describe the laser system. In this thesis, the semiconductor lasers studied are class B lasers in which $\tau_c \geq \tau_p \gg \tau_{pol}$. In this case, an additional equation that describes the carrier density N is in need. As a consequence, the generation of chaotic oscillations from a semiconductor laser is easier than a class A laser. The play of one additional degree of freedom such as Q-switching, optical injection, and optical feedback is able to trigger those unstable dynamics (Arecchi, Meucci, et al., 1982). In particular, the vertical cavity surface emitting lasers (VCSEL) is known from their two different polarizations, thus they are able to produce chaos without any external perturbations (Virte et al., 2013). For a class C laser, its τ_p , τ_c and τ_{pol} are of the same order of magnitude ($\tau_p \sim \tau_c \sim \tau_{pol}$), thus the laser system is described by three rate equations that include the carrier density, the electric field and the polarization P . Class C lasers such as NH_3 laser can generate chaotic oscillations by itself and no external control is required (Weiss, Klische, et al., 1985).

Figure 3.2 illustrates the physical processes that takes place within a semiconductor laser in EOF operation. In the active region, the amplitude-phase coupling between the returned light field and the intra-cavity one is ruled out by the field fluctuations in amplitude $|\Delta E|$ and phase $|\Delta\phi|$. The perturbation of the photon density that is caused by the re-injected field results in a fluctuation of both the carrier density and the optical gain. The latter that is attributed to the damping effect changes the refractive index through the α_H -factor, and then leads to a deviation of the lasing wavelength. In addition, another contribution of the wavelength fluctuation directly results from the phase fluctuation induced by the returned field. As a consequence, the interaction of the intensity and phase loop results in complex nonlinear dynamics when the laser operates with EOF. Severe optical instabilities

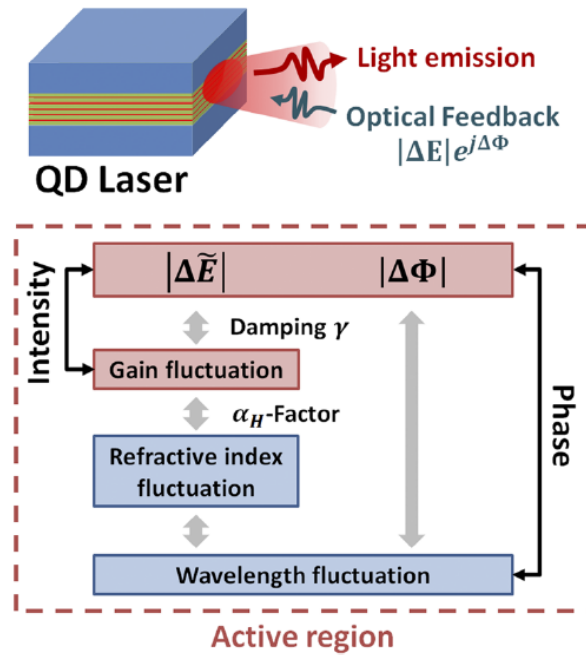


Figure 3.2: Schematic representation of the physical processes involved in a semiconductor laser under optical feedback. From Ref. (H. Huang et al., 2020)

such as coherence collapse are identified (Kane and Shore, 2005; Ohtsubo, 2012).

The impact of optical feedback on semiconductor lasers has been widely studied since 1970s (Broom et al., 1970; Risch and Voumard, 1977). In 1980, Lang and K. Kobayashi, 1980 proposed a model that was to analyze the dynamics of a diode laser subject to EOF. Then, extensive studies on the improvement of LK model and on the applications of those oscillation dynamics were investigated (Lenstra, Verbeek, and Den Boef, 1985; Henry and Kazarinov, 1986; Mørk, Mark, and Tromborg, 1990; Frédéric Grillot, Bruno Thedrez, and Guang-Hua Duan, 2004). Despite the strong mode-hopping effect (Mork, Bjarne Tromborg, and Christiansen, 1988) and the chaotic oscillation that degrades the bit error rate (BER) in transmission (Grillot, Thedrez, Py, et al., 2002), it has been shown that the spectral linewidth of a laser can be either narrowed or broadened in different feedback conditions (G. Agrawal, 1984; Lenstra, Verbeek, and Den Boef, 1985). To have a complete picture of the laser dynamics under EOF, Tkach and Chraplyvy, 1986 identified five feedback regimes in a semiconductor distributed feedback (DFB) laser, which depend on the feedback ratio (feedback strength) and the external cavity length. As shown in Fig. 3.3, the laser operates in regime I where the feedback strength is quite weak. Due to the phase fluctuation caused by the returned field, the spectral linewidth of laser is

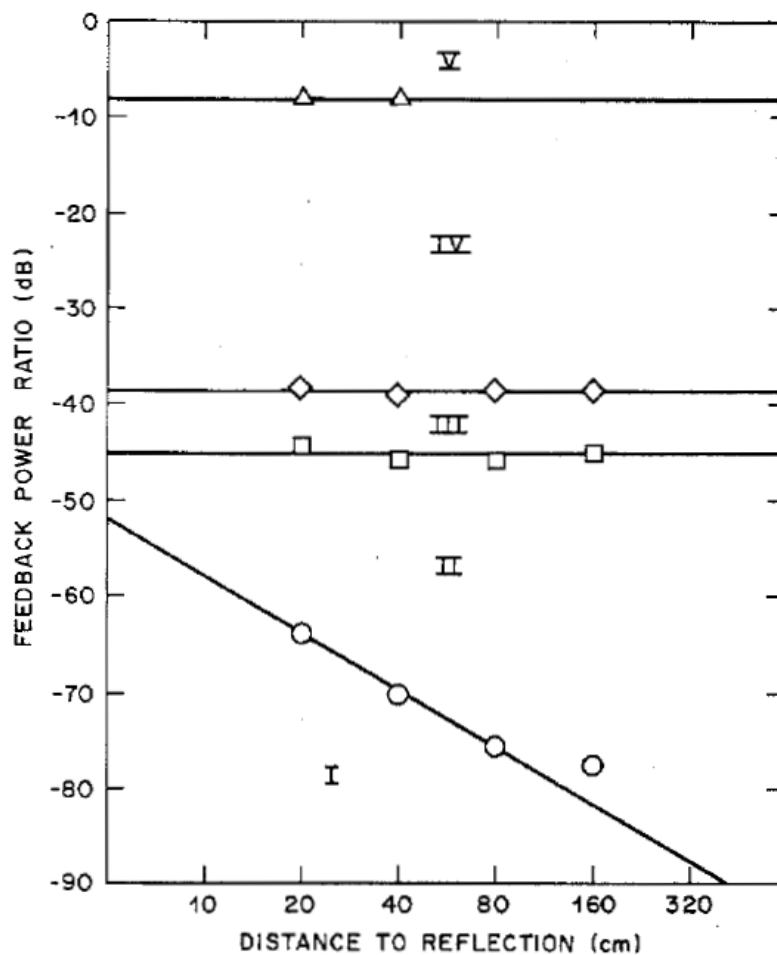


Figure 3.3: Feedback regimes in a semiconductor DFB laser. Regime I, stable regime in which the linewidth is either broadened or narrowed. Regime II, line splitting. Regime III, linewidth narrowing. Regime IV, unstable oscillations. Regime V, strong linewidth narrowing. From Ref. (Tkach and Chraplyvy, 1986)

either narrowed or broadened. In regime II where the external cavity length is long or the feedback strength is relatively strong, line splitting phenomena is observed. Such a behavior is attributed to the feedback phase induced mode hopping that arises between external cavity modes (ECMs). The ECMs are determined by the external cavity length whose frequencies are multiples of $c/2n_{ext}L_{ext}$, with n_{ext} the refractive index of the external cavity. The laser is restabilized by the EOF in regime III, in which the linewidth is reduced. In addition, the laser dynamics in this regime does not show a clear dependence on the external cavity length. Therefore, taking advantage of such a property allows for developing low-noise semiconductor lasers. In regime IV where the feedback strength is much improved,

the laser system is driven into the coherence collapse regime. On this route to chaos, the laser in general exhibits two frequencies with incommensurable ratio at the relaxation oscillation frequency and at the external cavity frequencies. Both frequencies interact with each other and result in the quasi-periodicity route to chaos as the feedback strength increases. Finally, the laser enters into regime V if the feedback strength is strong enough, where the laser is highly stable and shows a single narrow-linewidth longitudinal mode that is determined by the external cavity frequency. Nevertheless, this regime is very difficult to reach since the feedback strength is usually limited by the facet reflection. A practical approach to drive the laser into this regime is to utilize an antireflection coating on the facet that is subjected to the feedback (Temkin et al., 1986).

In EOF operation, characterizations of different feedback regimes are promising for versatile applications. On one hand, dynamics in this regime strongly alter the performance of a high-speed communication system, hence an optical isolator is required to avoid those undesired oscillations. On the other hand, the chaotic oscillations exhibit a much larger bandwidth than the 3-dB bandwidth that is determined by the relaxation oscillation frequency, thus it is also possible to take advantage of the deterministic chaos for applications such as secured or private communications (Spitz et al., 2021), light detection and ranging (LIDAR) systems with improved resolutions (J.-D. Chen et al., 2021), and random bit generators (Sciamanna and Shore, 2015). In addition, the EOF technique has been applied to semiconductor lasers and high power diode lasers to improve their noise properties (W. Jin et al., 2021; Vijayakumar et al., 2011). Last but not least, although the cartography depicted in Fig. 3.3 is first proposed for analyzing a single-mode semiconductor laser, following studies have extended its functionality to describe some sub-regimes of the coherence collapse (Klaus Petermann, 1991) or to address the short-cavity regime (Tager and Elenkrig, 1993).

3.2 Lang & Kobayashi equations

To analyze the dynamics of a semiconductor laser subject to optical feedback, the aforementioned LK model is a widely used theoretical method (Lang and K. Kobayashi, 1980). Assuming that the light field propagates in the external cavity with a single round-trip, the complex electric field $\tilde{E}(t)$ of a semiconductor laser in EOF operation is described as follows:

$$\frac{d\tilde{E}(t)}{dt} = \left\{ \frac{1}{2}(1 + i\alpha_H)[\Gamma G_N(N(t) - N_{tr}) - \frac{1}{\tau_p}] + i\omega_0 \right\} \tilde{E}(t) + \kappa \tilde{E}(t - \tau_{ext}) \quad (3.4)$$

with κ the feedback coefficient that is written as (Nikolaus Schunk and Klaus Petermann, 1988):

$$\kappa = \frac{1}{\tau_{in}} 2C_l \sqrt{\eta_F} \quad (3.5)$$

where $\tau_{in} = 2n_{in}L_c/c$ is the internal round-trip time with n_{in} and L_c the refractive index and the cavity length of the laser, respectively. The coupling coefficient from the facet to the external cavity C_l for a FP laser is expressed as (Frédéric Grillot, Bruno Thedrez, and Guang-Hua Duan, 2004):

$$C_l = \frac{1 - R_1}{2\sqrt{R_1}} \quad (3.6)$$

For a DFB laser, its C_l is more complex and is expressed as (Frédéric Grillot, 2009):

$$C_l = \frac{2(1 - |\rho_l|^2) \exp(-i\phi t) (q_0^2 + \kappa_0^2) L^2}{i\kappa_0 L(1 + \rho_l^2) - 2\rho_l q_0 L_c} \quad (3.7)$$

$$\frac{1}{2qL - \sum_{k=l,r} (1 - \rho_k^2) \kappa_0 L / [2iq_0 L \rho_k + \kappa_0 L(1 + \rho_k^2)]}$$

where $\rho_k = |\rho_k| \exp(i\phi_k)$ with $k = l, r$ the complex reflectivities of the left and right facets, r_2 and r_1 , respectively. L_c and κ_0 account for the laser cavity length and the coupling coefficient of the grating, respectively. $q_0 = \alpha_{tot} + i\delta_0$ with α_{tot} the total internal loss and δ_0 the detuning between the lasing and the Bragg wavenumbers.

In a semiconductor laser, the dynamics of the electric-field amplitude is much slower than the angular frequency ω_0 of the fast optical carrier. Assuming that $\tilde{E}(t) = \tilde{A}(t) \exp(i\omega_0 t)$, Eq. (3.4) can be re-expressed as:

$$\frac{d\tilde{A}(t)}{dt} = \left\{ \frac{1}{2} (1 + i\alpha_H) [\Gamma G_N(N(t) - N_{tr}) - \frac{1}{\tau_p}] + i\omega_0 \right\} \tilde{A}(t) \quad (3.8)$$

$$+ \kappa \tilde{A}(t - \tau_{ext}) \exp(-i\omega_0 \tau_{ext})$$

where the term $\exp(i\omega_0 t)$ accounts for the fast lasing oscillations and $\tilde{A}(t)$ denotes the slow envelop of the complex electric field. The above equation refers to the LK equation for a slow complex electric field after eliminating the fast optical carrier component. With $\tilde{A}(t) = A(t) \exp(i\phi(t))$, Eq. (3.8) can also be rewritten as follows:

$$\frac{dA(t)}{dt} + i \frac{d\phi(t)}{dt} A(t) = \frac{1}{2} [\Gamma G_N(N(t) - N_{tr}) - \frac{1}{\tau_p}] A(t) + \kappa A(t - \tau_{ext}) \cos(\theta(t))$$

$$+ i \left\{ \frac{\alpha_H}{2} [\Gamma G_N(N(t) - N_{tr}) - \frac{1}{\tau_p}] A(t) - \kappa A(t - \tau_{ext}) \sin(\theta(t)) \right\} \quad (3.9)$$

where $A(t)$ and $\phi(t)$ denote the amplitude and the phase of the field, respectively, and,

$$\frac{dA(t)}{dt} = \frac{1}{2} \left[\Gamma G_N (N(t) - N_{tr}) - \frac{1}{\tau_p} \right] A(t) + \kappa A(t - \tau_{ext}) \cos(\theta(t)) \quad (3.10)$$

$$\frac{d\phi(t)}{dt} = \frac{\alpha_H}{2} \left[\Gamma G_N (N(t) - N_{tr}) - \frac{1}{\tau_p} \right] - \kappa \frac{A(t - \tau_{ext})}{A(t)} \sin(\theta(t)) \quad (3.11)$$

with

$$\theta(t) = \omega_0 \tau_{ext} + \Phi(t) - \Phi(t - \tau_{ext}) \quad (3.12)$$

On the other hand, the rate equation for the carrier density is expressed as follows (Ohtsubo, 2012):

$$\frac{dN(t)}{dt} = \frac{\eta_i I}{qV} - \frac{N(t)}{\tau_c} - G_N (N(t) - N_{tr}) A^2(t) \quad (3.13)$$

At the steady-state where $d/dt = 0$, the constant output power leads to $A(t) = A(t - \tau_{ext}) = A_s$ and $N(t) = N_s$. The steady-state phase Φ_s can be written as $\Phi_s = (\omega_s - \omega_0)t$ with ω_s the frequency at the steady-state (Bjarne Tromborg, Osmundsen, and Olesen, 1984; Ohtsubo, 2012). Finally, the steady-state solutions for Eqs. (3.10), (3.11) and (3.13) are written as follows:

$$A_s^2 = \frac{\eta_i I / qV - N_s / \tau_c}{G_N (N_s - N_{tr})} \quad (3.14)$$

$$\omega_s - \omega_0 = \Delta\omega_s = -\kappa [\alpha_H \cos(\omega_s \tau_{ext}) + \sin(\omega_s \tau_{ext})] \quad (3.15)$$

$$N_s - N_{tr} = \Delta N_s = -\frac{2\kappa}{\Gamma G_N} \cos(\omega_s \tau_{ext}) \quad (3.16)$$

3.3 Light-current characteristics under optical feedback

According to Eq. (3.16), the EOF affects the laser system by decreasing the carrier density that is required for emission. As a consequence, the threshold current is reduced. Assuming that the feedback strength remains weak ($\eta_F \ll 1$), the threshold current I_{th} can be expressed as follows:

$$I_{th} = I_0 (1 - 2\kappa \cos(\omega_s \tau_{ext})) \quad (3.17)$$

For a fixed external cavity length, Fig. 3.4 (a) displays the L-I characteristics of a QD FP laser in the free-running operation (black) and in the EOF operation with different feedback strength ($\eta_F = 1.7\%$, 3.4% and 6.7%) (Heming Huang, 2017). In agreement with Eq. (3.17), a 7 mA reduction of the threshold current is observed with the increase of η_F to its maximum value. On the other hand, Fig. 3.4 (b) depicts

the L-I curves of another semiconductor laser by fixing its feedback strength but varying the external cavity length from 15 cm (dotted red line) to 150 cm (broken blue line). Its L-I curve in free-running operation (solid black line) is shown for a reference. In both feedback conditions, $\sim 30\%$ reductions of I_{th} are observed, indicating that the external cavity length in the coherent regime does not largely affect the threshold properties in EOF operation. In addition, the output power exhibits residual undulations as the bias current increases, which is attributed to the interaction between the ECMs and the laser cavity modes. Figure 3.5(a) illustrates the distribution of resonant modes of the laser and of the external cavities in the integer resonant condition, where $\tau_{ext}/\tau_{in} \in N$ (N is integer). For a fixed bias current, the frequency of the mode $N + 1$ is coincident with that of the mode M' and the laser oscillates with these photon pairs. However, the variation of gain bias changes the frequencies of the laser cavity modes thus resulting in a mismatch between these photon pairs, which shifts the laser cavity resonant modes towards the low frequency side, relative to the ECMs. As a consequence, the constructive and the destructive interferences induced by the current variation will enhance or reduce the output power, respectively, thus the output power shows an undulation behavior. Nevertheless, phenomena will be minimized if the laser operates in the non-resonant condition where $\tau_{ext}/\tau_{in} \notin N$, as shown in Fig. 3.5(b). Assuming that the modes M and N are perfectly matched at the beginning, thus the modes M' and $N + 1$ are mismatched in this case. While the increase of current reduces the frequencies of the laser cavity modes thus leading to a mismatch between the modes M and N , the matching between the modes M' and $N + 1$ improves. Therefore, a new pairs of oscillating photons will be generated much quicker in the non-resonant conditions and the power undulation effect will be minimized.

3.4 Phase conditions

According to Eq. (3.15), the EOF also affects the light field through its phase, which is expressed as follows:

$$\Delta\omega_s\tau_{ext} = -C\sin\phi_0 \quad (3.18)$$

with

$$C = \kappa\tau_{ext}\sqrt{1 + \alpha_H^2} = \frac{\tau_{ext}}{\tau_{in}}2C_l\sqrt{1 + \alpha_H^2}\sqrt{\eta_F} \quad (3.19)$$

$$\phi_0 = \omega_s\tau_{ext} + \arctan(\alpha_H) \quad (3.20)$$

where $\Delta\omega_s\tau_{ext}$ denotes the phase difference between the intra-cavity field and the delayed field. C accounts for a feedback parameter that depends on the α_H -factor,

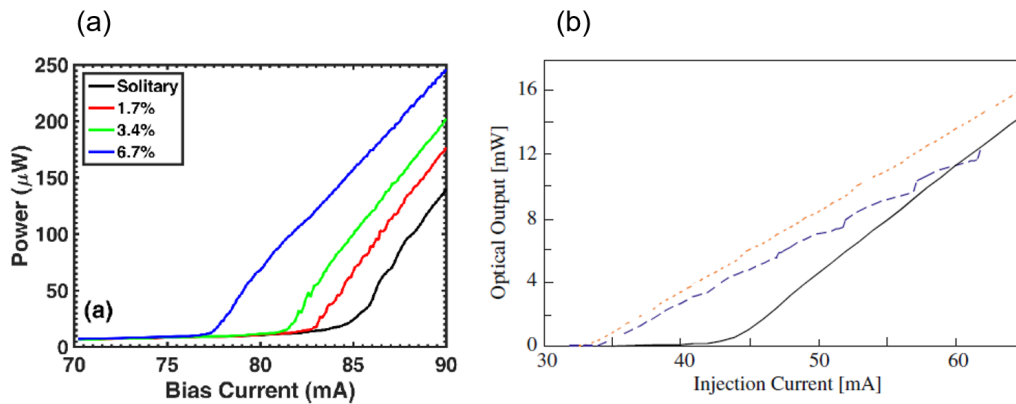


Figure 3.4: (a) L-I curves of a QD FP laser in free-running operation (black) and for three different amounts of feedback ($\eta_F = 1.7\%$, 3.4% and 6.7%). The external cavity length L_{ext} is fixed. From Ref. (Heming Huang, 2017). (b) L-I curves of a semiconductor laser in free-running operation (solid black line), and with identical η_F but different L_{ext} at 15 cm (dotted red line) or at 150 cm (broken blue line). From Ref. (Ohtsubo, 2012).

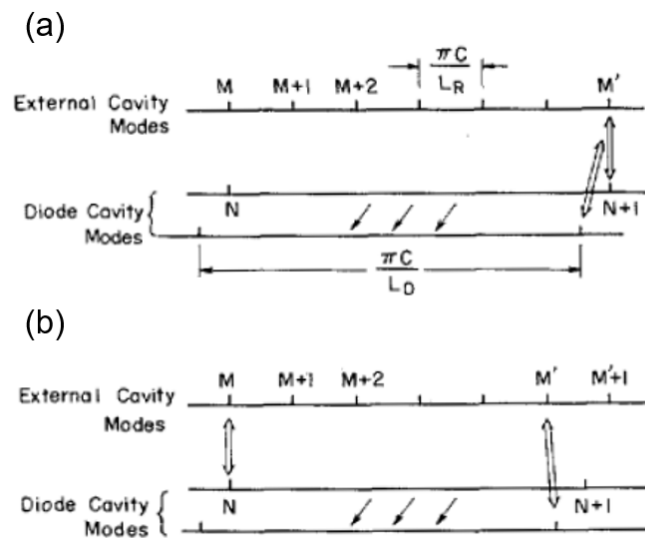


Figure 3.5: Relationship between the laser cavity modes and external cavity modes, in (a) integer resonant condition ($\tau_{ext}/\tau_{in} \in N$, N is integer), and in (b) non-resonant condition ($\tau_{ext}/\tau_{in} \notin N$). From Ref. (Lang and K. Kobayashi, 1980).

the feedback delay time τ_{ext} and the feedback strength η_F . The number of solutions of Eq. (3.18) is highly determined by the value of C , which is shown by a (C, ϕ_0) space in Fig. 3.6. The roman numbers represent the number of solutions, meaning that the laser is stable against EOF with a $C \leq 1$, where only one solution is found; however, with a $C > 1$, the increased numbers of solutions depending on ϕ_0 indicates that the laser suffers from severe instabilities.

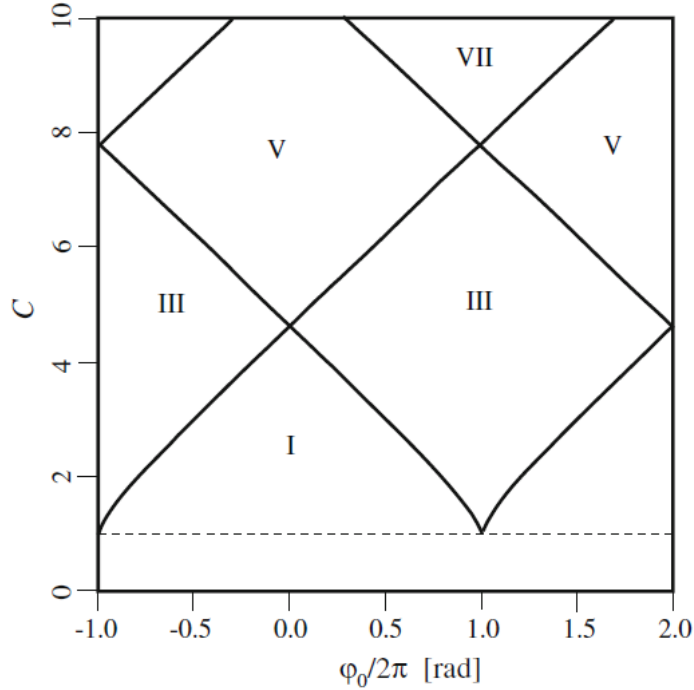


Figure 3.6: Number of solutions for Eq. (3.18) in (C, ϕ_0) space. The roman numbers represent the number of solutions. From Ref. (Ohtsubo, 2012).

Another way to schematically represent the solutions for Eq. (3.18) is to calculate the interception between $y = \omega_s \tau_{ext}$ and $y = \omega_s \tau_{ext} + C \sin[\omega_s \tau_{ext} + \arctan(\alpha_H)]$. To analyze a real laser system, Fig. 3.7 depict the case for (a) a QW laser and for (b) a QD laser. The main difference between these devices is the α_H -factor, which is fixed at 4 and at 1 for the former and the latter, respectively. While fixing the external cavity length at 10 cm, the increase of feedback strength from -35 dB (green) to -25 dB (red) is enough to drive the QW laser into unstable oscillation regime, whereas the QD one remains stable in presence of a sole solution with the η_F increased up to -20 dB (blue). These results reveal that the α_H plays a crucial role in determining the feedback insensitivity of a semiconductor laser. It is worth stressing that Henry and Kazarinov, 1986 also proposed an approach to illustrate

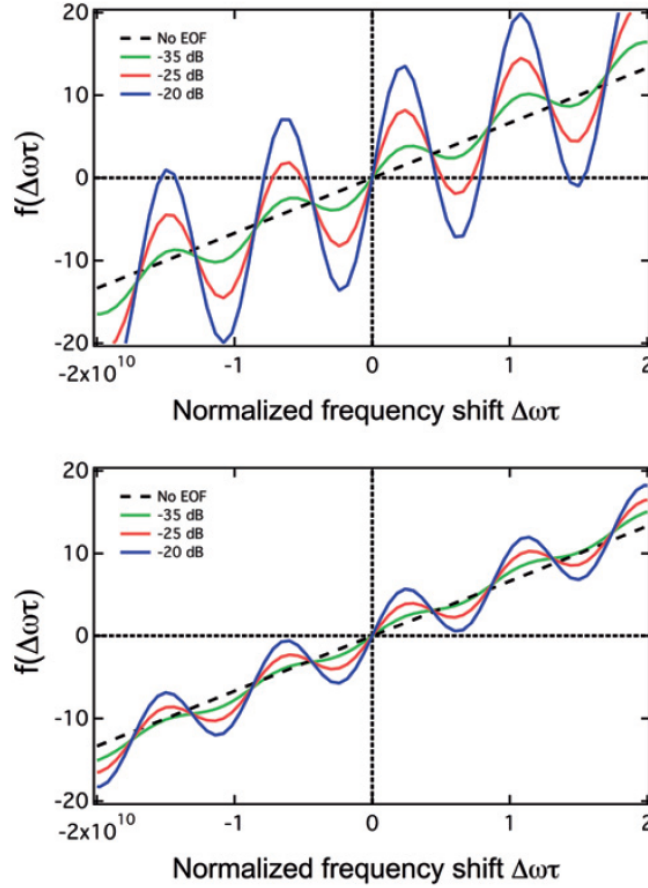


Figure 3.7: Number of solutions for Eq. (3.18) for (a) a QW laser with $\alpha_H = 4$, and for (b) a QD laser with $\alpha_H = 1$. In both cases, the external cavity length is fixed to 10 cm, while the feedback strength is -35 dB (green), -25 dB (red), and -20 dB (blue). The black dashed line corresponds to the free-running operation. From Ref. (Frédéric Grillot, J. C. Norman, et al., 2020).

the possible oscillations by using the carrier density variation that is dependent on the phase difference $\Delta\omega_s\tau_{ext}$, readers are invited to consult Ref. (Henry and Kazarinov, 1986) for further information.

As a consequence of the phase variation due to the EOF, the optical spectral linewidth $\Delta\nu$ of a semiconductor laser is largely affected and is expressed as follows:

$$\Delta\nu = \frac{\Delta\nu_0}{(1 + C\cos\phi_0)^2} \quad (3.21)$$

with ν_0 the free-running optical spectral linewidth. To explain what happens in Fig. 3.3, the spectral linewidth of a semiconductor laser as a function of C is depicted in Fig. 3.8, in which different feedback regimes are marked. The stable solution case $C \leq 1$ is represented by regime I, where the linewidth is either reduced or

broadened by the feedback phase. In regime II where the $C > 1$ but it remains low, the occurrence of ECMs make the linewidth very sensitive to the feedback phase. Nevertheless, an increased number of ECMs contributes to minimize the influence of feedback phase and to stabilize the laser into regime III. Further increasing the C above its critical level, the laser enters into regime IV where its linewidth is dramatically broadened.

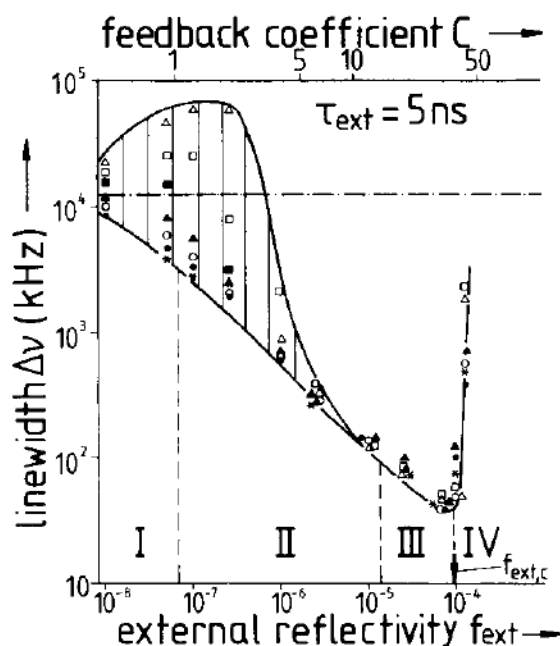


Figure 3.8: Optical spectral linewidth as a function of the feedback strength. The markers represent different feedback phase conditions. roman numbers represent the feedback regimes. From Ref. (Klaus Petermann, 1995).

3.5 Critical feedback level for coherence collapse

As aforementioned, the occurrence of the unstable oscillations from a semiconductor laser in EOF operation has been extensively studied, since the control of those laser dynamics is promising for versatile applications. In Sec. 3.4, the author introduces how the feedback strength and phase determines the laser dynamics. In this section, the conditions for experimentally reaching the critical feedback level that is associated to the onset of unstable oscillations is performed. Figure 3.9 illustrates the onset of regime IV as a function of the feedback strength and the external delay time. The dashed line represents the condition $C = 1$, below which the laser is unconditionally stable against the EOF. However, $C = 1$ is not a sufficient condition for ensuring a stable behavior since it does not account for the regimes II

and III. The vertical line corresponds to the condition $f_{RO} \times \tau_{ext} = 1$ with f_{RO} the relaxation oscillation frequency, which separates the short- and long-cavity regimes on the left and right sides, respectively. In the long-cavity regime ($f_{RO} \times \tau_{ext} > 1$), the critical level is independent on the external delay time but is determined by the intrinsic laser properties (Frédéric Grillot, Bruno Thedrez, and Guang-Hua Duan, 2004). In contrary, the critical level r_{crit} in the short-cavity regime ($f_{RO} \times \tau_{ext} < 1$) increases with the decrease of τ_{ext} .

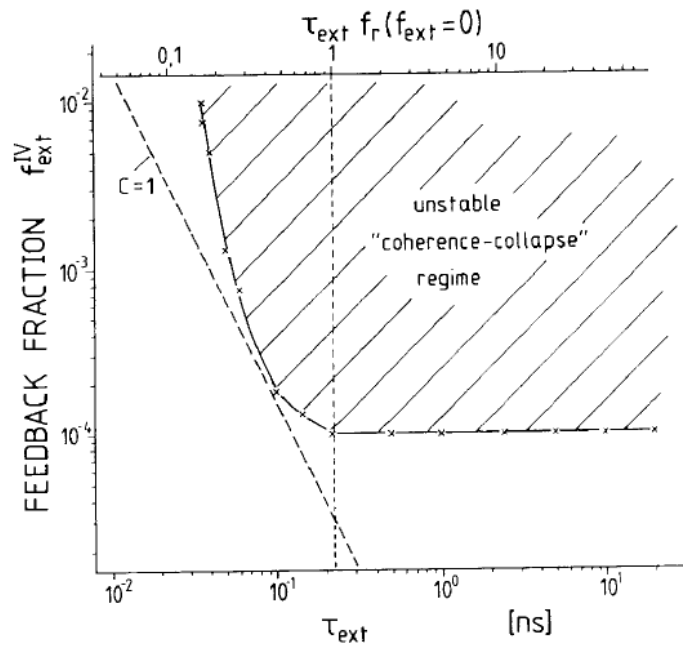


Figure 3.9: The critical feedback level r_{crit} as a function of the delay time τ_{ext} (solid line). The dashed line marks $C = 1$, and the vertical line indicates $f_{RO} \times \tau_{ext} = 1$. From Ref. (Schunk and Petermann, 1989).

It is worth stressing that the information given by Fig. 3.9 still misses some important physical properties in the short-cavity regime (SCR). Figure 3.10(a) and (b) depicts the r_{crit} of a semiconductor laser and its f_{RO} as a function of the external cavity length L_{ext} in the SCR, in which strong undulations of the r_{crit} caused by the external cavity length variation are identified. Such an effect is directly resulted from the interferences between the laser cavity modes and the ECMs, as introduced in Sec. 3.3. In the integer resonant feedback conditions (i.e., $f_{RO}/f_{ext} \in N$, N is integer), the constructive interferences between the laser cavity modes and the ECMs results in a strong mode competition. This mechanism is confirmed by the abrupt jump of the f_{RO} around its free-running value, as represented by the black vertical line at 3.25 GHz. As a result, the feedback insensitivity of the laser is improved in this mode

switching process, in presence of a large increase of the r_{crit} in the integer resonant conditions. Last but not least, the periodic undulations of feedback sensitivity as a function of the external cavity length are valid for all dynamic states including the period-one (P1), the period-two (P2), the quasi-period (QP) and the chaos.

Despite the undulations of the feedback insensitivity in the SCR, the quasi-stable r_{crit} in the long-cavity regime (LCR) that only depends on the intrinsic laser properties is promising for analyzing the laser's tolerance for EOF. One of the commonly used definitions of the r_{crit} is written as follows (Helms and Petermann, 1990):

$$r_{crit} = \frac{\tau_{in}(Kf_R^2 + 1/\tau_{ext})^2}{16C_l^2} \left(\frac{1 + \alpha_H^2}{\alpha_H^4} \right) \quad (3.22)$$

where K and τ_{ext} denote the K-factor and the effective carrier lifetime, respectively. It is worth stressing that Eq. (3.22) along with other definitions of the r_{crit} (Binder and Cormack, 1989; YAMADA and SUHARA, 1990; Mork, Bjarne Tromborg, and Jannik Mark, 1992) are all simplified expressions for the r_{crit} which ignore some laser physics in EOF operation. However, those equations allow us to qualitatively analyze the laser's tolerance for back-reflections. In particular, Eq. (3.22) gives insights for controlling the occurrence of the nonlinear dynamics of a semiconductor laser in EOF operation, which is technically important for developing a feedback insensitive laser source for different applications.

3.6 Towards a reflection-resistant optical transmitter

In this thesis, the author focuses on the development of reflection-resistant lasers for PIC applications. Therefore, several optimization paths can be considered based on the definition of Eq. (3.22).

- A high front facet reflectivity that leads to a low C_l is a preferred option. In practical, an as-cleaved front facet whose reflectivity equals to 32% ($C_l=0.6$) offers a good balance between a high feedback tolerance and sufficient optical output power. Besides, the increase of cavity length thus the τ_{in} is also beneficial for improving the critical level; however, the consequent increase of photon lifetime will limit the 3-dB bandwidth, which will be discussed in Chap. 4.
- The reflection insensitivity can be also improved by considering increasing the damping factor. In this case, the gain fluctuation induced by the photon-density variation can be suppressed thus results in the increase of r_{crit} . To this

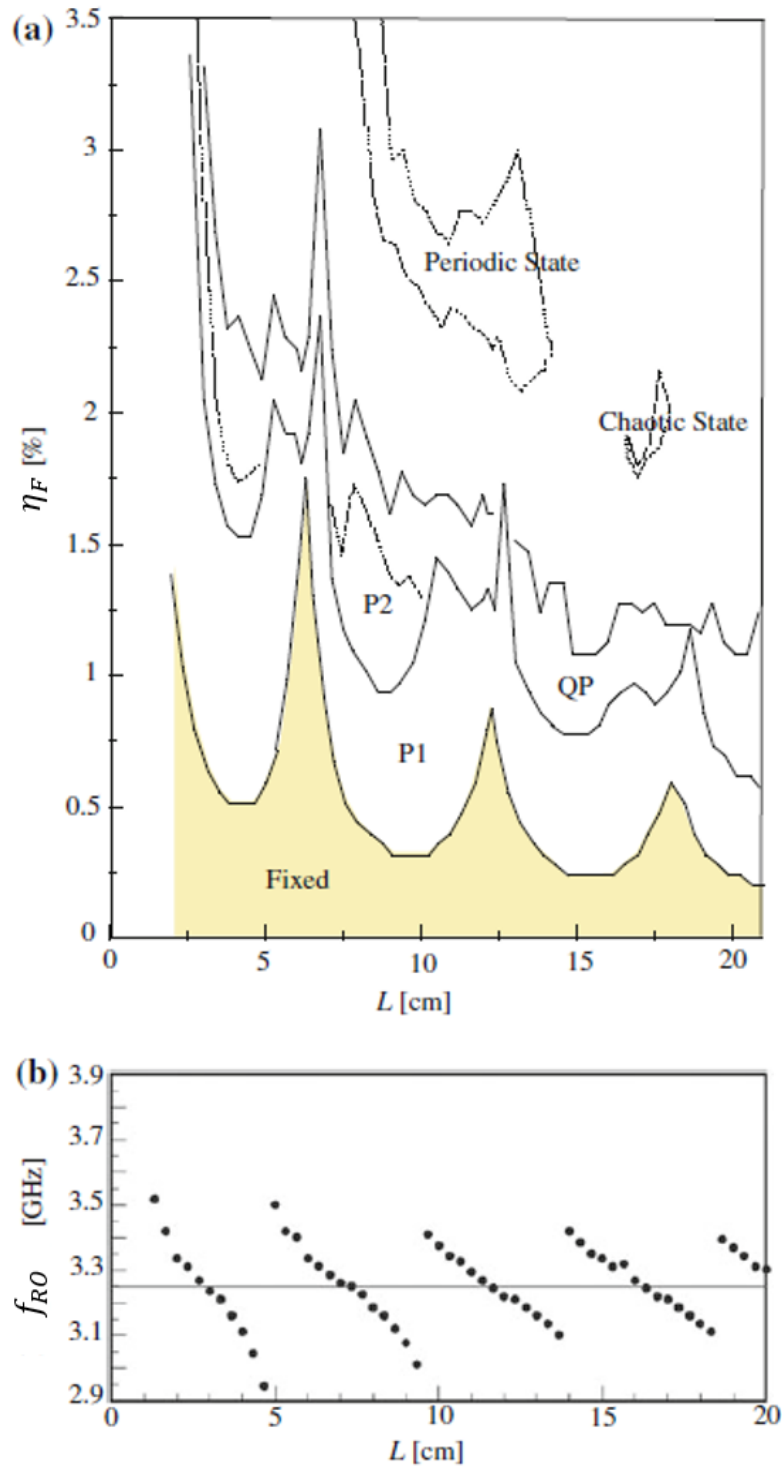


Figure 3.10: (a) Feedback strength η_F and (b) relaxation oscillation frequency f_{RO} as a function of the external cavity length L_{ext} (solid line). The black vertical line at 3.25 GHz in (b) represents the f_{RO} in free-running operation. P1, period-one; P2, period-two; QP, quasi-period. From Ref. (Ohtsubo, 2012).

end, the QD is a promising gain medium for developing a reflection-resistant semiconductor laser, owing to its stronger damping compared to the QW (Coldren, Corzine, and Mashanovitch, 2012).

- It is a promising option to decrease the α_H -factor thus to decouple the interaction between the intensity and phase of the intra-cavity field. By well controlling the self-organized growth technique of the epitaxy process, a near-zero α_H is expected in QD. In contrary, the α_H of QW is a rather constant material parameter that ranges from two to about five due to the linear dependence of both the refractive index and gain (Coldren, Corzine, and Mashanovitch, 2012).

Besides these direct conclusions of Eq. (3.22), recent studies also give insights for improving the the laser's tolerance for EOF by taking into account other parameters that are related to the laser configuration. First, the feedback parameter C defined in Eq. (3.19) can be re-expressed as follows (Frédéric Grillot, J. C. Norman, et al., 2020):

$$C = \frac{\omega_s \tau_{ext}}{Q} \sqrt{1 + \alpha_H^2 \sqrt{\eta_F}} \quad (3.23)$$

with Q the quality factor of the laser cavity. In semiconductor lasers, the non-radiative recombinations such as the Shockley-Read-Hall (SRH) is found to affect the carrier lifetime through the following relationship:

$$\frac{1}{\tau_{ext}} = \frac{1}{\tau_c} + \frac{1}{\tau_{SRH}} \quad (3.24)$$

where τ_c denotes the carrier lifetime without the contribution of SRH. Therefore, Eqs. (3.23) and (3.24) provide useful guidelines for designing lasers by considering:

- Utilizing a high-Q cavity (quality factor $> 10^5$) to reduce the C below 1. In this case, the laser operating in regime I is always tolerant for EOF regardless the feedback strength (Gomez et al., 2020).
- Taking advantage of the SRH recombination in epitaxial QDs on silicon. Despite the SRH mechanism that could be detrimental to laser performance when epitaxially growing QDs on Si (Buffolo et al., 2019), the decrease of the effective carrier lifetime due to the τ_{SRH} could give rise to an improved r_{crit} . In addition, a recent study reveals that the SRH also affects the feedback insensitivity of a QD laser through its α_H -factor (S. Zhao and Frédéric Grillot, 2021).

In particular, the dual-state emission behavior in QD laser also impacts its tolerance for EOF. Prior work demonstrated that the suppress of ES emission is beneficial for improving the laser's stability against EOF (Heming Huang, Jianan Duan, et al., 2018). Last but not least, a larger beam divergence of the laser emission is beneficial for decreasing the effective feedback power thus makes the laser more resistant to reflections, however, the consequent degraded beam quality needs to be addressed.

3.7 Dynamics of QD laser in long-delay optical feedback operation

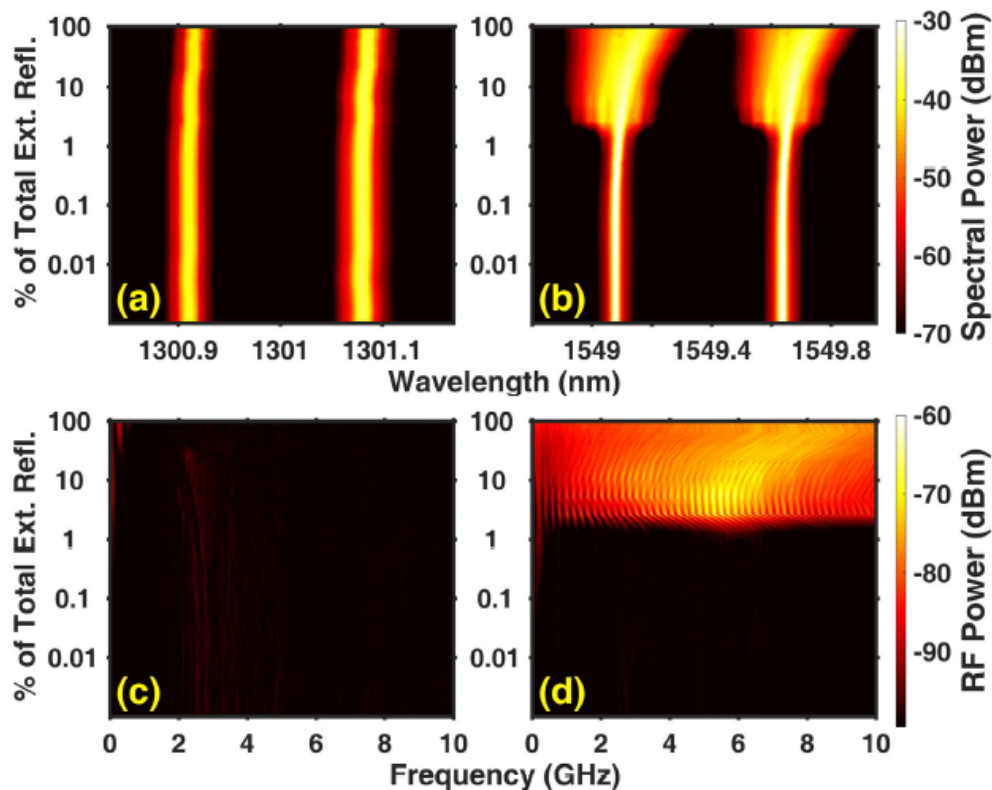


Figure 3.11: Optical and RF spectral mappings as a function of the feedback strength η_F for the QD laser on Si [(a) and (c)] and for the QW laser [(b) and (d)] at $3 \times I_{th}$. The vertical axis is in logarithmic scale. 100% η_F means -7.4 dB. From Ref. (Jianan Duan, Heming Huang, et al., 2019)

QD laser is known from its high tolerance for EOF, owing to its near-zero α_H -factor. Compared to the reflection sensitive QW devices, the QD laser can be a promising solution for the development of PICs in which the on-chip optical isolator is no longer required. A prior work from the author's group demonstrated that the epitaxial QD laser on silicon exhibited a much stronger tolerance for EOF than the QW device in the long-cavity regime with an external cavity length at 7 meters.

Corresponding external cavity frequency at 14 MHz thus satisfies the condition for long-delay optical feedback where $f_{RO}/f_{ext} > 1$. Figures 3.11 depict the optical and the RF spectral mappings as a function of the feedback strength for the QD laser on Si [(a) and (c)] and for the QW laser [(b) and (d)] at $3 \times I_{th}$. The maximum feedback strength for both devices is limited to 18% (-7.4 dB) due to the optical loss after the light propagates through the optical fibre. With the increase of η_F to its upper-limit, the QD laser remains stable without showing any dynamics. In contrary, the QW one easily enters into the coherence collapse regime under a weak optical feedback with η_F being 1.7% of its upper-limit.

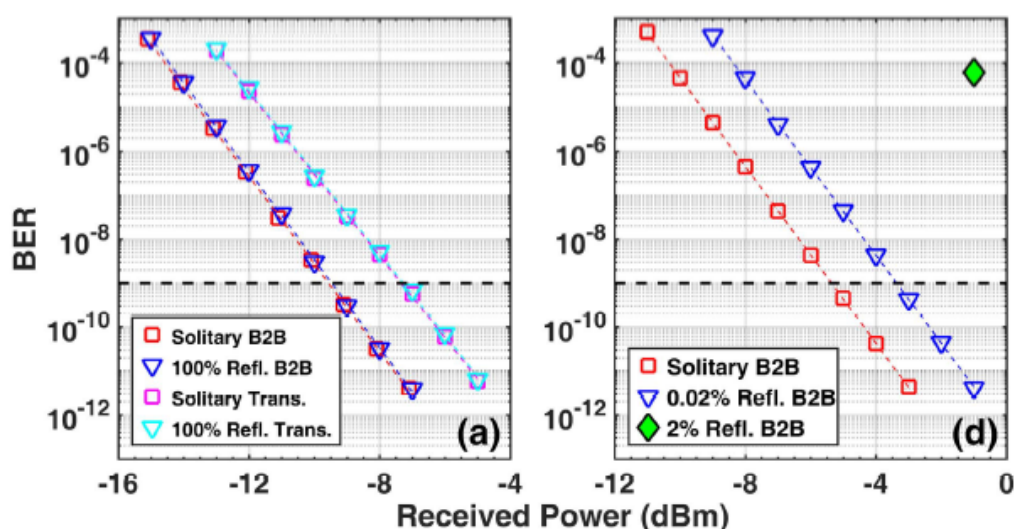


Figure 3.12: BER plots versus received optical power for (a) the QD laser and for (b) the QW laser. From Ref. (Jianan Duan, Heming Huang, et al., 2019)

As a consequence of the coherence collapse, the transmission performance of laser could be largely degraded. To evaluate the impact of the EOF on the transmission dynamics of both lasers, the bit-error-rates (BERs) in the external modulation operation with a modulation rate of 10 Gbps are investigated. Figure 3.12(a) depicts the BERs as a function of the received optical power of the QD laser in free-running operation with back-to-back configuration (B2B, red) and after 2 km transmission (magenta). with the maximum η_F applied to it, same measurements were repeated in the B2B configuration (blue) and after 2 km transmission (cyan). Results reported revealed that the QD laser is tolerant for EOF in transmission operation, in presence of error-free behaviors with $BER < 10^{-12}$. In contrary, its counterpart suffers from a strong degradation in EOF operation. Figure 3.12(b) depicts the BERs in B2B operation as a function of the received optical power of the QW laser in different

feedback conditions. Compared to the free-running case (red), a weak η_F at 0.02% (blue) gave a 2 dB power penalty to the QW laser at all BER levels. Further increasing the η_F to 2% (green symbol), the BER increases to the level of 10^{-4} due to the coherence collapse.

Despite the remarkable results, three questions remain to be addressed.

- First, what is the largest feedback strength that the QD laser endures. In this study, the maximum feedback strength limited to 18% prevents us to identify any dynamics of the QD laser subject to EOF. However, the laser can suffer from a much larger feedback strength in an extreme condition. Pursuing the onset of coherence collapse regime is promising for extending the applications of QD lasers.
- Second, an external cavity whose length is 7 m is too long to be encountered on a PIC. The laser's tolerance for EOF on the scale of a PIC remains to be investigated. A further step on the analysis of laser dynamics in the short-cavity feedback regime where $f_{RO}/f_{ext} < 1$ is worth investigating.
- Third, despite the high-performance in the external modulation operation, the laser performance in direct modulation is important to be studied. In particular, the investigations of the impact of different feedback dynamics on the transmission performance are meaningful for the development of isolator-free PICs.
- Fourth, on an InP substrate where InAs quantum-dash (QDash) is commonly used gain medium for lasers, an investigation of the laser's sensitivity to optical feedback remains to be performed. In particular, understanding how the polarization anisotropy of dashes with respect to the cavity axis affects the nonlinear properties thus the reflection insensitivity of lasers is meaningful for designing feedback-resistant QDash lasers for InP-based PICs.

In the following sections, the author tries to answer these questions by using experimental results.

3.8 QD lasers studied

InAs/GaAs FP QD lasers epitaxially grown on Si

The 1.3 μm epitaxial InAs/GaAs QD lasers on Si are fabricated within the group of Prof. John Bowers at University of California, Santa Barbara, USA. In this

dissertation, the influence of p-modulation doping is investigated, and two types of QD devices are presented. The first one is undoped in the active region, whereas the other one is p-type doped in the gain medium with a doping level at $5 \times 10^{17} \text{cm}^{-3}$. Figure 3.13(a) depicts the AFM image of the QD morphology. The active region consists of five periods of InAs QDs embedded in $\text{In}_{0.15}\text{Ga}_{0.85}\text{As}$ QWs, as shown in Fig 3.13(b) where the cross-section transmission electron microscopy is displayed. Figure 3.13(c) depicts the epitaxial structure based on the typical design of the laser. The 2.55 ML thick InAs is deposited at 500°C and 0.113 ML/s with a V/III ratio of 35. The whole active region is then sandwiched by a $1.4 \mu\text{m}$ $\text{Al}_{0.4}\text{Ga}_{0.6}\text{As}$ GRINSCH with p-cladding material on top and another $1.4 \mu\text{m}$ n-cladding on the bottom. The bottom cladding is grown at 580°C while the top cladding is grown at 550°C to minimize interdiffusion in the active region. Owing to the reduced dot size fluctuation, the QD density is $6.5 \times 10^{10} \text{cm}^{-2}$ with a photoluminescence (PL) full-width at half maximum below 30 meV. Uniform QDs are highly desired for realizing high-performance QD laser, whose benefits include the improvement of modal gain, differential gain, and thermal stability (Kenichi Nishi, Takemasa, et al., 2017; Shang et al., 2021). The whole structure of active region is then directly grown on an on-axis (001) GaP/silicon wafer in a Veeco Gen-II molecular beam epitaxy chamber. Further details of the epitaxial growth are available elsewhere (J. C. Norman, Daehwan Jung, Z. Zhang, et al., 2019).

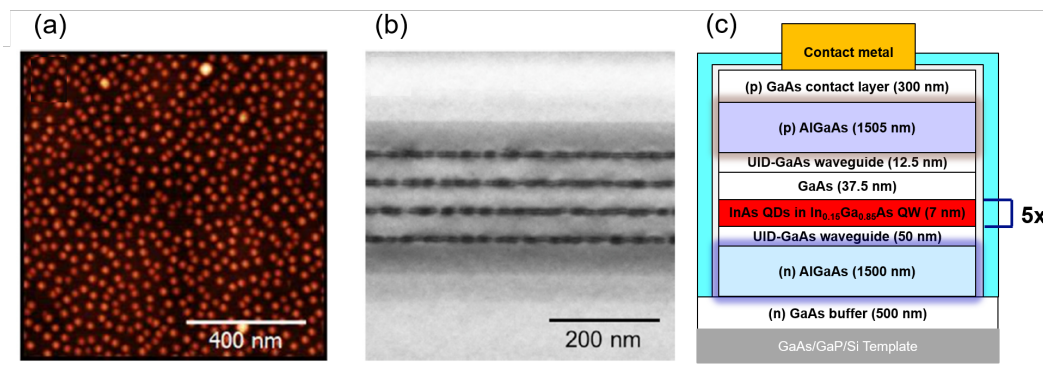


Figure 3.13: (a) $1 \times 1 \mu\text{m}^2$ AFM image of the QD morphology. (b) Cross-section scanning transmission electron micrograph displays five layers of InAs quantum dots within the active region. (c) Schematic of the laser epi-structure. (a) and (b) are from Ref. (J. C. Norman, Daehwan Jung, Z. Zhang, et al., 2019)

The Fabry-Perot (FP) cavities of both devices are fabricated with standard dry etch and electron beam metal deposition techniques. The cavity length of these two lasers are similar, which is 1.1 mm for the undoped one and 1.35 mm for the other; while

they share the same ridge width at $3.5 \mu\text{m}$. The facets that are formed by cleaving using ion beam deposition of repeated periods of $\text{SiO}_2/\text{Ta}_2\text{O}_5$ give reflectivities at 60% (front) and 99% (rear) to the undoped laser, and 32% on both facets to the p-doped one.

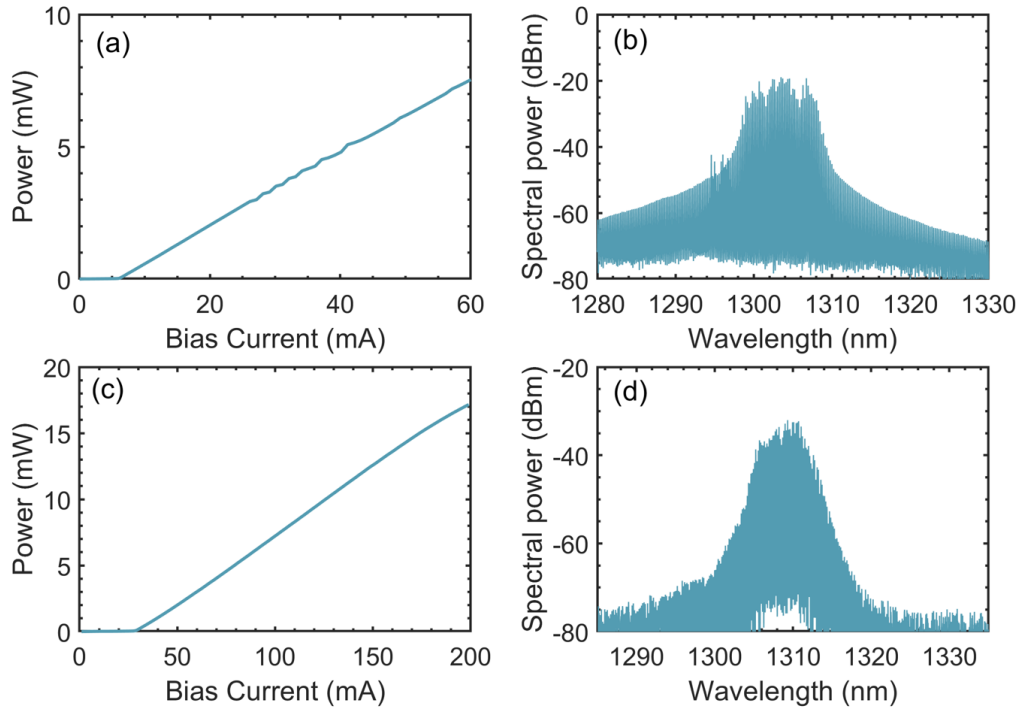


Figure 3.14: Light-current characteristics and optical spectra measured at $5 \times I_{th}$ for undoped [(a) and (b)] and p-doped [(c) and (d)] QD laser.

Figures 3.14 depict the light current characteristics as well as the optical spectra at $5 \times I_{th}$ for the undoped [(a) and (b)] and p-doped [(c) and (d)] QD devices at 20°C . Both lasers do not exhibit the ES emission, which can be confirmed by the absence of the power decrease as the bias current increases in the full range of current measured (Heming Huang, Jianan Duan, et al., 2018). Due to the p-modulation doping that increases the number of holes in the valence states of QDs, the increased optical absorption and nonradiative recombination gives rise to the higher threshold current I_{th} at 32 mA observed from the p-doped QD laser (Z. Zhang et al., 2018). However, the undoped one begins to lase at 6 mA.

Despite the inconvenience from the high threshold current, the p-type doping is beneficial for decreasing the α_H -factor. Figure 3.15 displays the above-threshold α_H at gain peak as a function of the gain current for the p-doped (burgundy) and the undoped (blue) QD laser. The α_H -factors at threshold current are measured

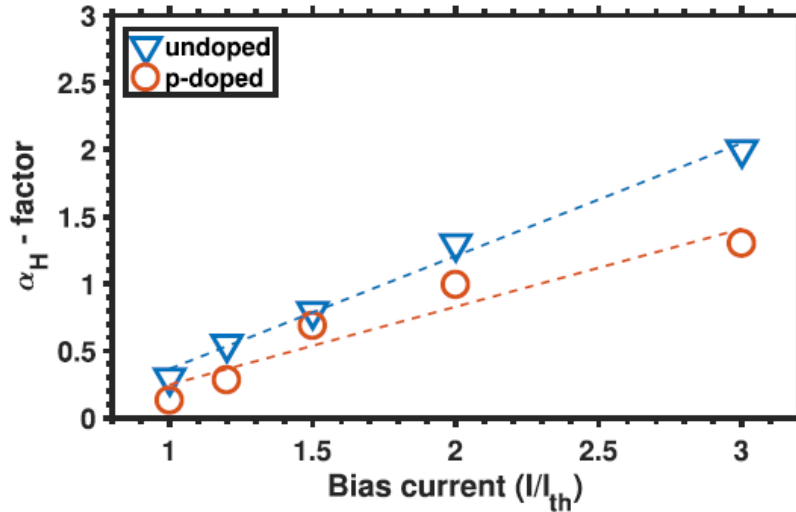


Figure 3.15: The above-threshold α_H -factor of the p-doped (burgundy) and the undoped (blue) QD laser with the bias current ranging from $1 \times I_{th}$ to $3 \times I_{th}$ at 20°C . The dashed lines are for guiding eyes only. From Ref. (H. Huang et al., 2020).

by the amplified spontaneous emission (ASE) method, which will be introduced in Chap. 4. On the other hand, the α_H -factors above threshold are measured by the optical injection method (G. Liu, X. Jin, and S.-L. Chuang, 2001). In this study, both the epitaxial QD devices on Si exhibit remarkable low α_H -factors, compared to the QD laser grown on native substrate as shown in Chap. 4. The threshold value for the p-doped laser is as low as 0.13 whereas that for the undoped one is slightly increased to 0.3. The benefit of p-doping is clearly seen from the lower level of α_H in the full current range from $1 \times I_{th}$ to $3 \times I_{th}$ in the p-doped device. Despite the increase of α_H above threshold, the p-doped QD laser still exhibits a quite low α_H around 1 at $3 \times I_{th}$. Such a significant feature is attributed to the high quality material as well as the reduced TDD that reduces the inhomogeneous gain broadening and concentrates the oscillator strength at the resonant wavelength. In addition, the benefits of p-doping also include the increase of modal gain thus the output power (J. C. Norman, Z. Zhang, et al., 2019), and the improvement of thermal stability (Shang et al., 2021). Importantly, a recent study reveals that the issue of a high threshold current induced by p-doping can be addressed by applying an optimized p-doping level (Saldutti et al., 2020).

InAs/InP FP QDash lasers

The InP-based QDash devices are fabricated within the group of Prof. John Bowers at University of California, Santa Barbara, USA. Figure 3.16(a) depicts the atomic

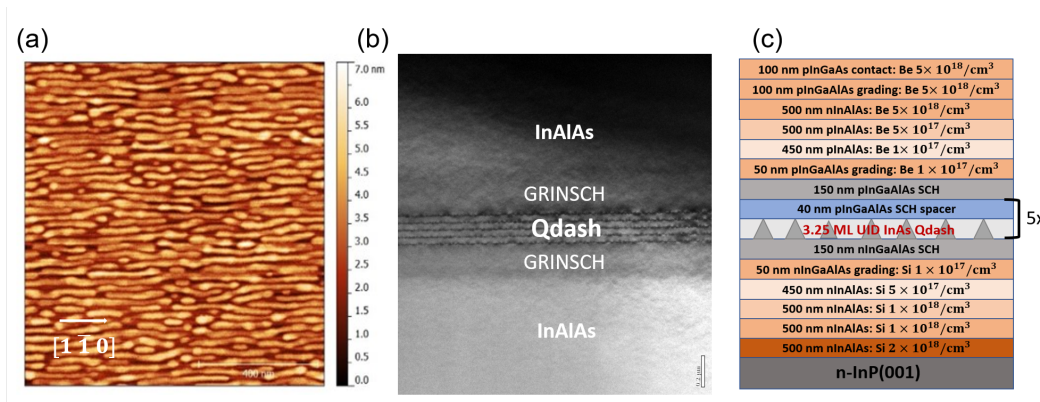


Figure 3.16: (a) $1 \times 1 \mu\text{m}^2$ AFM image of the QDash morphology. The QDashes are elongated in the $[1 \bar{1} 0]$ direction. The average height and width is about 7 nm and 20 nm, respectively. (b) Cross-section TEM image of the $[1 \bar{1} 0]$ surface at $9000\times$ magnification highlights the 5 layers of QDash. The electron beam energy was 200 keV. (c) Schematic of the laser epi-structure.

force microscopy (AFM) image of the QDash morphology. The QDashes are elongated in the $[1 \bar{1} 0]$ direction with an average length of 200 nm, due to a higher indium surface diffusion in this direction. The polarization of dashes is then determined by the included angle between the axis of dashes and the axis of cavity. Figure 3.16(b) displays the cross-section transmission electron microscopy of the QDash lasers. The structure except for the active region was grown at a constant temperature of 500°C , whereas the remaining QDash gain medium is grown at 485°C . The optimum photoluminescence (PL) characteristics are obtained by applying a total InAs deposition of 3.25 monolayer (ML), a V/III ratio of 18, and a growth rate of 0.4 ML/s. Post-nucleation growth interruption is also utilized to further tune the wavelength under As_2 overpressure at 1×10^{-6} torr for 60 s. The PL FWHM is about 100 meV for the QDash nanostructures studied. A detailed epi-structure of the laser is shown in Fig. 3.16(c). The active region of devices studied contains five layers of dashes that are spaced by 40 nm thick $5 \times 10^{17} \text{ cm}^{-3}$ p-modulation doped separated confinement heterojunction (SCH) spacer to improve the lasing properties. The SCH layers on both sides of the active region are made of 150 nm thick $\text{In}_{0.527}\text{Ga}_{0.234}\text{Al}_{0.239}\text{As}$. The bottom and top cladding layers are formed by n- and p-type $\text{In}_{0.523}\text{Al}_{0.477}\text{As}$ with different doping rates whose lattice are well matched to the InP substrate at the bottom. In the following context, devices with different orientations of QDash are compared. The first one with QDash parallel to cavity axis has a ridge waveguide width of $2.5 \mu\text{m}$, whereas the second one whose dashes are perpendicular to the cavity axis has a $4 \mu\text{m}$ -wide ridge waveguide. Both

devices have a cavity length of 1.25 mm and are as-cleaved with the reflectivities at 32%. Despite the fact that the increase of ridge width could give rise to the increase of threshold current and α_H -factor (Letal et al., 1998; Duan, Huang, Jung, et al., 2018), it does not change the conclusion of this study. Discussions are presented hereinafter.

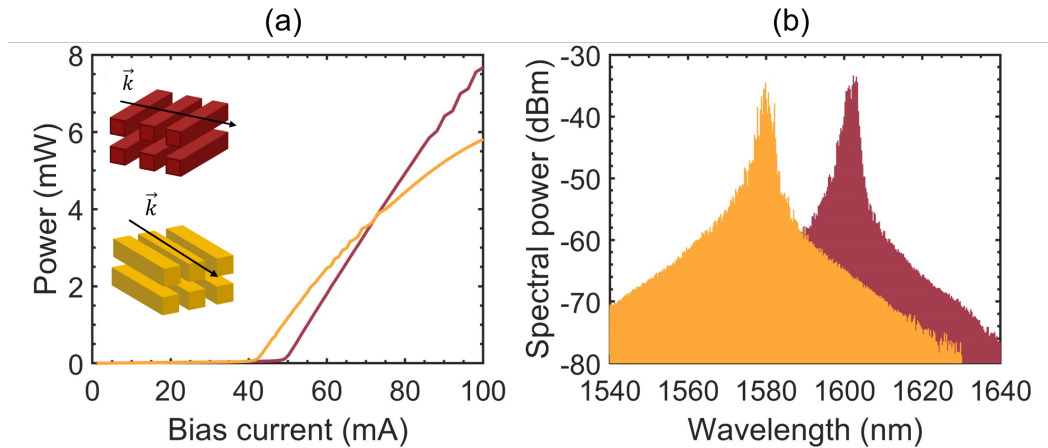


Figure 3.17: (a) Light-current characteristics and (b) optical spectra measured at $1.5 \times I_{th}$ for QDash oriented parallel (gold) and perpendicular (burgundy) to the cavity axis. Insets in (a) illustrate the dashes orientation with respect to the wave propagation direction \vec{k} .

Figures 3.17 depict (a) the light current characteristics and (b) the corresponding optical spectra measured at $1.5 \times I_{th}$ of the two lasers with dashes oriented parallel (gold) to the cavity axis and with dashes oriented perpendicular (burgundy) to the cavity axis. Illustrations of the dashes orientation with respect to the wave propagation direction \vec{k} (i.e., cavity axis) are shown in the insets of Fig. 3.17(a). Both devices exhibit sole GS emission, the gain peak of the former device is at 1576 nm, whereas that of the latter one is at 1596 nm. The observed wavelength shift is attributed to the different transition matrix element offered by the polarization of QDashes (Ukhanov et al., 2002). Due to the compressive strain in dashes, the large conduction band-to-light hole band (C-LH) transition plays the dominant role in the device with dashes parallel to cavity axis, whereas in the laser with dashes perpendicular to cavity axis, the narrow conduction band-to-heavy hole band (C-HH) transition dominates. Therefore, the different bandgap leads to the gain peak wavelength red-shift by rotating the dashes from parallel to perpendicular to cavity axis. On the other hand, the threshold current I_{th} of the perpendicular device is 49 mA whereas that of the parallel one is lower at 43 mA. The higher threshold

current observed in the former laser is attributed to the wider ridge waveguide and the higher optical loss induced by the large number of holes in the active region (Letal et al., 1998; Ukhanov et al., 2002).

As a consequence of the different transition matrix element, the gain properties as well as the α_H -factor of these two devices exhibit a different manner. Figure 3.18(a) displays the spectral dependence of the net modal gains with the increase of bias current from below to threshold, which are extracted by the ASE method for the device with dashes oriented parallel (gold) or perpendicular (burgundy) to the cavity axis. The higher differential gains observed in the perpendicular QDash laser results in lower α_H -factors, as shown in Fig. 3.18(b). The black dashed lines represent the wavelength for optical gain peaks. Despite the fact that the wider ridge of the perpendicular device could give rise to the increase of α_H -factor (Duan, Huang, Jung, et al., 2018), the value of the perpendicular QDash laser is always lower than that of the parallel one in the full wavelength range. In particular, the value at gain peak is 1.5 for the former, against 2.5 for the latter. The decrease of α_H -factor is mainly attributed to the increase of differential gain by rotating the dash orientation from parallel to perpendicular with respect to the cavity axis.

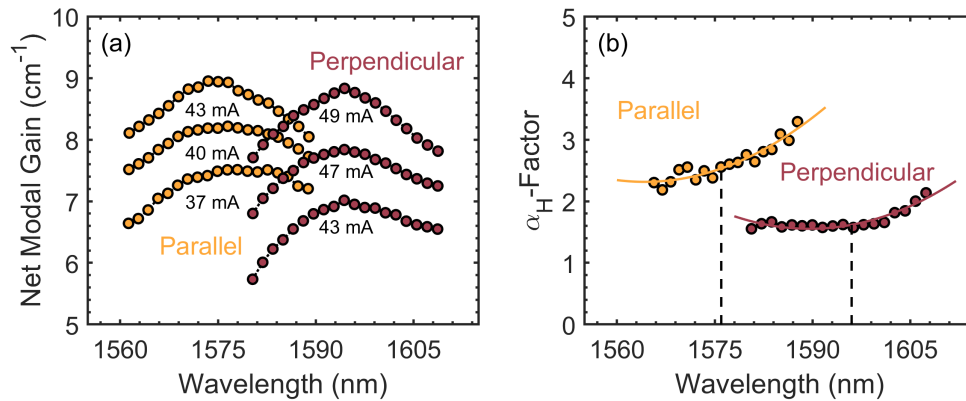


Figure 3.18: Spectral dependence of (a) net modal gain in different bias conditions from below to threshold and (b) threshold α_H -factor for QDash laser with dashes parallel (gold) or perpendicular (burgundy) to the cavity axis.

3.9 Optical feedback apparatus in experiments

As mentioned in Sec. 3.5, the laser dynamics in the SCR and in the LCR exhibits different behaviors. To analyze these peculiar dynamics of QD lasers, both the EOF operations in the SCR and in the LCR are performed in this dissertation. Importantly, the former illustrates how the QD lasers behave with intra- and inter-

chip back-reflections on a PIC.

Setup for coherent optical feedback in the short-cavity regime

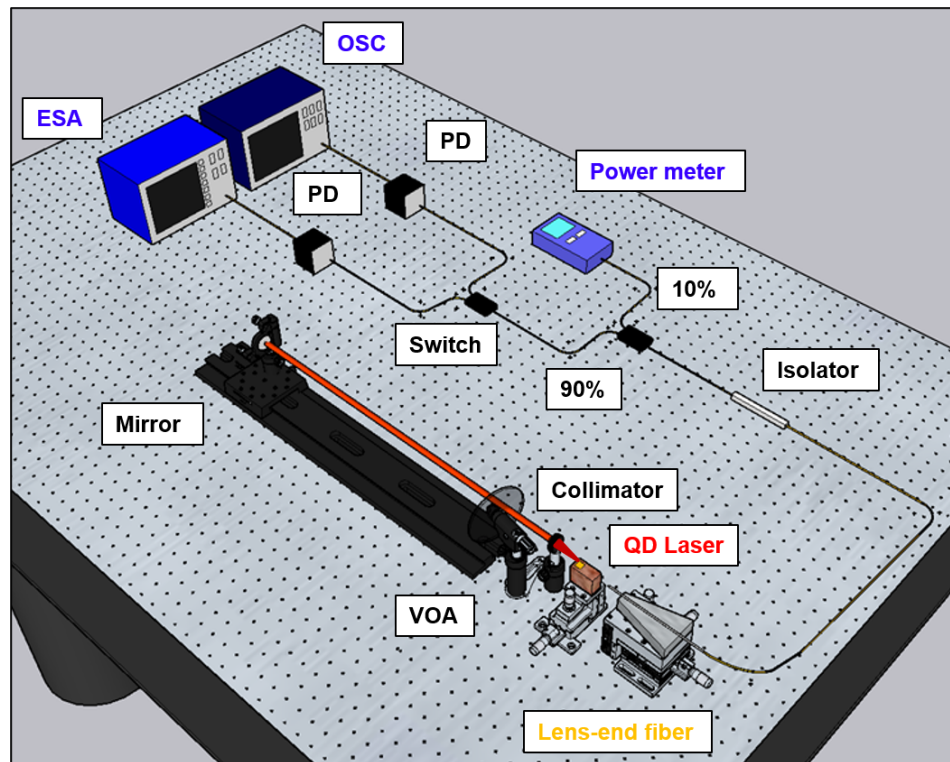


Figure 3.19: Experimental setup for the short-delay coherent external optical feedback measurement. VOA, variable optical attenuator; PD, 12 GHz photodiode; ESA, electrical spectrum analyzer; OSC, oscilloscope.

Figure 3.19 depicts the free-space optical feedback setup for coherent optical feedback characterizations in the short-cavity regime. The laser under test is mounted on a suspended optical table to minimize the environmental perturbations. For a symmetric as-cleaved coated device such as the p-doped epitaxial QD laser on Si, the setup is separated into two parts: one part at the side of front facet is for optical feedback operation and the other at the rear facet side is for light detection and analysis. The free-space external cavity is placed outside the laser's front facet, in which the lasing emission is collimated and is reflected by a movable mirror mounted on an optical rail. The latter allows for adjusting the external cavity length from 4 cm up to 50 cm. In practical, reducing the L_{ext} to a few centimeters is complex in free-space operation, hence it is necessary to well arrange the experimental apparatuses. As aforementioned, the condition for SCR operation is determined by both the relaxation oscillation frequency of the laser and the external cavity frequency

through the relationship $f_{RO}/f_{ext} < 1$. For instance, the f_{RO} of the p-doped QD laser is 2 GHz at 160 mA, hence the corresponding ratio of f_{RO}/f_{ext} ranging from 0.5 to 7 allows for finely probing the laser dynamics in transition from SCR to LCR. For each measurements at different L_{ext} , the focus of the collimator needs to be readjusted in order to precisely send the coupled light onto the mirror. Besides, owing to the reduced optical loss from the setup, the achievable feedback strength monitored by the VOA that accounts for the coupling loss between the facet and the external cavity ranges from 0.04% (-34 dB) to ~70% (-1.55 dB), which allows us to tailor the laser dynamics in a much wider feedback range. On the light detection path, laser emission from the rear facet is coupled by an AR coated lens-end fibre and is isolated to avoid any back reflection from this path. The coupled light is then sent to an electrical spectrum analyzer and an oscilloscope for further analysis.

Setup for coherent optical feedback in the long-cavity regime

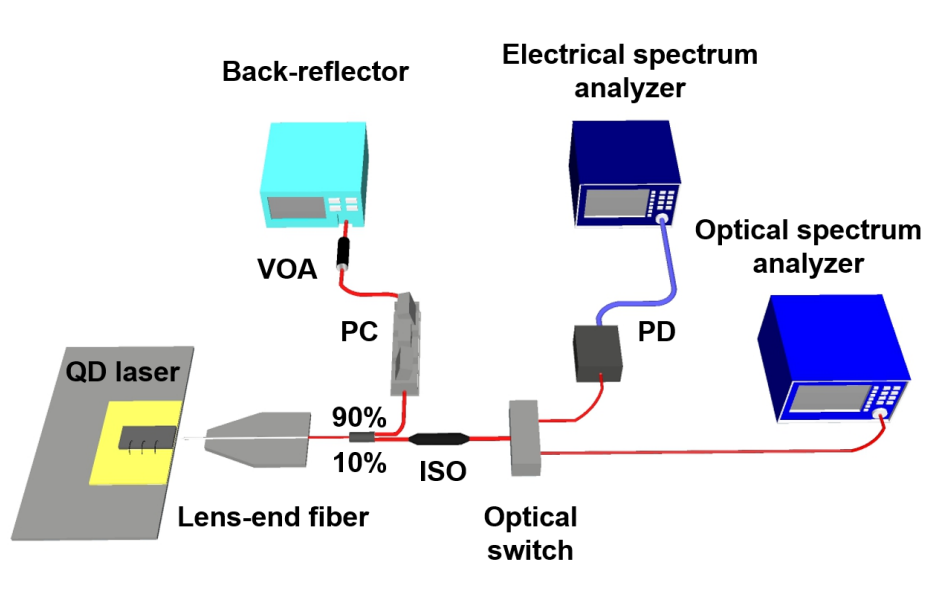


Figure 3.20: Experimental setup used for the long-delay coherent external optical feedback measurement. ISO, optical isolator; PD, photodiode; PC, polarization controller; VOA, variable optical attenuator.

Figure 3.20 depicts the optical fibre based experimental setup for coherent optical feedback characterizations in the long-cavity regime. The laser emission from the front facet is firstly coupled by an anti-reflection (AR) coated lens-end fibre. A 90/10 fibre beam splitter is used to divide the light into two paths. 90% power of the light is sent to a 14 meters-long SMF optical fibre as the external cavity, at the end of which a variable optical attenuator (VOA) is used to control the feedback strength

and a backreflector (BKR) is applied to reflect the light back to the laser cavity. Corresponding external cavity frequency f_{ext} at 7 MHz satisfies the conditions for LCR where $f_{RO}/f_{ext} > 1$. As aforementioned, the laser is more sensitive to the back-reflections in the LCR than in the SCR. Therefore, the LCR setup provides the most strict condition for characterizing the laser's tolerance for EOF. In addition, a polarization controller is inserted in the feedback path to compensate the fibre dispersion in the external cavity and to maximize the optical feedback namely to have the reflected light in the transverse electric (TE) polarization. In such a long-delay configuration, the impact of the feedback phase is negligible (Tkach and Chraplyvy, 1986); the loss from the setup is also an issue that limits the feedback strength. Nevertheless, the achievable η_F with this setup ranges from $\sim 0\%$ (-60 dB) to $\sim 30\%$ (-5.2 dB), depending on the coupling ratio of device. The remaining 10% power from the fibre beam splitter is then isolated and sent to the optical and the electrical spectrum analyzers for further analysis.

3.10 Dynamics of QD laser subject to external optical feedback

Owing to the near-zero α_H -factor along with a low SRH recombination lifetime, the epitaxial QD lasers on silicon exhibit a strong tolerance for EOF (S. Zhao and Frédéric Grillot, 2021). A previous work from the author's group demonstrate that the epitaxial QD laser on silicon does not show any unstable dynamics in the LCR with a maximum feedback strength at 18% (-7.4 dB) (Jianan Duan, Heming Huang, et al., 2019). Therefore, it is important to reduce the external cavity length and to increase the maximum feedback strength to tailor the laser dynamics in EOF operation. Figures 3.21 displays the feedback dynamics of the p-doped QD laser in transition from SCR to LCR, in which the radio-frequency (RF) spectrum (left column), time series (middle column) and phase portraits (right column) are performed. In this study, the operating temperature of laser is kept at 30°C . The device is biased at 160 mA ($4.4 \times I_{th}$) where its relaxation oscillation frequency is 2 GHz. Various dynamic states are identified by probing the feedback conditions.

- **Regular pulse package (RPP).** The occurrence of the RPP oscillation is observed in the ultra short-cavity regime where $f_{RO}/f_{ext} < 0.5$. An example shown in Figs. 3.21 (a) is measured when the QD laser operates with $\eta_F=68.2\%$ (-1.66 dB) and L_{ext} being 4 cm ($f_{ext}=3.75$ GHz). As shown in (a-ii), a series of regular pulses oscillating at f_{ext} are modulated by a slow envelope, whose repetition frequency f_{RPP} being 55 MHz is clearly depicted

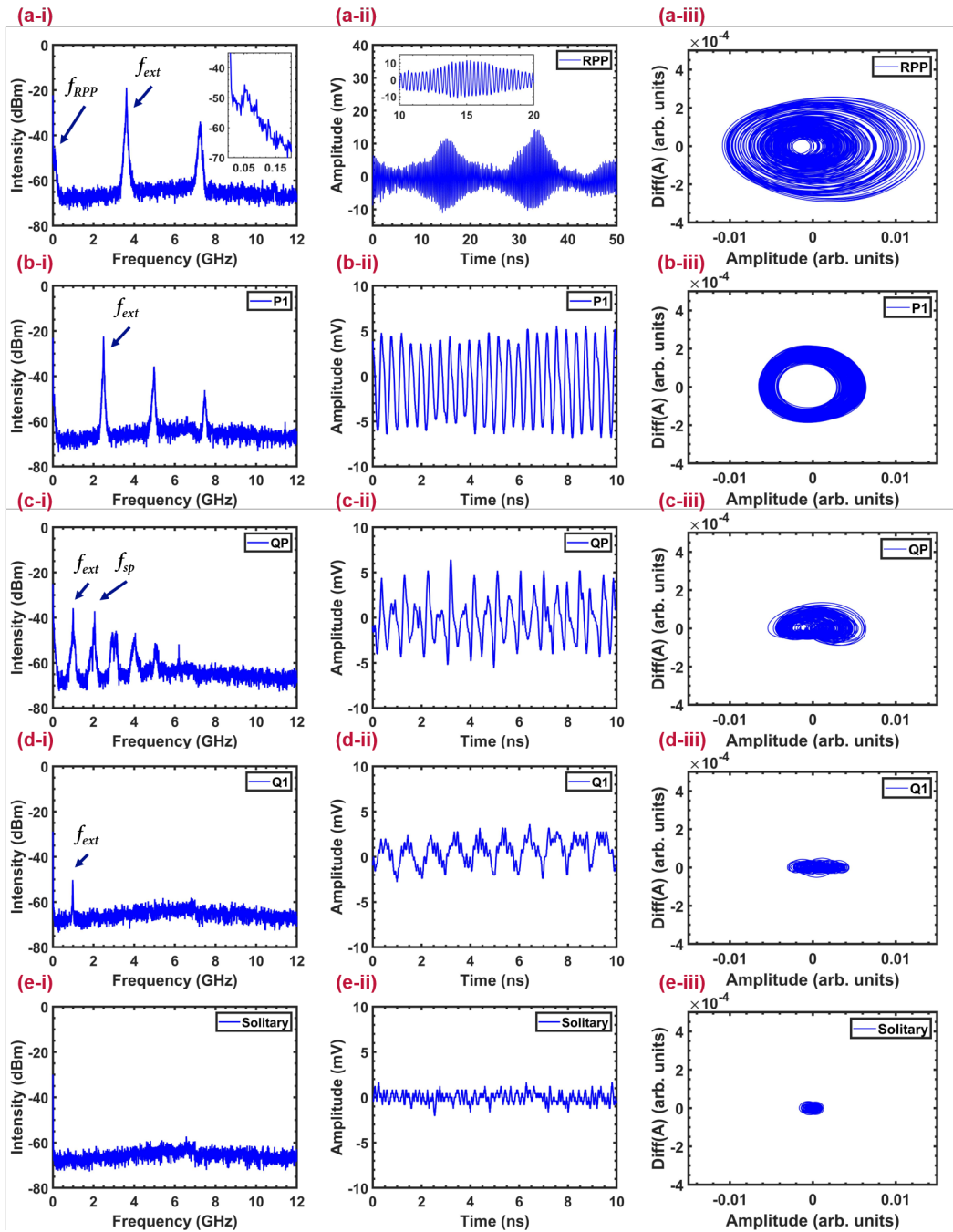


Figure 3.21: Electrical spectra (left), time series (middle), and phase portraits (right) of the p-doped QD laser with $(\eta_F, L_{ext}) =$ (a) $(68.2\%, 4 \text{ cm})$, (b) $(68.2\%, 6.5 \text{ cm})$, (c) $(68.2\%, 15 \text{ cm})$, (d) $(33\%, 15 \text{ cm})$, and (e) solitary, when it is biased to 160 mA. f_{ext} , frequency of the external cavity; f_{sp} , self-pulsation frequency.

in the inset of (a-i). The fast oscillation at f_{ext} within one envelop is highlighted in the inset of (a-ii). The phase portraits shown in (a-iii) demonstrates that the slow oscillation frequency coincident with f_{RPP} does not bring huge discrepancy from the single-frequency pulsations since only one cycle can be identified. Despite that, the laser system still suffers from a strong instability induced by the feedback phase. To stably generate the RPP oscillations, it would be important to further reduce the external cavity length to fully probe the pure RPP regime from which the laser output resembles to a mode-locked laser.

- **Period-one (P1).** The QD laser exhibits a P1 oscillation behavior in the SCR. Figures 3.21(b) depict the case when the QD laser operates with the same $\eta_F=68.2\%$ (-1.66 dB) but extending the L_{ext} to 6.5 cm ($f_{ext}=2.3$ GHz). As shown in (b-ii), the oscillation frequency of laser at this state is determined by the f_{ext} , whose higher harmonics can be identified in the RF domain, as depicted in (b-i). The single-frequency oscillation behavior is also confirmed by the phase portraits, where a pretty regular cycle is identified in (b-iii). For the QD laser studied, the frequency of P1 oscillation exhibits a tunable range from 1.2 to 3 GHz.
- **Quasi-period (QP).** The QD laser exhibits more complex feedback dynamics in the LCR. The QP oscillation in presence of dual-frequency oscillation is observed when a strong feedback strength is applied. Figures. 3.21(c) display the QP dynamics with the L_{ext} fixed to 15 cm ($f_{RO}/f_{ext} \approx 2$) while maintaining the η_F at 68.2%. At the QP state, the laser oscillates with both the f_{ext} and the self-pulsation frequency f_{sp} , the latter is determined by the relaxation oscillation frequency of laser. As aforementioned, the f_{sp} fluctuates around f_{RO} as the L_{ext} changes due to the mode competition, when the L_{ext} is shorter than the coherence length L_{coh} of laser. The influence of L_{ext} on f_{sp} can be eliminated once the L_{ext} exceeds the coherence length, which is about several hundred meters for a narrow-linewidth QD laser (Heming Huang, L.-C. Lin, et al., 2018).
- **Quasi-period-one (Q1).** The Q1 oscillation takes place in the LCR when the feedback strength remains low. To stabilize the QD laser and to trigger the Q1 dynamics from it, the η_F is decreased to 33% (-4.8 dB) while fixing the L_{ext} at 15 cm, as shown in Figs. 3.21(d). Different from the aforementioned P1 state, the laser oscillates at f_{ext} without showing any higher harmonic at

this stage; the intensity of Q1 oscillation is also much lower than that of the P1. As a consequence, the waveform shown in (d-ii) is largely influenced by the high frequency noise, which makes the corresponding phase portraits hardly to be distinguished from those at the solitary state (without feedback), as depicted in (d-iii). In addition, the Q1 oscillation is a typical behavior that occurs in regime II, the f_{ext} along with its higher harmonics are much easier to be observed in the ultra long-cavity regime, where the f_{ext} is on the order of megahertz.

To be a reference, the spectra for the solitary state are shown in Figs. 3.21(e). For the QD laser studied, it does not show any chaotic dynamics from SCR to LCR, even if it operates with a strong optical feedback whose strength $\approx 70\%$. In contrary, the QW lasers suffer from strong instabilities against optical feedback. In general, they exhibit chaotic oscillations with η_F below 5% in both SCR and LCR (Ohtsubo, 2012; Jianan Duan, Heming Huang, et al., 2019); those features definitely limit their applications for isolator-free integration. As a consequence, the chaos-free QD laser reported in this dissertation exhibits a strong potential to be applied to PICs to improve their robustness against chip-scale back reflections.

3.11 Route to periodic oscillations in QD laser

To control the dynamic states of the QD laser in EOF operation and to search for their potential applications in microwave photonic technologies, it is necessary to analyze their occurrence conditions. Figures 3.22(a) and (b) depicts a mapping of the dynamic states of the p-doped QD laser as a function of the feedback strength and the external cavity length, when the device operates at 125 mA ($3.4 \times I_{th}$) and 160 mA ($4.4 \times I_{th}$), respectively. Corresponding oscillation frequencies are shown in (b) and (d). In this study, the onset of each periodic oscillation is defined as the corresponding excited oscillation frequency being 5 dB above the free-running noise level. In Figs. 3.22, the boundary between the SCR and the LCR is represented by the vertical red dashed lines. Note that such a boundary differs from the bias condition of the laser since the f_{RO} moves from 1.5 GHz to 2 GHz with the increase of the gain current from 125 mA to 160 mA. To improve the precision, measurements are performed by varying the L_{ext} every centimeter in the SCR while larger steps are taken in the LCR. In agreement with prior studies, the boundaries associated with unstable oscillations exhibit strong undulations in SCR due to the mode competition between the internal and the external cavity modes. In the LCR, the undulations

from the instability boundaries are largely suppressed, however, the fluctuation of the f_{sp} around the free-running f_{RO} as the L_{ext} changes still exists. In both bias conditions, the RPP oscillations (marked in orange) only take place in the ultra-short delay regime where $f_{RO}/f_{ext} < 0.5$, due to the strong feedback phase (Heil et al., 2001). Extending the L_{ext} to $f_{RO}/f_{ext} \approx 1$, the QD laser only exhibits P1 oscillations (marked in green). In the SCR, the QD laser remains at the solitary state (S, black) if the η_F is lower than 35%. More dynamic states can be observed in the LCR. With the increase of η_F , the device remains stable with a weak feedback strength, until it oscillates at f_{ext} thus enters into Q1 regime (marked in magenta), then it enters into the QP regime (marked in blue) in presence of a dual-frequency oscillation at both the f_{ext} and the f_{RO} . Discussions in Chap. 2 demonstrate that the α_H -factor of a QD laser increases with its bias current due to the gain compression. Such an effect also results in the degradation of the laser's tolerance for EOF, in presence of an overall lower instability boundary when the device operates in a higher bias condition at 160 mA.

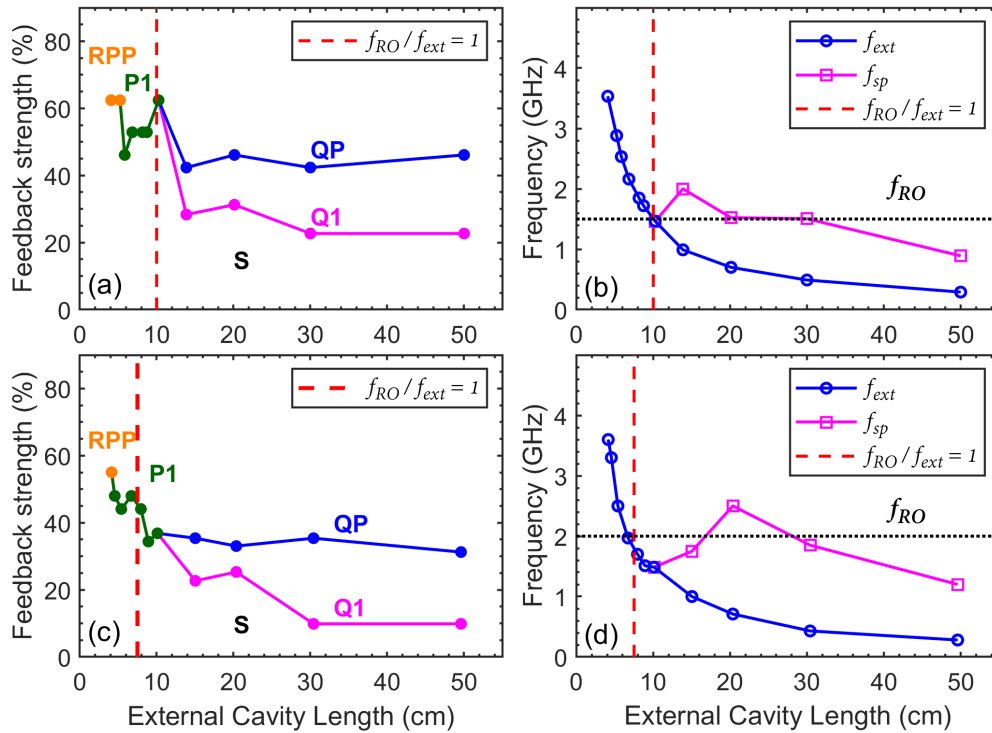


Figure 3.22: Mappings of the dynamic states and the oscillation frequencies of the p-doped QD laser in different feedback conditions at 125 mA [(a) and (b)] and at 160 mA [(c) and (d)]. The vertical red dashed lines depict the boundaries of the SCR and the LCR. The horizontal dotted black lines illustrate the free-running f_{RO} .

3.12 Impact of the p-doping on the feedback dynamics

Results shown in Fig. 3.15 reveal that the laser benefits from a lower α_H -factor by applying the p-doping technique. In this section, the impact of p-doping on the laser's tolerance for EOF in the short-cavity regime is performed. Figure 3.23 depicts the feedback strength associated to the onset of periodic oscillations $r_{ext,p}$ as a function of the external cavity length for the p-doped (burgundy) and undoped (gold) QD laser that operate at $\sim 3 \times I_{th}$, corresponding boundaries of SCR and LCR are marked by dashed or dotted lines in same colors. The operating temperature of the p-doped laser is $30^\circ C$, whereas that for the undoped one is $20^\circ C$. As described in Chap. 4, the as-cleaved facets (32%/32% power reflectivities) of the p-doped device make it more open to the external world than the undoped one (60%/99% power reflectivities), which is not always favorable for maintaining the tolerance to optical feedback (Frédéric Grillot, J. C. Norman, et al., 2020). Nevertheless, the p-doped laser clearly exhibits a much stronger resistance to EOF than its counterpart even at a higher operating temperature, in presence of a higher $r_{ext,p}$ in the full transition from SCR to LCR. For instance, in the LCR where the external cavity length is 30 cm, the $r_{ext,p}$ of the p-doped QD laser at 21.5% (-6.7 dB) is 16 dB higher than that of the undoped device. This remarkable performance improvement is mainly attributed to the decreased α_H -factor owing to the p-doping (H. Huang et al., 2020). In addition, both QD lasers show a remarkable tolerance for inter-chip-scale back reflection in absence of chaotic behavior. The improvement of feedback resistance with decreasing L_{ext} reveals that these devices can be still reflection-resistant on the intra-chip scale. As a consequence, although the p-doping could give the laser some undesired properties such as a higher threshold current, it is still a promising technique to improve the laser's tolerance for back-reflections and it fits well the needs for high-performance PICs operating without optical isolator.

3.13 Impact of the dash orientation on the feedback insensitivity

As a consequence of the different α_H -factor induced by the dashes orientation, the feedback sensitivity of the QDash laser is affected. Figures 3.24 depict the laser dynamics of both the QDash lasers subject to long-delay optical feedback. The RF and the optical responses for the device whose dashes are parallel to the cavity axis are shown in (a) and (c), respectively; whereas those for the perpendicular one are shown in (b) and (d). In these measurements, the optical fibre based external cavity is 7 meters long. Both lasers operate at $1.5 \times I_{th}$ and the temperature is kept at $20^\circ C$. With the increase of feedback strength from -60 dB ($\sim 0\%$) to -7 dB ($\sim 20\%$), they

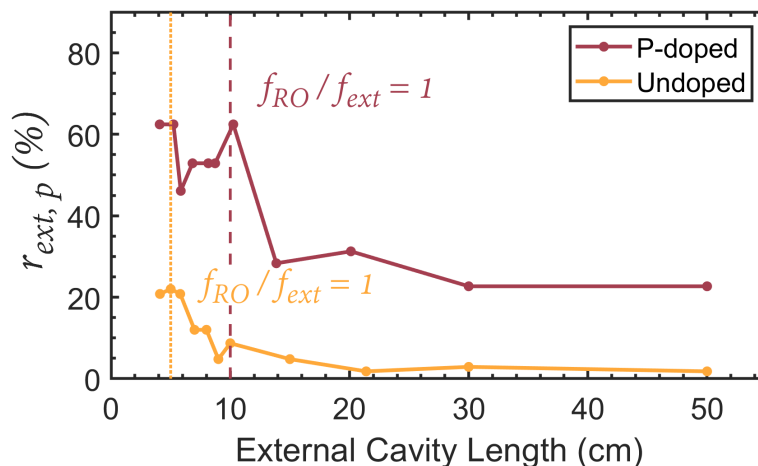


Figure 3.23: The onset of periodic oscillations $r_{ext,p}$ associated with L_{ext} of the p-doped (burgundy) and undoped (gold) QD laser. Both devices operate at $\sim 3 \times I_{th}$. The vertical dashed burgundy and dotted gold lines depict the boundaries of the SCR and the LCR of the p-doped and the undoped device, respectively.

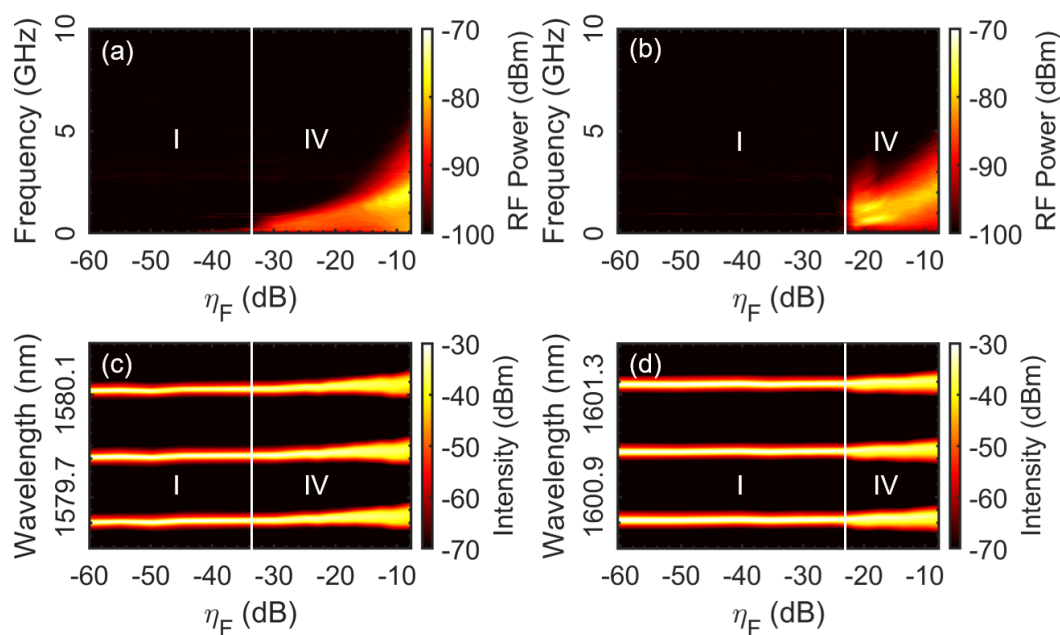


Figure 3.24: RF power mapping and the optical power mapping as a function of the feedback strength for the QDash laser whose dashes are oriented parallel [(a) and (c)] or perpendicular [(b) and (d)] to the cavity axis. Both devices operate at $1.5 \times I_{th}$ at 20°C .

suffer from a strong coherence collapse, during which both of them show a full transition from the steady-state to the periodic oscillation states and further to the chaotic oscillation state. In addition, both lasers directly enters into regime IV from regime I with a feedback strength at the r_{crit} in absence of the transition in regime II and III. The suppression of regime II is attributed to the low bias operating condition where the gain compression remains low. Nevertheless, the lower α_H -factor offered by the perpendicular dashes is beneficial for largely improving the laser's tolerance for EOF. Compared to the parallel device whose r_{crit} is -34 dB, a 11 dB improvement of the r_{crit} to -23 dB is observed in the perpendicular laser.

3.14 Summary

In this chapter, comprehensive investigations of the multimode and monomode optical feedback dynamics is performed. The characterizations of QD/QDash FP lasers allow for understanding their sensitivity to external perturbations with a view of the carrier dynamics and gain properties. The main results are summarized as:

- Epitaxial QD lasers on Si are tolerant for chip-scale parasitic reflections without showing any chaotic behavior. Such a remarkable feature results from the low SRH recombination lifetime along with the near-zero α_H -factor that strongly decouples the interaction between the intra- and the reflected light field. An optimum p-modulation doping level in QDs enables the laser a 16 dB improvement of the feedback insensitivity. The outstanding properties of QDs give insights for developing QD-based isolator-free single-frequency distributed feedback (DFB) lasers for high-speed communication (Wan et al., 2020). Taking advantage of the high tolerance for the defects that arise during the epitaxial growth of III-Vs on Si, QD laser can be a key component for high-performance and low-cost photonic integrated circuits .
- The periodic oscillations in QD lasers are highly dependent on the external cavity length. The dynamics in the short-cavity regime such as the RPP and the P1 oscillations take place in a strong feedback condition with a η_F beyond 35%. Nevertheless, the laser becomes less tolerant for EOF in the long-cavity regime in presence of a 2 dB decrease of the feedback level that is associated with the onset of unstable oscillations. This degradation behavior is mainly attributed to the occurrence of regime II in which the laser oscillates with the external cavity frequencies. Despite the remarkable feedback insensitivity that makes the QD laser an ideal solution for isolator-free applications, the P1

oscillation whose frequency is tunable on the order of gigahertz gives insight to develop all-optical microwave oscillators based on QD.

- While utilizing the QDash as the gain medium of a semiconductor laser, its polarization with respect to the cavity axis affects the lasing properties such as the gain properties and the α_H -factor. Owing to the reduced bandgap by rotating the dashes perpendicular to the cavity axis, the α_H is reduced from 2.5 to 1.5. Therefore, it is promising to utilize the perpendicular QDash laser to have a higher tolerance for EOF. Compared to the parallel QDash laser, the perpendicular one exhibits a 11 dB improvement of the critical feedback level. Such a feature gives insights for developing InP-based high-performance optical interconnects for C- and L-band optical communication.

QUANTUM-DOT DISTRIBUTED FEEDBACK LASER WITH LARGE OPTICAL MISMATCH

This chapter presents the investigations of a single-mode InAs/GaAs QD distributed feedback (DFB) lasers with a design of optical wavelength detuning (OWD), which means the mismatch between the Bragg wavelength and the optical gain peak. A positive OWD at room temperature aims at developing a high-temperature tolerant QD laser for uncooled photonic integrated circuits (PICs). Experimental investigations including the continuous-wave behaviors, the α_H -factor measurements, the noise properties, the modulation dynamics and laser dynamics subject to external optical feedback (EOF) are performed to give a complete picture on how the OWD influences on the laser performance.

4.1 Introduction to distributed feedback laser

Soon after the demonstration of low-threshold double heterostructure (DH) laser at the end of 1960s, studies on DFB lasers began. Driven by the increasing demand for high-speed fibre-optic communications, the conventional Fabry-Perot (FP) resonant cavity was no longer the first option due to the limit of modulation capacity. A single-mode laser is expected to have a tight mode control for the transverse (electric (TE) or magnetic (TM)), lateral, and longitudinal modes during high-speed direct modulation. To do so, the control of transverse mode can be realized by modifying the facets reflectivities and loss for TE and TM modes; the control of lateral mode can be achieved by designing an appropriate waveguide. The last one is based on the wavelength selectivity of the laser cavity. As a consequence, the threshold gain of the lasing mode should be significantly smaller than that for the other longitudinal modes in a single-mode laser. In other word, the ratio of the lasing mode power to any of the side mode power is larger than 30 dB.

To realize wavelength selection, approaches including the short-cavity laser, the coupled-cavity lasers and the injection-locked lasers were developed (Morthier and Vankwikelberge, 2013). Nevertheless, the performance of those structures are not satisfying due to the complexity and the poor reliability. In this context, the DFB and the Distributed Bragg Reflector (DBR) structure provide reliable solutions for single-mode laser. In both configurations, the optical resonance is realized by the

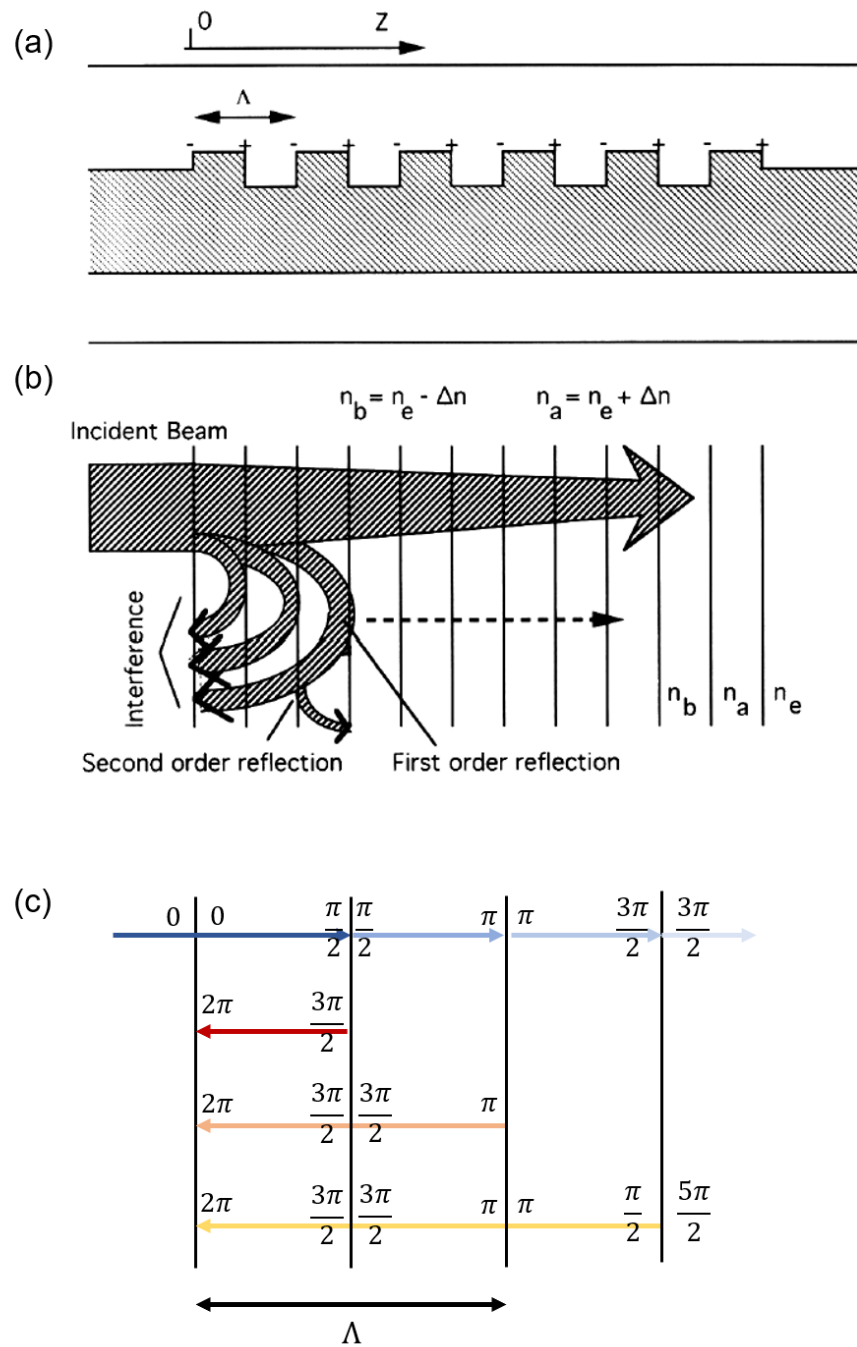


Figure 4.1: (a) Schematic of a corrugated Bragg grating with a periodicity of Λ . (b) Bragg reflection characteristic of the subsequent reflectivities. (c) Phases corresponding to each wave propagation after a distance of $\Lambda/2$. From Ref. (Morthier and Vankwikelberge, 2013).

periodic variation of the effective refractive index of a corrugated optical waveguide inside the laser cavity, rather than the facet reflectivities in the case of a FP cavity. That means the laser emission can be realized without coating on both facets in a DFB laser (i.e. power reflectivities $\approx 0\%$). Besides, the periodicity of the corrugated grating is able to select a unique longitudinal mode by giving it the maximum reflectivity. The so-called Bragg wavelength λ_B is expressed as follows:

$$\lambda_B = 2\Lambda n_e \quad (4.1)$$

where Λ denotes the period of the Bragg grating and n_e is the effective refractive index of the waveguide in absence of the grating. Figure 4.1(a) illustrates the infinite waveguide structure with a rectangular index grating of finite length. The periodic corrugated structure results in a periodic change in the refractive index, as shown in Fig. 4.1(b). Assuming that the intra-cavity field propagates along the z -axis from $z = 0$, a part of it will in turn be reflected by the interface of each refractive index change and will propagate backward. It is worth stressing that these second-level reflections will also undergo further reflections, however, the reflected power is much lower. In the end, the reflected waves go back to the beginning point $z = 0$, where it will interfere constructively or destructively with the incident wave. In particular, the light oscillating at the Bragg wavelength experiences a phase shift π after propagating each distance Λ , meaning that the phases of the subsequent reflectivities along the grating alternate between 0 and π . The phases corresponding to each wave propagation after a distance of $\Lambda/2$ are highlighted in Fig. 4.1(c). As a consequence, the field whose wavelength is λ_B adds up constructively at $z = 0$ and maintain its power for the next resonance in the cavity. In contrary, other waves lose their power due to the destructive interferences at $z = 0$.

Figure 4.2 depicts the schematic diagram of (a) a DFB laser and (b) a DBR laser. The Bragg grating of a DBR laser is fabricated in a waveguide that is placed outside the active region. To enable the laser a high-performance, the optical losses from the external grating and the passive waveguide need to be minimized. In the case of a DFB laser, however, the Bragg grating is fabricated above or within the active region. In addition, the structure of the Bragg grating could be fabricated with different types to realize the wavelength selection. The example shown in Fig. 4.1(a) represents the index-coupled DFB grating, which creates a periodic variation in the real part of the refractive index. The second type of grating can be fabricated with periodic gain or loss variations within the active region, which is named as gain-coupled DFB grating. Despite the different structure from the first one, the

descriptions of Fig. 4.1(a) remain valid for the second one except for the fact that the phases of the subsequent reflectivities along the gain or loss grating alternate between $-\pi/2$ and $\pi/2$. The third type that includes both the contributions of the index and the gain coupling is referred to complex-coupled DFB grating.

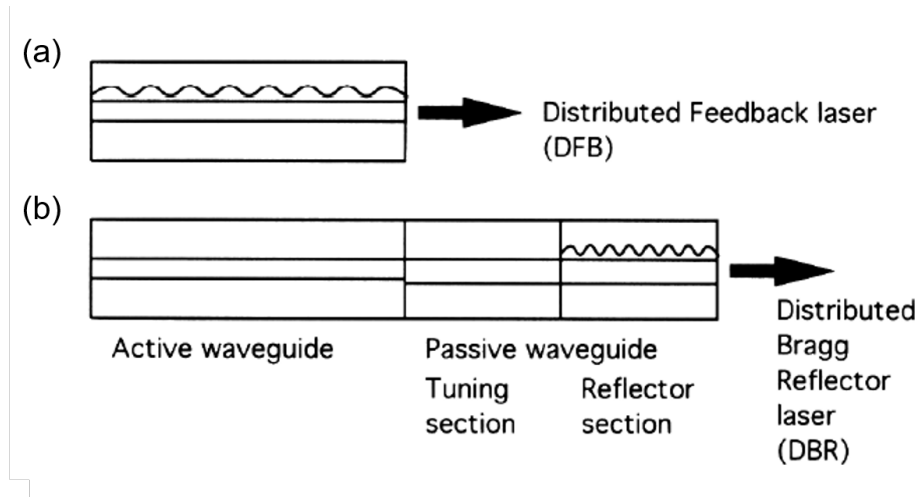


Figure 4.2: Schematic diagram of (a) DFB laser and (b) DBR laser. From Ref. (Morthier and Vankwikelberge, 2013).

4.2 Coupled wave equations

To analyze the wavelength selection in a periodic Bragg grating, the coupled wave theory is a commonly used analytical tool owing to its ease of understanding. In a semiconductor laser in which a transversely and laterally confined structure is included, the electric field E that propagates along the z -axis must satisfy the one-dimensional homogeneous wave equation expressed as follows:

$$\left[\frac{d^2}{dz^2} + k^2(z) \right] E(z) = 0 \quad (4.2)$$

with $k(z)$ the wave propagation constant that is written as (Kogelnik and C. Shank, 1972):

$$k^2 = k_0^2 n^2(z) \left(1 + j \frac{2\alpha(z)}{k_0 n(z)} \right) \quad (4.3)$$

where k_0 denotes the free space wave propagation constant, $\alpha(z)$ and $n(z)$ account for the amplitude gain coefficient and the refractive index, respectively. Due to the corrugated structure, the refractive index and the amplitude gain coefficient that include the perturbations in the grating is expressed as follows (Soda et al., 1987):

$$n(z) = n_e + \Delta n \cos(2\beta_0 z + \Omega) \quad (4.4)$$

$$\alpha(z) = \alpha_e + \Delta \alpha \cos(2\beta_0 z + \Omega + \theta) \quad (4.5)$$

where n_e and α_e are the steady-state values for the refractive index and the amplitude gain, respectively. Δn and $\Delta\alpha$ account for the amplitude modulation terms, Ω denotes the non-zero residue phase at the z -axis origin and β_0 is the propagation constant. θ accounts for the relative phase difference between perturbations of the refractive index and amplitude gain.

Assuming that the incident plane wave vertically enters into the periodic and lossless waveguide at an angle of $\pi/2$, the incident wave will experience the same degree of refractive index change so that it will be reflected back to the point $z = 0$. For a waveguide that consists of N periodic corrugations, there will be N reflected wavelets. Therefore, the phase differences between reflected wavelets must be a multiple of 2π , which is written as:

$$2\beta_0\Lambda = 2m\pi \quad (4.6)$$

with m an integer that accounts for the multiple resonance within a distance Λ . Eq. (4.6) is thus the Bragg condition with β_0 the Bragg propagation constant. Assuming that the higher-order Bragg resonance ($m > 1$) is negligible, Eq. (4.6) can be re-expressed as follows:

$$\beta_0 \equiv \frac{2\pi n_e}{\lambda_B} \equiv \frac{n_e \omega_B}{c} = \frac{\pi}{\Lambda} \quad (4.7)$$

where λ_B and ω_B denote the Bragg wavelength and the Bragg frequency, respectively. Eq. (4.1) is thus derived from Eq. (4.7).

On the other hand, with small signal analysis, the perturbations of the refractive index and gain are always smaller than their average values ($\Delta n \ll n_e$, $\Delta\alpha \ll \alpha_e$), the wave propagation constant $k(z)$ can be calculated by substituting Eqs. (4.4) and (4.5) into Eq. (4.3) such as:

$$k^2(z) = k_0^2 n_e^2 + 2jk_0 n_e \alpha_e + 2k_0 [k_0 n_0 + j\alpha_0] \Delta n \cos(2\beta_0 z + \Omega) + 2jk_0 n_e \Delta\alpha \cos(2\beta_0 z + \Omega + \theta) \quad (4.8)$$

Then, assuming that $\alpha_e < \beta$ and $\theta = 0$, with $k_0 n_e$ replaced by β , Eq. (4.8) is simplified to

$$k^2 \approx \beta^2 + 2j\beta\alpha_e + 4\kappa\beta\cos(2\beta_0 z + \Omega) \quad (4.9)$$

with κ the coupling coefficient that is expressed as follows:

$$\kappa = \frac{\pi\Delta n}{\lambda} + j\frac{\Delta\alpha}{2} = \kappa_i + j\kappa_g \quad (4.10)$$

On substituting the above equation back into Eq. (4.2), one gets:

$$\frac{d^2 E}{dz^2} + \{\beta^2 + 2j\beta\alpha_e + 2\kappa\beta e^{j(2\beta_0 z + \Omega)} + 2\kappa\beta e^{-j(2\beta_0 z + \Omega)}\} E = 0 \quad (4.11)$$

It is worth stressing that only the longitudinal modes whose frequencies are close to the Bragg frequency satisfy the Bragg condition shown in Eq. (4.6) and are able to lase. In other word, those modes should satisfy the following relationship:

$$|\beta - \beta_0| \ll \beta_0 \quad (4.12)$$

and the detuning coefficient δ of them are defined as follows:

$$\delta = \beta - \beta_0 \quad (4.13)$$

Therefore, the solution for Eq. (4.11) is expressed as:

$$E(z) = R(z)e^{-j\beta_0 z} + S(z)e^{j\beta_0 z} \quad (4.14)$$

where $R(z)$ and $S(z)$ account for the complex amplitudes of the forward and backward propagating waves (Usami, Akiba, and Utaka, 1987). These two waves satisfy a coupled wave relationship such as:

$$-\frac{dR}{dz} + (\alpha_e - j\delta)R = j\kappa_{RS}S e^{-j\Omega} \quad (4.15)$$

$$\frac{dS}{dz} + (\alpha_e - j\delta)S = j\kappa_{SR}R e^{j\Omega} \quad (4.16)$$

where κ_{RS} and κ_{SR} denote the forward and the backward coupling coefficient, respectively, and are written as follows:

$$\kappa_{RS} = \kappa_i + j\kappa_g e^{-j\theta} \quad (4.17)$$

$$\kappa_{SR} = \kappa_i + j\kappa_g e^{j\theta} \quad (4.18)$$

As a consequence of the pair of coupled wave equations, the forward coupling coefficient κ_{RS} in Eq. (4.17) results in a coupling between the negative travelling electric field $S(z)$ and the counter propagating one $R(z)$. So do the backward coupling coefficient κ_{SR} . For the aforementioned three types of DFB laser, their coupling coefficients satisfy the following conditions:

- **Index-coupled DFB laser:** $\kappa_{RS} = \kappa_{SR} = \kappa_i$
- **Gain-coupled DFB laser:** $\kappa_{RS} = \kappa_{SR} = j\kappa_g$
- **Complex-coupled DFB laser:** $\kappa_{RS} = \kappa_{SR} = \kappa_i + j\kappa_g$

with the assumption that the relative phase difference θ is zero.

4.3 Stopband of a DFB laser

The stopband is a well-known behavior in a DFB laser. The periodic grating results in a gap in the optical spectrum. Figure 4.3 illustrates the propagation constant as a function of frequency in a lossless index grating with an infinitely length. The width of the stopband $Re(\Delta\beta)$ is determined by the coupling coefficient through the relationship $Re(\Delta\beta) = 2\kappa$. Inside it the waves exponentially decay due to the distributed reflections occurring when the coupling is strong. In contrary, the waves outside the stopband exhibit little interaction with the periodic grating thus keeping their power. For an index-coupled DFB laser, its stopband can be minimized by optimizing the facet reflectivities, the phase shifts and the coupling coefficient. In addition, the gain-coupled DFB grating is beneficial for eliminating the stopband owing to the extra gain in the waveguide that overcomes the decay.

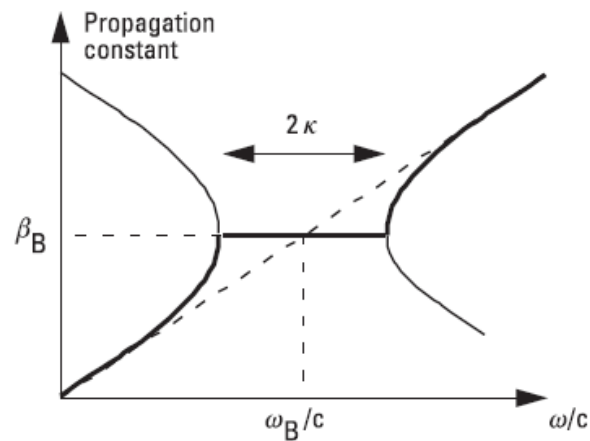


Figure 4.3: Dispersion diagram for an infinite index grating in a waveguide without loss or gain. From Ref. (Morthier and Vankwikelberge, 2013).

4.4 Coupling coefficient of the DFB grating

The definitions of coupled wave theory demonstrate that the coupling coefficient plays a crucial role in determining the lasing properties of a DFB laser. Figure 4.4 depicts the threshold gain as a function of the wavelength detuning for the longitudinal modes near the Bragg wavelength. The example shown here represents the case with no facet coating. Each solid line is used to represent the -4 to $+4$ mode whose threshold gain varies with the normalized coupling coefficient κL , with L the DFB grating length. A symmetric distribution behavior of the modes with respect to the ω_B are observed, no oscillation is found at the Bragg wavelength confirms that the oscillation within the stopband is suppressed. Besides, the -1 and the $+1$

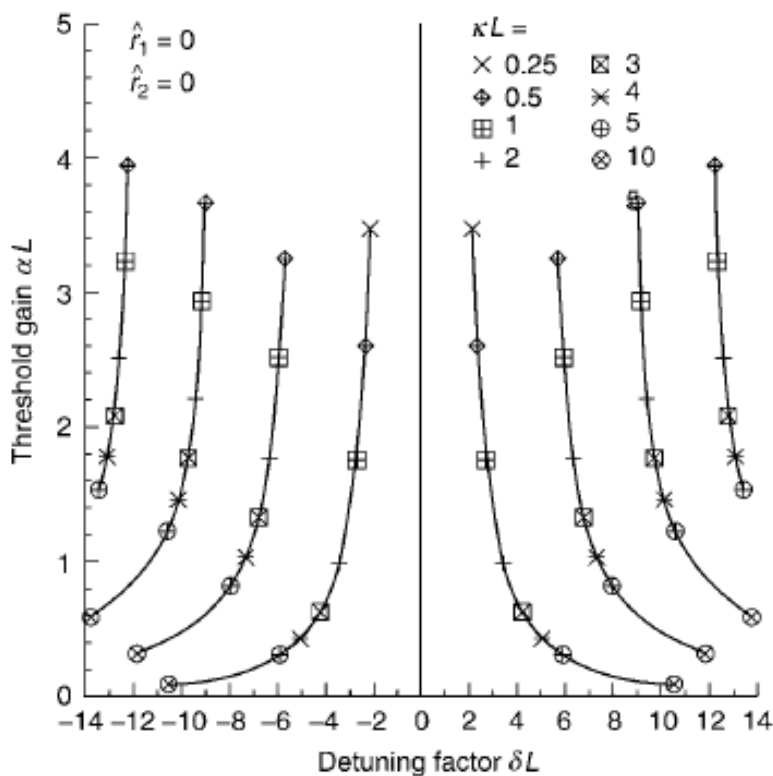


Figure 4.4: Relationship between the amplitude threshold gain and the detuning coefficient of a mirrorless index-coupled DFB Laser. From Ref. (Ghafouri-Shiraz, 2003).

modes have the same possibility to lase once the lasing condition is satisfied, since they have the same threshold gain. In addition, it is worth stressing that a large coupling coefficient is beneficial for decreasing the threshold current in this cavity configuration. For the +1 mode, its threshold gain largely decreases from 3.5 to ~ 0 with the increase of κL from 0.25 to 10.

Nevertheless, a large coupling coefficient is not always a preferred option since the DFB laser is sensitive to the facet reflectivities and the phase shifts. Figure 4.5 depicts the lasing characteristics of a DFB laser whose non-zero facet reflectivities are asymmetric. The amplitude reflectivity of its front and rear facet, r_1 and r_2 , equals to 0.0343 and 0.535, respectively. While fixing its corrugation phase Ψ_1 at π , the other phase Ψ_2 varies from $-\pi/2$ to $\pi/2$ with a step of $\pi/2$. For a fixed κL , the lowest threshold gain switches between the -1 mode and the +1 mode with the change of Ψ_2 . Besides, the wavelength of each mode also varies with the phase conditions. Such phenomena reveal that a DFB laser can emit light either at the Bragg wavelength or at another wavelength located within the stopband due to

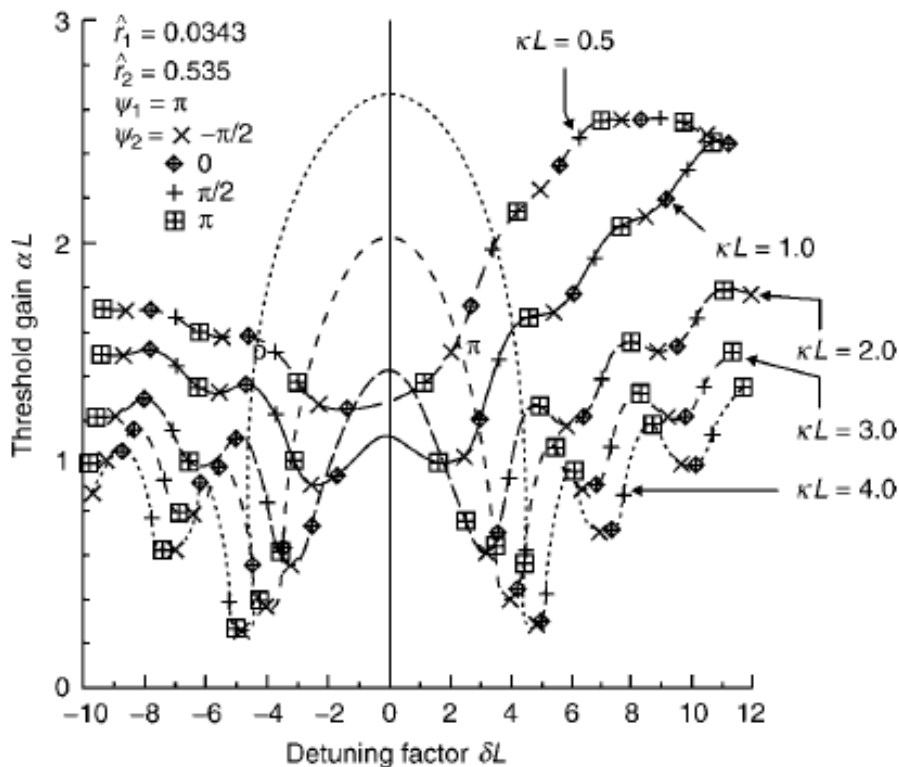


Figure 4.5: Relationship between the amplitude threshold gain and the detuning coefficient of an index-coupled DFB Laser with asymmetric facet reflectivities. The corrugation phase Ψ_1 is fixed while the other Ψ_2 varies. From Ref. (Ghafouri-Shiraz, 2003).

different cavity configurations including the facet reflectivities and the associated phase conditions. It is worth stressing that the corrugation phase also has a direct impact on the other lasing properties including the threshold current, the external efficiency and the feedback insensitivity (Grillot, Thedrez, Gauthier-Lafaye, et al., 2003). However, it difficult to be controlled due to tolerances inherent during the process of fabrication (Buus, 1985). Techniques such as the ion-beam etching (Itaya et al., 1985), electron-beam lithography (Muroya et al., 1997) and the phase control method (Mols et al., 1989) could be considered to adjust the corrugation phase.

Results shown in Figs. 4.4 and 4.5 show that a DFB laser could benefit from a lower threshold current by increasing the coupling κL . Nevertheless, the consequent longitudinal spatial hole burning (LSHB) is detrimental for the lasing performance and destroys the single-mode behavior. In presence of the LSHB within the laser cavity, the areas of strong optical field intensity will show a lower carrier density. To estimate the side-mode suppression in a DFB laser, it is an approach to calculate

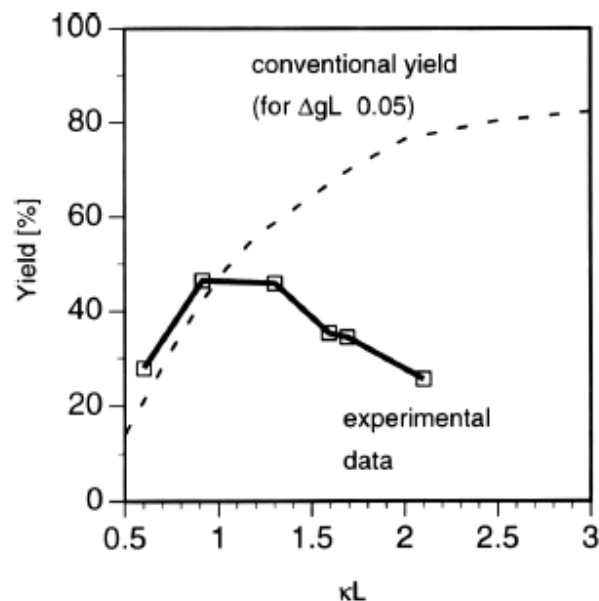


Figure 4.6: Experimental (solid line) and calculated (dashed line) yield of as-cleaved DFB lasers as a function of κL . From Ref. (David et al., 1991).

the threshold gain difference $\Delta g/L$, which denotes the difference in the threshold gain between the main mode and the first side mode. This parameter is dependent on the laser structure including the corrugation phase and the normalized coupling coefficient κL . In general, a $\Delta g/L > 0.1$ ensures a single-mode operation. Nevertheless, the value of $\Delta g/L$ is difficult to be controlled due to the random distribution of phases. To overcome this issue, the single-mode suppression can be also estimated by the yield of laser, which is defined as the percentage of lasers with a $\Delta g/L$ value larger than a certain predefined value. Figure 4.6 depicts the calculated yield (satisfying $\Delta g/L > 0.05$, dashed line) and the experimental obtained yield as a function of κL for an index-coupled DFB laser. The optimum yield is observed with $\kappa L = 1$, and a higher κL leads to a decrease of yield due to the LSHB. In addition, the position of the spatial holes exhibits a dependence of the coupling degree. In the case of under coupling ($\kappa L < 1$), the spatial holes tend to move to the edges of the grating; whereas the holes gather in the middle of the grating in the over coupling condition ($\kappa L > 1$). In the case of critical coupling ($\kappa L \approx 1$), the carrier distribution shows less pronounced holes. Last but not least, it can be considered to minimize the LSHB by utilizing techniques such as the nonuniform injection (Kotaki et al., 1989), the chirped grating using bent waveguide (Hillmer, Magari, and Suzuki, 1993), the rectangular grating with variable duty cycle (Morthier, David, et al., 1990) and the

gain-coupled grating (Sudoh et al., 1993).

4.5 Description of the InAs/GaAs QD-DFB laser studied

The GaAs-based QD-DFB laser device is fabricated by QD Laser, Inc., Japan. The active region of the device studied is grown from 8-layer InAs QDs on (100) GaAs substrate by using molecular beam epitaxy. Figure 4.7(a) displays a $0.5\mu\text{m} \times 0.5\mu\text{m}$ atomic force microscopy (AFM) image of InAs QDs. Owing to the improved growth sequence, the density of QDs is as large as $\sim 6 \times 10^{10} \text{ cm}^{-2}$ per layer. Each dot layer is separated by a p-doped GaAs spacer, which allows for a high modal gain up to about 50 to 60 cm^{-1} . The luminescence width at half-maximum of the active region is as narrow as $\sim 24 \text{ meV}$ at room temperature, as shown in Fig. 4.7(b), meaning that the inhomogeneous broadening caused by the size and shape distribution of the QDs is quite low.

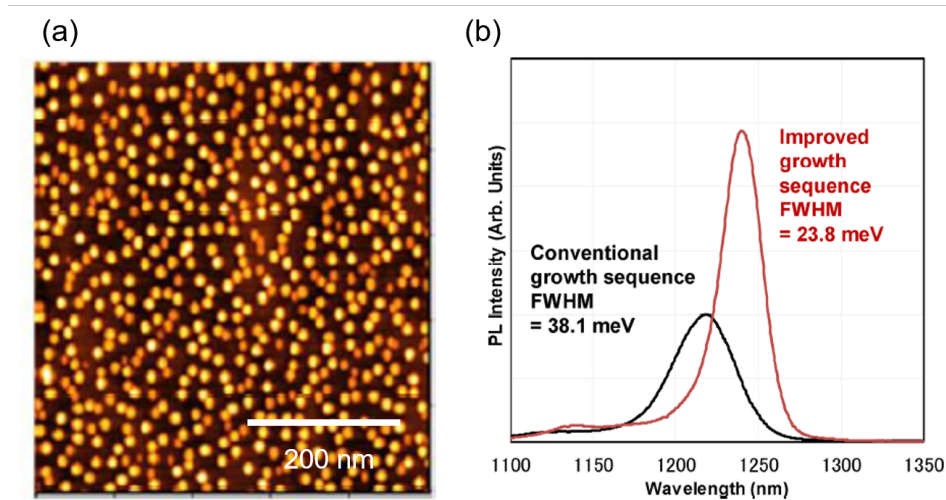


Figure 4.7: (a) $0.5\mu\text{m} \times 0.5\mu\text{m}$ Atomic force microscopy image of InAs QDs grown on GaAs substrate. (b) Photoluminescence spectrum of the active region of the laser studied after the improved growth sequence (red). From Ref. (Kenichi Nishi, Takemasa, et al., 2017).

The InGaP/GaAs index-coupled corrugated structure above the active region is fabricated with electron beam lithography and wet etching, and then it is formed by metal organic vapour phase epitaxy. The cavity length L_c and the coupling coefficient κ are designed to be $750 \mu\text{m}$ and 16 cm^{-1} , respectively, thus a normalized coupling coefficient κL of 1.2 is applied to avoid a strong LSHB. The laser is designed to operate at a high temperature thus the optical wavelength detuning (OWD) between the gain peak and the DFB oscillation wavelength is fixed at 25

nm at 25°C. A high-reflection (HR) coating with the reflectivity of 95% and an antireflection (AR) coating with the reflectivity of 3% are applied to the rear and front facets, respectively, to break the longitudinal symmetry thus allowing the laser to operate at a single longitudinal mode. Besides, this design is also able to maximize the output power from the output facet (Henry, 1985). More detailed device fabrication process information are available elsewhere (Nishi et al., 2013).

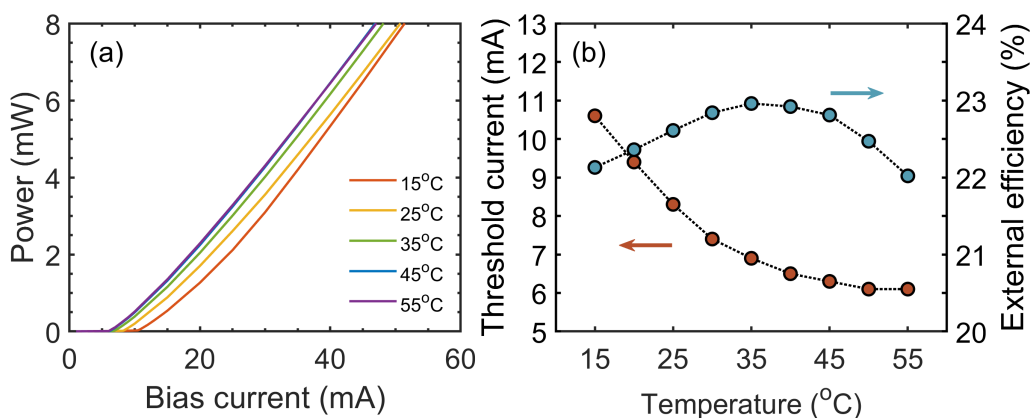


Figure 4.8: (a) Light-current characteristics with temperature ranging from 15 to 55°C. (b) Threshold current (burgundy) and external efficiency (jade) as a function of temperature.

Figure 4.8(a) depicts the light-current (L-I) characteristics of the QD-DFB laser operating under different temperatures. The device studied exhibits a strong thermal stability, by performing a sufficient output power over 15 mW from 15 to 55°C. The variation of the operating temperature T is found to influence the threshold current I_{th} (burgundy) and the external efficiency η (jade), as shown in Fig. 4.8(b). The latter is calculated through $\eta = \frac{q\lambda}{hc} \frac{\Delta P}{\Delta I}$, with h the Planck constant, c the speed of light, q the electron charge, and λ the lasing wavelength. The threshold current decreases with T down to a few milliamps meaning that a smaller OWD that occurs at a high temperature is beneficial for reducing the internal loss (H. Lu, Blaauw, and Makino, 1996). Besides, the benefit brought by a small OWD can also be confirmed by the increase of external efficiency in the temperature range from 15 to 40°C, and the maximum external efficiency is 23%. Once the temperature increases above 40°C, however, the active region of laser suffers from a stronger carrier thermalization that leads to more nonradiative recombination. Such an effect results in the decrease of the external efficiency, as depicted in Fig. 4.8(b). Nevertheless, it is worth stressing that this inconvenience can be partially compensated by the consecutive reduction of internal loss with the increase of temperature; up to 55°C, no reincrease of the

threshold current is observed.

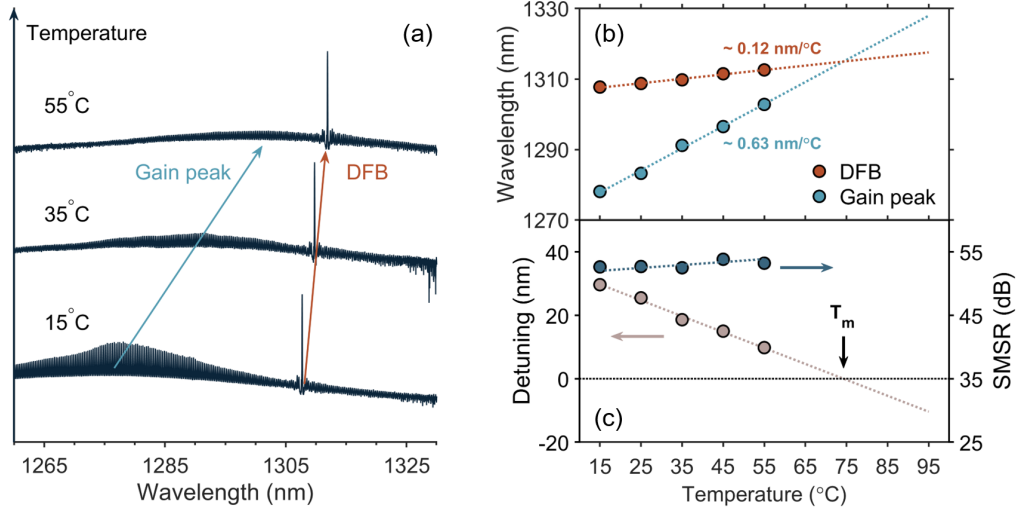


Figure 4.9: (a) Optical spectra of the QD-DFB laser from 15°C to 55°C ($2 \times I_{th}$). Temperature dependent (b) DFB wavelength (burgundy), optical gain peak (jade), (c) optical wavelength detuning (gray) and side-mode suppression ratio (emerald).

Figure 4.9(a) depicts the optical spectra of the device at $2 \times I_{th}$ by increasing the temperature from 15 to 55°C. The multimode lasing dynamics observed across the gain peak is magnified when decreasing the temperature down to 15°C. This multimode dynamic results from the contribution of the different QD populations that are desynchronized at a low temperature through the homogeneous gain broadening. In addition, the reduction of the gain and the multimode operation also illustrates why the output power decreases at a low temperature. Furthermore, in DFB semiconductor lasers, the temperature dependent OWD can be described by the following relationship:

$$\lambda_0 - \lambda_p \approx \left(\frac{d\lambda_0}{dT} - \frac{d\lambda_p}{dT} \right) (T - T_m) \quad (4.19)$$

where λ_0 and λ_p is the wavelength of the DFB mode and that at the gain peak, respectively, $d\lambda_0/dT$ and $d\lambda_p/dT$ are the corresponding temperature coefficients. The temperature where λ_0 coincident with λ_p is described as T_m . The corresponding evolution of the wavelength shift of λ_0 (burgundy) and λ_p (jade) as a function of temperature variation are shown in Fig. 4.9(b). The lasing wavelength of the DFB laser is determined by the temperature dependent refractive index of the material composed DFB laser active region whereas that of the gain peak is determined by the temperature dependent material gain. In the device studied, the temperature induced wavelength shift is at 0.12 nm/°C and 0.63 nm/°C for λ_0 and λ_p , respectively. From

Eq. (4.19), it turns out that the optimal performance of a DFB laser occurs at the temperature T_m where $\lambda_0 = \lambda_p$ (H. Lu, Blaauw, and Makino, 1996). For this device, the optical detuning vanishes for $T_m \approx 75^\circ\text{C}$, which corresponds to the optimum temperature condition. Figure 4.9(c) depicts the temperature dependent OWD (gray) and the side-mode suppression ratio (SMSR, emerald) of the DFB laser. Experimental results demonstrate that a high SMSR over 50 dB is always maintained over the entire temperature ranging from 15 to 55°C . As a consequence, the OWD technique has been applied to various semiconductor lasers to improve their performance at a high temperature (Katsuyama, 2009).

4.6 Extraction of linewidth enhancement factor

As discussed in Sec. 2.4, the linewidth enhancement factor (α_H -factor) is a vital gain medium parameter that largely affects the lasing properties. Since its initial definition and introduction in early 1980s, various techniques that are able to extract the α_H -factor have been developed. Examples can be classified into three types:

- Approximate measurement of the real and the imaginary part of the optical susceptibility based on the definition of Eq. (2.10). Methods such as the optical linewidth (Charles Henry, 1982) and the amplified spontaneous emission (ASE) exhibit high reliability and simplicity. However, these approaches are only valid for retrieving the α_H from below to threshold and for a FP laser (Hakki and Paoli, 1973; Vahala and Amnon Yariv, 1983).
- High-frequency modulation techniques such as the FM/AM (Harder, Vahala, and Amnon Yariv, 1983; Schimpe, Bowers, and T. L. Koch, 1986; Jean-Guy Provost and Frederic Grillot, 2011), the fibre Transfer Function (Devaux, Sorel, and Kerdiles, 1993), the shifted-wave interference Fourier transform spectroscopy (SWIFTS) (Opačak et al., 2021), and the sinusoidal optical phase modulation (SOPM) (Provost et al., 2011). These methods show their superiorities by allowing for extracting α_H above threshold. In particular, the last two are able to retrieve the α_H -factors over a wide spectral range.
- External optical control, including optical injection (Hui et al., 1990; C. Wang, Schires, et al., 2016; Herrera, Kovanis, and Lester, 2021), optical feedback (Yanguang Yu, Giuliani, and Donati, 2004), and four-wave mixing methods (C.-H. Lin, H.-H. Lin, and F.-Y. Lin, 2012).

The first type of methods allows for extracting the α_H -factor at the material level, whereas the other two types can be used to extract the α_H -factor at the device level. Note that all these aforementioned methods are indirect measurements for α_H thus the retrieved value is approximate. Depending on the laser structure, different methods should be applied to extract the α_H reliably. In this section, the methods that are able to retrieve the α_H -factor below- and above-threshold are performed independently. Several devices with different cavity designs are investigated for the α_H -factor extraction.

Amplified spontaneous emission method

Based on the definition of Eq. (2.10), extraction of the α_H -factor relies on the measurement of the carrier density dependent refractive index change, which can be represented by the carrier induced wavelength shift. By analyzing the optical spectra, the free-spectral range $\delta\lambda$ in a laser cavity is expressed as follows:

$$\delta\lambda = \frac{\lambda_m}{2nL} \quad (4.20)$$

where λ_m is the wavelength of any longitudinal mode, L is the cavity length. The change of the carrier-induced refractive index within the active region $d\delta n$ can be expressed by the modal wavelength shift λ_m as:

$$\frac{d\lambda_m}{\lambda} = \Gamma \frac{d\delta n}{n} \quad (4.21)$$

To extract the α_H , the measurement of gain variation is necessary. To do so, the change of material gain is equivalent to the change of net modal gain G_{net} , which is expressed as:

$$G_{net} = \Gamma g_m - \alpha_i = \alpha_m = \frac{1}{L} \ln\left(\frac{1}{\sqrt{R_1 R_2}} \frac{\sqrt{x-1}}{\sqrt{x+1}}\right) \quad (4.22)$$

with Γ the confinement factor, $R_{1,2}$ the facet reflectivities in intensity of the laser, and x the modal peak-to-valley ratio. Substituting Eqs. (4.21) and (4.22) in Eq. (2.10), the α_H -factor can be retrieved by measurable parameters as follows:

$$\alpha_H = -\frac{4\pi}{\lambda} \frac{d\lambda_m/dN}{dG_{net}/dN} = -\frac{2\pi}{L\delta\lambda} \frac{d\lambda_m/dN}{dG_{net}/dN} = -\frac{2\pi}{L\delta\lambda} \frac{d\lambda_m/dI}{dG_{net}/dI} \quad (4.23)$$

The ASE method is in general limited to multimode FP lasers. For monomode lasers that have a DFB grating, the gain properties is affected by the grating thus the accuracy of measurement is lower. It is worth stressing that the thermal effect

needs to be minimized, and a pulsed current source with a low duty cycle at a sub-microsecond rate is preferred. However, the resulted low signal-to-noise ratio and even irregular optical spectral line shape are inconvenient for complex devices such as two-section mode-locked laser and multi-section frequency comb laser. In this thesis, the lasers are pumped by continuous waves (CW) current. Laser emission is coupled by an AR coated lens-ended fibre and gets isolated before measured with a high-resolution optical spectrum analyzer (OSA).

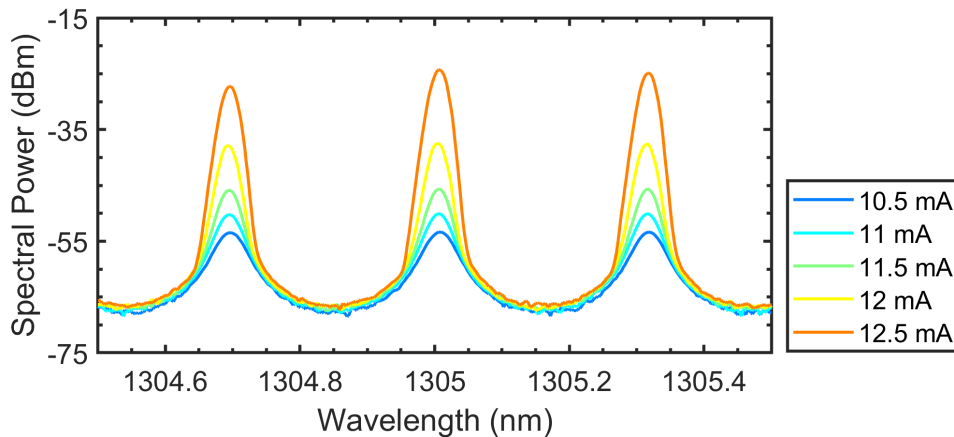


Figure 4.10: Sub-threshold optical spectra of QD laser for different bias currents.

An example for analyzing the ASE spectrum is shown in Fig. 4.10. The InAs/GaAs QD FP laser studied is also fabricated by QD Laser, Inc., Japan, with the same growth technique. The threshold current and the gain peak at threshold of this device is 12.5 mA and 1305 nm, respectively, at 20°C. By increasing the bias current from $0.84 \times I_{th}$ to $1 \times I_{th}$, the sub-threshold optical spectra of the QD laser can be used to measure a series of modal wavelength and net modal gain according to Eq. (4.22). The extracted gain spectra are represented in Fig. 4.11 in the same bias current conditions. For the longitudinal mode located at gain peak at around 1305 nm, Fig. 4.12(a) and (b) depicts the evolution of its net modal gain and modal wavelength as a function of the bias current, respectively. By fitting the below-threshold part, the differential gain and the wavelength shift, dG_{net}/dI and $d\lambda_m/dI$, respectively, are obtained.

To eliminate the thermal effects that occurs at a CW bias condition and to improve the reliability for retrieving the α_H -factor, a correction is necessary. Following the approach in Ref. (Lelarge et al., 2005), the wavelength red-shift above threshold $\Delta\lambda$ that is caused by thermal effect subtracted from the wavelength shift below

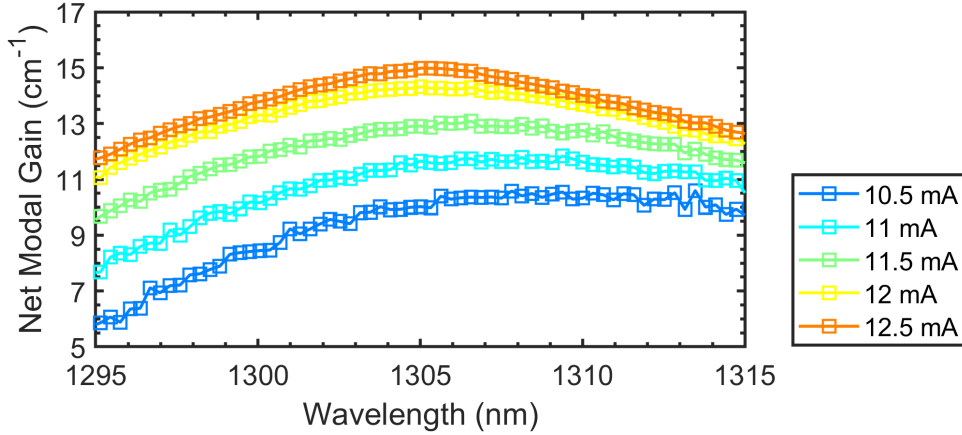


Figure 4.11: Spectral net modal gain of QD laser in various bias current conditions below threshold.

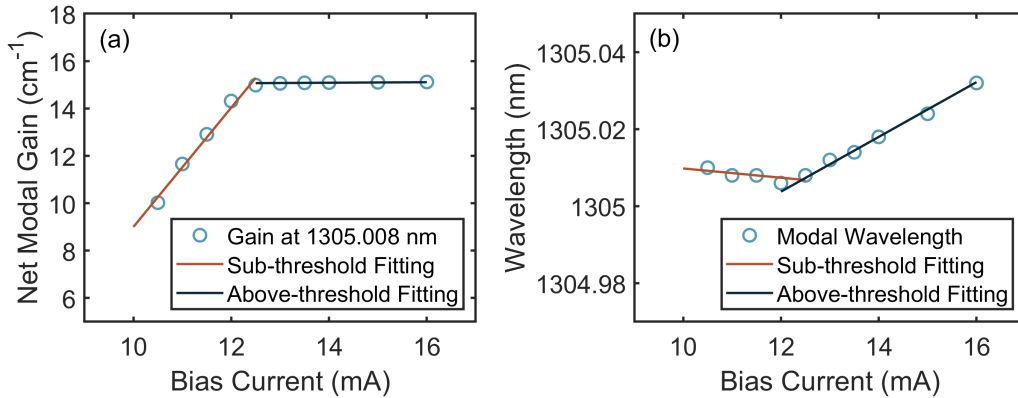


Figure 4.12: The net modal gain and modal wavelength as a function of bias current for the mode located at gain peak at around 1305 nm. Burgundy solid lines: linear fitting below threshold; emerald solid lines: linear fitting above threshold.

threshold. Eq. (4.23) can be re-expressed as follows:

$$\alpha_H = -\frac{2\pi}{L\delta\lambda} \frac{(d\lambda_m - \Delta\lambda)/dI}{dG_{net}/dI} \quad (4.24)$$

where $\Delta\lambda/dI$ is measured by fitting the above-threshold part of Fig. 4.12(b).

Based on the aforementioned ASE method, multimode lasers with different cavity configurations are investigated. Figure 4.13 depicts the spectral dependence of α_H -factor for the QD laser studied. In a range of 20 nm, the α_H -factor ranges from 0.4 to 1.8. It is worth stressing that the value located at the optical gain peak (marked by the vertical black dashed line) being 0.8 is much lower than that observed in QW or QDash devices, which is a peculiar feature offered by QDs.

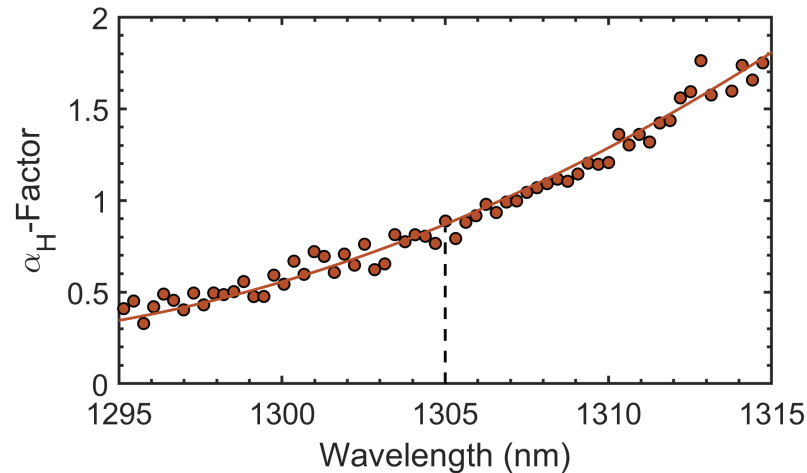


Figure 4.13: Spectral dependence of α_H -factor for InAs QD laser on GaAs substrate measured at threshold. The vertical black dashed represents the wavelength of the optical gain peak at threshold.

Sinusoidal optical phase modulation method

Similar with the well-developed FM/AM method that allows for retrieving the above-threshold α_H -factor of a single-mode laser, the sinusoidal optical phase modulation (SOPM) method also relies on the measurement of modulation dynamics. However, the major benefit offered by the SOPM technique comes from its ability to simultaneously measure the α_H over a wide spectral range and to access the α_H in the real operating condition of laser. Recently, the SWIFTS method exhibits its ability for measuring the spectrally resolved amplitudes and phases of each longitudinal mode (Opačak et al., 2021), which provides another important approach for spectral α_H -factor measurement.

Figure 4.14 illustrates a schematics of the experimental set-up for SOPM technique. The laser should be directly modulated by a sine wave signal within the small-signal modulation regime. To do so, the sinusoidal signal is supplied by a radio-frequency (RF) generator with a modulation frequency f_m ; an RF variable attenuator between the RF signal and the AC port of bias tee (BT) is used to control the modulation depth. Half of the RF signal divided by a RF power splitter (RFPS) is used to modulate a phase modulator (PM) at the same modulation frequency f_m , whereas an optical delay line (ODL) between the laser emission and the PM aims at controlling the delay between the optical and electrical signals. Finally, a high-resolution OSA is used to resolve the optical carrier and the modulation sidebands.

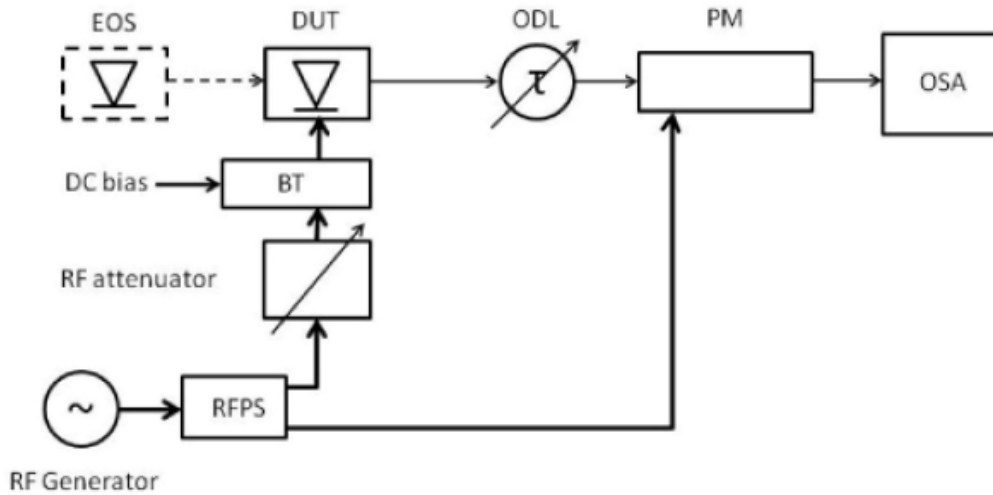


Figure 4.14: Schematics of the experimental set-up for the sinusoidal optical phase modulation method. EOS: External Optical Source; DUT: Device Under Test; ODL: Optical Delay Line; PM: Phase Modulator; OSA: Optical Spectrum Analyzer; BT: Bias Tee; RFPS: RF Power Splitter. From Ref. (Provost et al., 2011)

The extraction of α_H -factor is based on the following statements. The modulated laser emission is expressed as follows (Devaux, Sorel, and Kerdiles, 1993):

$$E(t) = A_{-1}e^{j(\Omega t - \omega_m t)} + A_0e^{j\Omega t} + A_{+1}e^{j(\Omega t + \omega_m t)} \quad (4.25)$$

where

$$A_{-1} = \sqrt{I_0 m} \frac{1 + j\alpha_H}{4} \quad (4.26)$$

$$A_0 = \sqrt{I_0} \quad (4.27)$$

$$A_{+1} = \sqrt{I_0 m} \frac{1 + j\alpha_H}{4} \quad (4.28)$$

with I_0 the DC light intensity, m the amplitude modulation depth, Ω the angular frequency of the laser, and ω_m the angular frequency of the modulation frequency. Then, the electrical field after phase modulation is expressed as:

$$S(t) = E\left(t - \frac{k}{4f_m}\right) \exp(j\phi(t)) \quad (4.29)$$

where

$$\phi(t) = \psi \cos(\omega_m t + \phi_0) \quad (4.30)$$

with ψ the amplitude of the phase modulation, k an integer ranging from 0 to 3 that depends on the optical delay, ϕ_0 the initial phase between the optical signal without

delay and the RF signal at the input of the phase modulator. As a consequence, each longitudinal mode is modulated by a low- and high-frequency sideband whose intensity I_{-1}^k and I_{+1}^k , respectively, is dependent on the delay length. The two frequency-domain parameters can be expressed as follows:

$$I_{-1}^k = |A_{-1}|^2 J_0(\psi)^2 + A_0^2 J_1(\psi)^2 + 2A_0 J_0(\psi) J_1(\psi) \text{Im}[A_{-1} \exp(j \frac{k\pi}{2} + \phi_0)] \quad (4.31)$$

$$I_{+1}^k = |A_{+1}|^2 J_0(\psi)^2 + A_0^2 J_1(\psi)^2 + 2A_0 J_0(\psi) J_1(\psi) \text{Im}[A_{+1} \exp(-j \frac{k\pi}{2} + \phi_0)] \quad (4.32)$$

where J_0 and J_1 are Bessel functions. To extract the α_H , a relationship that describes the modulation properties and the α_H -factor is written as follows (Schimpe, Bowers, and T. L. Koch, 1986):

$$\frac{2\beta}{m} = \alpha_H \sqrt{1 + (\frac{f_c}{f_m})^2} \quad (4.33)$$

where β is the frequency modulation depth, f_c is the corner frequency depending on the output power P , the modal gain g , and the gain compression related to the output power ϵ_p . It can be written as (Olofsson and Brown, 1992):

$$f_c = \frac{1}{2\pi} v_g \frac{dg}{dP} P \quad (4.34)$$

with

$$\frac{dg}{dP} = \frac{\epsilon_p g}{1 + \epsilon_p P} \quad (4.35)$$

where v_g denotes the group velocity in the laser cavity. Eq. (4.33) reveals that a sufficient high f_m is necessary for improving the accuracy of α_H -factor extraction in all methods that rely on amplitude and frequency modulation. Assuming that the f_m is much higher than f_c in the SOPM process, the α_H -factor is expressed as (Provost et al., 2011):

$$\alpha_H = \frac{\text{Im}(\sqrt{Q_{-1}Q_{+1}})}{\text{Re}(\sqrt{Q_{-1}Q_{+1}})} \quad (4.36)$$

where

$$Q_{-1} = (I_{-1}^1 - I_{-1}^3) + j(I_{-1}^0 - I_{-1}^2) \quad (4.37)$$

$$Q_{+1} = (-I_{+1}^1 + I_{+1}^3) + j(I_{+1}^0 - I_{+1}^2) \quad (4.38)$$

In this thesis, the SOPM method is applied to the OWD-assisted QD-DFB laser to retrieve its α_H -factor. To do so, the f_m is fixed at 12 GHz, which satisfies $f_m \gg f_c$.

The temperature dependent OWD influences on the α_H is investigated. First, the author gives an example of the delay length dependent optical spectra of the device studied when it operates at $2 \times I_{th}$ under 55°C . Figure 4.15(a) depicts the optical spectra corresponding to four different delays equally spaced by $1/f_m$ being 20.3 ps. By increasing the delay length k/f_m from $k = 0$ to 3, four I_{-1}^k and I_{+1}^k are extracted. The effective α factors measured in different operating conditions by following Eq. (4.33) are shown in Fig. 4.15(b). For a fixed temperature while increasing the bias current, the increase of α_H -factor in agreement with previous work (Frédéric Grillot, Béatrice Dagens, et al., 2008; H. Huang et al., 2020) is attributed to the gain compression, as explained in Sec. 2.6. The observed stable α_H against the current variation indicates that the gain compression of the device studied is quite low. For instance, the α_H enlarges from 2 to 2.6 with increasing the bias current from $2 \times I_{th}$ to $6 \times I_{th}$ at 55°C . Given that the QD-DFB laser exhibits a sole GS emission, the second term in Eq. (2.37) can be omitted, and the ϵ_p can be extracted by curve-fitting the power dependent α_H . In this study, the measured ϵ_p slightly changes from 2×10^{-2} to $7 \times 10^{-2} \text{ mW}^{-1}$ with the increase of temperature from 15 to 55°C . These low values are rather found similar to those of QW lasers than those observed on other QD devices (Frédéric Grillot, Béatrice Dagens, et al., 2008; Jianan Duan, Y. Zhou, et al., 2020). Such an improvement could be attributed to the mismatched Bragg grating that gives rise to the decrease of gain nonlinearity (J. Huang and Casperson, 1993). Nevertheless, these results demonstrate that the above-threshold α_H -factor is strongly affected by the temperature assisted wavelength mismatch. For instance, the α_H reduces from 3.4 to 2 with the increase of temperature from 15 to 55°C , when the device operates at $2 \times I_{th}$. Such an effect is attributed to the decrease of internal loss thus the increase of differential gain at a smaller OWD. Nevertheless, the α_H measured at 2 is still much higher than its intrinsic value at 0.8, as shown in Fig. 4.13, meaning that the operating condition remains to be improved. Therefore, the α_H can be further minimized once the temperature increases to its optimum condition T_m where the OWD approaches zero. Nevertheless, due to the increase of internal loss in the negative OWD condition which possibly results in the decrease of differential gain (H. Lu, Blaauw, and Makino, 1996), the α_H -factor could be reincreased when the operating temperature is higher than T_m .

Despite the convenience, the SOPM as well as other FM/AM methods are valid for retrieving a current modulation driven α_H -factor, that is to say the $2\beta/m$. That means the accuracy of the measured α_H depends on the modulation frequency and the optical noise. In particular, the above-threshold α_H -factor depends on a complex

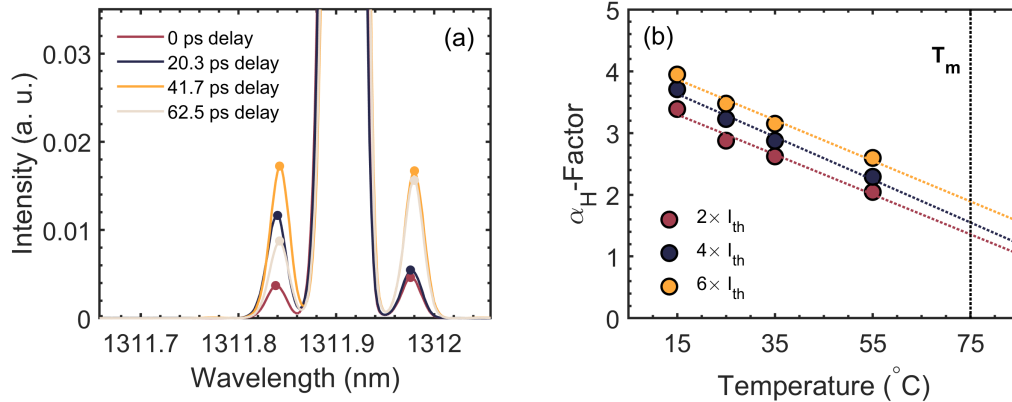


Figure 4.15: (a) Optical spectra around the DFB mode and the modulation sidebands of the QD-DFB laser measured at $2 \times I_{th}$ under 55°C . The spectra obtained for 4 different optical delays are normalized to the main lobes. (b) Effective α_H -factor in different operating conditions.

combination of multiple effects such as the optical power (Nakajima and Bouley, 1991; Frédéric Grillot, Béatrice Dagens, et al., 2008), the type of the cavity (DFB, FP) (Furuya, 1985; Westbrook, 1985), and the gain nonlinearities (spectral and spatial hole burnings, carrier-heating) (G. P. Agrawal, 1989; G. P. Agrawal, 1990; Zilkie et al., 2008). Thus, extraction of the α_H above threshold may mask some basic features of the semiconductor material. In addition, the extraction of α_H for FP laser is more complex than the DFB one. Utilizing the SOPM technique, a high f_m results in a large mode spacing between the main lobe and the sidebands, that means a large enough free-spectral range (FSR) is necessary to avoid any crosstalk from the sidebands. As a consequence, it is more reliable to retrieve the α_H -factor close to threshold, since it allows for measuring the α_H dependence on carrier concentration and photon energy that are not accessible in the real operating conditions above threshold.

4.7 Characterization of relative intensity noise and modulation properties

QDs are known from their low-noise properties, which are promising for developing high-speed optical interconnects. In particular, single-mode DFB laser plays a crucial role in wavelength-division multiplexing (WDM) system; however, the Bragg grating is observed to determine the lasing properties, as discussed hereinabove. In this context, it is of first importance to optimize the laser design to improve their noise and modulation performance. In this dissertation, the author focuses on the characterization of the relative intensity noise (RIN) spectra of the QD-DFB laser

studied, in which the noise level, the relaxation oscillation frequency f_{RO} and the damping factor γ are analyzed.

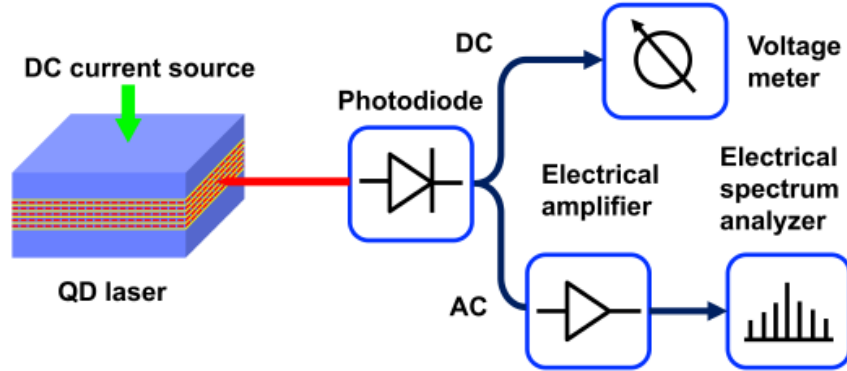


Figure 4.16: Experimental setup used for characterizing the RIN of QD lasers. From Ref. (Jianan Duan, Y. Zhou, et al., 2020).

Figure 4.16 displays the experimental configurations for RIN characterization. The laser emission is coupled into a lens-end fibre before it is captured by a low-noise photodiode whose bandwidth is 10 GHz. The DC and the AC signal of the RF output are separated by a bias tee, the former is then measured by a voltage meter. The AC signal is amplified by a broadband amplifier with a typical small-signal gain of 30 dB before it is sent to the electrical spectrum analyzer (ESA) for further analysis. Despite the contribution of the shot noise that is induced by the random occurrence of photons, it is usually negligible and the measured RIN spectrum is mainly determined by the contributions of carriers when the RIN level is much higher than the shot noise level (A. Y. Liu, Komljenovic, et al., 2017; Y.-G. Zhou et al., 2017). To determine the RIN, the first step is to express the intrinsic laser noise S_{laser} , which can be written as (Y.-G. Zhou et al., 2017):

$$S_{laser} = S_{total} - S_{thermal} - S_{shot} \quad (4.39)$$

where S_{total} denotes the total noise that is measured by the ESA. $S_{thermal} = 4k_B T/R_L$ accounts for the thermal noise, in which k_B is the Boltzmann constant, T is the temperature, and R_L being 50Ω is the load resistance of the ESA. $S_{thermal}$ is determined when there is no laser emission, hence it is a parameter that is independent with the optical power. S_{shot} denotes the shot noise that is expressed as $S_{shot} = 2qI_{DC}R_L$ with q the elementary charge and I_{DC} the DC current. Thus, the RIN can be

expressed as follows (Y.-G. Zhou et al., 2017):

$$RIN = 10 \log_{10} \left[\frac{(S_{total} - S_{thermal}) / (RBW \times G) - S_{shot}}{P_{DC}} \right] \quad (4.40)$$

where P_{DC} denotes the electrical DC power, RBW is the resolution bandwidth of the ESA, which is 200 kHz in our case. G accounts for the total gain brought by the experimental setup that includes the amplifier, which can be measured by a vector network analyzer (VNA).

Figure 4.17(a) depicts an example of bias current dependent RIN spectra for the QD-DFB device measured at 20°C. With a threshold current at 9.5 mA in this temperature condition, the spectra of the device are measured by increasing the current from 11 to 27 mA. Owing to the low spontaneous emission factor in QDs, a low RIN level of -150 dB/Hz at 10 GHz is identified in this study. With the increase of bias current, the peak of the relaxation oscillation frequency moves from 1 GHz to about 4 GHz, until the received power attained the maximal limit of the photodiode beyond $3 \times I_{th}$ (0.72 mW). Both the f_{RO} and the γ can be independently retrieved from the RIN spectrum, by doing a curve-fitting via the following relationship (Coldren, Corzine, and Mashanovitch, 2012; Jianan Duan, Y. Zhou, et al., 2020):

$$RIN(\omega) = \frac{a + b\omega^2}{(\omega^2 - \omega_{RO}^2)^2 + \omega^2\gamma^2} \quad (4.41)$$

where ω_{RO} denotes the angular frequency of the relaxation oscillation and ω is the angular frequency. a and b are the coefficients used for the curve-fitting, which have been introduced in Chap. 2.

Figure 4.17(b) displays the damping factor as a function of the squared f_{RO} at 20°C (jade) and at 55°C (burgundy). According to Eq. (2.32), the K-factor can be extracted by doing a curve-fitting of such a linear evolution. As shown in Fig. 4.17(c), the K-factor at 20°C and at 55°C is 2.87 ns and 1.72 ns, respectively. Based on the definition in Eq. (2.33), the lower K-factor at 55°C is beneficial for enlarging the maximum 3-dB bandwidth. Such an improvement of modulation performance at a high temperature is attributed to the reduced mismatch between the Bragg grating and the optical gain peak that increases the differential gain (Hantschmann et al., 2018). To clarify, another expression of K-factor that includes the laser configurations is written as follows (Fiore and Markus, 2007):

$$K = 4\pi^2 \left[\tau_p + \left(\frac{\Gamma a_p}{a} \right) \tau_p \right] \quad (4.42)$$

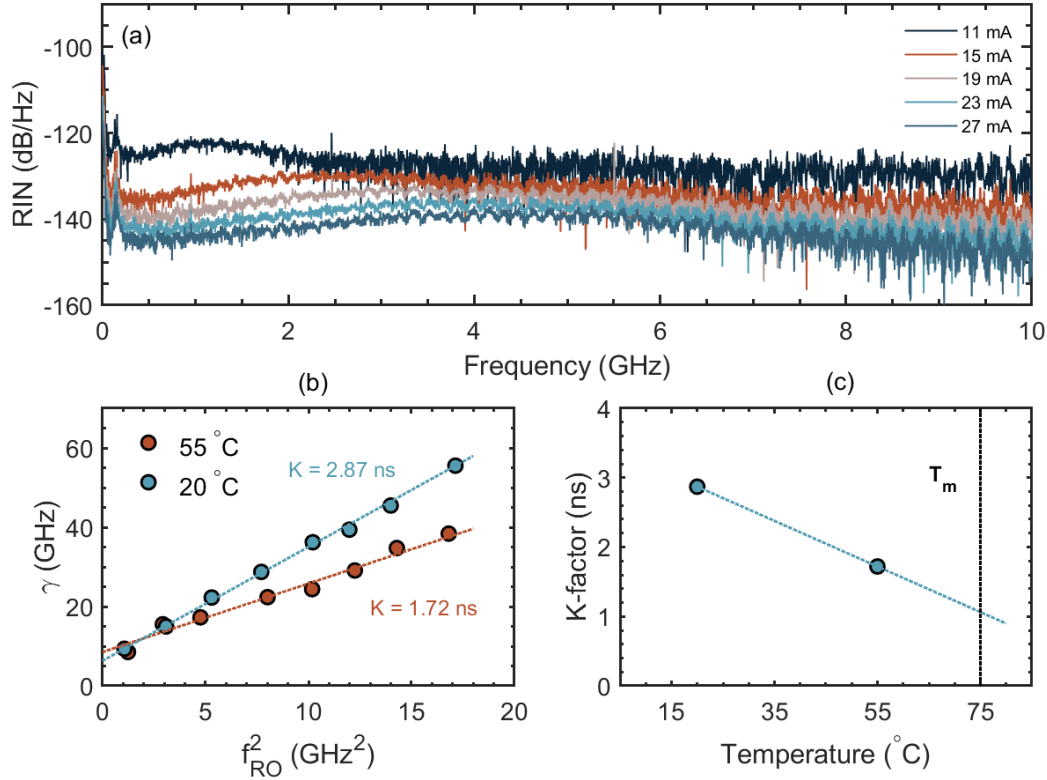


Figure 4.17: (a) Measured RIN spectra at several bias currents at 20°C. (b) Extracted damping factor γ as a function of the squared relaxation oscillation frequency f_{RO}^2 at 20°C (jade) and at 55°C (burgundy). (c) Tendency of K-factor versus the temperature, T_m is marked by the black dashed line.

where

$$a_p = -\left(\frac{dg}{dN_p}\right)|_N = \frac{\epsilon_s g_m}{1 + \epsilon_s N_p} \approx \epsilon_s g_m \quad (4.43)$$

with τ_p the photon lifetime that is proportional to cavity length, Γ the confinement factor and a the differential gain. ϵ_s , g_m and N_p account for the gain compression factor, the material gain and the photon density, respectively. Therefore, it is of importance to minimize the OWD or to apply the p-modulation doping to the active region to ensure an optimum laser performance in terms of the K-factor. The second statement comes from the fact that the differential gain can be increased by the p-doping technique (Inoue et al., 2018; J. C. Norman, Z. Zhang, et al., 2019). Moreover, these results demonstrate that a large OWD at room temperature is an efficient technique to develop a high-performance laser source for high-temperature applications. In addition, Eqs. (4.42) and (4.43) reveal that the laser cavity length as well as the gain compression play crucial roles in determining the K-factor. Since the DFB device under test is not designed for high-speed operation, its 750- μm -long

cavity is partially responsible for the large K-factor thus the narrow modulation bandwidth. A commonly used approach to improve the modulation capacity is to reduce the cavity length below $500 \mu m$ (Arsenijević and Dieter Bimberg, 2016). Last but not least, the QDs are known from their large gain compression, which is a typical drawback that restricts the modulation capacity if they are applied to a laser. Nevertheless, due to the possible decrease of gain nonlinearity with the design of OWD, the QD device studied has a gain compression factor as low as that of a QW laser, as discussed in Sec. 4.6.

4.8 Dynamics in long-delay optical feedback operation

Despite the remarkable properties such as the feedback insensitivity offered by QDs, the Bragg grating gives an extra degree of freedom to the laser. Besides, InAs QDs that are grown on native GaAs substrate also give rise to a much longer Shockley-Read-Hall (SRH) recombination lifetime compared to the QDs that are directly grown on Si. As a result of these two effects, the dynamics of the QD-DFB laser studied under external optical feedback exhibits a dependence of the OWD. In extreme operating conditions, a complete route to chaos can be triggered from the QD-DFB laser. Figures 4.18 depict the dynamics of the DFB device subject to a long-delay optical feedback, when it operates at $25^\circ C$ where the optical wavelength detuning (OWD) is 25 nm. The experimental setup has been introduced in Chap. 3 Sec. 3.9. The optical fibre-based L_{ext} is fixed to 14 meters throughout these measurements. The first column displays the dynamics at $2 \times I_{th}$, and the second column displays those at $6 \times I_{th}$. The first and second rows present the RF spectra and the RF power mapping, whereas the third and fourth rows correspond to the optical spectra and the spectral power mapping. In the low bias condition at $2 \times I_{th}$, the DFB laser exhibits an incomplete route to chaos. With the increase of feedback strength, the device remains stable when the η_F is lower than 2.5%, then it skips regime II and III and directly enters into regime IV. On its route to chaos, the quasi-periodic (QP) oscillation behavior (gold spectrum in (a)) is firstly observed at the onset of regime IV, the chaotic oscillation (burgundy spectrum in (a)) is then fully developed with a higher η_F . Corresponding η_F to these spectra are marked by the gold and burgundy dashed lines in (c), respectively. On the other hand, the DFB laser remains single-mode oscillation except for the mode broadening in regime IV, as shown in (e) and (g). Readers are invited to consult the definitions of different feedback regimes in Chap. 3.

A complete route to chaos are identified when the bias current increases to $6 \times I_{th}$.

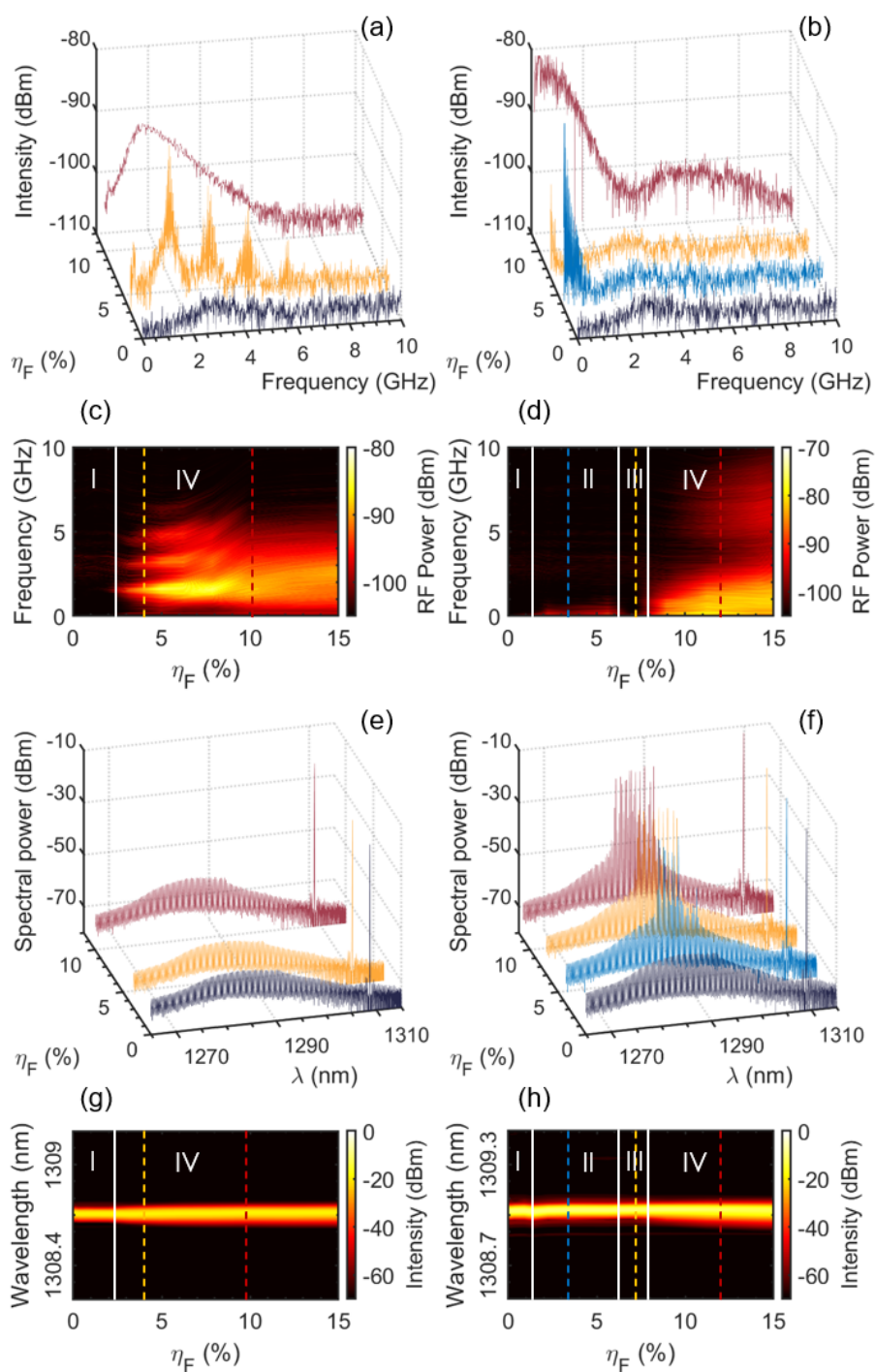


Figure 4.18: RF spectra and optical spectra in different r_{ext} conditions at 25°C , when the QD-DFB laser operates at $2 \times I_{th}$ [(a) and (e)] and $6 \times I_{th}$ [(b) and (f)]. Corresponding power mapping of the RF and optical spectra as a function of η_F at $2 \times I_{th}$ [(c) and (g)] and at $6 \times I_{th}$ [(d) and (h)].

All the η_F corresponding to the spectra in Figs. 4.18(b) and (f) are remarked by the dashed lines in the same colors in Figs. 4.18(d) and (h). In regime I where the η_F is below 2%, the DFB laser remains stable. While the η_F ranging from 2% to 6%, the laser enters into regime II where a quasi-period-one (Q1) behavior in presence of a series of low-frequency peaks induced by the external cavity are observed in the RF response (blue spectra in (b) and (d)). Instead of the mode hopping observed in a previous study (Tkach and Chraplyvy, 1986), the DFB mode in this study suffers from a wavelength fluctuation within the transition from regime I to regime II. In addition, the longitudinal modes near the optical gain peak get amplified by the EOF in regime II thus the laser exhibits a dual-wavelength lasing behavior. It is worth stressing that this is a peculiar dynamics in the OWD-assisted DFB device. Further increasing the η_F to $\sim 7\%$, the external cavity frequencies are largely suppressed that means the device restabilizes and enters into regime III (gold spectrum in (b)). Nevertheless, this operating regime is too narrow to observe the restabilization in the optical spectrum (gold spectrum in (f)). The critical feedback level r_{crit} is 8% in this operating condition, above which the laser enters into regime IV in presence of DFB mode broadening and chaotic oscillations (burgundy spectra in (b) and (f)). In such a high bias condition, the DFB laser is overdamped and it does not show any periodic oscillation in regime IV.

Let us recall the introduction of the stability of a semiconductor laser with EOF in Chap. 3 Sec. 3.4. A laser is unconditionally stable against EOF in regime I where the feedback parameter $C \leq 1$. In the LCR, the laser could be conditionally stable against EOF when $C > 1$, only if it skips the transition in regime II. The results of the QD-DFB laser demonstrate that the strength of the external cavity frequencies in regime II could be comparable with that of the periodic oscillations in regime IV, meaning that the impact of regime II is not always negligible. In addition, experimental results shown in Sec. 4.10 demonstrate that the BER performance degrades with the EOF within the transition in regime II. In this context, it would be important to stress that the operating regimes in which the laser exhibits single-mode emission under EOF could be crucial for realizing isolator-free photonic integration. Therefore, it is of importance to minimize the influence of regime II to enable the laser a desirable performance in EOF operation. To this end, one could consider reducing the external cavity length into the SCR to address this issue, as shown in Figs. 3.22. In the case of a QD laser for PIC applications, the instabilities caused by the intra- and inter-chip-scale back-reflections cannot be a great issue, given that the scale of intra- and the inter-chip is on the order of micrometers and centimeters,

respectively (Roelkens et al., 2010). Another approach to disable the regime II could be the reduction of OWD, which will be discussed hereinafter.

4.9 Impact of the optical wavelength detuning on the feedback insensitivity

The measurements of α_H -factor in Sec. 4.6 demonstrate that the OWD of the QD-DFB laser has a direct impact on its α_H . Therefore, it is of significant importance to analyze the laser's sensitivity for EOF with different OWD. Figures 4.19 display the laser dynamics in EOF operation at 55°C. The external cavity length remains at 14 meters, however, the OWD in this temperature condition is reduced to ~10 nm. Again, the first column displays the dynamics at $2 \times I_{th}$, and the second column displays those at $6 \times I_{th}$. The first and second rows depict the RF spectra and the RF power mapping, whereas the third and fourth rows correspond to the optical spectra and the spectral power mapping. Compared to the dynamical behaviors shown in Figs. 4.18, the reduction of OWD is beneficial for largely increasing the laser's tolerance for EOF. When the QD laser operates at $2 \times I_{th}$, its critical feedback level r_{crit} associated with the onset of regime IV is increased to 10%, above which the DFB mode broadens due to the coherence collapse. Similar with what happens at 25°C, the laser skips the regime II and III in this low bias condition. In regime IV, it firstly exhibits a QP oscillating behavior (gold spectra in (a) and (e)), and then follows with the chaotic oscillations (burgundy spectra in (a) and (e)). On the other hand, the device keeps its full transition from regime I to IV when the bias current is increased to $6 \times I_{th}$. Despite the similar onset of regime II at 3% as that at 25°C, the regime II is largely broadened thus leading to a much higher r_{crit} at 25%. In contrast to the regime II at 25°C, the strength of the external cavity frequencies are much weaker where the OWD is reduced. As a consequence, the laser keeps a single-frequency emission in transition from regime I to III, and it satisfies the condition for isolator-free application. The laser dynamics in regime II and in regime III are shown by the blue and the gold spectra in (b) and (f), respectively. With the increase of η_F above the r_{crit} , the overdamped device exhibits strong chaotic oscillations, in presence of both the broadening of DFB mode and the lasing of side modes, as shown by the burgundy spectra in (b) and (f).

To disable the regime II, it is an efficient approach to operate the laser in a low bias condition. Figures 4.20 depict (a) the critical feedback level r_{crit} and (b) the feedback boundary associated with the onset of periodic oscillations $r_{ext,p}$ of the QD-DFB laser in different operating conditions. The laser's tolerance for EOF improves with the increase of temperature, owing to the decrease of α_H -factor

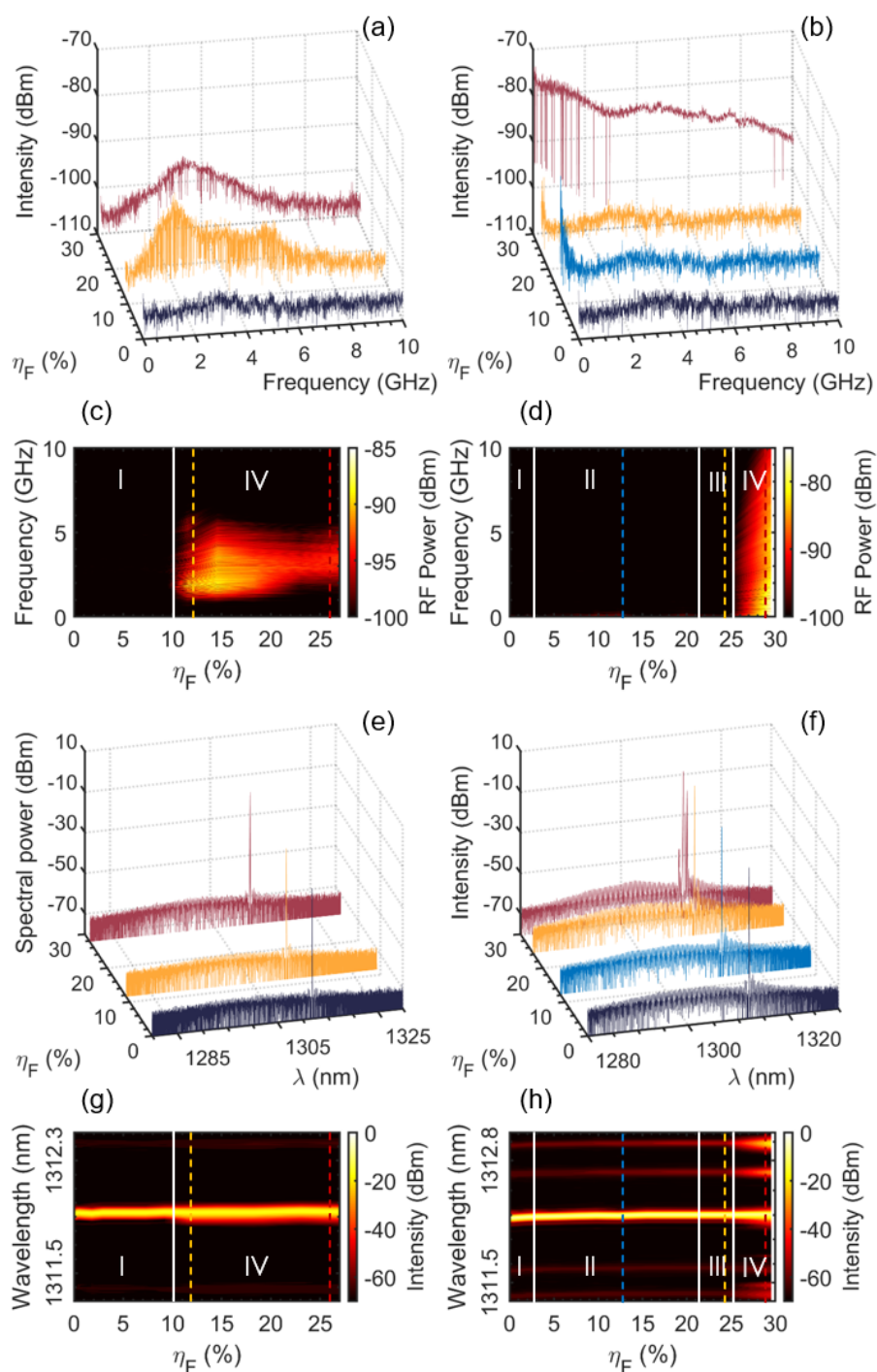


Figure 4.19: RF spectra and optical spectra in different r_{ext} conditions at 55°C , when the QD-DFB laser operates at $2 \times I_{th}$ [(a) and (e)] and $6 \times I_{th}$ [(b) and (f)]. Corresponding power mapping of the RF and optical spectra as a function of η_F at $2 \times I_{th}$ [(c) and (g)] and at $6 \times I_{th}$ [(d) and (h)].

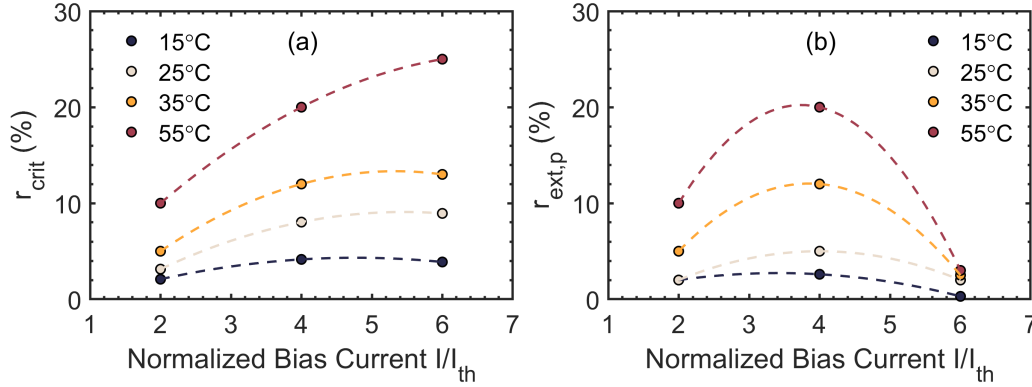


Figure 4.20: (a) Critical feedback level associated with the onset of regime IV r_{crit} and (b) the feedback level associated with the onset of periodic oscillations $r_{ext,p}$ in different operating conditions.

induced by the reduction of OWD. In all temperature conditions, on one hand, both the r_{crit} and the $r_{ext,p}$ increases with the bias current in the range of $2 \times I_{th}$ to $4 \times I_{th}$, owing to the increased intra-cavity photon density that partially compensates for the inconvenience of the large α_H (Azouigui et al., 2007; Shéhérazade Azouigui et al., 2009). On the other hand, a higher bias current above $4 \times I_{th}$ leads to a saturation of the r_{crit} and a decrease of the $r_{ext,p}$ due to the gain compression and the consequent large α_H -factor. In the optimum bias condition at $4 \times I_{th}$, the $r_{ext,p}$ increases from 2.6% (-15.9 dB) to 20% (-6.8 dB) as the temperature increases from 15 to 55°C, where the OWD is reduced from 30 to 10 nm. Last but not least, the operating temperature at 55°C is not the optimum condition for the DFB laser, since the OWD equalling to 10 nm remains large. It is worth stressing that the laser's tolerance can be further improved at its optimum temperature condition $T_m = 75^\circ C$.

4.10 Impact of the feedback dynamics on transmission properties

To develop a QD laser for isolator-free PIC applications, the investigations of its transmission performance in EOF operation are of importance. In this thesis, the author focuses on the analysis of the QD-DFB laser in direct modulation operation. Figure 4.21 depicts the experimental setup for Pulse Amplitude Modulation 4-level (PAM4) transmission with coherent optical feedback in the long-cavity regime. The 2 Gbaud pseudo-random bit sequence (PRBS) modulation format is generated from an arbitrary waveform generator (AWG), with the sequence length and the peak-to-peak modulation amplitude V_{pp} fixed to $2^{31} - 1$ and 2 V, respectively. After coupled by a lens-end fibre, the first 90% power of the modulated optical signal is

sent to the 14 meters-long optical fibre based external cavity for back reflection. The remaining 10% power of the laser emission is isolated and then it propagates in a 12 kilometers-long single-mode fibre (SMF) coil. In the case of back-to-back (B2B) configuration, the fibre coil is removed. The transmitted optical signal is finally captured by a 10 GHz photodiode (PD) and analyzed in an oscilloscope. The bit-error-rate (BER) is calculated by counting and comparing the original modulation signal and the received signal after transmission. In this study, the time duration for each signal counting is fixed to 5 ms, thus the minimum BER level is limited to 10^{-7} .

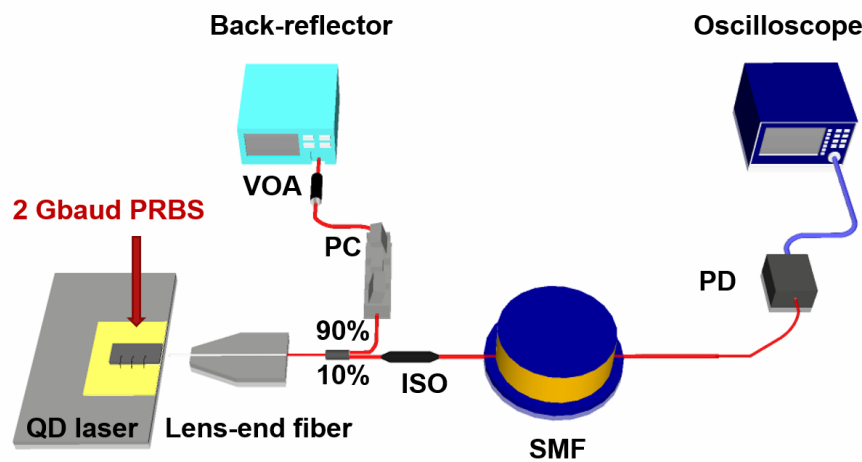


Figure 4.21: Experimental setup used for the PAM4 transmission with coherent external optical feedback. PRBS, pseudo-random bit sequence; ISO, optical isolator; SMF, single-mode fibre; PD, photodiode; PC, polarization controller; VOA, variable optical attenuator.

Figure 4.22 depicts the B2B BER versus the received optical power of the DFB device in the PAM4 transmission configuration. In these measurements, the laser operates at $6 \times I_{th}$ at 55°C , with a direct PAM4 modulation rate at 2 Gbaud. In free-running operation (black), the QD laser exhibits a penalty-free operation with $\text{BER} < 10^{-7}$. With the increase of feedback strength to the boundary of regime I at 3.2% (yellow), the error-free operation is maintained except for a power penalty of 1 dB for the BER level at 10^{-7} . Further increasing the feedback strength to 6.3% within the regime II (emerald), the influence of the external cavity frequencies is clearly observed from the decrease of BER as well as the increase of power penalty.

For instance, the minimum BER measured is 2×10^{-4} when the received power is -1 dBm; the power penalty for the same BER level is also increased by 4 dB due to the back-reflection. Nevertheless, the BERs in regime II are still below the threshold of the hard-decision forward error-correction (HD-FEC) at 5×10^{-3} (7% overhead), meaning that the laser is still tolerant for the EOF. Once the laser operates in regime IV, the strong coherence collapse makes the received data hardly to be distinguished. An example that is recorded when the feedback strength increases to 31.6% (burgundy) is shown in Fig. 4.22, in this case the BERs are above the HD-FEC threshold and are independent with the received optical power.

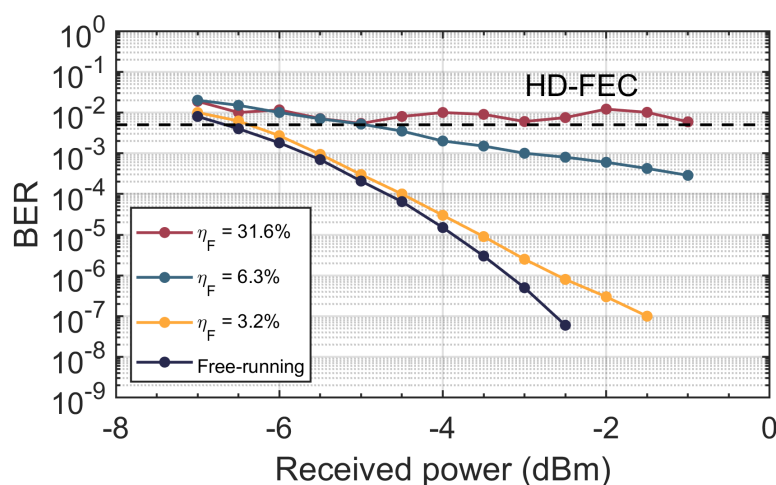


Figure 4.22: BER versus received optical power of the QD-DFB laser in the back-to-back PAM4 configuration with the feedback strength increasing from 3.2% (gold) to 6.3% (emerald) and further to 31.6% (burgundy). The BER plot in free-running operation (black) is performed as a reference. The laser operates at $6 \times I_{th}$ at 55°C .

The BER plots of the modulated optical signal in B2B (solid line) and after 12 km transmission (dashed line) are summarized in Fig. 4.23. The cases for free-running operation is shown by the black curves, whereas the cases for EOF operation with the feedback strength at 3.2% are represented by the burgundy curves. The 12 km transmission in a SMF optical fibre results in a power penalty of 2.5 dB for the BER level at 10^{-5} , which is attributed to the chromatic dispersion. Despite the increase of the minimum BER by two or three orders of magnitude in free-running or in EOF operation, the BERs are still below the HD-FEC threshold. Therefore, it is crucial for enabling the laser to operate in regime I to minimize the influence of the periodic oscillations induced by EOF. These results give insights for optimizing the operating conditions of the laser to meet the requirements of isolator-free transmission.

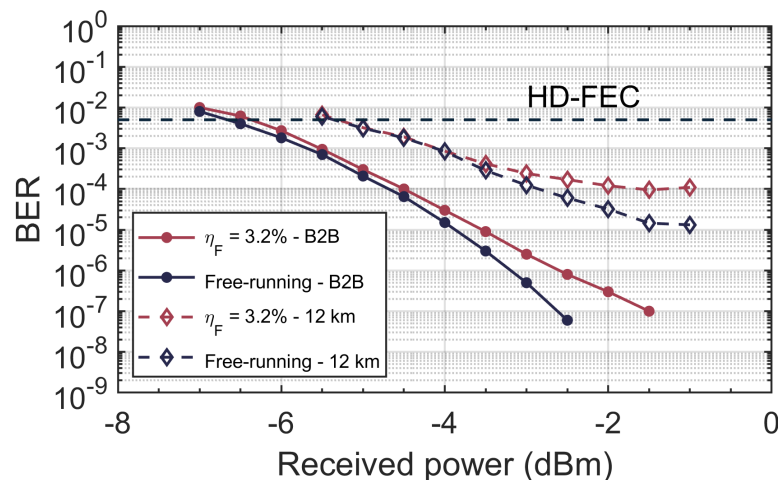


Figure 4.23: BER versus received optical power in the PAM4 configuration for back-to-back or after 12 km transmission when the QD-DFB laser is in free-running (black) or with the feedback strength at 3.2% (burgundy). The laser operates at $6 \times I_{th}$ at 55°C .

4.11 Summary

This chapter classifies the fundamental properties of a QD-DFB laser with a design of optical wavelength detuning. In particular, the ASE method, SOPM method, and the RIN characterization technique described in this chapter allow us to analyze the α_H -factor, the noise properties, and the modulation properties of the device studied. The influence of the OWD on the dynamics of laser when it is subject to EOF is investigated to give design rules for improving the laser's tolerance for back-reflections. The main parameters of the QD-DFB laser at 25°C and at 55°C are summarized in Tab. 4.1.

T ($^\circ\text{C}$)	OWD (nm)	I_{th} (mA)	K (ns)	RIN @ 10 GHz (dB/Hz)	α_H (@ $4 \times I_{th}$)	r_{crit} (@ $4 \times I_{th}$)
15	30	10.6	2.87 (20 $^\circ\text{C}$)	-155	3.4	2.6%
55	10	6.0	1.72	-155	2.3	20%

Table 4.1: Main parameters of the QD-DFB laser in different operating conditions.

The main results are summarized as follows:

- QD is a promising material to serve as the gain medium of a semiconductor laser, owing to its low α_H -factor. For a QD laser on native substrate, its α_H below 1 is significantly lower than that in a QW or QDash device (i.e., 2~5).

- QD exhibits a remarkable low-noise property. A low RIN level is measured at -155 dB/Hz in the range of 8-10 GHz. Together with the low α_H -factor, QD laser is a promising solution for developing highly stable optical interconnects for optical network and data centers.
- For a QD-DFB laser, a low mismatch between the Bragg grating and the optical gain peak is beneficial for improving the laser performance. With the reduction of the OWD from 30 to 10 nm, the threshold current and the α_H -factor show a 45% and a 43% decrease, respectively. The simultaneous decrease of the K-factor from 2.87 to 1.72 ns along with a 9 dB improvement of the feedback level that is associated with the onset of unstable oscillations pave the way for developing single-frequency QD lasers that are tolerant for high-temperature and back-reflections for uncooled and isolator-free PICs.
- Under EOF, the occurrence of regime II where the laser oscillates at the external cavity frequencies is detrimental to the BERs in the direct modulation operation. To address this issue, approaches such as operating the laser in the low bias conditions, reducing the external cavity length into the short-cavity regime, and reducing the OWD can be considered.

DESIGN AND OPTIMIZATION OF QUANTUM-DOT OPTICAL FREQUENCY COMB

Optical frequency comb (OFC) plays an important role in spectroscopy, microwave photonics, high-resolution LIDAR system, and optical communication with WDM architecture. In 2005, John L. Hall and Theodor W. Hansch were awarded half of the Nobel prize owing to their contributions to the development of optical frequency comb technique. In this chapter, the dynamics of QD-based OFC are investigated by both theoretical analysis and experiments. This study aims at providing design rules for developing high-performance QD-OFC and introducing techniques such as external optical feedback and optical injection to improve the laser performance.

5.1 Introduction to optical frequency comb

Since the introduction of the laser frequency comb in the late 1990s, it has played as a “light gear” that enables a reliable and accurate approach for counting optical cycles on the femtosecond (10^{-15} s) time scale, and has revolutionized precise measurements of frequency and time. Before the OFC is available, it was once a big challenge to count, measure, and phase-coherently control the optical frequencies by utilizing the radio frequencies due to the difference in frequency of a factor of 10^5 . As a result of this gap, there are limitations in the timing keeping at hundreds of terahertz as well as in the tests of fundamental physics such as the optical spectroscopy of energy eigenstates in atoms and molecules. To overcome this issue and to connect the radio and the optical domains, techniques including the harmonic frequency chain and the optical interval division were developed (Schnatz et al., 1996; Nakagawa, Kourogi, and Ohtsu, 1993), however, these systems would never be widely available due to their complexity and poor reliability. Despite that, the latter gave insight for simplifying the system and its idea was used later in the modern OFC with a slightly different manner. It is worth stressing that this situation is radically changed by the OFC technique which provides an elegant way to connect the frequency and the phase of optical oscillators to those in electronic circuits.

Figure 5.1 illustrates an simplified optical clockwork analogy that describes how the connection is established whether from microwave to optical, from optical to microwave, or from optical to optical. In the first case where the frequency comb

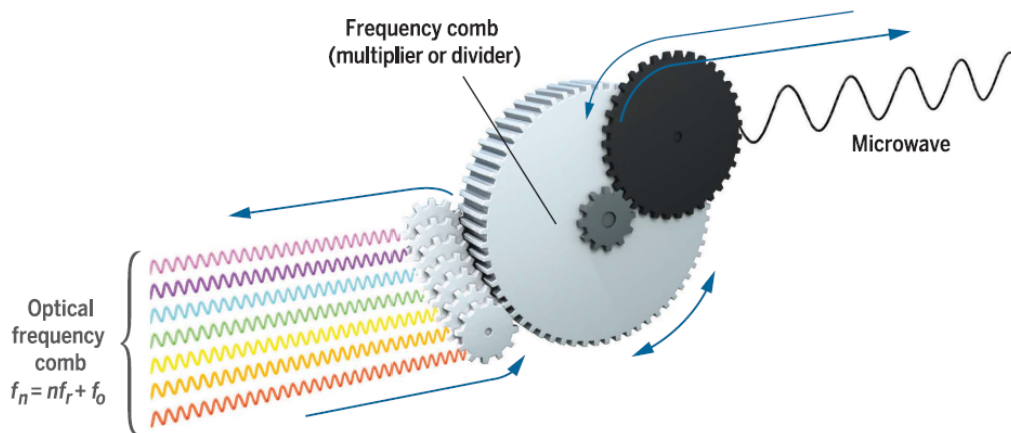


Figure 5.1: Sketch of a frequency comb that functions in a manner analogous to a light gear. It links the radio frequencies f_r and f_0 to a vast array of optical frequencies f_n . From Ref. (Diddams, Vahala, and Thomas Udem, 2020).

transfers the radio frequency (black sinusoid microwave) to a very broad spectrum of equally spaced optical frequencies f_n (linked to small gray gears), their relationship is expressed as follows:

$$f_n = nf_r + f_0 \quad (5.1)$$

where f_r and f_0 denote the repetition frequency and an offset frequency that is common to all the modes, respectively. In general, both the f_r and the f_0 are in the range of 0.1 to 10 GHz, however, a large n on the order of 10^5 leads to the f_n approaching near-infrared frequency band. Figure 5.2 depicts the time-domain spectrum and the corresponding frequency-domain response of an OFC, in which the frequencies introduced in Eq. (5.1) are represented. The repetition rate is determined by the laser cavity length through the following relationship:

$$f_r = \frac{v_g}{2L_c} \quad (5.2)$$

with v_g the group velocity of the light in the cavity and L_c the length of the laser cavity. In an ideal case, the optical pulses are generated exactly every n cycles of the continuous wave light wave, thus the f_0 in Eq. (5.1) can be removed. Nevertheless, the intra-cavity pulse wave propagates at a phase velocity that is different from v_g due to the dispersion in the laser cavity. As a result, the output pulse wave is shifted with respect to the pulse envelope by a constant amount $\Delta\phi$ from pulse to pulse, in presence of a slight variation of the repetition rate of laser. It is worth stressing that this pulse wave shift accumulates during the generation of pulses. On the other

hand, the mode spacing between each comb line in the frequency-domain is fixed to f_r , however, the full spectrum is shifted by a carrier-envelope offset frequency f_0 induced by the $\Delta\phi$ which is expressed as follows:

$$f_0 = \frac{\Delta\phi f_r}{2\pi} \quad (5.3)$$

While the aforementioned descriptions are devoted to the case for the transfer from microwave to optical, they are valid for the other two cases for the transfer from optical to microwave and from optical to optical. Readers are invited to consult a recent article from Diddams, Vahala, and Thomas Udem, 2020 for more details.

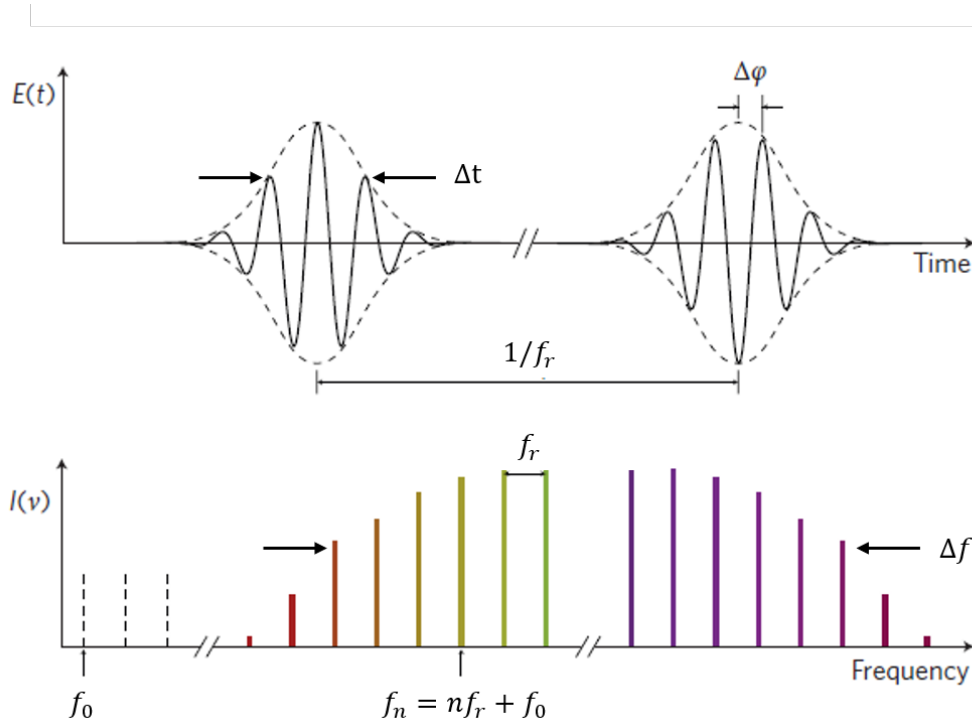


Figure 5.2: Time-domain spectrum of a frequency comb pulse train along with the corresponding frequency-domain response, which illustrates the equally spaced comb lines. The FWHM of the optical pulse and the optical bandwidth are represented by Δt and Δf , respectively. From Ref. (Schliesser, Picqué, and Hänsch, 2012).

In addition to the time-frequency relationship shown in Fig. 5.2, a relationship between the time domain and the frequency domain descriptions allows for better understanding the frequency comb dynamics. To begin with, the intra-cavity laser field is expressed as follows:

$$E(z, t) = \sum_n E_n(t) u_n(z) \cos[\Psi_n(t)] \quad (5.4)$$

where $u_n(t)$ is the passive cavity modes. $E_n(t)$ and $\Psi_n(t)$ account for the mode amplitude and phase, respectively. Therefore, the frequency comb is developed once the following condition is satisfied:

$$\Psi_n(t) = (f_0 + n f_r)t + \phi_n \quad (5.5)$$

with ϕ_n the phase of each longitudinal mode. Then, the pulse duration Δt that is inversely proportional to the gain bandwidth Δf can be described by the time-bandwidth product (TBP) such as:

$$TBP = \Delta t \Delta f \quad (5.6)$$

where Δt and Δf account for the full-width at half-maximum (FWHM) of the optical pulse and the optical bandwidth, respectively. The TBP is a parameter that includes the contribution of chirp caused from the α_H -factor. Depending on the pulse shape, the TBP has different expressions such as (T. L. Koch and John E Bowers, 1984; Lazaridis, Debarge, and Gallion, 1995):

$$\Delta t \Delta f = \begin{cases} \frac{2 \ln 2}{\pi} \sqrt{1 + \alpha_H^2} & \text{(Gaussian-shape pulse)} \\ \left(\frac{2 \operatorname{arcosh}(\sqrt{2})}{\pi^2} \right) \operatorname{arcosh}[\cosh(\pi \alpha_H) + 2] & \text{(Sech}^2\text{-shape pulse)} \end{cases} \quad (5.7)$$

Consequently, a low α_H -factor is beneficial for decreasing the TBP thus reducing the pulse width. Taking advantage of the near-zero α_H of QD, high-performance OFC with ultrafast optical pulses on the order of 100 fs have been developed (Rafailov, Cataluna, and Sibbett, 2007; Liu, Jung, et al., 2018).

5.2 Frequency comb technologies

The generation of frequency comb relies on a combination of laser physics, including the ultrafast optical pulse generation, nonlinear optics, and electro-optics. For different potential applications of frequency combs, the controlling of the comb spacing, the stability of pulse energy and the timing jitter are necessary. In this section, some of the most common techniques for generating OFC and extending their spectral bandwidth are performed.

Mode-locked laser frequency combs

Soon after the first demonstration of the laser in 1960, studies on the mode-locked lasers have begun (Hargrove, Richard L Fork, and Pollack, 1964). In the early 1980s, the mode-locking technique was able to generate femtosecond time-scale optical pulses (R. Fork, Greene, and Charles V Shank, 1981). Those laser sources

that were utilized for the measurements of ultrafast dynamics in material system paved the way for developing high-bandwidth frequency combs. To realize mode-locking, both active and passive approaches can be applied. In the former case, mode-locking is achieved by adding an externally driven intra-cavity loss modulator with the modulation frequency fixed to f_r , as depicted in Fig. 5.3(a). In this case, the modulator acts like a periodic shutter which opens once per pulse round-trip time in the laser cavity. As a consequence, the initial laser emission is shortened every time it passes through the modulator, however, it has a lower limit due to the per-pass pulse-broadening mechanisms. In addition, the mode spacing of the laser is directly determined by the modulation frequency that is matched precisely to the cavity mode spacing, thus the active mode-locking technique can be utilized for harmonic mode-locking generation. Nevertheless, the drawbacks of active mode-locking limit its further applications. First, the need of an externally driven modulator makes the laser system of high complexity. Second, it becomes ineffective for generating very short pulses due to the modulator. In this context, passive mode-locking soon becomes a promising approach which has been widely used in mode-locked lasers. In a passively mode-locked laser, the externally driven modulator is replaced by a nonlinear optical element whose loss depends on the laser pulse intensity. To realize mode-locking, the loss decreases with the increase of pulse intensity in presence of the loss modulation being synchronized automatically with the laser pulses. Figure 5.3(b) shows a sketch of a passively mode-locked laser whose nonlinear optical element is the commonly used saturable absorber (SA). In contrast to the actively mode-locked device, the pulse-shortening action in the passively mode-locked laser remains effective even for very short pulses if the response time of the SA is sufficiently fast. At the steady-state, the circulating short pulse maintains its shape indefinitely through a balance between nonlinearity and dispersion. As a consequence, the generated pulse train with identical envelop results in a perfectly regular comb dynamics.

The well-established mode-locked lasers using Ti:sapphire and erbium-doped fibre have proven to be reliable approaches for frequency comb generation (Spence, Kean, and Sibbett, 1991; Droste et al., 2016). Typical Ti:sapphire lasers oscillate with a gain peak around 800 nm. A short pulse duration below 100 fs allows for generating a Fourier-limited spectral bandwidth over 5 THz. On the other hand, the mode-locked lasers using the erbium-doped fibre as their gain medium have been the most widespread and mature frequency comb technology owing to their ability to emit in the 1.55 μm range, which are highly desired for the fibre-optic communication. In

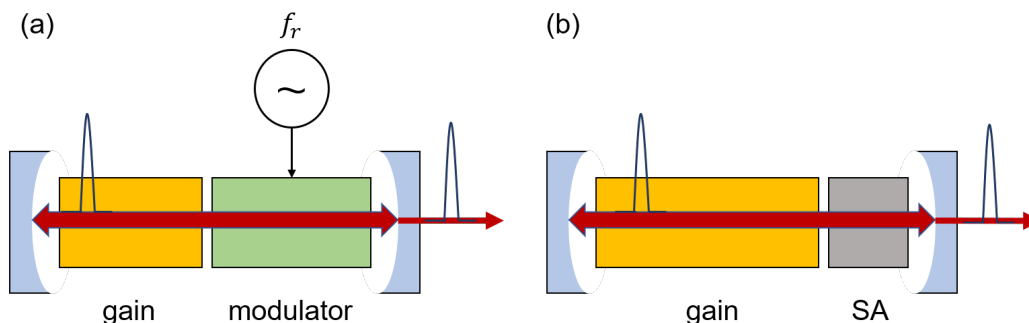


Figure 5.3: Sketch for (a) active mode-locking, with an intra-cavity modulator driven at the repetition rate; and (b) passive mode-locking, with the repetition rate determined by the laser cavity length. SA, saturable absorber.

particular, the fibre based comb system is a robust solution for generating octave-span spectra by taking advantage of the polarization-maintaining highly nonlinear fibre (PM-HNLF) technique (Sinclair et al., 2015). Lasers using Yb-, Tm-, Ho-, or Er fluoride-doped fibre as well as nonlinear optical processes have expanded the frequency comb spectra from extreme ultraviolet (XUV) to mid-infrared (MIR) spectral range (Cingöz et al., 2012; Schliesser, Picqué, and Hänsch, 2012; Fermann and Hartl, 2013).

Despite the high-performance of Ti:sapphire and fibre lasers, they tend to be rather bulky and inefficient. Semiconductor laser is then regarded as a promising option, which provides a solution of compactness and integrability along with direct electrical control. The mode-locked laser diodes that are based on bulk or QW have shown picosecond and high-repetition-rate optical pulses generation in the near-infrared spectral range (E. Avrutin, Marsh, and Portnoi, 2000). In this context, the QD exhibits a strong potential to serve as the gain and the absorption medium for a mode-locked laser to generate ultrashort optical pulses on the order of 100 fs, by taking advantage of its ultra-broad bandwidth and ultrafast carrier dynamics (Rafailov, Cataluna, and Sibbett, 2007; ZG Lu, JR Liu, Raymond, et al., 2008).

Electro-optic frequency combs

Generation of a frequency comb can also be realized by employing an electro-optic (EO) modulator inside an optical resonator and driving it with a microwave signal that matches the optical resonator mode spacing (Motonobu Kourogi, Ken'ichi Nakagawa, and Motoichi Ohtsu, 1993). Different from the active mode-locking approach, the EO frequency comb relies on an input continuous-wave (CW) single-frequency

laser rather than an intra-cavity gain medium. In addition, the EO modulation technique allows for independent electrical tuning of the repetition rate and the central frequency. A sketch of the EO modulation approach for frequency comb generation is shown in Fig. 5.4. To modulate the input CW laser, the RF optical phase is applied to be $\pi V/V_\pi \cos(2\pi f_r t)$ with f_r the repetition frequency and V the voltage amplitude of the driving RF signal. The half-wave voltage V_π is a constant that determines the amount of RF power required to make a phase change of π . V_π is dependent on the EO coefficient of the material and the waveguide structure, and its magnitude generally increases with the RF frequency. In the case of lithium niobate EO modulator, the value of V_π ranges from ~ 2 V to 11 V at 10 GHz. As a result, the generated sidebands are resonantly amplified and further generate sidebands themselves. To enlarge the optical bandwidth of the output frequency comb, the modulation index which is expressed as $\Delta\theta = \pi V/v_\pi$ must be maximized. Therefore, an EO modulator with a low V_π along with a strong tolerance for RF power is beneficial for enhancing the comb dynamics. It is worth stressing that an optimized configuration that includes several phase modulators in tandem is an efficient approach to further increase the comb bandwidth (Torres-Company and Weiner, 2014). However, the temporal phases need to be well aligned in time by utilizing phase shifters, and the effective modulation index should be increased by a factor of N that is the number of modulators. Besides, the microwave phase noise is largely increased due to the multiplicative nature of this configuration. To minimize the consequent phase noise and maintain the comb dynamics, it is promising to utilize an optical cavity filter or nanophotonic silicon nitride waveguides (Beha et al., 2017; Carlson et al., 2018). On the other hand, the comb line spacing of an EO modulated laser is determined by the modulation frequency and it is limited to the bandwidth of the modulator. The bandwidth of a commercially available lithium niobate modulator is about 40 GHz. However, it can be considered to broaden the bandwidth of EO modulators approaching 100 GHz by optimizing the waveguide design in lithium niobate (Macario et al., 2012) or by taking advantages of the ultrafast Pockels effect offered by the silicon–organic hybrid (SOH) platform (Alloatti et al., 2014). To broaden the frequency comb bandwidth, a recent study reveals that the EO-modulated frequency comb can also serve as the master source for injection locking a single-frequency vertical cavity surface-emitting laser (VCSEL) (Doubria et al., 2021).

Despite the simplicity, some disadvantages of the coupled-cavity monolithic EO frequency comb generators restrict their further applications. First, in the case of FP resonator configuration, a high degree of matching between the modulation fre-

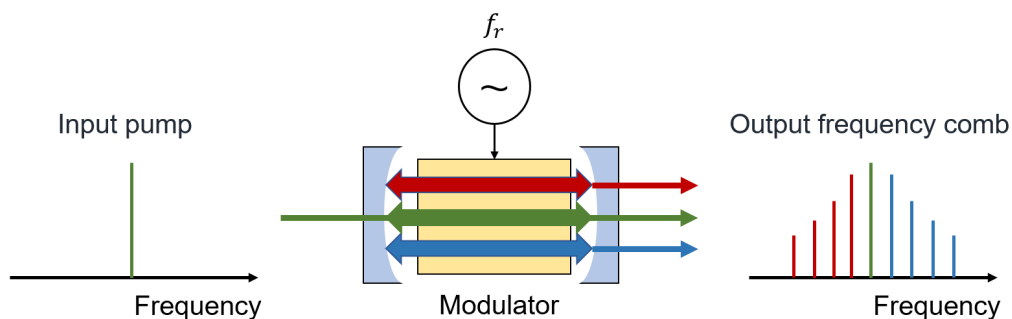


Figure 5.4: Sketch for electro-optic modulated frequency comb, with the repetition rate determined by the modulation frequency.

quency and the mode spacing of the resonator must be ensured. Second, the input CW laser must be precisely tuned to one of the optical resonance to trigger the comb dynamics. As a consequence, the operating stability and the flatness of the comb spectrum are not satisfying. To overcome these issues, approaches such as employing several EO amplitude and/or phase modulators in tandem (Torres-Company and Weiner, 2014), utilizing highly nonlinear fibres with normal dispersion profile (C.-B. Huang, Park, et al., 2008), and exploiting the four-wave mixing effect by using a nonlinear medium (Supradeepa and Weiner, 2012) have been developed. Nevertheless, the consequent complexity of the whole system remains to be addressed.

Microresonator frequency combs

Frequency comb can also be produced from a CW single-frequency laser through a third-order optical susceptibility $\chi^{(3)}$ assisted microresonator. This kind of frequency comb generator, which is also named as microcomb, is based on the Kerr nonlinearity at milliwatt power levels through the resonant enhancement of light in a whispering-gallery microresonator or in a microring resonator. The microcomb exhibits a strong potential for commercialization, owing to its prospect of integrability on a semiconductor chip. Figure 5.5 depicts a sketch of the frequency comb generation in a microring resonator. The principle of a microcomb is to confine the light by total internal reflection around the perimeter of an air-dielectric interface. Therefore, a low-loss resonator in presence of a high quality factor (Q-factor) is beneficial for improving the pump efficiency. An achievable Q-factor ranging from 10^6 to 10^{11} leads to extremely low thresholds for nonlinear optical effects, i.e., sub micro-watt power level. On the other hand, the microresonator modes are determined by a multiple of the frequency of its perimeter. In the case of resonators

made from a third-order nonlinearity $\chi^{(3)}$ material, the CW pump photons (green) propagating in it are annihilated by a number of two and create a new pair of photons: a frequency upshifted signal (blue) and a frequency downshifted idler (red). The generated photon pairs have frequencies that are equally spaced with respect to the pump. It is worth stressing that the efficiency of sidebands generation attains its maximum if the signal and idler frequencies coincide with the microresonator modes; the high Q microresonator is also necessary for reducing the optical cavity decay rates and realizing the frequency conversion. In what follows, the parametric oscillations including both the degenerate and the nondegenerate four-wave mixing (FWM) process results in the frequency comb behavior in presence of multiple sidebands. In the case of degenerate FWM, only one pump source is required which has been explained by the process described above. However, the occurrence of nondegenerate FWM relies on two pump sources, which is what happens when the generated signal and idler sidebands themselves serve as seeds for further parametric frequency conversions. It is worth stressing that the cavity dispersion which changes the free spectral range (FSR) with wavelength decreases the efficiency for the nondegenerate FWM that occurs at the modes far from the central frequency. In other word, the generated comb bandwidth is limited by the cavity dispersion. Approaches such as the lithographic control (Brasch et al., 2016; Pfeiffer et al., 2017) or taking advantage of other materials including aluminum nitride (Z. Gong et al., 2018), lithium niobate (Y. He et al., 2019) and III-V semiconductors (L. Chang et al., 2020; Xiang et al., 2021) can be considered to improve the optical bandwidth thus realizing octave-span frequency combs.

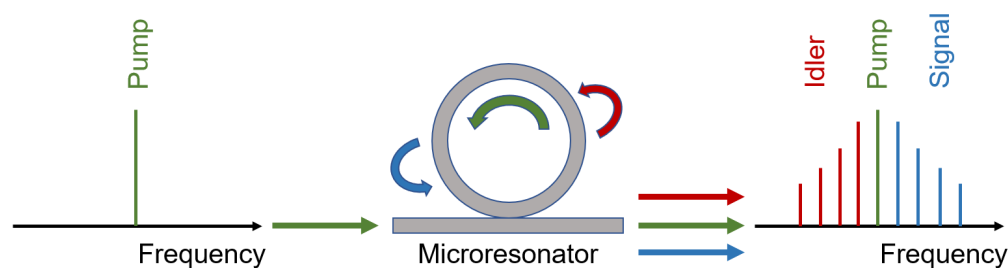


Figure 5.5: Sketch for microresonator frequency comb. The dielectric resonator made of a $\chi^{(3)}$ nonlinear material is pumped by a single-frequency CW laser. Signal and idler sidebands are generated by a parametric frequency conversion through both degenerate and nondegenerate FWM.

Despite the tremendous progress in microcomb system including their applications

in optical frequency synthesis (Spencer et al., 2018) and optical atomic clocks (Newman et al., 2019), their monolithic integration on a PIC remains complicated. At present, it is still a challenge to integrate some components such as the lasers, the amplifiers and other optical fibre components on a single semiconductor chip.

5.3 Applications of optical frequency combs

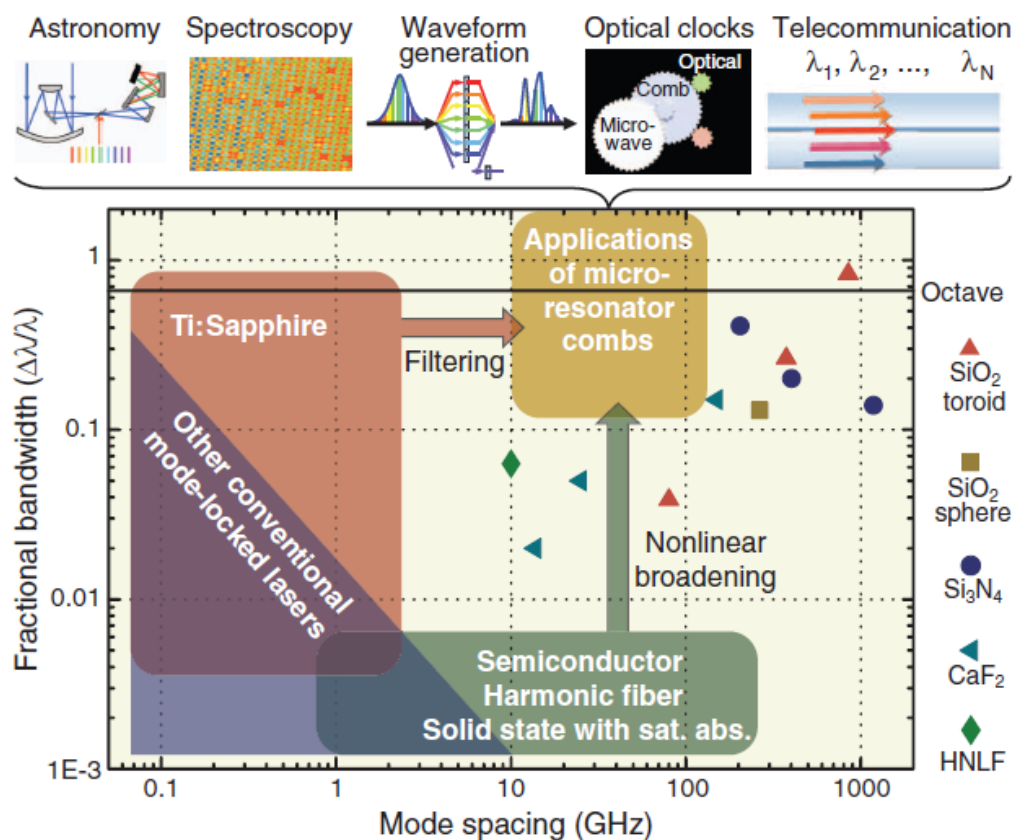


Figure 5.6: Optical frequency comb technologies as a function of their mode spacing and fractional bandwidth. The frequency combs with high-repetition-rate and large-bandwidth (gold regime) is required for a variety of applications including astrophysical spectrometer calibration, telecommunications, optical arbitrary waveform generation, and spectroscopy. The stars represent the cases of microresonator-based frequency combs made from different materials. From Ref. (Kippenberg, Holzwarth, and Diddams, 2011).

To evaluate the performance of an optical frequency comb, its repetition rate and optical bandwidth should be analyzed. Figure 5.6 gives a complete picture of the achievable comb line spacing and the fractional optical bandwidth from different frequency comb technologies. The fractional optical bandwidth is defined as $\Delta\lambda/\lambda$ with $\Delta\lambda$ the spectral bandwidth and λ the optical wavelength. The condition for

octave-spanning is represented by the vertical black line around $\Delta\lambda/\lambda = 0.7$. For the OFC generated by the mode-locking technique, it is a challenge to realize a high repetition rate beyond 10 GHz along with an ultra-broad optical bandwidth approaching the condition for octave-spanning. In contrary, the microresonator-based OFC made from different materials exhibit a superior performance in presence of both a large mode spacing and an octave-span bandwidth. These remarkable features pave the way for developing high-performance comb source for a number of applications including astronomical spectrograph calibration (C.-H. Li et al., 2008; Suh, Yi, et al., 2019), frequency comb spectroscopy (Diddams, Leo Hollberg, and Mbele, 2007), optical and microwave waveform synthesis (C.-B. Huang, Z. Jiang, et al., 2008; Spencer et al., 2018), optical atomic clocks (Newman et al., 2019), LIDAR (Trocha et al., 2018), dual-comb spectroscopy (Suh, Q.-F. Yang, et al., 2016), and high-speed coherent telecommunication (Marin-Palomo et al., 2017; Songtao Liu, X. Wu, et al., 2019). Despite these advantages, it is still a challenge to reduce the mode spacing to the range of 10 to 100 GHz while maintaining a large fractional bandwidth beyond 10% in a microresonator-based OFC. To reduce the FSR of the resonant cavity, it is obligatory to increase the size of microresonator. Nevertheless, a simultaneously increase of the Q factor is necessary to attain the same level of resonant power enhancement, given that the optical finesse is defined as the FSR divided by the width of the resonance (Kippenberg, Holzwarth, and Diddams, 2011).

Optical frequency combs were originally developed to solve the problem of measuring and counting optical frequencies, which was once a challenge to be realized by radio frequencies. However, the applications of OFC have expanded beyond their initial prospects after several decades of development. While EO modulated comb and microresonator-based comb are pushing the limit of high repetition rate and broad gain bandwidth, the conventional mode-locked comb is the most robust and widely used technology. In particular, semiconductor mode-locked laser is still a promising solution for low-cost photonic integration, owing to its small-footprint, energy-efficiency and availability for mature CMOS platform.

5.4 Towards an optical frequency comb for silicon photonic integrated circuits

Semiconductor QDs are known from their high tolerance for the defects that arise during the epitaxial growth of III-V material on Si, which have been regarded as the first option to be the source for a silicon PIC. Meanwhile, their outstanding properties including the ultrafast carrier dynamics, the ultra-broad bandwidth and

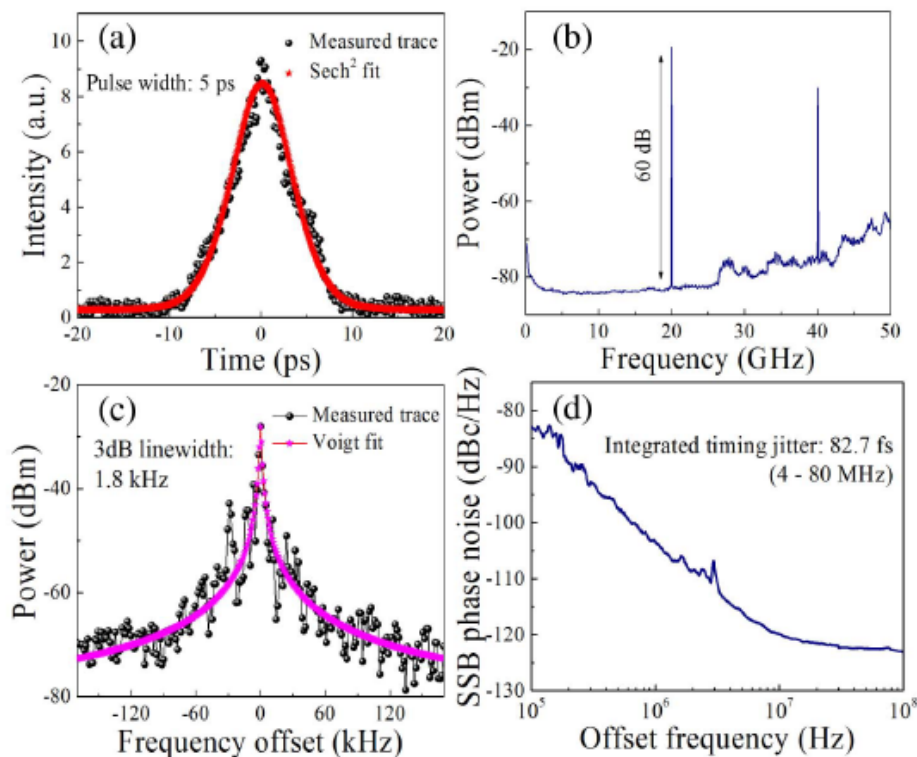


Figure 5.7: Characterizations of an epitaxial QD-MLL on Si: (a) autocorrelation traced pulse duration; (b) RF spectrum in a span of 50 GHz; (c) narrow span RF linewidth of the repetition frequency; (d) single-sideband phase noise plot in the narrowest pulse width condition. From Ref. (Songtao Liu, X. Wu, et al., 2019).

the near-zero α_H -factor exhibit a strong potential to serve as the gain and absorption medium for an OFC. In particular, the low-noise QD-based frequency comb lasers allow us to utilize their comb lines independently for coherent applications. In contrary, the large RF linewidth on the order of megahertz in QW devices prevents them from those applications (Philip J Poole et al., 2021). In this context, the QD-based frequency comb is a promising solution for low-cost, energy-efficient and large-scale silicon PICs. Recently, Songtao Liu, X. Wu, et al., 2019 reported a high-performance epitaxial QD mode-locked laser (QD-MLL) on Si with 4.1 Tbits/s transmission capacity. Benefiting from the chirped QDs whose inhomogeneous broadening is improved, the QD-MLL exhibits a 6.1 nm-wide 3-dB bandwidth in which 58 comb lines are identified. On the other hand, the device reported demonstrates a remarkable temporal performance. Figures 5.7 display the static characterizations of the QD-MLL including its pulse width and noise properties. The narrowest pulse duration of the device reported is 5 ps, which remains to be

reduced since it is still one order of magnitude larger than that of its counterparts grown on native substrate (ZG Lu, JR Liu, Raymond, et al., 2008). However, the QD-MLL on Si exhibits a remarkable performance in terms of both intensity and phase noise. While ensuring a high signal-to-noise ratio (SNR) over 60 dB for the fundamental repetition frequency, the 3-dB linewidth is as low as 1.8 kHz, which is comparable to the state-of-the-art high-speed semiconductor mode-locked lasers (Carpintero et al., 2009; Zhenguo Lu et al., 2021). In particular, its timing jitter being 82.7 fs from 4 to 80 MHz of the ITU-T specified range is a record value that is lower than the timing jitter in any passively mode-locked semiconductor laser.

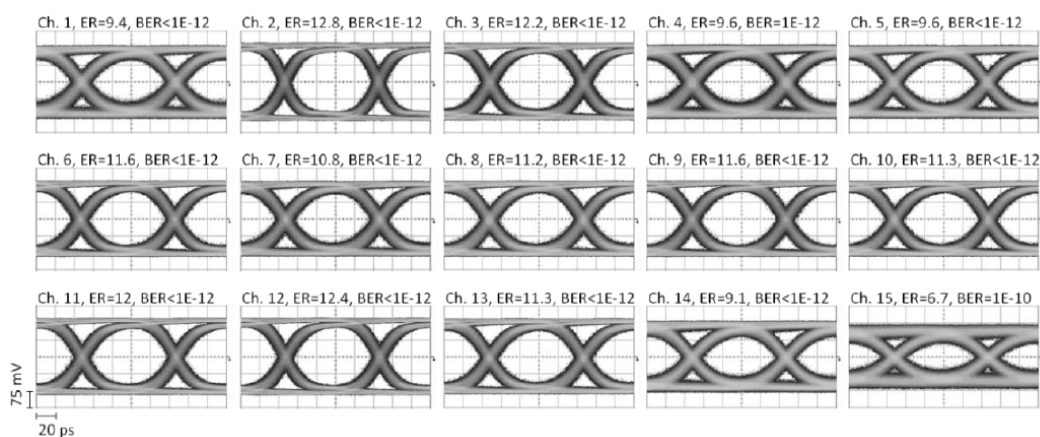


Figure 5.8: Transmission characterizations of a QD-based comb laser on Si: eye diagrams of its 15 channels with corresponding extinction ratio (ER) and bit-error-rate (BER) values. Each channel is modulated by an external optical modulator with 10 Gbit/s pseudo-random bit sequence. From Ref. (Kurczveil, C. Zhang, et al., 2018).

According to the ITU-T G.694.1 standard, an optical frequency comb with a large mode spacing over 100 GHz is highly desired to meet the requirements of DWDM applications. Given that it is a challenge to reduce the cavity length of a mode-locked laser to a few hundred micrometer, taking advantage of the harmonic mode-locking technique is a promising approach. A recent work from the Hewlett Packard Labs, Palo Alto, USA demonstrates a QD-based frequency comb laser wafer bonded to Si substrate whose mode spacing is 102 GHz (Kurczveil, C. Zhang, et al., 2018). Based on the 6th harmonic mode-locking, the device reported exhibits a 3-dB bandwidth over 8 nm in which 15 comb lines are identified. Figures 5.8 display the eye diagrams of each channel that is modulated by an external 10 Gbit/s pseudo-random bit sequence (PRBS) signal. All these comb channel show high

transmission performance with the extinction ratio (ER) higher than 9.6 and the bit-error-rate (BER) lower than 10^{-12} .

These remarkable performances reveal that the QD is an ideal solution for on-chip comb sources either wafer bonded or directly grown on Si wafer. To further improve the performance of QD-based frequency combs in terms of phase noise and optical bandwidth, both investigations on theoretical analysis and experiments will be discussed in the following sections.

5.5 Delay-differential equation model

To analyze the QD-based frequency comb lasers that are based on mode-locking technique, a delay-differential equation (DDE) model is introduced. First proposed by Vladimirov and Turaev, 2005, the DDE model is an excellent theoretical tool to analyze the dynamics of MLLs. In particular, this model is a much easier analytical tool than the traveling wave equations (TWE) owing to its reduced demand for computational power and its ability to study the case of a slow SA (Rossetti, Paolo Bardella, and Montrosset, 2011). The DDE model was first derived for a passively ring cavity MLL, and it has been extended to analyze two-section passively MLLs (Vladimirov, Bandelow, et al., 2010; Rossetti, Xu, et al., 2011), hybrid MLLs (Fiol et al., 2010), and MLLs that have complicated nonlinear process such as external optical injection (Rebrova et al., 2011) and external optical feedback (Otto et al., 2012). In the simulation, the two-section passively MLL is assumed to have a linear Fabry-Perot cavity, in which an actively pumped gain section and a SA section are included. Three coupled DDEs to describe the slowly varying field amplitude ε , the dimensionless saturable gain G and loss Q in the gain section and SA section, respectively, are expressed as follows:

$$\begin{aligned} \gamma^{-1}\dot{\varepsilon}(t) + \varepsilon(t) &= \sqrt{\kappa} \exp\left[\frac{1}{2}\{(1 - i\alpha_g)G(t - T) \right. \\ &\quad \left. - (1 - i\alpha_q)Q(t - T)\}\right] \varepsilon(t - T) \end{aligned} \quad (5.8)$$

$$\dot{G}(t) = J_g - \gamma_g G(t) - e^{-Q(t)} (e^{G(t)} - 1) |\varepsilon(t)|^2 \quad (5.9)$$

$$\dot{Q}(t) = J_q - \gamma_q Q(t) - r_s e^{-Q(t)} (e^{Q(t)} - 1) |\varepsilon(t)|^2 \quad (5.10)$$

where γ is the finite width of the gain spectrum that is Lorentzian-shaped. As aforementioned, the pulse width is roughly inversely proportional to the γ . κ denotes the linear cavity losses. The α_H -factor of the gain section and the absorber

section are denoted by α_g and α_q , respectively. The round trip time T of the MLL is the inverse of the repetition frequency f_r through the relationship $T = 1/f_r$. In Eqs. (5.9) and (5.10) that describe the carrier dynamics, the J_g and J_q account for the unsaturated pump rate and absorption in the gain and SA section, respectively. The carrier decay rate in the gain and SA section are denoted by the γ_g and γ_q , respectively. Finally, the r_s is the ratio of the saturation energies in the gain and SA sections.

In what follows, the saturable G and Q as well as the κ can be also expressed by measurable dimensionless parameters (Raghunathan et al., 2012):

$$G = (g_{mod}(J) - \alpha_i)(1 - r_{SA})L_c \quad (5.11)$$

$$Q = (a_0 + \alpha_i)r_{SA}L_c \quad (5.12)$$

$$\kappa = \sqrt{R_1 R_2} \quad (5.13)$$

where the $g_{mod}(J)$ is the pump current dependent modal gain, the α_i is the cavity internal loss coefficient, and a_0 is the unsaturated absorption coefficient of the SA section. The ratio of the SA section length to the cavity length is represented by r_{SA} . The R_1 and R_2 account for the power reflectivities of the front and rear facet, respectively. Then, the unsaturated J_g and J_q are derived from the G and Q through the following relationship (Raghunathan et al., 2012):

$$J_g = \frac{(\gamma_g/\gamma_q)G}{\eta_g T} \quad (5.14)$$

$$J_q = \frac{Q}{r_s \eta_q T} \quad (5.15)$$

with η_g and η_q the pump and absorption efficiency in the gain and SA section, respectively.

It is worth stressing that the model described in this paper excludes the configuration of laser cavity such as the tapered gain section. In contrast to the models that are based on frequency-domain approach (Kreuter, Witzigmann, and Fichtner, 2011; Weng W Chow, Songtao Liu, et al., 2020), the time-domain based model described in this dissertation does not account for the gain dispersion that occurs at the longitudinal modes far way from the optical gain peak (G. P. Agrawal, 1991). Nevertheless, the DDE model that includes the α_H -factor gives insights for extending its functionality to describe the frequency-domain mechanisms, given that the α_H -factor is a spectrally distributed parameter that includes the gain dispersion (Duan,

Huang, Jung, et al., 2018). In addition, its improved simplicity and computational efficiency compared to the TWE model is beneficial for developing a high-efficient design tool for passively mode-locking dynamics.

In this study, the influence of external optical feedback (EOF) on the mode-locking dynamics is investigated. To analyze the effect of EOF operation, the equivalent facet reflectivity described in Eq. (3.3) is further reshaped to the power reflectivity R_{re} such as:

$$R_{re} = R_1 \left(1 + \frac{2(1 - R_1)}{\sqrt{R_1}} \sqrt{\eta_F} \cos(\omega\tau_{ext}) \right) \quad (5.16)$$

Let us recall that Eq. (5.16) is only valid for the weak feedback conditions. Therefore, the effect of EOF would be represented by the equivalent facet reflectivity thus the quality factor of the laser cavity. Based on this static approach, Eq. (5.13) is re-expressed as:

$$\kappa = \sqrt{R_{re} R_2} \quad (5.17)$$

In the following sections, the calculated results are performed by both time-domain pulse train and corresponding radio-frequency (RF) spectra on the linear scale. The latter is calculated by integrating the steady-state temporal traces over 5 ns (≈ 100 round-trips). Given that the amplitude and the phase noise of the power spectral density (PSD) is not included in our model (Otto et al., 2012), the intensity of the fundamental repetition frequency f_r would be used to reflect the level of phase noise and timing jitter. The effect of phase noise remains to be investigated in further work.

5.6 QD-OFC studied

Passively mode-locked QD lasers

The 1.3- μm passively mode-locked laser (MLL) is fabricated within the group of Prof. John Bowers at University of California, Santa Barbara, USA. Different from the FP lasers, an extra SA section that is isolated from the gain section is required for passively mode-locking. Figure 5.9(a) depicts a sketch of the device studied while (b) displays its epi-structure. The growth techniques for the active region of the QD-MLL are similar with those for the aforementioned FP devices, except for the QDs that are chirped. The chirped QDs, which means the height of each QD layer is slightly changed, is an approach to broaden the bandwidth of the gain spectrum while maintaining a flat gain profile (K. C. Kim et al., 2010). The p-doped active region is sandwiched by an upper and lower unintentionally doped (UID) 50 nm GaAs waveguide, above which a 1400 nm p-type AlGaAs layer and a 300 nm p-type

top contact layer are clad. Then, the whole structure is grown on a 1400 nm n-type AlGaAs layer which follows a 1000 nm n-type bottom contact layer. The GaAs buffer is finally grown on a GaP/Si template ultimately achieving a low threading dislocation density (TDD) value of $7 \times 10^6 \text{ cm}^{-2}$.

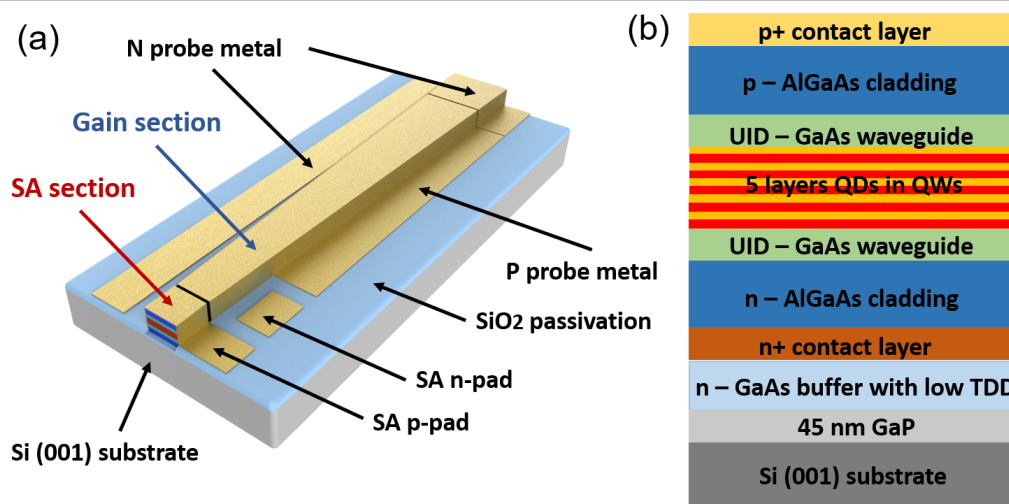


Figure 5.9: Sketch of (a) the QD-MLL on Si (not to scale). (b) Corresponding epitaxial structure of the device. SA, saturable absorber.

A $2048 \mu\text{m}$ -long cavity gives the laser a fundamental repetition rate of $\approx 20 \text{ GHz}$. To study the impact of the SA section length on the mode-locking dynamics, two devices with the same total cavity length but different SA section length are investigated in this thesis. The first one whose SA length to cavity length ratio r_{SA} is 8% holds a $5 \mu\text{m}$ -wide straight gain section, whereas the other one with a r_{SA} of 5% has a trapezoidal gain section whose width ranges from 3 to $6 \mu\text{m}$. The SA section is placed at the front facet of the cavity, a $10 \mu\text{m}$ -long isolation length to the gain section gives an isolation resistance around $15 \text{ k}\Omega$. For the latter device, the tapered gain section is designed to improve the mode-locking performance in terms of pulse width and output power (C. Weber et al., 2015; Bardella et al., 2018). For both lasers, the power reflectivities of the front and rear facet are coated at 32% and 95%, respectively.

A reverse bias voltage on the SA is required for passively mode-locking. Figures 5.10 depict the SA reverse voltage dependent light-current characteristics as well as the optical spectra of the device whose r_{SA} is 8% [(a) and (c)] and 5% [(b) and (d)]. Experiments are performed at 20°C while the optical spectra are measure at $2 \times I_{th}$. For all SA bias, the increase of r_{SA} from 5% to 8% result in an increase of

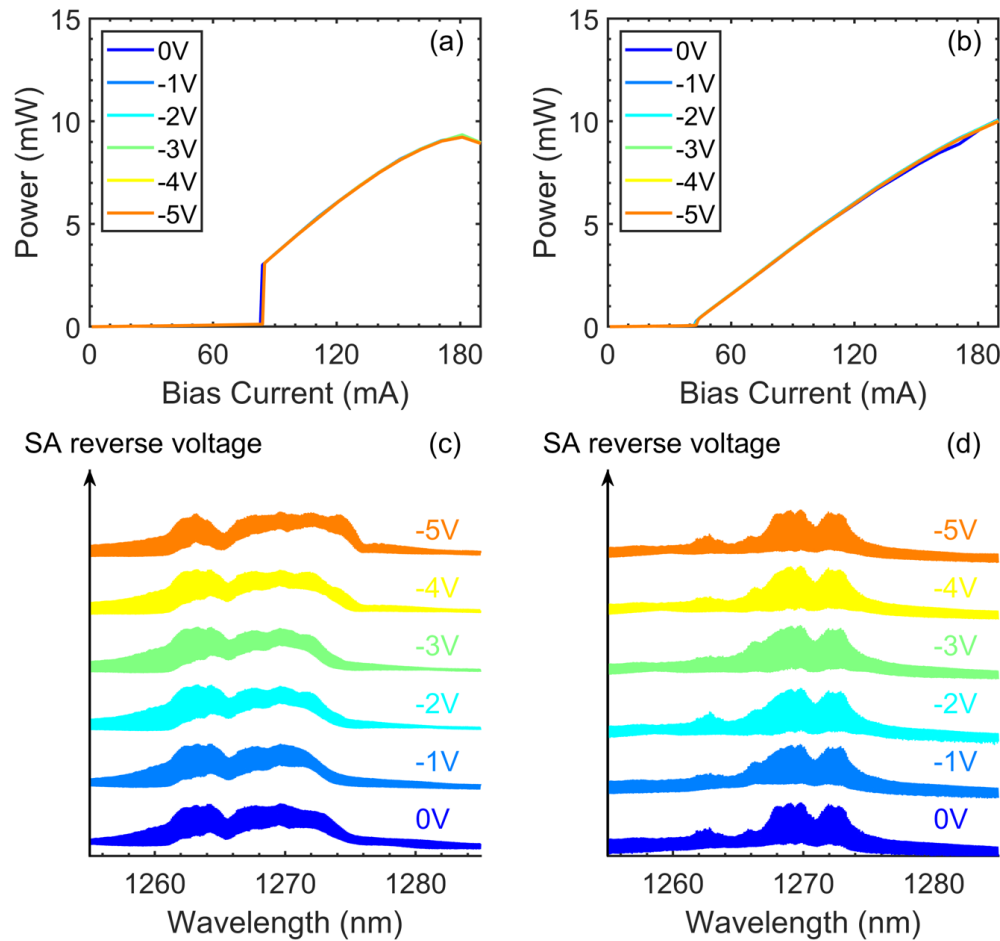


Figure 5.10: SA reverse bias dependent light-current characteristics and optical spectra measured at $2 \times I_{th}$ for the QD-MLL whose SA length ratio is 8% [(a) and (c)] and 5% [(b) and (d)] at 20°C .

I_{th} from 43 to 85 mA. Such a phenomena is attributed to the higher internal loss induced by the longer SA section, whose presence also limits the output power of laser. In particular, the step-like sudden power rise at threshold of the device with r_{SA} at 8% results from the nonlinear saturation effect within the SA section when the intra-cavity power increases with the forward biased current, which leads to an overall cavity loss decrease (Songtao Liu, J. C. Norman, et al., 2018; Songtao Liu, X. Wu, et al., 2019). In addition, both the threshold current and the output power of these devices remain at the same level with the increase of the SA reverse bias from 0 to -5 V, meaning that the total internal loss of the cavity is barely changed by the bias voltage. This unusual phenomena is attributed to the short SA section that restricts the absorption efficiency. In general, the internal loss exhibits a clear dependence of the SA reverse bias when the r_{SA} is beyond 10% (Rossetti, Xu, et al.,

2011; Songtao Liu, J. C. Norman, et al., 2018). It is worth stressing that the mode-locking effect is strengthened by utilizing a relatively long SA section (C.-Y. Lin, Xin, et al., 2009). From the optical spectra, the device with r_{SA} at 8% exhibits a clear flat-top behavior and a broad 3-dB bandwidth over 10 nm. For the other one with r_{SA} at 5%, its optical frequency behavior is rather like continuous-wave, meaning that its mode-locking efficiency is much lower than that of the former one. With the increase of SA reverse voltage from 0 to -5 V, the optical bandwidth of both devices is slightly improved. The different behavior in the optical frequency domain could be attributed to the variation of α_H -factor due to the SA bias, which will be introduced in Sec. 5.7. Last but not least, both lasers exhibit spiky-like emission spectra due to the multiple physics of QDs as well as their nonuniformity caused by the chirped structure.

Multi-section frequency comb QD laser

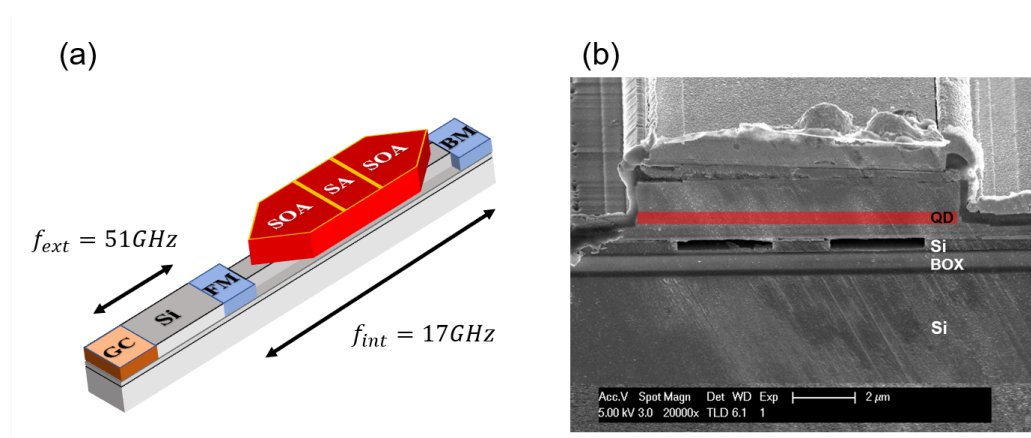


Figure 5.11: (a) Sketch of the hybrid-silicon QD comb laser. SOA, semiconductor optical amplifier; SA, saturable absorber; FM, front mirror; BM, back mirror; GC, grating coupler. (b) SEM image of the cross section of the device.

The 1.3- μm hybrid-silicon optical frequency comb (OFC) laser is fabricated within the Hewlett Packard Labs, Palo Alto, USA. Figure 5.11(a) depicts a sketch of the device studied. Its 2.3-mm-long internal cavity gives a 17 GHz free spectral range (FSR) in the frequency domain, in which a 120- μm -long SA at the center along with two 1200- μm -long semiconductor optical amplifier (SOA) placed at each side are embedded. The active region is made of a commercial GaAs-based QD-containing epi stack that is wafer bonded to a silicon-on-insulator (SOI) wafer. A SEM image of the cross section of the active region is shown in Fig. 5.11(b). The front and rear facets of the internal cavity are connected to a front mirror (FM) and a back mirror

(BM) whose power reflectivities are $\sim 50\%$ and $\sim 100\%$, respectively. Outside the FM, a 0.75-mm-long (51 GHz) external cavity is utilized to further enlarge the FSR to 102 GHz, owing to the vernier effect. First, the SA that is placed at the center is able to operate the laser as a colliding MLL and to increase the FSR from 17 GHz to 34 GHz. Second, the 51 GHz external cavity can further increase the FSR to the 6th harmonic of the intrinsic FSR through the fractional resonant optical feedback, as introduced by Eugene A Avrutin and Russell, 2009. Nevertheless, in the latter case, a strong enough reflectance is necessary to trigger the harmonic mode-locking dynamics. To this end, the power reflection of the grating coupler (GS) that is placed outside the external cavity is coated at $\sim 10\%$, while the remaining power is coupled out for further analysis. To trigger the frequency comb dynamics, a reverse bias on the SA section V_{SA} should be applied, which is similar as what happens in a MLL. A mode converter (not shown in the sketch) between the active hybrid waveguide and the passive Si waveguide is used to transfer the laser emission across those waveguides. More detailed device fabrication process information are available in Refs. (Kurczveil, Seyedi, et al., 2017; Kurczveil, C. Zhang, et al., 2018). It is worth stressing that the range of currents in which the stable harmonic mode-locking operation takes place is relatively narrow (Eugene A Avrutin and Russell, 2009). When the gain current I_{gain} is out of its optimum operating conditions, unstable self-pulsation occurs thus the device exhibits a CW-like emission rather than a pulsating mode-locking behavior. Besides, the high-loss external cavity as well as the grating coupler result in a low output power (i.e. below $50 \mu W$), which prevents us to observe any dynamics in both the time- and the radio-frequency domain.

Figure 5.12(a) depicts a mapping of the coupled power of the device studied in different SA and SOA bias conditions. The threshold current I_{th} that is marked by the white dashed line slightly increases from 32 to 38 mA as the reverse voltage increases from 0 V to -6 V. This effect is attributed to the increased internal loss at a high SA reverse bias, which results from the change of refractive index thus the mode shifting due to the SA bias. In contrast to the QD-MLL described hereinabove, both the gain current and the SA reverse bias largely affect the lasing behaviors. Figure 5.12(c) and (d) display the optical spectrum of the QD-OFC with the gain current biased at $3 \times I_{th}$ and $5 \times I_{th}$, respectively, while fixing the SA voltage at -6 V. Due to the thermal effect, the increase of bias current leads to a red-shift of the central comb wavelength from 1305 to 1312 nm. Meanwhile, both the bandwidth and the flatness of the comb spectrum are improved with the increase of gain current owing to the homogeneous broadening of QDs. At $3 \times I_{th}$, there are 12 lines above the noise

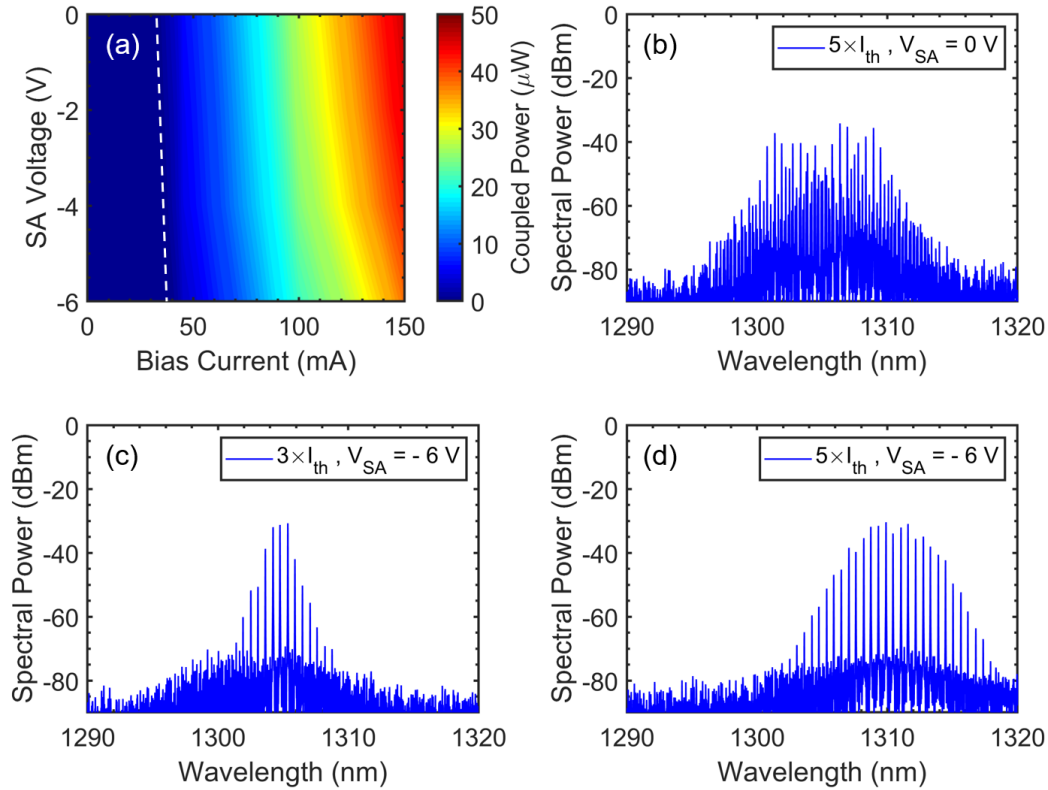


Figure 5.12: (a) Mapping of the coupled power of the QD-OFC in different bias conditions on the SA and on the SOAs. The evolution of the threshold current with the SA reverse voltage is marked by the white dashed line. Optical spectra measured with $(I_{gain}, V_{SA}) =$ (b) $(5 \times I_{th}, 0 \text{ V})$, (c) $(3 \times I_{th}, -6 \text{ V})$, (d) $(5 \times I_{th}, -6 \text{ V})$

floor and 3 lines within 3 dB bandwidth, however, the value for those parameters increases to 26 and 8, respectively, at $5 \times I_{th}$. A prior work reveals that a high SA reverse bias is beneficial for improving the dynamics of a multi-section colliding device in terms of the pulse width (Xin et al., 2007), which is similar as the one described in this study. Figure 5.12(b) depicts the optical spectrum of the QD-OFC with the gain current biased at $5 \times I_{th}$ but decreasing the SA voltage to 0 V. Compared to the emission spectrum shown in Fig. 5.12(d), a collapse of the frequency comb dynamics occurs which means a sufficient high SA reverse voltage must be ensured to enable the frequency comb generation from this device.

5.7 Impact of the saturable absorber reverse bias on the linewidth enhancement factor

Due to the passive section, it is more complex to extract the α_H -factor from a multi-section mode-locked laser. A prior study revealed that a reverse voltage

biased on the SA is beneficial for accelerating the absorber recovery time thus shaping a series of ultra short optical pulses (Rafailov, Cataluna, and Sibbett, 2007). However, the SA reverse bias also affects the mode-locking dynamics through the gain properties of the laser's active region. In this study, the α_H of the QD-MLL and the QD-OFC is measured by using the ASE method. Let us recall the definition of differential gain dG_{net}/dI and differential wavelength $d\lambda_m/dI$ in Eq. (4.24), where the values of these parameters are calculated by curve fitting the modal gain and the modal wavelength as a function of the gain current. On one hand, the dG_{net}/dI is extracted by curve fitting the current below threshold. On the other hand, one needs to eliminate the thermal effect by subtracting the wavelength shift above threshold from that below threshold to calculate a reliable $d\lambda_m/dI$. Due to the spiky-like gain profile, the gain properties of the QD-MLL, i.e., the differential gain, the differential wavelength, and the α_H , show a large dispersion against the variation of modal wavelength. In this case, we focus on one longitudinal mode near gain peak to carry out the most reliable measurement. Figure 5.13(a) depicts the differential gain (emerald) and the differential wavelength (burgundy) as a function of the SA reverse voltage of the QD-MLL whose SA section length ratio is 5%. The increase of SA voltage from 0 to -2 V results in a decrease of the differential gain from 5.7 to $3.7\text{cm}^{-1}/\text{mA}$, then the differential gain no longer shows a clear dependence on the SA bias ranging from -2 to -5 V. Nevertheless, the negative differential wavelength keeps its increase from -0.47×10^{-3} to $-1.42 \times 10^{-3}\text{nm}/\text{mA}$ with the increase of SA voltage from 0 to -5 V. As a result of the change of differential gain and differential wavelength with respect to the SA reverse bias, the α_H -factor is largely affected. Figure 5.13(b) depicts the corresponding α_H -factors as a function of the SA voltage for the same longitudinal mode of the QD-MLL (burgundy).

For the QD-OFC, its gain properties are quasi independent of the modal wavelength owing to the flat gain profile. Therefore, we focus on its entire comb spectrum at threshold and calculate an average α_H through the following relationship (Cappelli et al., 2015):

$$\alpha_e = \sqrt{\frac{1}{\Delta f} \int_{comb} df' \alpha^2(f')} \quad (5.18)$$

with Δf the width of the comb spectrum and f' the frequency of the laser emission. The calculated average α_H -factors at threshold of the QD-OFC are represented by the emerald symbols in Fig. 5.13(b).

Assuming that the QD is a two-level atomic system and that the center of the

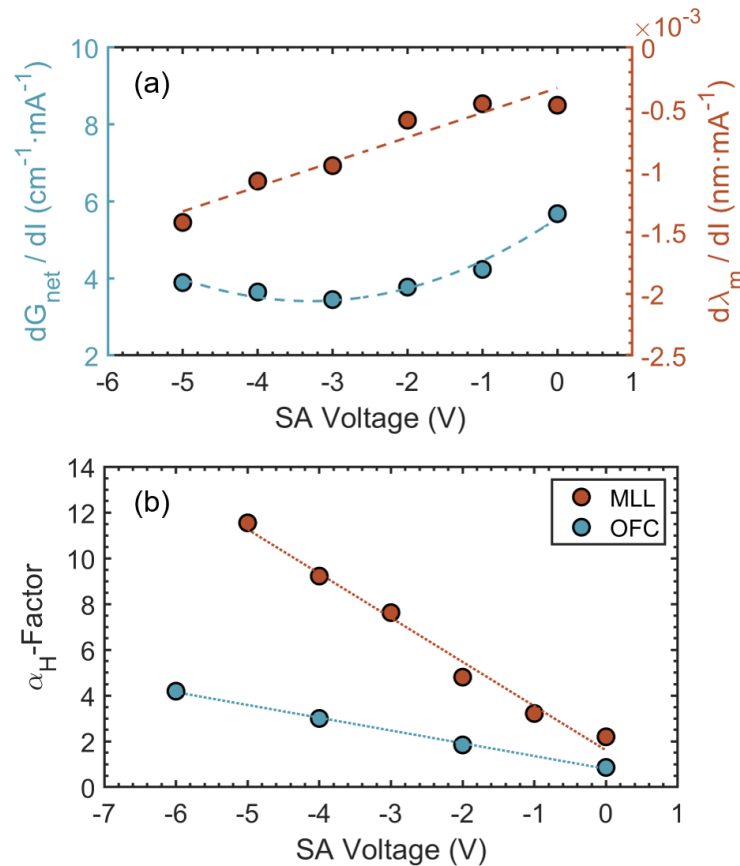


Figure 5.13: (a) Characterization of the QD-MLL whose r_{SA} is 5%: the differential gain (emerald) and the differential wavelength (burgundy) as a function of SA reverse voltage for a longitudinal mode near gain peak. (b) Threshold α_H -factor as a function of SA reverse voltage for the same mode of the QD-MLL (burgundy) and for a longitudinal mode near gain peak of the QD-OFC (emerald). Measurements at threshold are performed by ASE method.

frequency comb spectrum coincides with the center frequency of the QD transition, Eq. (5.18) can be re-written as follows:

$$\Delta f = 2\sqrt{3}\Gamma\alpha_e \quad (5.19)$$

where Γ denotes the homogeneous broadening of the QD transition. In this study, the α_H of both devices increases with the SA reverse voltage, which is mainly attributed to the increased differential wavelength at a higher SA bias. The overall larger α_H observed from the QD-MLL is attributed to the chirped QDs that are applied to the gain medium (K. C. Kim et al., 2010). In addition, the measured α_H -factors shown here are effective values that include both the contributions of the gain and the absorber. Evidently, the α_H of each section is different and both

of them affect the laser dynamics. A further study on retrieving the α_H of each section independently remains to be investigated. Despite a large α_H -factor is usually detrimental to the stability of semiconductor laser, it improves the optical bandwidth of the frequency comb source. Based on the definition of Eq. (5.19), the large α_H -factor resulting from the high SA reverse voltage can be a positive point on improving the frequency comb dynamics and the optical bandwidth, as observed from the lasing behaviors in Figs. 5.10 and 5.12. In addition, the improvement of optical bandwidth could be also attributed to the four-wave mixing in QDs. A recent study reveals that a single-section QD laser that excludes the SA section is able to generate frequency comb through the four-wave mixing process (Weng W Chow, Songtao Liu, et al., 2020), owing to the rich optical nonlinearities offered by QDs (Jianan Duan, Weng W Chow, et al., 2021). For the QD-MLL and the QD-OFC studied, similar process might happen since the FWM mechanism is also dependent on the α_H -factor (Akiyama, Kuwatsuka, et al., 2002). In particular, both the sign and amplitude of the α_H that is associated to the different individual processes play important roles in determining and amplifying the corresponding $\chi^{(3)}$ susceptibility (G. P. Agrawal, 1988). Nevertheless, one needs to avoid the destabilization of a mode-locked laser that occurs in a high SA reverse bias condition where the α_H -factor is too large (Songtao Liu, X. Wu, et al., 2019; Auth et al., 2019). A detailed discussion on the mode-locking dynamics dependent on the α_H will be performed in the next section.

5.8 Impact of the linewidth enhancement factor on the mode-locking dynamics

In this section, analysis of the mode-locking dynamics for the QD-MLL whose r_{SA} is 8% are performed. Given that the gain section of the device studied is isolated from the SA section, the α_H -factor of the gain α_g should be independent with the SA reverse bias. Therefore, the theoretical simulations based on the DDE model follow two criteria:

- The effect of the pump current on the gain section is performed by the modal gain $g_{mod}(J)$;
- The effect of the bias voltage on the SA section is described by the α_H -factor of the SA α_q

In this study, the parameters for the simulations are given in Tab. 5.1, unless stated

otherwise.

Symbol	Value	Symbol	Value
γ	1.5 ps ⁻¹	α_i	7.7 cm ⁻¹
γ_g	1 ns ⁻¹	α_0	18.45 cm ⁻¹
γ_q	75 ns ⁻¹	R_1	0.32
r_s	10	R_2	0.95
L_c	2048 μm	η_g	0.01
L_{ext}	12 m	η_q	0.01
n	3.66	α_g	0.2
r_{SA}	0.08		

Table 5.1: Parameter values used in numerical simulations.

Figures 5.14 display the calculated and the experimentally recorded mode-locking dynamics of the device studied in different operating conditions. For each dynamic state, its time-domain responses are performed by the absolute value of the amplitude $|\varepsilon|$ (burgundy solid line), the saturable gain G (gold dashed line), the total loss $Q_t \equiv Q + |\ln\kappa|$ (gray dashed line), and the net modal gain $G_{net} \equiv G - Q_t$ (black dashed line) in the steady-state.

- Q-switched mode-locking (QSML).** If the α_q is fixed while increasing the modal gain above threshold, the laser firstly exhibits the QSML dynamics at the onset of lasing. Figure 5.14(a) shows the time traces of the laser when it operates with a g_{mod} of 9.1 cm⁻¹ and a α_q of 2, the fundamental 20 GHz pulse train that is modulated by a low Q-switching frequency f_{QS} is identified. The inset depicts the corresponding RF spectrum, where the f_{QS} signal is identified as the sidebands of the fundamental f_r . At this stage, the pulse duration is typically broad and the RF peak intensity remains low. Figure 5.14(e) displays the recorded experimental RF spectrum of the QD-MLL in QSML operation, when its gain section is biased at 95 mA and the reverse voltage applied to the SA is -2 V. In contrast to the simulation, the RF peak SNRs in experiment are quite high; in general, the SNRs are above 60 dB. These high SNRs observed are mainly attributed to the sudden power rise near threshold, which is not considered in the simulation.
- Fundamental mode-locking (FML).** For all α_q in simulation, a reasonable large g_{mod} contributes to stabilizing the MLL by reducing its pulse width and improving its RF peak intensity, hence the laser enters into the FML

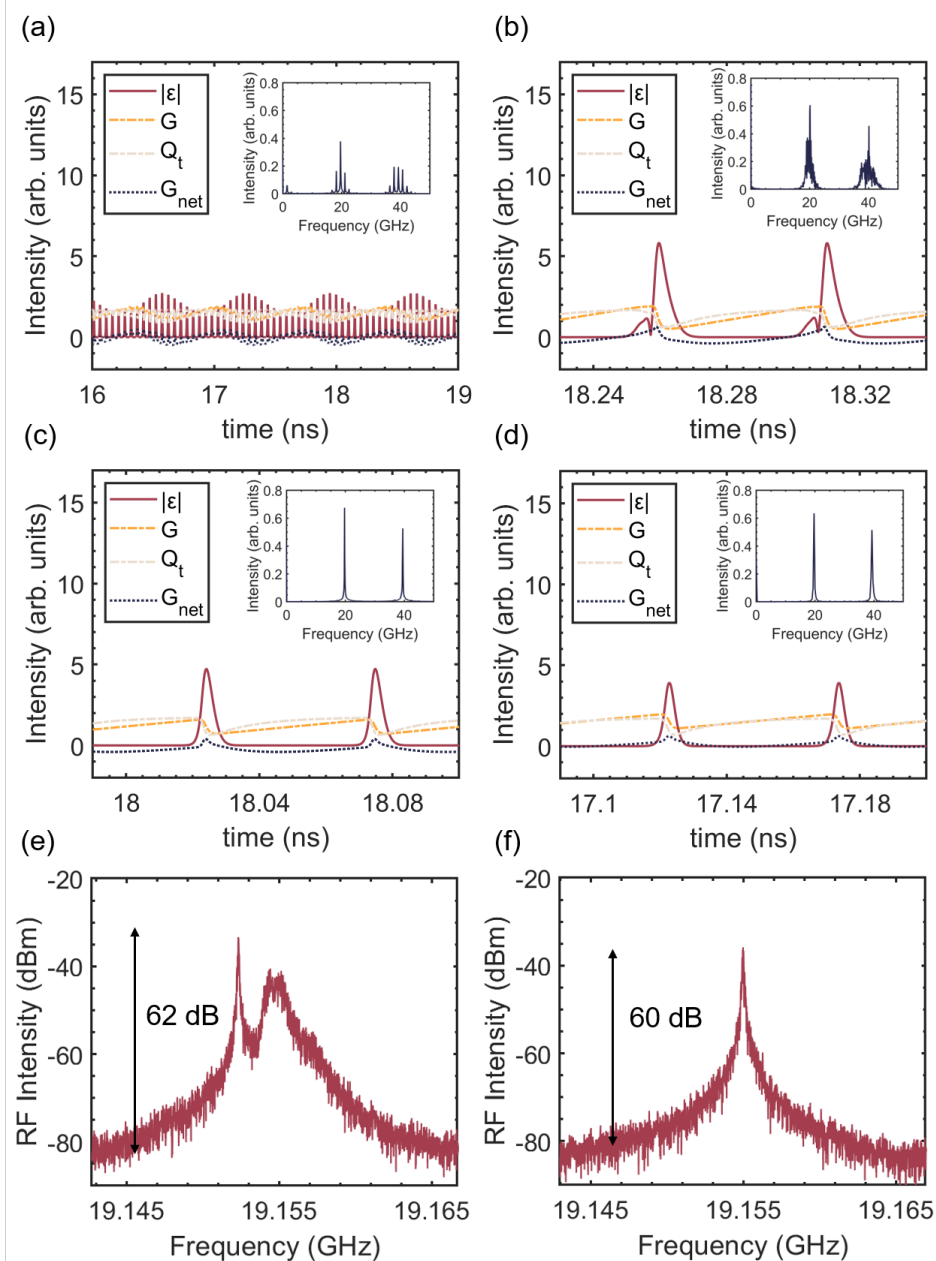


Figure 5.14: Calculated dynamics of the QD-MLL performed by time traces and inset the RF spectra in different operating conditions: (a) Q-switched mode-locking (QSMML) with $(g_{mod}, \alpha_q) = (9.1 \text{ cm}^{-1}, 2)$; (b) unstable fundamental mode-locking (uFML) with $(g_{mod}, \alpha_q) = (14.6 \text{ cm}^{-1}, 2)$; (c) fundamental mode-locking (FML) with $(g_{mod}, \alpha_q) = (11.8 \text{ cm}^{-1}, 2)$; and (d) FML with $(g_{mod}, \alpha_q) = (11.8 \text{ cm}^{-1}, 5)$. Recorded experimental RF response: (e) QSMML with $(I_{gain}, V_{SA}) = (95 \text{ mA}, -2 \text{ V})$ and (f) FML with $(I_{gain}, V_{SA}) = (160 \text{ mA}, -2 \text{ V})$.

regime. An example of the mode-locking behavior at this stage is shown in Fig. 5.14(c), when the device operates with a g_{mod} of 11.8 cm^{-1} and a α_q of 2. In this ideal operating condition, the G_{net} remains negative during the pulse interval but becomes positive during the short lasing time, then the regular 20 GHz pulse train is generated. In this operating regime, the average pulse width of more than 100 calculated pulses is around 3 ps. With the increase of the α_q from 2 to 5 while keeping the g_{mod} at 11.8 cm^{-1} , the pulse width keeps at ~ 3 ps, as shown in Fig. 5.14(d). Nevertheless, the drawback brought by a large α_q can be seen from the unstable background at the leading edge of a pulse, where the G_{net} becomes positive before the outset of a pulse emission. Even if the pulse shape remains in a good condition, its amplitude decreases thus leading to a lower RF peak intensity. It is worth stressing that the pulse width narrowing caused by a high SA reverse bias observed in previous experiments (Songtao Liu, X. Wu, et al., 2019; Auth et al., 2019) can be attributed to the increase of absorption; however, that is not the case of this study since the absorption of the device studied is barely changed by the SA reverse bias due to the short SA section. In experiment, the maximum SNR of 60 dB along with the minimum RF linewidth of 150 kHz is recorded in the FML regime, as shown in Fig. 5.14(f). This optimum RF spectrum is captured when the device operates with 160 mA applied to the gain section and -2 V applied to the SA.

- **Unstable fundamental mode-locking (uFML).** The QD-MLL eventually operates with the uFML behavior if the g_{mod} is further increased and is out of the optimum conditions. In this operating regime, multiple pulses propagating during one round-trip time in the cavity results in the noise background in the RF response, as depicted in Fig. 5.14(b) and its inset, when the QD-MLL operates with a g_{mod} of 14.6 cm^{-1} and a α_q of 2. In experiment, the author does not make further efforts to record the laser dynamics in uFML regime, since the output power of the device studied begins to roll over after 180 mA, as shown in Fig. 5.10(a). This phenomena is also a sign of uFML operation (Meinecke et al., 2019).

To have a complete picture of the mode-locking dynamics, the calculated pulse width and the RF peak intensity as a function of the SA bias assisted α_q and the gain current assisted g_{mod} are shown in Figs. 5.15(a) and (b), respectively. The experimentally recorded RF peak SNRs as a function of the SA reverse bias and

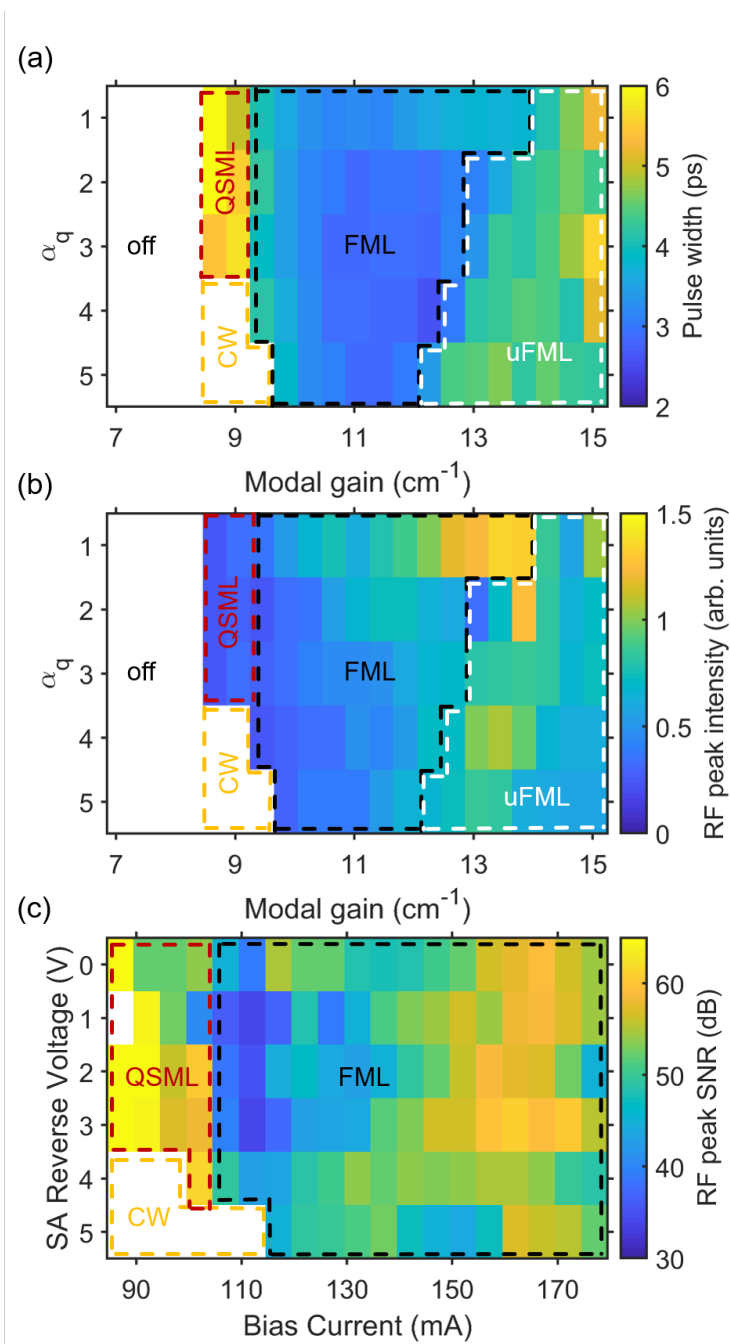


Figure 5.15: Calculated mappings of (a) the pulse width and (b) the RF peak intensity as a function of the modal gain and α_q of the QD-MLL. (c) Experimental mapping of the RF peak signal-to-noise ratio (SNR) as a function of the gain current and SA reverse voltage obtained from the same device.

the gain current are depicted in Fig. 5.15(c). In simulation, the threshold modal gain $\approx 8.5 \text{ cm}^{-1}$ is barely changed with the increase of α_q from 1 to 5, which is in agreement with the light-current characteristics shown in Fig. 5.10(a). The pulse width rebroadening effect in the high modal gain condition (uFML, white dashed region) that has been observed in recent experimental work (Songtao Liu, X. Wu, et al., 2019; Auth et al., 2019) is also reproduced by using the DDE model. In particular, the impact of α_H -factor on the mode-locking stability can be seen from the reduction of FML regime (black dashed region) as the α_q increases. In addition, the generation of QSML dynamics (burgundy dashed region) becomes less efficient when the α_q increases above 3, where the laser rather exhibits continuous-wave (CW, gold dashed region) oscillations before enters into the FML regime. It is worth stressing that the experimental results match the trend of simulation quite well. For the QD-MLL studied, the QSML dynamic is hardly to be triggered at a high SA reverse bias over -4 V, where the α_q is quite large. In agreement with simulation, the laser exhibits a CW behavior at this stage.

5.9 Impact of the saturable absorber section length ratio on the mode-locking dynamics

It has been extensively studied that the mode-locking dynamics is affected by both the length and the position of the SA section placed inside the laser cavity (Thompson et al., 2009; Javaloyes and Balle, 2010; Rossetti, Xu, et al., 2011; Meinecke et al., 2019). Although a reasonable long SA section is found to be beneficial for reducing the pulse duration (Thompson et al., 2009; Songtao Liu, J. C. Norman, et al., 2018), a prior study reveals that a long SA section is detrimental for the mode-locking stability (Rossetti, Xu, et al., 2011). In particular, a prior experimental work demonstrated that a large r_{SA} could reduce the pulse width but increased the RF linewidth simultaneously (Thompson et al., 2009). Such a finding is not a good news for developing a ultrafast comb source with low noise properties.

In this section, the influence of the r_{SA} on the mode-locking performance is performed. By using both simulation and experiments, the author tries to give a guideline to improve the performance of a QD-MLL. Figures 5.16(a) and (b) display the calculated mappings of the pulse width and the RF peak intensity as a function of the r_{SA} and the modal gain, respectively. In simulation, the α_q is assumed to be 1. With the increase of the r_{SA} from 5 to 17%, the modal gain at threshold increases from 8.5 to 11 cm^{-1} due to the increased internal loss. When the device operates in the FML regime (black dashed region), its minimum pulse

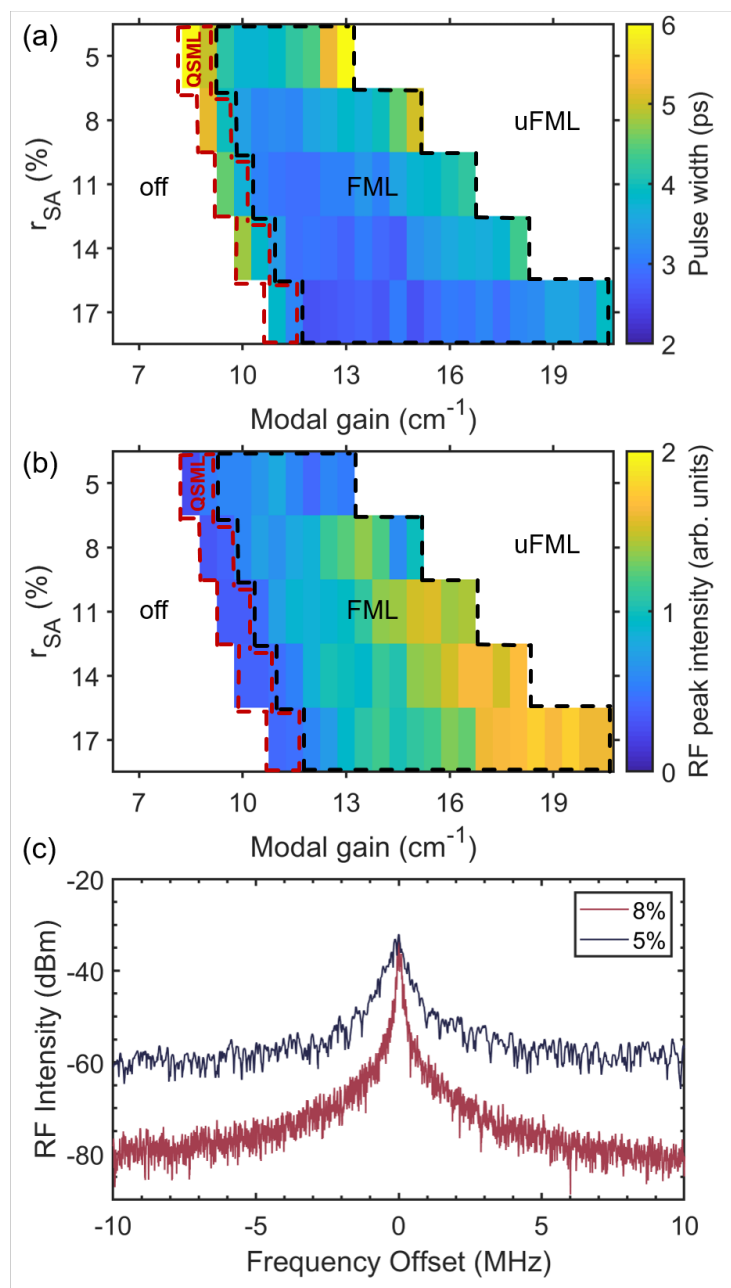


Figure 5.16: Calculated mappings of (a) the pulse width and (b) the RF peak intensity as a function of the modal gain and the SA section length ratio r_{SA} . (c) Recorded experimental RF response of the QD-MLL whose r_{SA} is 5% (black) and 8% (burgundy) in the optimum conditions.

width decreases with the r_{SA} , which is in agreement with prior studies both in simulation and experiments (Thompson et al., 2009; Rossetti, Xu, et al., 2011). In particular, the calculated results demonstrate that both a large r_{SA} and a large modal gain contribute to increase the RF peak intensity. Figure 5.16(c) depicts the experimental RF spectra of the QD-MLL with the r_{SA} being 5% (black) and 8% (burgundy) in their optimum conditions. For the first device whose r_{SA} is lower, its best mode-locking performance takes place when it is biased with -2 V on the SA and 115 mA ($2.6 \times I_{th}$) on the gain; whereas for the second one whose r_{SA} is larger, that happens when its SA is biased at -3 V and its gain is pumped at 160 mA ($1.9 \times I_{th}$). By increasing the r_{SA} from 5 to 8%, the RF linewidth is largely reduced from 700 to 150 kHz and a 15 dB improvement of SNR is observed, thus matching the trend of the simulation quite well. In addition, a recent study demonstrates that the RF linewidth can be further reduced to 1.8 kHz if the r_{SA} increases to 14% (Songtao Liu, X. Wu, et al., 2019). Nevertheless, it is worth stressing that a limited modal gain in a MLL is the bottleneck that restricts its mode-locking performance when the SA section is too long, due to the increased intra-cavity noise induced by the internal loss. In experiment, it has been observed that both a rebroadening of the RF linewidth and a decrease of the SNR take place when the r_{SA} is higher than 20% (Thompson et al., 2009). As a consequence, the pulse width and the SNR of the fundamental repetition frequency of a MLL can be improved simultaneously, however, an optimum r_{SA} that balances the gain and the loss of the active region is required.

5.10 Stabilization of quantum-dot mode-locked laser by external optical feedback

In Chap. 3, the author introduces how the external optical feedback (EOF) affects the laser dynamics. Depending on both the feedback strength η_F and the external cavity length L_{ext} , a semiconductor laser exhibits a route to coherence collapse within the transition from regime I to regime IV. During this full transition, the stability of laser is either improved or degraded. In particular, the laser dynamics subject to EOF is strongly dependent on the α_H -factor of the active region, which gives insights for controlling the laser performance through the α_H in EOF operation (Frédéric Grillot, J. C. Norman, et al., 2020). In the case of a semiconductor mode-locked laser, the EOF also plays a crucial role in affecting its mode-locking dynamics (Solgaard and K. Y. Lau, 1993). It has been extensively studied that the EOF is an efficient approach to stabilize a MLL by reducing its frequency noise and timing

jitter (Eugene A Avrutin and Russell, 2009; C.-Y. Lin, Frédéric Grillot, et al., 2010; Verolet et al., 2020), which is highly desired for the coherent communication system and PIC applications. Prior studies reveal that the reduction of RF linewidth takes place at the integer resonant condition where the external cavity delay time τ_{ext} is a multiple of the repetition rate τ_{in} (i.e., $\tau_{ext}/\tau_{in} \in N$, N is integer) (C.-Y. Lin, Frédéric Grillot, et al., 2010; Otto et al., 2012), however, the RF linewidth can also suffer from a strong rebroadening when the external cavity length is out of the optimum conditions. For instance, a large destabilization of a MLL is observed in the exact integer resonant (i.e., $\tau_{ext}/\tau_{in} \equiv N$) and the non-resonant feedback conditions (i.e., $\tau_{ext}/\tau_{in} \notin N$) (C.-Y. Lin, Frédéric Grillot, et al., 2010; Rosales, Kamel Merghem, et al., 2011). In addition, an experimental work demonstrate that the stability of the RF linewidth narrowing against the change of L_{ext} can be improved by applying a strong feedback strength beyond -25 dB, in this case the RF linewidth rebroadening phenomena is drastically minimized (Rosales, Kamel Merghem, et al., 2011).

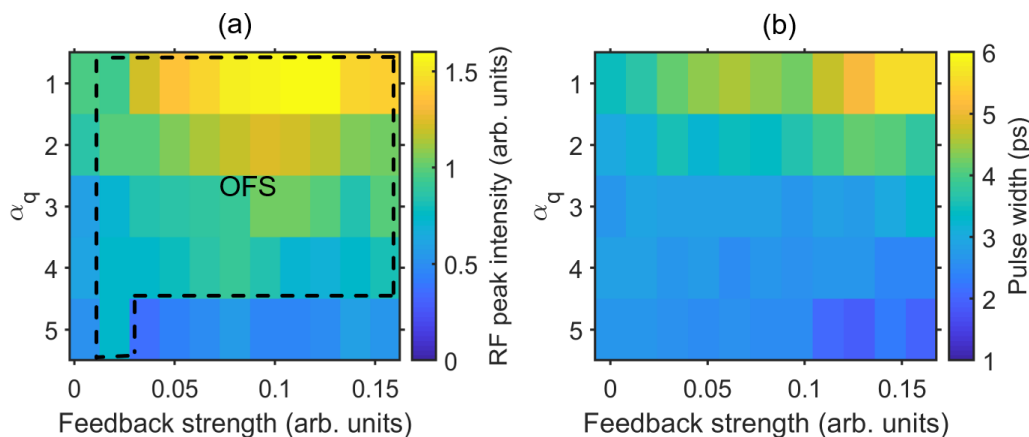


Figure 5.17: Calculated mappings of (a) the RF peak intensity and (b) the pulse width as a function of the feedback strength η_F and α_q .

Prior theoretical studies demonstrated that the degree of optical feedback stabilization (OFS) to a semiconductor MLL differs from the α_H -factor (Eugene A Avrutin and Russell, 2009; Christian Otto, 2014). However, a connection between the α_H -factor and the operating conditions remains to be investigated. In this thesis, we thus go a step beyond by investigating the impact of the SA bias dependent α -factor on the stabilization of a QD-MLL. Following the definition of Eq. (5.16), the modal gain is fixed to 11.8 cm^{-1} in simulation. Given that the EOF operation in experiment is in the long-cavity regime and the device operates in the integer resonant condition, the τ_{ext} is set to be $2400 \times \tau_{in}$.

Still focusing on the QD-MLL whose r_{SA} is 8%, Fig. 5.17(a) depicts the calculated mapping of the RF peak intensity as a function of the α_q and the feedback strength η_F . In the case of a α_q below 4, the intensity of f_r increases with the feedback strength, which means the phase noise is improved. The conditions for the OFS operation where the RF peak intensity is amplified is highlighted with the black dashed region in Fig. 5.17(a). Despite the fact that Eq. (5.16) has some limitations for analyzing the effect of EOF (i.e., it is only valid for the weak optical feedback), it gives an approach to explain the phase noise improvement. In the integer resonant feedback condition where the external cavity is in phase with the laser cavity, the EOF gives rise to an increase of the equivalent facet reflectivity. As a consequence, the effective quality factor of the laser cavity is increased which results in the improvement of phase noise. However, the efficiency for phase noise improvement decreases with the increase of α_q , which can be seen from the decrease of the maximum RF peak intensity as the α_q increases. In particular, the intensity of f_r becomes quasi independent of the feedback strength when the α_q is larger than 4.

On the other hand, the calculated mapping of the pulse width is shown in Fig. 5.17(b), where the same operating conditions are maintained. In contrast to what happens on the phase noise, a strong feedback strength could give rise to an increase of pulse width. However, such a pulse width broadening effect is minimized by increasing the α_q beyond 2. This phenomena has been observed experimentally in Ref. (Merghem et al., 2009).

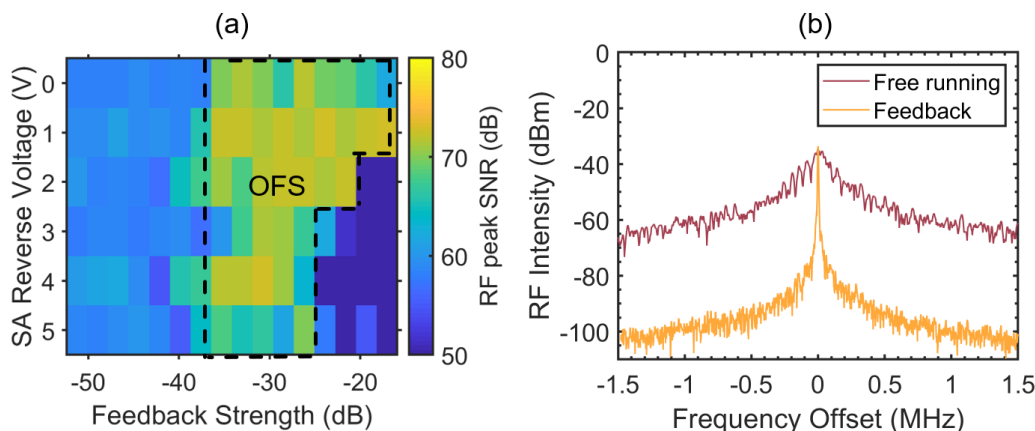


Figure 5.18: (a) Experimental mapping of the RF peak SNR as a function of the η_F and V_{SA} , when the device operates at 167 mA. (b) Experimental RF spectra in free-running operation (burgundy) and in optical feedback operation (gold) with $(I_{gain}, V_{SA}, \eta_F) = (167 \text{ mA}, -1 \text{ V}, -34 \text{ dB})$.

In experiment, the device studied also operates in the integer resonant condition to realize a stable RF linewidth narrowing and the setup has been shown in Fig. 3.20. Figure 5.18(a) depicts the experimental mapping of the RF peak SNR as a function of the SA reverse bias and feedback strength, when the same device operates with the optimum gain current at 167 mA. If the SA reverse bias is unchanged, the SNRs remain at the same level in the weak feedback regime in which the η_F is lower than -40 dB. A higher feedback strength contributes to operating the laser system in the OFS regime, in which a 5 ~ 13 dB increase of SNR and a 10 ~ 40-fold reduction of RF linewidth are identified. In the optimum feedback condition (gold), the RF linewidth is strongly reduced from 160 to 4 kHz and the SNR improves from 59 to 72 dB with respect to the free-running case (burgundy), as shown in Fig. 5.18(b). The optimum feedback condition occurs with a -34 dB feedback strength applied, when the QD-MLL is biased at 167 mA on the gain section and -1 V on the SA section. The level of RF linewidth can thus be used for estimating the pulse-to-pulse rms timing jitter through the following relationship:

$$\sigma_{pp} = T \sqrt{\frac{\Delta\nu NT}{2\pi}} \quad (5.20)$$

where $\Delta\nu$ and N account for the 3-dB RF linewidth and the number of periods between two compared pulses, respectively. Following Eq. (5.20), the pulse-to-pulse rms timing jitter is largely reduced from 60 to 10 fs/cycle in the optimum feedback condition.

Experimental results also reveal that a large V_{SA} assisted α_q decreases the efficiency for phase noise improvement. For instance, the maximum η_F that ensures a 10 dB improvement of SNR is beyond -20 dB in the case of a low V_{SA} below -1 V, whereas a η_F over -25 dB leads to a strong destabilization when the V_{SA} is higher than -3 V. In addition, the improvement of SNR becomes less efficient when the V_{SA} is above -4 V. In this study, the maximum increase of the SNR in the EOF operation is reduced by a factor of 8 dB with the increase of SA bias from 0 to -5 V. Nevertheless, in the optical feedback destabilization regime in which a strong η_F above -25 dB and a high V_{SA} over -3 V are applied, the RF peak SNR redecreses below its free-running value. Such a destabilized behavior due to coherence collapse is not reproduced in simulation, since they are not included in our model. As aforementioned in Sec. 3.1, the definition of r_{re} is only valid for a η_F relatively low, however, the lasing destabilization taking place at a η_F above -25 dB means that the amplified external cavity resonance arises complex dynamics.

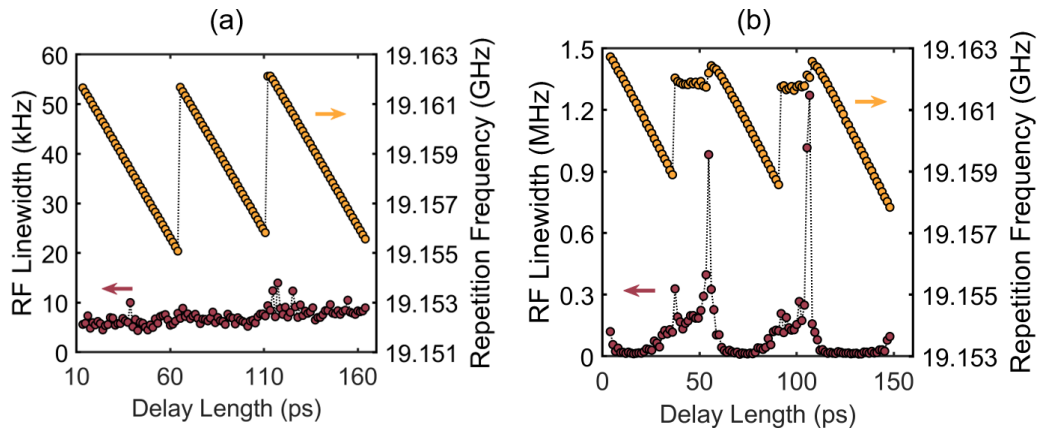


Figure 5.19: Variation of the repetition frequency (gold) and the RF linewidth (burgundy) as a function of the external cavity length change in experiment, when the device operates with $(I_{gain}, V_{SA}, \eta_F) =$ (a) (167 mA, 0 V, -34 dB) and (b) (167 mA, -3 V, -34 dB).

Despite the fact that the integer resonant feedback is beneficial for improving the phase noise, a degradation of the phase noise could take place when the external cavity is out of phase with the laser cavity. As a result, the RF linewidth could be periodically changed with the variation of external cavity length. However, the influence of the external cavity length variation could be minimized when the α_q is low. When the QD-MLL operates with 167 mA applied to the gain section and under -34 dB EOF, Figs. 5.19(a) and (b) depict the variations of the fundamental repetition frequency f_r (gold) and the RF linewidth (burgundy) as a function of the change of L_{ext} in the case of 0 V or -3 V applied to the SA section, respectively. In the first case, on one hand, the RF linewidth ranging from 4 to 16 kHz exhibits a high degree of stability against the delay length variation in absence of evident rebroadening. On the other hand, the frequency pulling of the f_r induced by the plasma effect shows a 50 ps periodicity, which corresponds to the f_r of 20 GHz. When the SA reverse bias increases to -3 V, large destabilizations of both the RF linewidth and the f_r take place. Within one period of the delay length variation, the QD-MLL in turn operates in the integer resonant, the exact integer resonant, and the non-resonant conditions. In the latter two cases, the RF linewidth rebroadens well beyond its free-running value at 160 kHz due to the decrease of effective quality factor of the laser cavity. Such a destabilization heightens in the non-resonant conditions, where an 8-fold enlargement of the RF linewidth to 1.3 MHz is observed. In addition, the f_r no longer shows a delay length dependence outside the interval

of the OFS operation. Theoretical analysis of the observed phase noise properties remain to be investigated, however, a prior study has partially reproduced those behaviors (Christian Otto, 2014). Last but not least, a recent study reveals that the OFS efficiency can be further improved by reducing the L_{ext} to tens of centimeters (Verolet et al., 2020).

5.11 Frequency comb bandwidth improvement by optical injection

Optical injection-locking (OIL) is a well-known technique that is able to influence the laser dynamics (E. K. Lau, Wong, and M. C. Wu, 2009). The first OIL operation on a semiconductor laser was realized in 1980 (S. Kobayashi and Kimura, 1980). Since then, both theories and experiments were developed to understand the OIL mechanism (Y. Yamamoto, 1980; Otsuka and Tarucha, 1981; Lang, 1982). With the development of long-haul fibre-optic communication in late 1980s, the OIL technique exhibited a strong potential to be applied to the direct-detection fibre links to improve their performances. Examples as the reduction of chirp-induced dispersion and nonlinear distortion (C. Lin and Mengel, 1984; Meng et al., 1998), the decrease of intensity and frequency noise (Mogensen, Olesen, and Jacobsen, 1985; Nikolaus Schunk and KLAUS Petermann, 1986; JM Liu et al., 1997), and the increase of relaxation oscillation frequency thus the modulation bandwidth (Henry, Olsson, and Dutta, 1985; Simpson, JM Liu, and Gavrielides, 1995; Hayat et al., 2009) have been reported. In particular, Chrostowski et al., 2007 demonstrate that the OIL allows for largely increasing the resonance frequency of a DFB laser diode from 3 to 100 GHz, which is promising for developing high-speed and compact sources for PIC applications.

While the OIL is reliable to improve the radio frequency performance of a laser diode, it is still a question that whether it could be used to improve the laser performance in the range of optical frequencies. In a prior work where a QDash mode-locked semiconductor laser was investigated (Sooudi et al., 2013), it seemed that the OIL is detrimental to the optical bandwidth. In that study, the time-bandwidth product of the comb source is reduced by 50% with OIL applied, however, at the price of a 50% reduction of gain bandwidth. Soon after that, a similar study on a VCSEL-based comb laser from Prior et al., 2016 demonstrated a reduction of pulse width with OIL operation, which gave insight for increasing the comb bandwidth by using the OIL approach.

In this section, the influence of optical injection on the QD-based frequency comb

laser is performed. Figure 5.20 depicts the experimental setup for analyzing the laser dynamics in optical injection operation. The laser emission is coupled out by a lens-end fibre before it is sent to the port 2 of a three-port fibre-based optical circulator. The output of an external single-frequency master laser is coupled into the optical circulator through the port 1 to inject locking the slave laser. To this end, a polarization controller is added to the path of master laser emission to compensate the fibre dispersion in it and to maximize the injection strength. Besides, the isolation from port 2 to port 1 must be higher than 30 dB to eliminate any back-reflection. In the end, the output from the port 3 is captured by an optical spectrum analyzer with a resolution of 10 pm for the characterizations of laser dynamics.

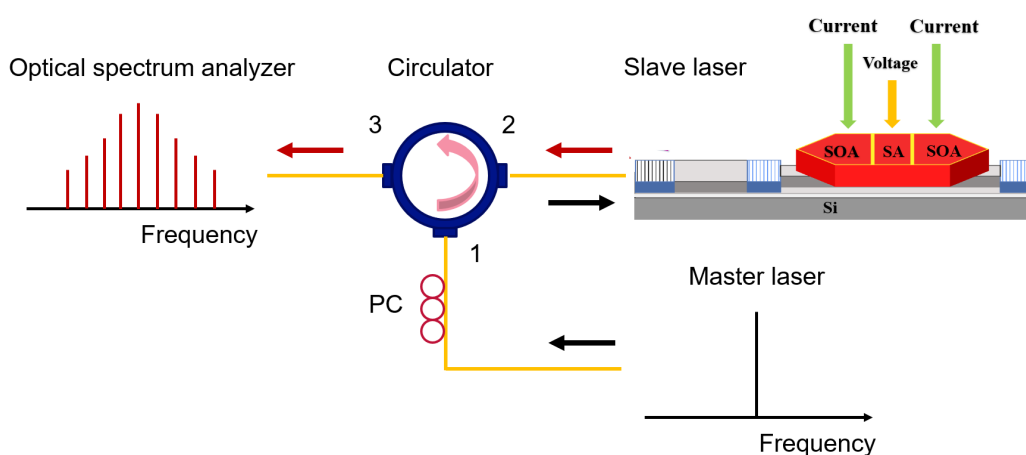


Figure 5.20: Experimental setup for optical injection operation. PC, fibre-based polarization controller.

In OIL operation, both the optical detuning and the injection ratio R_{inj} play crucial roles in determining the laser dynamics. The latter is calculated as follows:

$$R_{inj} = P_{ml} - P_{out} + 2 \times (l_{ext} + l_{fm} + l_{gc}) \quad (5.21)$$

where P_{ml} and P_{out} denote the injection power of the master laser and the free-space output power of the slave comb laser. l_{ext} , l_{fm} and l_{gc} in turn account for the losses from the external cavity waveguide, from the front mirror and from the grating coupler, respectively. It is a challenge to determine the exact value for the injection strength due to the intra-cavity coupling loss induced by the complex structure. However, given that the losses from the mirror and the grating coupler are -3 dB and -9 dB, respectively, the total losses from the external cavity would exceed -25 dB. In this study, the output power of the master laser and the slave comb laser is

6 dBm and -6 dBm, respectively, thus resulting in a weak injection strength below -12 dB. For the QD-OFC studied, its flat-top behavior make the gain peak hard to be determined; besides, the frequency comb region is also dependent on the bias current on the SOA. Therefore, the author uses the injection wavelength rather than the optical detuning to analyze the lasing behaviors.

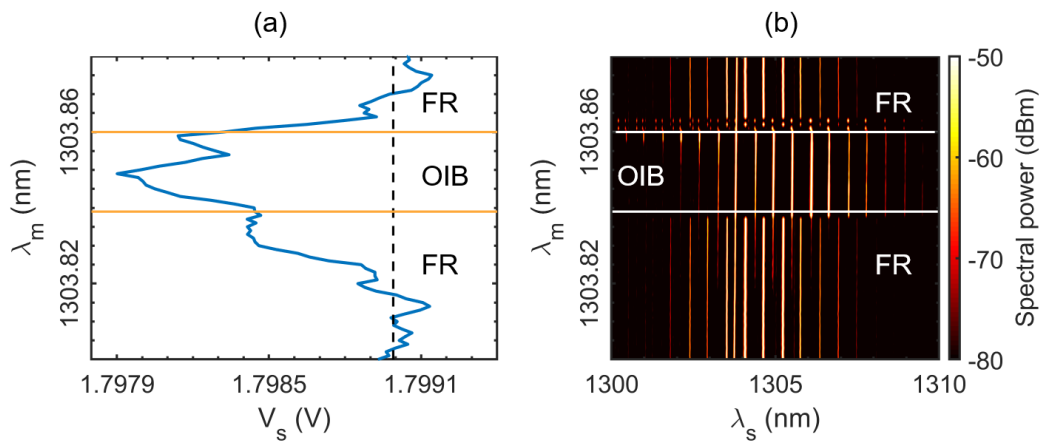


Figure 5.21: Characterization of the inter-mode optical injection: (a) wavelength of the master laser as a function of the voltage of the slave QD-OFC. (b) Spectral power of the comb laser as a function of its wavelength and the master laser wavelength. OIB, optical injection broadening regime. FR, free-running regime.

In the case of inter-mode optical injection, Fig. 5.21(a) depict the voltage of the comb laser V_s as a function of the injection wavelength of the master laser λ_m , when the device operates at $3 \times I_{th}$ with -6 V applied to the SA section. With the increase of injection wavelength in the interval of two comb lines outside the 3-dB bandwidth, the slave comb laser enters into the optical injection broadening (OIB) regime in presence of a decrease of voltage compared to the free-running case. Figure 5.21(b) display a mapping of the spectral power of the comb laser as a function of the wavelength of itself and of the master laser. A red-shift of the frequency comb region is observed in the OIB regime. Despite the 3-dB gain bandwidth does not show any clear improvement, the full bandwidth above the noise floor increases from 5 to 6 nm (i.e., from 1 to 1.2 THz) along with the comb line number increasing from 11 to 13. However, it is a challenge to keep this regenerated dynamics. In this study, the OIB regime only takes place when the master laser wavelength ranges from 1303.839 to 1303.86 nm (i.e., an operating window of 21 pm).

On the other hand, an intra-mode optical injection is beneficial for largely improving

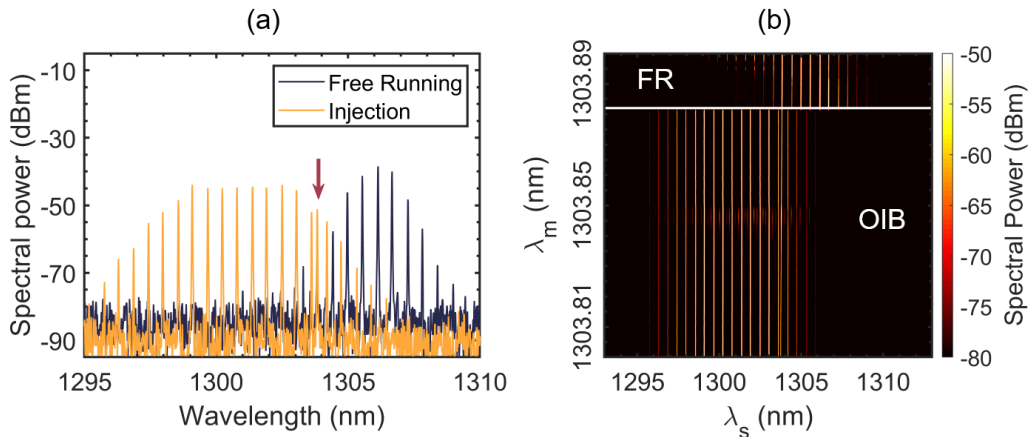


Figure 5.22: Characterization of the intra-mode optical injection: (a) optical spectra of the QD-OFC in free-running (black) and in optical injection (gold) operation. (b) Spectral power of the comb laser as a function of its wavelength and the master laser wavelength. OIB, optical injection broadening regime. FR, free-running regime.

the laser performance. Figure 5.22(a) depicts the optical spectra of the comb laser in free-running operation (black) and in intra-mode optical injection operation (gold). The longitudinal mode that is injected is marked by the red arrow. Figure 5.22(b) display the mapping of the spectral power of the comb laser as a function of its wavelength and injection wavelength of the master laser in the same condition. Despite the frequency comb region suffers from an overall blue-shift, the laser dynamics is strongly improved in presence of the 3-dB bandwidth increasing from 1 to 3.5 nm (i.e., from 204 to 714 GHz) along with the full bandwidth above the noise floor increasing from 5 to 9.5 nm (i.e., from 1 to 1.94 THz). Besides, the regenerated comb dynamics exhibits a much higher tolerance for the variation of the injection wavelength than the inter-mode injection case. In the case of intra-mode injection, the operating window for the master laser wavelength is larger than 82 pm. Last but not least, the occurrence of the OIB regime also exhibits a dependence of the SA bias assisted α_H -factor. If the SA section is biased at 0 V where the frequency comb dynamics is not fully developed, the optical injection operation has little impact on the laser dynamics. In this study, the high-loss integrated external cavity of the QD-OFC prevents us from analyzing the frequency comb dynamics under a stronger optical injection. In future work related to this topic, the influences of the injection strength as well as the operating temperature would be investigated.

5.12 Summary

In this chapter, investigations on the design and optimization of QD-based optical frequency comb lasers are performed. Based on both theoretical analysis and experiments, the author gives several guidelines for developing CMOS available, low-noise and high-bandwidth optical frequency combs. The main results are summarized as follows:

- QD is promising to serve as the gain and the absorber for a frequency comb laser, owing to its ultrafast carrier dynamics, ultra-broad optical bandwidth and low-noise properties. In particular, the reverse voltage applied to the SA section not only accelerates the absorber recovery time thus generating a shorter optical pulse, but also decreases the stability of mode-locking through the increase of α_H -factor. As a consequence of the high reverse SA bias assisted large α_H , both the SNR of the fundamental repetition frequency and its RF linewidth degrade. Therefore, the near-zero α_H -factor offered by QD paves the way for developing highly stable and low-noise OFC for PIC applications.
- For a conventional two-section QD-MLL in which a high modal gain is ensured, a reasonable long SA section is beneficial for reducing the pulse duration and increasing the SNR simultaneously. With the increase of the SA length ratio from 5% to 8%, a 15 dB increase of the SNR along with 4-fold reduction of the RF linewidth is identified.
- Optical feedback operation is an efficient technique to improve the phase noise of a QD-MLL. In the optimum feedback condition, the laser exhibits a 13 dB increase of SNR along with a 40-fold reduction of the RF linewidth from 160 to 4 kHz. The consequent reduction of pulse-to-pulse timing jitter from 60 to 10 fs/cycle gives insight for developing ultra stable photonic oscillators by taking advantage of the optical feedback technique. The SA bias assisted α_H -factor also plays an important role in the optical feedback stabilization process. In the case of a low α_H applied, the stabilized QD-MLL exhibits a high degree of tolerance for the variation of feedback strength and external cavity length.
- Optical injection operation is a reliable approach to improve the optical bandwidth of an OFC. In the intra-mode optical injection condition, the 3-dB optical bandwidth of a QD-based frequency comb laser exhibits a 3.5-fold

increase in presence of the comb line number increasing from 3 to 8. While a large α_H -factor is in general detrimental to the stability of mode-locking in the radio-frequency domain, it contributes to the improvement of optical bandwidth. Besides, a large α_H -factor is beneficial for improving the efficiency for bandwidth broadening in optical injection operation.

NONLINEAR FREQUENCY CONVERSION IN EPITAXIAL QUANTUM-DOT LASER ON SILICON

Four-wave mixing (FWM) is a well-known nonlinear process in a material that has third-order susceptibility $\chi^{(3)}$. Depending on the pump photon numbers, such a mechanism can be classified by degenerate FWM and nondegenerate FWM. As a consequence of FWM, two new photons are generated, which are named as signal and idler. After several decades of development, FWM provides a reliable solution for optical wavelength converter, self mode-locking and quantum states of light generation. In this chapter, investigations of the FWM mechanism in epitaxial QD lasers on silicon are performed. Both theoretical analysis and experimental results demonstrate that QD laser is a promising source for both classical and quantum photonic integrated circuits.

6.1 Introduction to four-wave mixing

In Chap. 2, a brief introduction to the optical nonlinearities has been performed. Eq. (2.62) explains how the two pump photons generate a new pair of photons through the $\chi^{(3)}$ nonlinear process. Derived from Eq. (2.62), the energy conservation is verified as follows:

$$2\hbar\nu_d + 2\hbar\nu_p = \hbar\nu_d + \hbar\nu_p + \hbar\nu_s + \hbar\nu_i \quad (6.1)$$

with ν_d and ν_p the frequencies of the two pump photons, drive and probe, respectively. The frequencies of the new generated signal and idler, ν_s and ν_i , respectively, are written as follows:

$$\begin{aligned} \nu_s &= 2\nu_d - \nu_p \\ \nu_i &= 2\nu_p - \nu_d \end{aligned} \quad (6.2)$$

Eq. (6.1) describes the case for nondegenerate FWM where the four frequencies are different from each other. Figure 6.1 illustrates the nondegenerate case where four equally-spaced frequencies coexist. The stronger one among the pump photons is referred as the drive (yellow), whereas the weaker one is the probe (green). The new generated signal (red) and idler (blue) are located at the low-frequency side and at the high-frequency side, respectively. The conversion efficiency in FWM operation

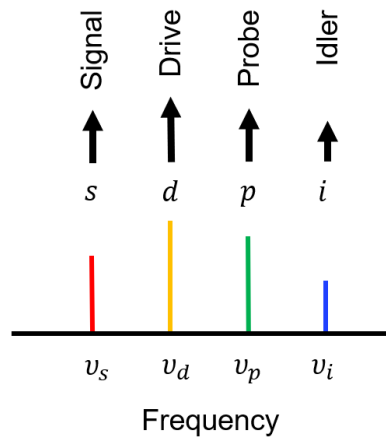


Figure 6.1: Illustration of the nondegenerate FWM process, the interaction of the drive and probe photons leads to the generation of signal and idler.

is dependent on the intensity, the phase, the polarization and the frequency detuning between the two pump photons. The FWM bandwidth is dependent on the frequency detuning which is expressed as $\Delta\nu = \nu_p - \nu_d$. Depending on the frequencies of drive and probe, there are two conversion processes:

- **Antistokes or down-conversion.** This process is the case displayed in Fig. 6.1 where the frequency detuning is positive. As a result, the frequency of the signal is lower than the drive frequency.
- **Stokes or up-conversion.** This process takes place when the frequency detuning is negative in presence of the signal frequency higher than the drive frequency.

Along with the FWM bandwidth, the normalized conversion efficiency (NCE) is also an important parameter to evaluate the nonlinear conversion efficiency in FWM operation, which is defined as follows (Koltchanov et al., 1996; C. Wang, Frédéric Grillot, et al., 2013):

$$\eta_{NCE} = \frac{P_s}{P_p P_d^2} \quad (6.3)$$

where P_s , P_p , P_d account for the power of signal, probe and drive, respectively. The above equation indicates that the NCE is directly determined by the $\chi^{(3)}$ non-linearity hence it gives an insight for the FWM conversion at the material level. Eq. (6.3) is firstly proposed to a semiconductor optical amplifier (SOA), however, the nonradiative recombinations that exist in a semiconductor laser is not taken into

account by it. In addition, another definition is also widely used to evaluate the conversion efficiency (CE), which is expressed as:

$$\eta_{CE} = \frac{P_s}{P_p} \quad (6.4)$$

In contrast to the NCE, the CE is more explicit and it gives a description of the nonlinear conversion at the device level.

Along with the nondegenerated FWM, the degenerated and nearly degenerated FWMs are also commonly observed mechanisms in a $\chi^{(3)}$ material, which have been utilized as an efficient approach to generate optical frequency combs from an on-chip microresonator (Kippenberg, Holzwarth, and Diddams, 2011). Their differences from the first case described in this section come from the fact that two of the four photons are perfectly or nearly identical. However, their occurrences are all based on the $\chi^{(3)}$ optical nonlinearity. As a result, FWM is able to transfer a signal that is modulated on an optical channel onto another one in the range of optical frequency, which is the principle to realize an optical wavelength converter. In addition, approaches such as the cross-gain and cross-phase modulations or electro-optic (EO) modulation can lead to a frequency conversion efficiently, however, the channel spacing is limited to the modulation format transparency and the bandwidth of the RF modulator (Yoo, 1996; Torres-Company and Weiner, 2014). In this context, the optical frequency converters and the optical frequency combs that are based on FWM pave the way for developing high-performance sources for dense wavelength-division multiplexing (DWDM) technologies and for all-optical signal processing on a photonic integrated circuit (PIC) (Vivien and Pavesi, 2016).

6.2 Four-wave mixing in quantum-dots

As aforementioned, the FWM conversion efficiency is dependent on the frequency detuning. This effect is attributed to the different mechanisms such as the carrier density pulsation (CDP), the spatial hole burning (SHB) and the carrier heating (CH) that affect the $\chi^{(3)}$ susceptibility in different detuning conditions. The relationship between them is expressed as follows:

$$\chi^{(3)} = \chi_{CDP}^{(3)} + \chi_{SHB}^{(3)} + \chi_{CH}^{(3)} \quad (6.5)$$

where $\chi_{CDP}^{(3)}$, $\chi_{SHB}^{(3)}$ and $\chi_{CH}^{(3)}$ account for the contributions of these mechanisms to the $\chi^{(3)}$ susceptibility. Figure 6.2 depicts the FWM efficiencies as a function of the absolute frequency detuning that are attributed to the different mechanism in

semiconductor QDs. The CDP plays a predominant role in determining the $\chi^{(3)}$ coefficient in the low detuning condition where $\Delta\nu$ is below 100 GHz. However, the contributions from the SHB and the CH predominate the FWM efficiency in the large detuning condition where $\Delta\nu$ approaches terahertz. In addition, the FWM efficiencies in the full detuning range are at the same level for the cases of stokes (All (+)) and antistokes (All (-)), which is attributed to the near-zero α_H -factor offered by QDs. As introduced in Chap. 2, a zero α_H results in the symmetric $\chi^{(3)}$ with respect to the sign of frequency detuning. The larger the α_H , the larger the discrepancy between the $\chi^{(3)}$ in stokes and in antistokes condition. As a consequence, the FWM efficiencies in QD devices exhibit a high degree of symmetry between the stokes and antistokes cases (Heming Huang, Schires, et al., 2015; Jianan Duan, Weng W Chow, et al., 2021).

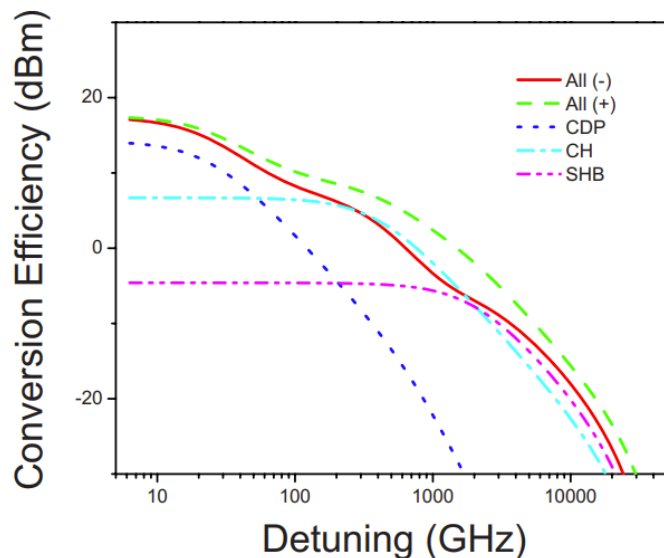


Figure 6.2: Contributions from carrier-density pulsation (navy), carrier heating (blue), and spectral-hole burning (purple) to the FWM efficiency. The cases for stokes and antistokes are represented by All (+) and All (-), respectively. From Ref. (D. Nielsen and S. L. Chuang, 2010).

On the other hand, a near-zero α_H -factor is also beneficial for maximizing the FWM efficiency. Figure 6.3(a) depicts the FWM efficiency as a function of the frequency detuning for a QD SOA. The case for a bulk SOA is shown in Fig. 6.3(b) for comparison. Owing to the low α_H -factor in QDs, the FWM gain in stokes and antistokes conditions not only show a higher degree of symmetry, but also exhibit a much stronger conversion power level than the bulk device. For instance, the FWM gain of the QD SOA is around -13 dB when the positive frequency detuning

is fixed to 100 GHz, whereas that of the bulk SOA is about 3 dB lower in the same detuning condition. The discrepancy between the FWM gain of these two devices enlarges as the frequency detuning increases. In general, the QD devices including the SOAs and the lasers can realize a high FWM bandwidth exceeding terahertz and a high conversion efficiency approaching 0 dB (Meuer et al., 2011; Heming Huang, Schires, et al., 2015).

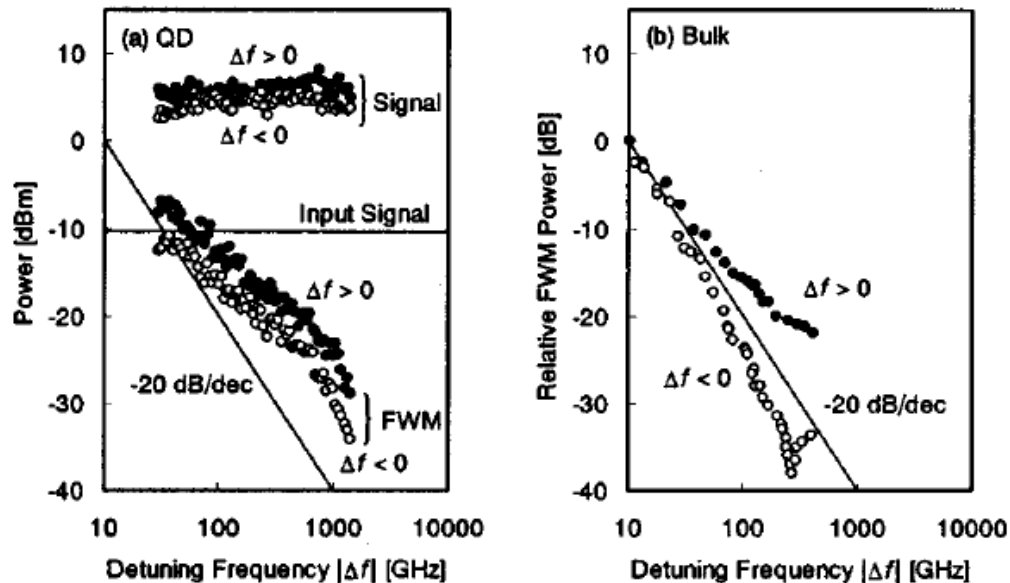


Figure 6.3: FWM efficiency as a function of frequency detuning for (a) and (b) bulk. The stokes case is defined as $\Delta f > 0$ in this paper. From Ref. (Akiyama, Kuwatsuka, et al., 2002).

6.3 Towards QD-based self-mode-locked optical frequency comb and quantum light generator

To realize an efficient FWM conversion, $\chi^{(3)}$ nonlinear materials such as photonic crystal fibre (Tuan et al., 2013), microresonator (Kippenberg, Holzwarth, and Diddams, 2011; Xiang et al., 2021) and III-V semiconductors (Su et al., 2005; Meuer et al., 2011; Contestabile, Maruta, and Kitayama, 2014) are widely used approaches. Compared to the last approach, the length of dozens of centimeters makes the fibre-based converter not an ideal solution for photonic integration applications; the high quality factor cavity required for the microresonator-based converter prevents it from a low-cost solution in the near future. Therefore, the mature SOAs and semiconductor lasers provide a solution of small-footprint, electric pump available,

large conversion efficiencies due to the simultaneous availability of gain, and the ease of integration with other components. In this context, semiconductor QD is promising to serve as the on-chip FWM generator, owing to its rich $\chi^{(3)}$ optical nonlinearities along with its high emission performance on silicon substrate. A direct application of this peculiar property of QD is to use it as an on-chip source for self-mode-locked frequency comb generation with neither the external pump photons nor the saturable absorber (SA) (Gosset et al., 2006). Despite the mode-locking behavior generated from a single-section semiconductor laser could be attributed to the unaccounted saturable absorption from the uneven current injection, it can be also attributed to the self-mode-locking (SML) mechanism that occurs in a material with rich optical nonlinearities (Weng W Chow, Songtao Liu, et al., 2020). By utilizing QD or QDash as the gain medium, single-section Fabry-Perot (FP) lasers grown either on native substrate or Si substrate are observed to generate sub-picosecond pulse width, kilohertz RF linewidth and terahertz optical bandwidth (Rosales, Murdoch, et al., 2012; Joshi et al., 2014; Liu, Jung, et al., 2018). Figures 6.4 depict the time domain and RF domain response of an epitaxial self-mode-locked QD laser on Si. The device reported exhibits a repetition rate at 31 GHz with an optimum RF linewidth of 100 kHz. In particular, the 490 fs pulse width observed is comparable with the state-of-art of semiconductor mode-locked laser.

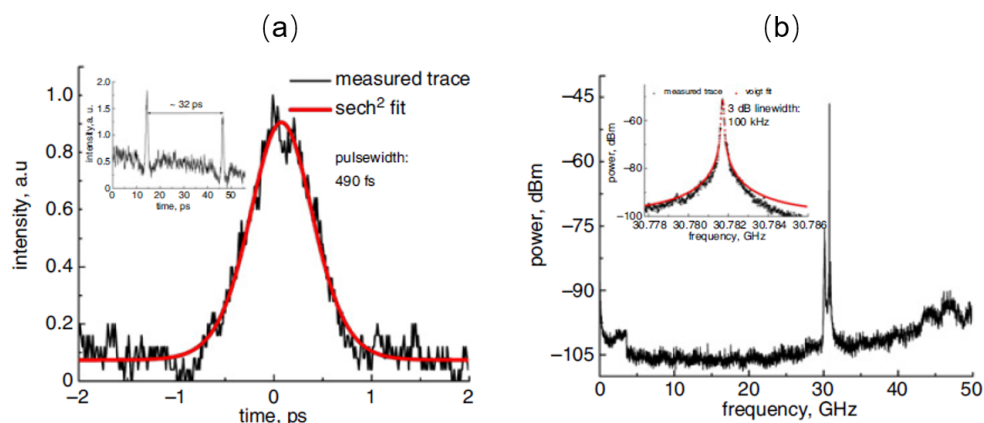


Figure 6.4: Characterizations of an epitaxial self-mode-locked QD laser on Si: (a) sech^2 -shape optical pulse and (b) RF response. From Ref. (Liu, Jung, et al., 2018).

In addition to the SML, the FWM technique exhibits a strong potential to be applied to generate quantum states of light. Its application to an on-chip microresonator enables it to generate dissipative kerr soliton (DKS), which paves the way for

enlarging the optical bandwidth to the octave-span (Kippenberg, Gaeta, et al., 2018). Owing to the rich $\chi^{(3)}$ nonlinear susceptibility and the consequent strong degenerate FWM of microresonator, on-chip light squeezer with dual-pump configuration exhibits a squeezed noise level below the photocurrent shot noise, as shown in Fig. 6.5 (Y. Zhao et al., 2020). These pioneering work give insights for developing CMOS available quantum light generators by taking advantage of the rich optical nonlinearities of QD. In this context, it is crucial to understand and to maximize the FWM efficiency of QD laser before it is available for reliably generating the self-mode-locked frequency comb and the quantum states of light.

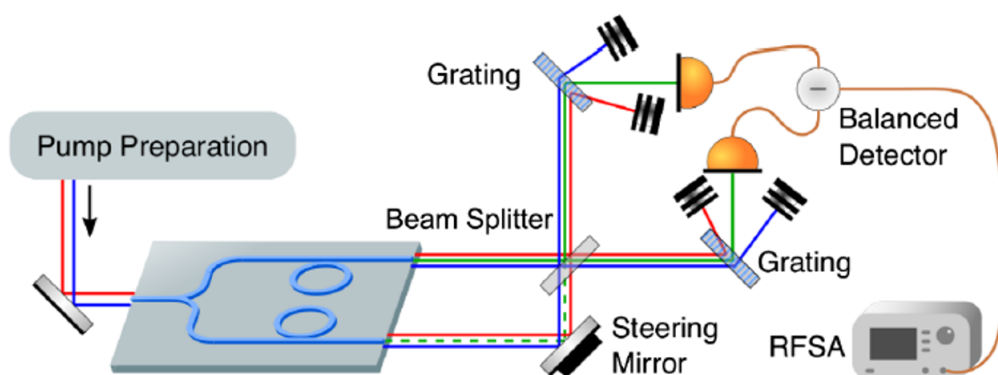


Figure 6.5: Experimental schematic for light squeezing in microresonators. From Ref. (Y. Zhao et al., 2020).

The FWM theories for SOAs have been extensively studied (Koltchanov et al., 1996; Diez et al., 1997). However, some basic properties in the process of lasing such as the absorption and the nonradiative recombinations are not taken into account, thus the FWM process in a semiconductor laser can not be reliably reproduced by those theories. In this thesis, investigations of the FWM mechanism in epitaxial QD lasers in both theoretical analysis and experiments are performed. The simulation model described in this chapter takes into account the enhanced cavity resonances and the reduced amplified spontaneous emission noise during the process of lasing. Other optical nonlinear contributions including the mode competition, gain saturation, carrier-induced refractive index, α_H -factor and creation of combination tones are all included in this model to have a complete picture of the FWM in a semiconductor laser. The model performed in this thesis exhibits its potential to be an analytical tool for band-structure engineering to optimize device design. Experiments are performed to verify the validity of theory. Comparisons of the FWM efficiency and

bandwidth between the QD and the QW lasers are investigated to demonstrate how a PIC can benefit from the enhanced FWM efficiency of QD.

6.4 Theory of nondegenerate four-wave mixing

Based on the concept of Fig. 6.1, a theoretical model which is developed by Dr. Weng W. Chow within Sandia National Laboratories, Albuquerque, USA is described as follows. The model takes into account the injected intensities of the incoming drive and probe, I_d^{inj} and I_p^{inj} , respectively, and the outgoing intensities of the drive, probe and signal, I_d^{out} , I_p^{out} and I_s^{out} , respectively. The intra-cavity intensities are expressed by I_d , I_p and I_s . The remaining idler along with other nonlasing modes are collectively denoted by I_n . In this study, the third-order nonlinear susceptibility is re-expressed by $\chi_{sdpd}^{(3)}$, which accounts for the three fields circulating within the laser cavity.

To study what happens in the case of semiconductor laser and to extract the related coefficients, the gain saturation, mode competition and multi-wave mixing on equal footing (D. Nielsen and S. L. Chuang, 2010) must be well taken into account. Therefore, our simulation is based on a semiclassical treatment that involves the intensity of cavity modes (Sargent III, Scully, and Lamb Jr, 1974). The I_d , I_p , I_s and I_n can thus be expressed by the following relationships:

$$\frac{d}{dt}i_d = \left(g_d^{sat} - \frac{\nu_0}{Q}\right)i_d + \frac{c}{2Ln_b}\sqrt{T_1 i_d^{inj}}i_d + s \quad (6.6)$$

$$\frac{d}{dt}i_p = \left(g_p^{sat} - \frac{\nu_0}{Q}\right)i_p + \frac{c}{2Ln_b}\sqrt{T_1 i_p^{inj}}i_p + s \quad (6.7)$$

$$\frac{d}{dt}i_s = \left(g_s^{sat} - \frac{\nu_0}{Q}\right)i_s + \sqrt{2}|\vartheta_{sdpd}|i_d\sqrt{i_s i_p} + s \quad (6.8)$$

$$\frac{d}{dt}i_n = \left(g_n^{sat} - \frac{\nu_0}{Q}\right)i_n + s \quad (6.9)$$

where the intensities of the four fields are transformed to dimensionless quantities:

$$i_m = \frac{2}{\epsilon_0 c n_b} \left(\frac{\varphi}{2\hbar\gamma}\right)^2 I_m \quad (6.10)$$

with ϵ_0 and c the permittivity and speed of light in vacuum. n_b denotes the background refractive index, φ and γ are the dipole matrix elements of the active region and the dephasing rate, respectively. The ratio of the average cavity mode frequency ν_0 and the cavity quality factor Q is expressed as follows:

$$\frac{\nu_0}{Q} = \frac{c}{n_b} \left[\alpha_{abs} - \frac{1}{2L} \ln(R_1 R_2) \right] \quad (6.11)$$

with α_{abs} the intra-cavity absorption, L the laser cavity length, R_1 and R_2 the facet power reflectivities. The saturated modal gain of each cavity mode g_m^{sat} ($m = d, p, s, n$) is written as:

$$g_m^{sat} = \frac{g_m}{1 + \kappa_{mm}i_m + \sum_{k \neq m} \kappa_{m,k}i_k} \quad (6.12)$$

where g_m is the unsaturated (small signal) modal gain, κ_{mm} is the self gain compression factor and $\kappa_{m,k}$ denotes the cross gain compression factor. The spontaneous emission s in Eqs. (6.6) - (6.9) is described by:

$$s = \frac{\hbar\nu_0\beta B_{2d}}{2\varepsilon_0 n_B^2 d_l} \left(\frac{\wp}{2\hbar\gamma} \right)^2 n_{e0} n_{h0} \quad (6.13)$$

with β the spontaneous emission factor, B_{2d} the bimolecular carrier recombination coefficient, and d_l the thickness of each layer of QDs. n_{e0} and n_{h0} denote the density of the electrons and holes in the ground states.

The gain parameters including g_m , κ_{mm} and $\kappa_{m,k}$ are dependent on the carrier densities. In this study, a comparison of the FWM efficiency between the QD and QW laser is investigated. However, the electronic structures of these two gain media are different. As such, the descriptions of the carrier densities are not identical for these devices. The following definitions are only valid for the QD laser. However, the reader are invited to consult the case for QW laser by a multimode semiclassical theory which has been reported previously (Frédéric Grillot, J. C. Norman, et al., 2020; Weng W Chow, Songtao Liu, et al., 2020). For QD laser, the carrier densities at the ground states are expressed as (Weng W Chow and S. W. Koch, 2005; Waldmueller et al., 2006):

$$\begin{aligned} \frac{dn_{e0}}{dt} = & -\frac{\varepsilon_0 n_b^2 d_l}{\hbar\nu_0 \Gamma_{conf}} \left(\frac{2\hbar\gamma}{\wp} \right)^2 \sum_m g_m^{sat} i_m - \gamma_r (n_{e0} - n_{e0}^{eq}) \\ & - B_{2d} n_{e0} n_{h0} - \gamma_{nr} n_{e0} - C_{2d} n_{e0}^2 n_{h0} \end{aligned} \quad (6.14)$$

$$\begin{aligned} \frac{dn_{h0}}{dt} = & -\frac{\varepsilon_0 n_b^2 d_l}{\hbar\nu_0 \Gamma_{conf}} \left(\frac{2\hbar\gamma}{\wp} \right)^2 \sum_m g_m^{sat} i_m - \gamma_r (n_{h0} - n_{h0}^{eq}) \\ & - B_{2d} n_{e0} n_{h0} - \gamma_{nr} n_{h0} - C_{2d} n_{e0} n_{h0}^2 \end{aligned} \quad (6.15)$$

The stimulated emission effect is described by the first terms on the right-hand side of the above equations, where Γ_{conf} denotes the mode confinement factor. The effect of carrier relaxation of all the states towards quasi-equilibrium is described by the

second terms, where γ_r and $n_{e0,h0}^{eq}$ account for the effective carrier scattering rate and the quasi-equilibrium densities, respectively. The carrier equilibrium is assumed to take place within each density group. It is worth stressing that $n_{e0,h0}$ never equal to $n_{e0,h0}^{eq}$ due to dynamic population bottleneck. The last terms with γ_{nr} and C_{2d} account for carrier losses from defect that originates from Shockley-Read-Hall recombination and Auger scattering, respectively.

Given that the active region of the QD device is a dot-in-well (DWELL) structure, the carrier densities in the excited states n_{e1} , n_{h1} , and those in the QW layers n_{e2} , n_{h2} are written as follows:

$$\begin{aligned} \frac{dn_{e1}}{dt} = & -\gamma_r (n_{e1} - n_{e1}^{eq}) - B_{2d}n_{e1}n_{h1} \\ & -\gamma_{nr}n_{e1} - C_{2d}n_{e1}^2n_{h1} \end{aligned} \quad (6.16)$$

$$\begin{aligned} \frac{dn_{h1}}{dt} = & -\gamma_r (n_{h1} - n_{h1}^{eq}) - B_{2d}n_{e1}n_{h1} \\ & -\gamma_{nr}n_{h1} - C_{2d}n_{e1}n_{h1}^2 \end{aligned} \quad (6.17)$$

$$\begin{aligned} \frac{dn_{e2}}{dt} = & \frac{\eta J}{e} - \gamma_r (n_{e2} - n_{e2}^{eq}) \\ & -B_{2d}n_{e2}n_{h2} - \gamma_{nr}n_{e2} - C_{2d}n_{e2}^2n_{h2} \end{aligned} \quad (6.18)$$

$$\begin{aligned} \frac{dn_{h2}}{dt} = & \frac{\eta J}{e} - \gamma_r (n_{h2} - n_{e2}^{eq}) \\ & -B_{2d}n_{e2}n_{h2} - \gamma_{nr}n_{h2} - C_{2d}n_{e2}n_{h2}^2 \end{aligned} \quad (6.19)$$

where J is the injected current density and η is the injection efficiency from electrodes to QW states.

To calculate the saturated gain g_m in Eq. (6.12), we use the following expressions that is given by semiclassical laser theory:

$$g_m = [f_{e0,m} + f_{h0,m} - 1] \frac{\nu_0 \wp^2 N_{qd} \Gamma_{conf}}{\epsilon_0 n_b^2 \hbar \gamma d_l} \Lambda_m \quad (6.20)$$

where

$$\Lambda_m = \int_{-\infty}^{\infty} d\omega \frac{1}{\sqrt{2\pi}\Delta_{inh}} \exp \left[-\left(\frac{\omega - \omega_0}{\sqrt{2}\Delta_{inh}} \right)^2 \right] L(\omega - \nu_m) \quad (6.21)$$

$$L(\omega - \nu_m) = \frac{\gamma^2}{\gamma^2 + (\omega - \nu_m)^2} \quad (6.22)$$

the quantity inside the square bracket in Eq. (6.20) describes the population inversion. $f_{e0,m}$ and $f_{h0,m}$ account for the Fermi functions evaluated for the instantaneous

ground state densities n_{e0} and n_{h0} , which contribute to the lasing transition at frequency ν_m . Δ_{inh} is assumed to be the width of the Gaussian distribution inhomogeneous broadening in QDs and QWs.

Then, the self- and cross gain-compression factors of QDs in Eq. (6.12) can be expressed as follows:

$$\kappa_{mm} = 3 \frac{\gamma}{\gamma_{ab}} \frac{1}{\Lambda_m} \int_{-\infty}^{\infty} d\omega \frac{1}{\sqrt{2\pi}\Delta_{inh}} \exp \left[- \left(\frac{\omega - \omega_0}{\sqrt{2}\Delta_{inh}} \right)^2 \right] \times L^2(\omega - \nu_m) \quad (6.23)$$

$$\begin{aligned} \kappa_{m,k} &= \frac{\gamma}{\gamma_{ab}} \left(1 + \frac{\zeta_{mk}}{2} \right) \frac{1}{\Lambda_m} \\ &\times \int_{-\infty}^{\infty} d\omega \frac{1}{\sqrt{2\pi}\Delta_{inh}} \exp \left[- \left(\frac{\omega - \omega_0}{\sqrt{2}\Delta_{inh}} \right)^2 \right] \\ &\times \left\{ +Re \left\{ \begin{array}{l} 2L(\omega - \nu_m) L(\omega - \nu_k) \\ D_{\gamma_{ab}}(\nu_k - \nu_m) D_{\gamma}(\omega - \nu_m) \\ \times [D_{\gamma}(\nu_k - \omega) + D_{\gamma}(\omega - \nu_m)] \end{array} \right\} \right\} \end{aligned} \quad (6.24)$$

where

$$D_{\alpha}(x) = \frac{\alpha}{\alpha + ix} \quad (6.25)$$

γ_{ab} denotes the scattering rate within the QDs. ζ_{mk} accounts for the effects of spatial hole burning in presence of carrier diffusion, which is written as:

$$\zeta_{mk} = \frac{1}{L} \int_0^L dz \cos [2(k_m - k_k)z] = \delta_{m,k} \quad (6.26)$$

In case of carrier diffusion plays the dominate role, $\zeta_{mk} = 1$ for all combinations of m and k .

To extract the $\chi_{sdpd}^{(3)}$ susceptibility of the QD laser, Eqs. (6.14) - (6.19) should be solved. θ_{sdpd} in Eq. (6.8) denotes the relative phasing angle coefficient that is varied to fit the experimental data (Sargent III, Scully, and Lamb Jr, 1974). Thus, $\chi_{sdpd}^{(3)}$ is expressed by the following relationship:

$$\chi_{sdpd}^{(3)} = \frac{\sqrt{2}n_b}{\nu_0\Gamma_{conf}} \left(\frac{\wp}{2\hbar\gamma} \right)^2 |\theta_{sdpd}| \quad (6.27)$$

The intensity of signal is then determined by $\chi_{sdpd}^{(3)}$ through θ_{sdpd} . Recent studies demonstrate that θ_{sdpd} can be derived from a first-principle based multimode laser

theory (Weng W Chow, Songtao Liu, et al., 2020; Frederic Grillot et al., 2020). In FWM operation, θ_{sdpd} is expressed by including the fields of drive, probe and signal:

$$\begin{aligned}
|\theta_{sdpd}| &= (f_{e,s} + f_{h,s} - 1) \frac{v_0 \wp^2 N_{QD}^{(2d)} \Gamma_{conf}}{2\epsilon_0 n_b^2 \hbar \gamma d_l} \frac{\gamma}{\gamma_{ab}} \frac{1}{2} (1 + 2\zeta) \\
&\times \int_{-\infty}^{\infty} d\omega \frac{1}{\sqrt{2\pi}\Delta_{inh}} e^{-[(\omega-\omega_0)/\sqrt{2}\Delta_{inh}]^2} \\
&\times \left| \begin{array}{c} D_\gamma(\omega + \nu_p - 2\nu_d) \\ \times D_{\gamma_{ab}}(\nu_p - \nu_d) [D_\gamma(\nu_p - \omega) + D_\gamma(\omega - \nu_d)] \end{array} \right| \quad (6.28)
\end{aligned}$$

with ν_d and ν_p the frequency of drive and probe, respectively. The frequency of the signal ν_s is thus determined by $\nu_s = 2\nu_d - \nu_p$.

Finally, the author introduces a quantity ξ that depends only on the electronic structure and broadenings associated with carrier scattering to describe the $\chi_{sdpd}^{(3)}$ coefficient, by solving Eqs. (6.20), (6.27) and (6.28):

$$\begin{aligned}
\xi &\equiv \chi_{sdpd}^{(3)} \frac{c\Gamma_{conf}}{n_b g_s} \\
&= \frac{\sqrt{2}c}{v_0 \Lambda_s} \left(\frac{\wp}{2\hbar\gamma} \right)^2 \frac{\gamma}{\gamma_{ab}} \frac{1}{2} (1 + 2\zeta) \\
&\times \int_{-\infty}^{\infty} d\omega \frac{1}{\sqrt{2\pi}\Delta_{inh}} e^{-[(\omega-\omega_0)/\sqrt{2}\Delta_{inh}]^2} \\
&\times \left| \begin{array}{c} D_\gamma(\omega + \nu_p - 2\nu_d) \\ \times D_{\gamma_{ab}}(\nu_p - \nu_d) [D_\gamma(\nu_p - \omega) + D_\gamma(\omega - \nu_d)] \end{array} \right| \quad (6.29)
\end{aligned}$$

with g_s the material small signal gain of the active region.

Following the definition of Eq. (6.29), we now have a FWM coefficient that is determined by the $\chi_{sdpd}^{(3)}$ coefficient and is independent of the laser configuration, such as confinement factor, QD density, heterostructure layer thicknesses and injection current. A comparison between the $\chi_{sdpd}^{(3)}$ dependent frequency conversion efficiencies of QD and QW devices can thus be made, regardless of their different configurations. Despite the improvement of the FWM model for analyzing a semiconductor laser, the effects of group velocity dispersion (GVD) as well as the self phase modulation (SPM) caused by the lossy cavity is not included in this model. It is worth stressing that these two effects play important roles in determining the self-mode-locking efficiency in a single-section MLL and the FWM efficiency in microring resonators (Jiao et al., 2013; Kippenberg, Holzwarth, and Diddams, 2011). Therefore, further studies for completing the FWM theories remain to be investigated.

6.5 Devices studied and input parameters for the model

The epitaxial QD laser on Si with p-modulation doping in the active region has been described in Sec. 3.8. Due to its 1.35 mm-long cavity length, the free spectral range (FSR) is found at about 30 GHz. For the QW laser, its FP cavity length is 400 μm that results in a 100 GHz FSR, the same as-cleaved coatings as those on the QD laser are applied to both facets. The device parameters for the simulations are listed in Tab. 6.1.

Device parameter	Symbol	Value	
		QD	QW
QD/QW layers	n_{qd}	5	6
QD density	N_{qd}	$4 \times 10^{14} \text{ m}^{-2}$	N/A
QD/QW layer thickness	d_l	7 nm	8 nm
Barrier thickness	d_b	40 nm	40 nm
Waveguide cross section	$w \times d_{wg}$	$4.9 \mu\text{m} \times 0.3 \mu\text{m}$	$1.4 \mu\text{m} \times 0.218 \mu\text{m}$
Cavity length	L	1.1 mm	450 μm
Facet reflectivities	R_1, R_2	0.32, 0.32	0.32, 0.32
Mode spacing	Δ_c	30 GHz	100 GHz
Inhomogeneous width	Δ_{inh}	10 meV	0
Mode confinement factor	Γ_{conf}	0.06^\dagger	0.22

Table 6.1: Device parameters. † Computed for QW embedding QDs.

Model parameter	Symbol	Value	
		QD	QW
Dephasing rate	γ	$1 \times 10^{13} \text{ s}^{-1}$	$2 \times 10^{13} \text{ s}^{-1}$
QD-QW scattering rate	γ_r	$1 \times 10^{13} \text{ s}^{-1}$	N/A
Inter-QD scattering rate	γ_{ab}	$5 \times 10^{11} \text{ s}^{-1}$	N/A
Defect loss rate	γ_{nr}	$2 \times 10^9 \text{ s}^{-1}$	$0.05 \times 10^9 \text{ s}^{-1}$
Bimolecular recombination coefficient	B_{2d}	$1.4 \times 10^{-8} \text{ m}^2 \text{ s}^{-1}$	$2.0 \times 10^{-8} \text{ m}^2 \text{ s}^{-1}$
Auger coefficient †	C_{2d}	$3.5 \times 10^{-22} \text{ m}^4 \text{ s}^{-1}$	$3.5 \times 10^{-22} \text{ m}^4 \text{ s}^{-1}$
Spontaneous emission factor	β	1×10^{-3}	1×10^{-5}
intra-cavity absorption	α_{abs}	1600 m^{-1}	2000 m^{-1}
Spatial hole burning	ζ_{mk}	0.5	<0.5

Table 6.2: Model input parameters. † Calculated from $C_{2d} = C_{3d}/d_{qw}^2$ with $C_{3d} = 1.7 \times 10^{-38} \text{ m}^6 \text{ s}^{-1}$.

To determine the values of the remaining parameters for the simulation, a fitting between the simulated data and the experimental one is required. The values listed

in Tab. 6.2 are substituted in the model to have the calculated curves shown in Fig. 6.6. Figure 6.6(a) depicts the light-current curves of the QD (burgundy) and QW (jade) lasers measured at 25°C. The threshold current I_{th} of the QD and QW device is 34 mA and 14 mA, respectively. The higher threshold current observed from the former device is attributed to the p-type doping in the active region, which increases the optical loss by increasing the free carrier absorption that results from the large number of holes in the QDs. The optical spectra of the QD (burgundy) and QW (jade) lasers at $2 \times I_{th}$ are shown in Figs. 6.6(b) and (c), respectively. The optical gain peak of the QD laser being 1295 nm is 18 nm longer than that of its counterpart. The black points depict the calculated power of each mode. As shown, the simulations well reproduce the spectral shape in experiments. The good agreement between the calculated and measured optical spectra gives reasonable values for the intra-cavity absorption α_{abs} , the injection efficiency η , the defect loss rate γ_{nr} , the scattering rates γ , γ_r , γ_{ab} and the spatial hole burning parameter ζ_{mk} . When the modes near the optical gain peak begin to lase, a strong mode competition takes place. Such an effect is identified by the simulation in the presence of the spiky spectra. Despite the small discrepancy near the gain peak, it is important to show these calculated spectra since the mode competition phenomena is not clearly performed by the experimental one. In addition, the values of some parameters listed in Tab. 6.2 are in agreement with those reported in earlier studies (Seebeck et al., 2005; Matsusue and Sakaki, 1987; Coldren, Corzine, and Mashanovitch, 2012).

6.6 Low group velocity dispersion in quantum-dot laser

The GVD is regarded as a limiting factor for a large optical bandwidth generation in a microresonator-based OFC, due to the increased mismatch between the frequency comb modes and the cavity modes that decreases the FWM efficiency (Kippenberg, Holzwarth, and Diddams, 2011). Same effect can be also observed in conventional FP resonant cavity, in presence of the free spectral range (FSR) of the cavity varying with the wavelength. Note that the GVD effect is no longer negligible if the pulse duration is reduced to the level of hundreds femto-seconds (Jiao et al., 2013). It is worth stressing that a low GVD is beneficial for shortening the pulse duration and increasing the optical bandwidth. It has been reported that approaches such as dual grating dispersion compensators allow for largely reducing the pulse duration by more than 15 fold (Jimyung Kim, Choi, and Delfyett, 2006). Recently, approaches including external optical feedback and multi-section waveguides design have been applied to FP cavity quantum-cascade lasers (QCL) for GVD compensation in order

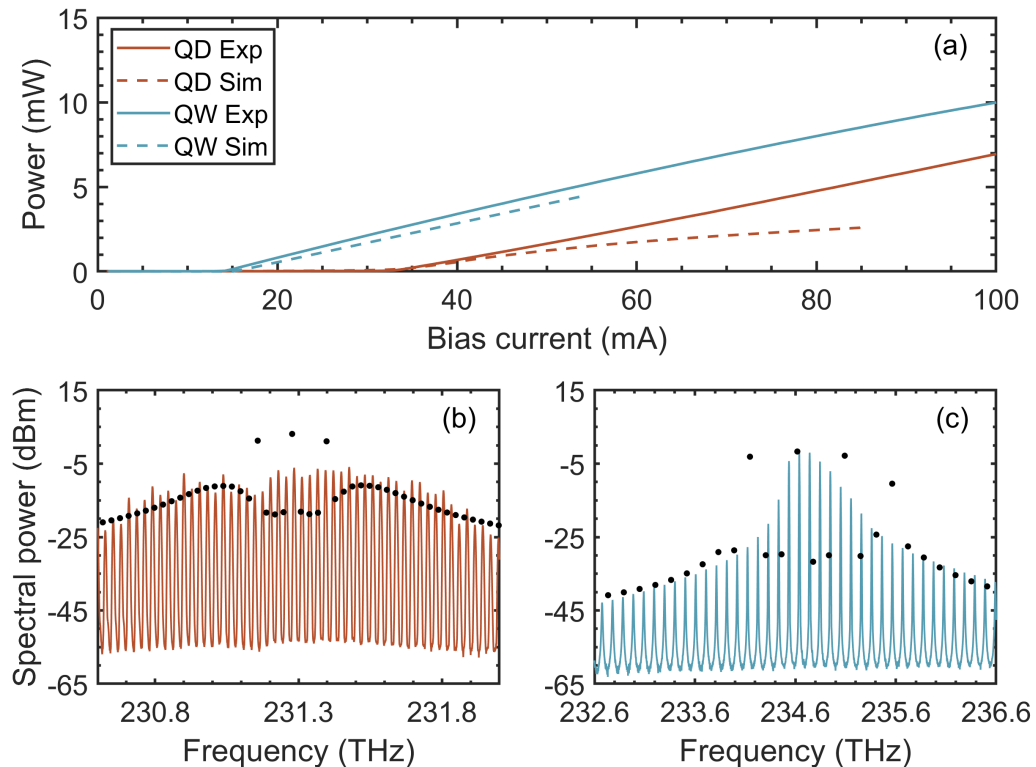


Figure 6.6: (a) Light-current characteristics of the QD (burgundy) and QW (jade) laser. Measured and calculated curves are performed by solid and dashed lines, respectively. Experimental optical spectrum of (b) QD and (c) QW laser at $2 \times I_{th}$. Calculated mode powers are performed by the black points. Measurements are taken at 25°C .

to improve the frequency comb bandwidth (Hillbrand et al., 2018; R. Wang et al., 2020). Despite the absence of GVD effect in our theoretical model, it has a direct impact on the FWM efficiency in the semiconductor laser and an experimental study is worth investigating. Figure 6.7(a) depicts the optical spectrum (jade) and corresponding FSR as a function of frequency (burgundy) for the QD laser when it operates at $2 \times I_{th}$. The case for QW laser is shown in Fig. 6.7(b). The QD laser has a low GVD in presence of the FSR ≈ 28 GHz barely changing with the mode frequency within a range of 6 THz. In contrary, the GVD in the QW device is much larger, which is confirmed by the decrease of FSR from 104 to 102 GHz with the increase of mode frequency from 231.6 to 237.6 THz. As a consequence, the near-zero GVD in QD allows the laser to have a high FWM efficiency as well as a high FWM bandwidth. The OFC technology can thus take advantage of the low-dispersion semiconductor QDs to realize high-performance self-mode-locked

lasers.

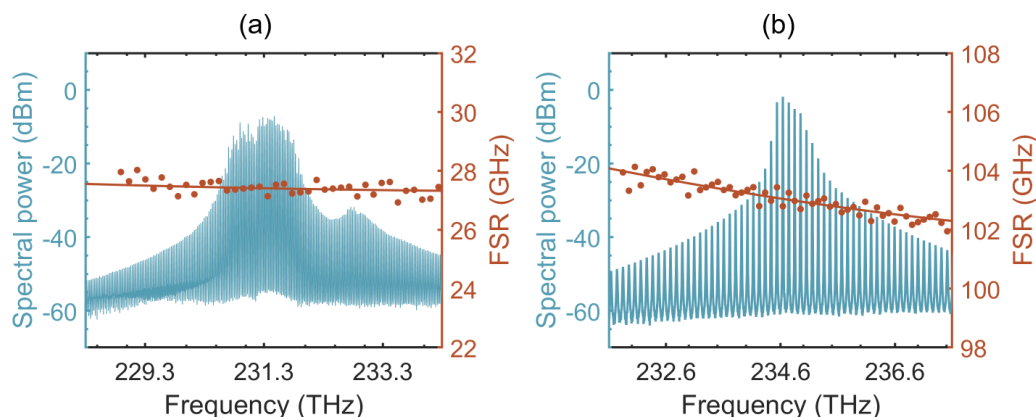


Figure 6.7: Optical spectrum (jade) and corresponding free spectral range (FSR) as a function of longitudinal mode frequency (burgundy) for (a) QD and (b) QW laser at $2 \times I_{th}$. The burgundy solid lines are guiding lines for the variation of FSR.

6.7 Nondegenerate four-wave mixing apparatus in experiments

Figure 6.8 depicts the experimental setup for the dual-pumped nondegenerate FWM operation. To realize a high FWM efficiency, the drive and the probe lasers should be single-frequency tunable sources with narrow-linewidth. The outputs of drive and probe lasers are firstly incorporated by a 90/10 fibre-based optical coupler and then they are sent into the QD/QW laser from the port 1 to port 2 of an optical circulator and a lens-end fibre. The polarization controllers that are inserted into the paths of drive and probe lasers are used to align the polarization of these two pump lasers with that of the QD/QW laser for maximizing the conversion efficiency. For the optical circulator, an isolation above 30 dB from the port 2 to the port 1 must be ensured to eliminate any undesired back-reflection. The output of the FWM light is coupled out from the port 2 of the optical circulator and finally it is sent to an optical spectrum analyzer (OSA) with a 20 pm resolution through the port 3. In this study, the temperature conditions for the QD and QW lasers are fixed to 25°C by using a thermoelectric cooler.

In nondegenerate FWM operation, the drive laser is applied to one longitudinal mode of the QD/QW laser near its gain peak to lock the other lasing modes below threshold. Ensuring that the laser operates in the stable-locking regime in presence of the optical signal-to-noise ratio (OSNR) of the drive laser above 30 dB, the probe laser is applied to generate the signal and idler. It is worth stressing that the probe

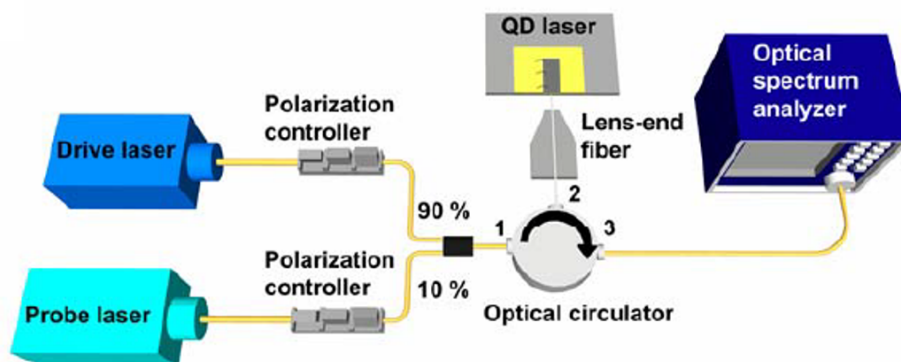


Figure 6.8: Experimental setup for nondegenerate four-wave mixing experiments. From Ref. (Jianan Duan, Weng W Chow, et al., 2021).

frequency must be well adjusted if it is injected to a resonant laser. In the case of a SOA, the probe can be injected to an arbitrary position on the gain profile and its frequency can be tuned continuously. Nevertheless, it is crucial to tune the probe frequency coincident with the peak of one resonant side mode of a laser to minimize the cavity loss thus to have the maximum conversion efficiency. As a result, the probe frequency variation is discrete and the frequency detuning must be fixed to a multiple of the FSR of the laser. Figures 6.9(a) and (b) depict the optical spectra for the QD and QW lasers in Stokes nondegenerate FWM operation, respectively. In both cases, the frequency detuning equals to the FSR (i.e., probe-drive mode number difference $\Delta m = 1$). To determine the conversion efficiency, the power of the drive, probe, and signal are directly extracted from the optical spectra. In addition, all the optical losses including the fibre loss and the coupling loss are taken into account to avoid any underestimation of the conversion efficiency. The plots in different colors shown in Figs. 6.9 illustrate how the signal power increases with the probe power. Owing to the enhanced FWM efficiency by utilizing the QD as the active region, both signal and idler photons are generated in the QD laser, however, the idler is absent in the QW device.

6.8 Enhanced four-wave mixing efficiency in quantum-dot lasers

To evaluate the FWM efficiency of the QD laser, a comparison between the theory and the experiments is performed to verify the validity of the model described in this chapter. In this study, the FWM efficiency is determined by the relationship between the ratio of the signal power to drive power r_{sd} and the ratio of the

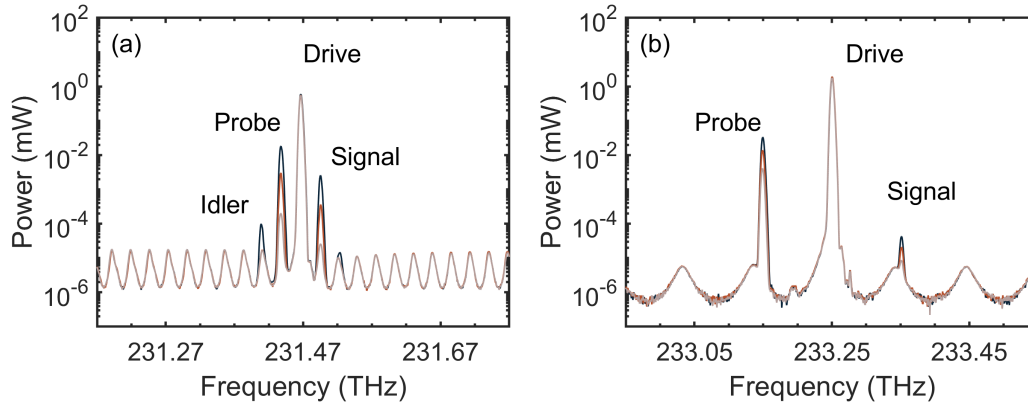


Figure 6.9: Optical spectra in Stokes FWM operation for (a) QD laser with frequency detuning of 30 GHz and (b) QW laser with frequency detuning of 110 GHz (probe-drive mode number difference $\Delta m = 1$). The spectra with the increase of probe power are marked in different colors.

probe power to drive power r_{pd} ; whereas the FWM bandwidth is determined by the frequency detuning $\Delta\nu$. Therefore, the conversion efficiency in FWM operation that is described in Eq. (6.4) can be re-expressed by $\eta_{CE} = r_{sd}/r_{pd}$. Figure 6.10(a) depicts the calculated decimal logarithm of the ratio of signal power to drive power $lg(r_{sd})$ as a function of the decimal logarithm of the ratio of probe power to drive power $lg(r_{pd})$ and the frequency detuning. For the QD laser studied, its r_{sd} increases with the r_{pd} and decreases with the frequency detuning. The high symmetry between the Stokes (i.e. $\Delta\nu < 0$) and anti-Stokes (i.e. $\Delta\nu > 0$) operation is attributed to the near-zero α_H -factor (Duan, Huang, Jung, et al., 2018; Weng W Chow, Songtao Liu, et al., 2020). In particular, the calculated r_{sd} as a function of the r_{pd} when the frequency detuning is fixed to ≈ 30 GHz (dotted lines) and ≈ 1.1 THz (dashed lines) are shown in Fig. 6.10(b). The case for Stokes and anti-Stokes is represented in burgundy and in jade, respectively. Corresponding experimental data are represented by the different markers in same colors. Despite the small discrepancy between the simulation and the experiment at a large frequency detuning and at a low r_{pd} , the theoretical model reproduces the experimental results quite well.

A comparison of the FWM efficiency and the FWM bandwidth between the QD and QW laser is then performed in this section. Figure 6.11(a) depicts the calculated r_{sd} as a function of the r_{pd} for the QD (dotted lines) and the QW (dashed lines) laser, with the frequency detuning fixed to ≈ 110 GHz. The case for Stokes and anti-Stokes is represented in burgundy and in jade, respectively. Corresponding experimental

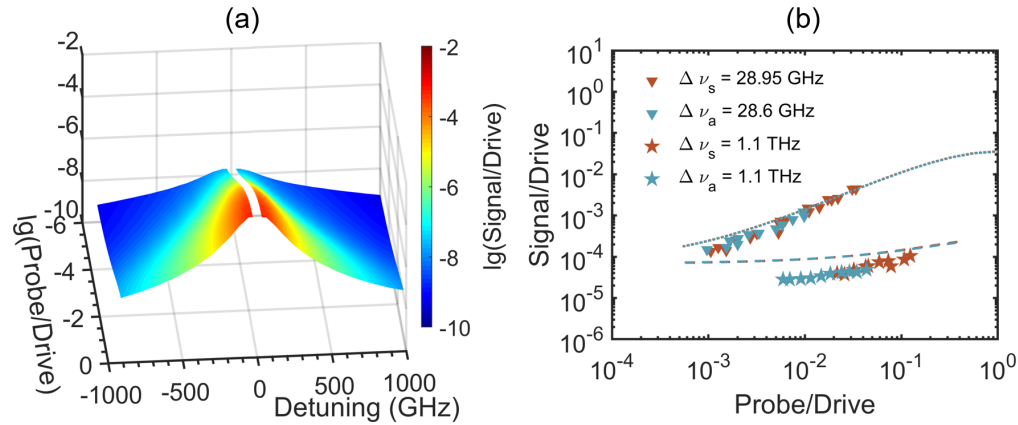


Figure 6.10: (a) Mapping of the calculated signal power versus drive power $lg(r_{sd})$ as a function of the probe power versus drive power $lg(r_{pd})$ and the frequency detuning $\Delta\nu$ for the QD laser. (b) r_{sd} versus r_{pd} for QD laser with different $\Delta\nu$.

data are represented by the different markers in same colors. The perfect agreement between the simulation and the experiment observed from the QW device indicates that the model described in this chapter is an efficient simulation tool to reproduce the FWM process in semiconductor lasers. Nevertheless, the observed discrepancy between the theory and experiments in the QD laser reveals that the FWM efficiency of epitaxial QD laser on Si has not attained its theoretical limit yet. Despite that, the FWM efficiency of QD laser is still about 20 times higher than that of its counterpart in experiment, which is attributed to its improved $\chi_{sdpd}^{(3)}$ nonlinear susceptibility that contributes to the increase of the intensity of signal. In this study, the calculated FWM coefficient ξ for the QD and the QW laser is $4.75 \times 10^{-21} m^3 V^{-2}$ and $2.92 \times 10^{-22} m^3 V^{-2}$, respectively, which is in agreement with the experimental results. Figure 6.11(b) displays the calculated r_{sd} as a function of the frequency detuning for the QD (dotted lines) and QW (dashed lines) laser, with the r_{pd} fixed to 0.02. Again, the case for stokes and antistokes is represented in burgundy and in jade, respectively. Corresponding experimental data are represented by the different markers in same colors. In the full range of frequency detuning up to 1.5 THz, the experimental r_{sd} of QD laser always exhibits a 10~20 time improvement compared to that of the QW laser. Besides, the maximum measurable FWM bandwidth of the QD laser is twice larger than that of its counterpart, which is attributed to its low GVD along with a stronger SHB mechanism that occurs in the large-detuning condition (Asryan and Suris, 2000). The remarkable optical nonlinearities as well as the enhanced FWM efficiency of QD laser give insight for developing compact, low-

cost and energy-efficient self-mode-locked optical frequency combs and quantum light generators for PIC application. Last but not least, it is worth stressing that the FWM efficiency of the QD laser can be further improved. In contrary, the QW laser has attained its theoretical limit.

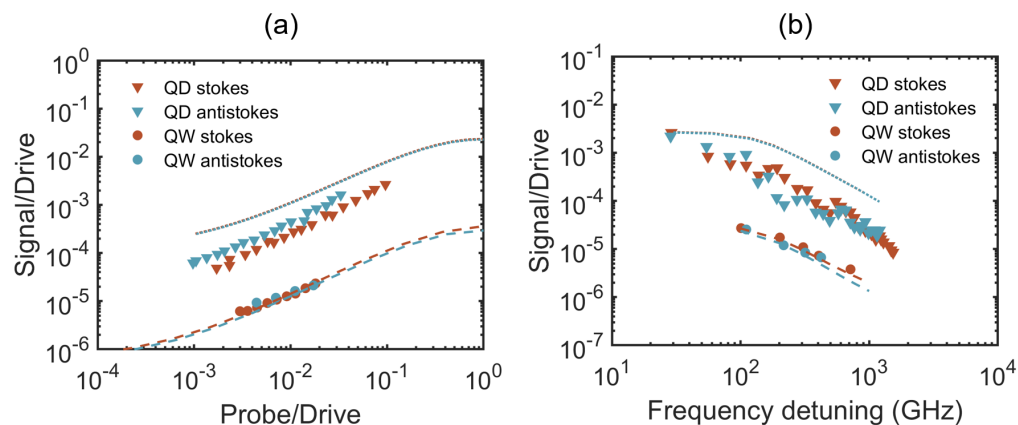


Figure 6.11: (a) r_{sd} versus r_{pd} with $\Delta\nu \approx 110$ GHz for QD (dotted line) and QW (dashed line) laser. (b) r_{sd} versus $\Delta\nu$ with $r_{pd} = 0.02$ for QD (dotted line) and QW (dashed line) laser. Experimental results are shown by the symbols.

6.9 Summary

In this chapter, investigations of the nondegenerate FWM mechanism in an epitaxial QD laser on Si are performed. An improved theoretical model is described to address the issue of conventional FWM theories for SOA by including the peculiar physics during the lasing process. Experimental results are investigated to verify the validity of this model. Furthermore, the FWM properties of a commercial QW laser is investigated for comparison. The main results are summarized as follows:

- For both QD and QW laser, the theoretical model described in this chapter is able to reproduce the experimental results quite well. After addressing the weakness of the conventional FWM theories for SOAs, this model is an efficient analytical tool for band-structure engineering to improve the FWM efficiency in semiconductor lasers, which is meaningful for applications that require the FWM operations.
- In both simulation and experiment, the FWM efficiency of the QD laser is more than one order of magnitude higher than that of the commercial QW laser. Besides, the FWM bandwidth of the former device is twice larger than

that of the latter one. This study gives insights for developing compact, small-footprint, energy-efficient and low-cost self-mode-locked optical frequency combs and quantum light generators by taking advantage of the rich optical nonlinearities along with the CMOS availability of QD. These findings highlight the crucial role of light emitters made with QDs for the integrated WDM technologies on silicon and for the possible application in future quantum photonic integrated circuits.

CONCLUSIONS AND PERSPECTIVES

This thesis is devoted to studying the nonlinear properties and dynamics of quantum-dot (QD) lasers and to searching for their potential applications.

First, a comprehensive investigation of the dynamics of multimode QD lasers subject to external optical feedback (EOF) is performed. Different devices including epitaxial InAs/GaAs QD Fabry-Perot (FP) laser on Si and InAs/InP quantum-dash (QDash) FP laser are analyzed. Benefiting from the near-zero α_H -factor, QD-based semiconductor laser that are epitaxially grown on Si exhibits a high degree of tolerance for chip-scale back-reflections without showing any chaotic oscillation. An optimum p-modulation doping level in QDs allows for an extra 16 dB improvement of the feedback insensitivity. With a feedback strength above 45% (-3.5 dB) which is well beyond what the laser can suffer from a PIC, periodic oscillations are triggered from the QD laser studied. Experimental results also demonstrate that the external cavity length plays a crucial role in determining the laser's resistance to optical feedback. In general, the feedback level associated to the onset of periodic oscillation decreases with the increase of external cavity length. In this study, the laser's tolerance for EOF is decreased by 2 dB due to the occurrence of regime II in the long-cavity regime (LCR). Despite the inconvenience in LCR, it is worth stressing that the regime II is barely encountered on a PIC where the effective external cavity length is of a few centimeters. On an InP wafer where QDashes are commonly used gain media for laser, it is of importance to control their polarization to enable the laser a high degree of feedback insensitivity. By rotating the orientation of QDashes from parallel to perpendicular to the cavity axis, a 11 dB improvement of the critical feedback level that is associated to the coherence collapse is realized. These studies give insights for improving the reflection insensitivity of QD lasers that are grown on InP and Si substrate, which pave the way for developing highly stable on-chip sources for isolator-free integration.

Second, an InAs/GaAs QD distributed feedback (DFB) laser with a design of optical wavelength detuning (OWD) at room-temperature is analyzed. The OWD corresponds to the mismatch between the Bragg wavelength and the optical gain peak. The low intrinsic linewidth enhancement factor (α_H -factor) below 1 extracted from

the QD laser studied gives insights for developing chirp-free optical transmitter. Along with the low α_H -factor, the QD-DFB laser exhibits a remarkable low-noise property in presence of a low relative intensity noise (RIN) level at -155 dB/Hz in the radio-frequency (RF) range of 8-10 GHz. To further explore the possible applications of the QD-DFB to PICs, an investigation of the laser's static and dynamical properties with respect to the temperature variation is performed. Experimental results demonstrate that the laser performance improves with temperature, which is attributed to the reduction of the mismatch between the Bragg grating and the optical gain peak. For the device studied, an increase of temperature from 15 to 55°C results in a decrease of the OWD from 30 to 10 nm. As a consequence, the threshold current and the α_H -factor is reduced by a factor of 45% and 43%, respectively. Despite the QD laser is known from its large damping which restricts its modulation capacity, the reduction of OWD with increasing temperature is beneficial for partially offsetting this inconvenience. With the increase of temperature from 15 to 55°C, the K-factor of laser decreasing from 2.87 to 1.72 ns. In particular, the laser's tolerance for back-reflections exhibits an improvement of 9 dB with the reduction of OWD. Therefore, semiconductor QD along with the OWD technique provide a promising solution for high-performance single-frequency optical transmitters for uncooled and isolator-free PICs.

Third, the design and optimization of QD-based optical frequency comb (OFC) lasers are investigated. Owing to the ultrafast carrier dynamics, the ultra-broad gain bandwidth and the low-noise properties, QD is an ideal solution for OFC technologies. For an mode-locked laser (MLL) in which a saturable absorber (SA) section is included, it is worth stressing that the reverse voltage applied to it not only accelerates the SA recovery time, but also increases the α_H -factor of the active region. Both theoretical analysis and experimental results demonstrate that a low SA voltage assisted α_H is beneficial for improving the mode-locking stability. An investigation of the influence of SA section length reveals that a reasonable large SA section length ratio could improve the pulse duration and the signal-to-noise ratio (SNR) simultaneously. In experiment, a 15 dB increase of the SNR along with 4-fold reduction of the RF linewidth is identified when the SA length ratio increases from 5% to 8%. To further improve the performance of a QD-based MLL and OFC, external control including EOF and optical injection are investigated on the devices studied. In the optimum EOF operation, the QD-MLL exhibits a 13 dB increase of SNR along with a 40-fold reduction of the RF linewidth from 160 to 4 kHz. The consequent reduction of pulse-to-pulse timing jitter from 60 to 10 fs/cycle

gives insight for developing ultra stable photonic oscillators by taking advantage of the optical feedback technique. A low α_H -factor is also beneficial for improving the efficiency for the optical feedback stabilization (OFS) operation. In experiment, the QD-MLL in OFS operation exhibits an improved tolerance for the variation of feedback strength and external cavity length when the SA reverse bias decreases from -3 V to 0 V. Therefore, the near-zero α_H -factor offered by QD paves the way for developing highly stable and low-noise CMOS available frequency comb generators. In addition, the frequency comb dynamics can be largely improved by the optical injection technique. In experiment, the 3-dB optical bandwidth of a QD-based frequency comb laser is increased by 3.5-fold in the intra-mode optical injection condition.

Fourth, the four-wave mixing (FWM) mechanism in epitaxial QD laser on Si is analyzed by both theory and experiments. After addressing the weakness of the conventional FWM theories for semiconductor optical amplifier (SOA), the model described in this thesis is an efficient analytical tool for band-structure engineering to improve the FWM efficiency in semiconductor lasers. Benefiting from the improvement of third-order nonlinear susceptibility $\chi^{(3)}$ by more than one order of magnitude, the FWM efficiency of the QD laser is 10~20 times higher than that of the commercial quantum-well (QW) laser. Besides, the FWM bandwidth of the former device is twice larger than that of the latter one, owing to the stronger spatial hole burning (SHB) of QD. This study gives insights for developing compact, small-footprint, energy-efficient and low-cost self-mode-locked OFC and quantum states of light generators by taking advantage of the rich optical nonlinearities along with the CMOS availability of QD. The wavelength-division multiplexing (WDM) technologies and the quantum photonic integrated circuit (QPIC) can thus benefit from the high-performance QD lasers.

In future steps, various theoretical and experimental works can be envisioned:

- High-performance epitaxial QD-DFB laser on Si remains to be developed. Pioneering work have demonstrated InAs/GaAs QD-DFB lasers that are epitaxially grown on Si substrate (Y. Wang et al., 2018; Wan et al., 2020). Despite the low threshold current and the high side-mode-suppression-ratio (SMSR), those devices are limited to the output power. Another limiting factor of the QD lasers is their restricted modulation bandwidth caused by the strong damping. This inconvenience can be partially offset by tuning the OWD approaching zero. To take advantage of the low-noise properties as

well as the reflection-resistance of the QD-DFB laser, it is promising to utilize high-level pulse amplitude modulation (i.e. PAM4 and PAM8) format for high-speed PIC applications. In addition, high-performance single-frequency QD lasers that are CMOS available also exhibit a strong potential to serve as the pump sources for monolithic integrated microresonator-based OFC and on-chip quantum light generators (Diddams, Vahala, and Thomas Udem, 2020; Y. Zhao et al., 2020).

- Epitaxial QD lasers on Si are free of chaotic dynamics, however, they are reliable microwave generators. In different feedback conditions, various periodic oscillation states are generated and are performed in this thesis. In particular, the period-one (P1) oscillation whose frequency is determined by the external cavity frequency has a tunable range from several hundreds megahertz to a few gigahertz. Benefiting from the EOF technique as well as the mature CMOS industry, QD laser is an ideal solution for all-optical microwave oscillator. It is promising to further increase the microwave frequencies to dozens of gigahertz by utilizing a phase conjugate optical feedback configuration (Rontani et al., 2016). Therefore, the QD-based radio-over-fibre systems exhibit a strong potential to be applied to wireless networks such as picocellular systems and wireless personal area networks (WPAN) (Capmany and Novak, 2007).
- High-performance and low-cost optical transmitters operating in C- and L-band play important roles in long-haul optical communications. The mature InP platform remains the first option for $1.55 \mu\text{m}$ optical communication by providing desirable performance, however, it suffers from the high-cost InP wafer. It is used to be a challenge to directly grow InP-based laser sources on silicon wafer, due to the large lattice mismatch between InP and Si of 8%. Nevertheless, a recent work gives insights for overcoming this issue and provides an approach for epitaxially growing $1.55 \mu\text{m}$ QDash lasers on Si substrate (Luo et al., 2020). Further analysis on the dynamical properties of those devices remains to be investigated.
- QD-based OFC can take advantage of the EOF technique to have ultra-low noise properties. Benefiting from the huge progress in integrated microring technologies, the conventional optical fibre-based external cavity can be replaced by the high-Q microring resonator. A recent study demonstrates an hertz-linewidth semiconductor laser which is realized by intra-chip back-reflections within a microresonator (W. Jin et al., 2021). It is worth stressing

that the integrated EOF technique has been applied to a QW-based MLL and it results in a sub-kilohertz RF linewidth (X. Li et al., 2021). These recent studies give insights for developing ultra-low noise frequency comb lasers by taking advantage of both the QD and the CMOS available EOF technique.

- Epitaxial QD lasers on Si have shown remarkable high FWM efficiency, which give insights for developing CMOS available self-mode-locked frequency comb generator and quantum states of light generator. Recent studies demonstrate a dual-pump FWM configuration that allows for light squeezing within a microring resonator (Y. Zhao et al., 2020; Zhang et al., 2021). Given that monolithic microresonator-based OFC and quantum light generator integrated on a single chip remains a challenge, the QD laser could be a promising solution for both classical and quantum communication technologies.
- The group velocity dispersion (GVD) in the laser cavity has a direct impact on the FWM efficiency and the FWM bandwidth. The effect of GVD has been included in time-domain travelling-wave (TDTW) theory (Jiao et al., 2013). However, it is still a challenge to reproduce the FWM process that occurs in the frequency domain by using the time-domain theory. To further improve the FWM theory for semiconductor lasers, including the GVD effect to the frequency-domain model remains to be investigated.
- Owing to the two transparency atmospheric windows at 8 and 15 μm , the mid-infrared (MIR) frequency range (i.e., 2~20 μm) becomes an attractive communication band. A number of applications including biochemical and environmental sensing, medicine, astronomy and MIR free-space communications have emerged with the development of MIR technologies. Therefore, high-performance MIR light emitters such as quantum cascade lasers (QCL) and interband cascade lasers (ICL) are highly desired by those emerging applications (Cathabard et al., 2010; Hugi et al., 2012; Vurgaftman et al., 2015). Given that the semiconductor QW is the commonly used gain medium for current QCL and ICL, it is promising to take advantage of the QD to provide the QCL and ICL with novel functionality and high performance (Dmitriev and Suris, 2005). In addition, future integrated MIR lasers and sensors can also benefit from the low-cost silicon PICs platform by utilizing QD (Spott et al., 2018; Nguyen-Van et al., 2018).

BIBLIOGRAPHY

- Aasi, Junaid et al. (2013). “Enhanced sensitivity of the LIGO gravitational wave detector by using squeezed states of light”. In: *Nature Photonics* 7.8, pp. 613–619.
- Agrawal, G (1984). “Line narrowing in a single-mode injection laser due to external optical feedback”. In: *IEEE Journal of Quantum Electronics* 20.5, pp. 468–471.
- Agrawal, Govind P (1988). “Population pulsations and nondegenerate four-wave mixing in semiconductor lasers and amplifiers”. In: *JOSA B* 5.1, pp. 147–159.
- (1989). “Intensity Dependence of the Linewidth Enhancement Factor and Its Implications for Semiconductor Lasers”. In: *IEEE Photonics Technology Letters* 1.8, pp. 212–214.
 - (1990). “Effect of Gain and Index Nonlinearities on Single-Mode Dynamics in Semiconductor Lasers”. In: *IEEE Journal of Quantum Electronics* 26.11, pp. 1901–1909.
 - (1991). “Effect of Gain Dispersion on Ultrashort Pulse Amplification in Semiconductor Laser Amplifiers”. In: *IEEE Journal of Quantum Electronics* 27.6, pp. 1843–1849.
- Akahane, Kouichi, Naokatsu Yamamoto, and Masahiro Tsuchiya (2008). “Highly stacked quantum-dot laser fabricated using a strain compensation technique”. In: *Applied Physics Letters* 93.4, p. 041121.
- Akiyama, Tomoyuki, Mitsuru Ekawa, et al. (2005). “An Ultrawide-Band Semiconductor Optical Amplifier Having an Extremely High Penalty-Free Output Power of 23 dBm Achieved with Quantum Dots”. In: *IEEE Photonics Technology Letters* 17.8, pp. 1614–1616.
- Akiyama, Tomoyuki, Haruhiko Kuwatsuka, et al. (2002). “Symmetric highly efficient (~ 0 dB) wavelength conversion based on four-wave mixing in quantum dot optical amplifiers”. In: *IEEE Photonics Technology Letters* 14.8, pp. 1139–1141.
- Alferov, Zh I et al. (1971). “Investigation of the influence of the AlAs-GaAs heterostructure parameters on the laser threshold current and the realization of continuous emission at room temperature”. In: *Sov. Phys. Semicond* 4.9, pp. 1573–1575.
- Alloatti, Luca et al. (2014). “100 GHz silicon-organic hybrid modulator”. In: *Light: Science & Applications* 3.5, e173–e173.
- Arafin, Shamsul and Larry A Coldren (2017). “Advanced InP Photonic Integrated Circuits for Communication and Sensing”. In: *IEEE Journal of Selected Topics in Quantum Electronics* 24.1, pp. 1–12.

- Arakawa, Y and Hiroyuki Sakaki (1982). “Multidimensional quantum well laser and temperature dependence of its threshold current”. In: *Applied physics letters* 40.11, pp. 939–941.
- Arakawa, Yasuhiko and Mark J Holmes (2020). “Progress in quantum-dot single photon sources for quantum information technologies: A broad spectrum overview”. In: *Applied Physics Reviews* 7.2, p. 021309.
- Arcari, Marta et al. (2014). “Near-unity coupling efficiency of a quantum emitter to a photonic crystal waveguide”. In: *Physical review letters* 113.9, p. 093603.
- Arecchi, FT, GL Lippi, et al. (1984). “Deterministic chaos in laser with injected signal”. In: *Optics communications* 51.5, pp. 308–314.
- Arecchi, FT, R Meucci, et al. (1982). “Experimental evidence of subharmonic bifurcations, multistability, and turbulence in a Q-switched gas laser”. In: *Physical Review Letters* 49.17, p. 1217.
- Armani, DK et al. (2003). “Ultra-high-Q toroid microcavity on a chip”. In: *Nature* 421.6926, pp. 925–928.
- Arsenijević, Dejan and Dieter Bimberg (2016). “Quantum-dot lasers for 35 Gbit/s pulse-amplitude modulation and 160 Gbit/s differential quadrature phase-shift keying”. In: *Semiconductor Lasers and Laser Dynamics VII*. Vol. 9892. International Society for Optics and Photonics, 98920S.
- Aspect, Alain, Philippe Grangier, and Gérard Roger (1982). “Experimental realization of Einstein-Podolsky-Rosen-Bohm Gedankenexperiment: a new violation of Bell’s inequalities”. In: *Physical Review Letters* 49.2, p. 91.
- Asryan, Levon V and Robert A Suris (2000). “Longitudinal Spatial Hole Burning in a Quantum-Dot Laser”. In: *IEEE Journal of Quantum Electronics* 36.10, pp. 1151–1160.
- Auth, Dominik et al. (2019). “Passively mode-locked semiconductor quantum dot on silicon laser with 400 Hz RF line width”. In: *Optics express* 27.19, pp. 27256–27266.
- Avrutin, EA, JH Marsh, and EL Portnoi (2000). “Monolithic and multi-gigahertz mode-locked semiconductor lasers: constructions, experiments, models and applications”. In: *IEE Proceedings-Optoelectronics* 147.4, pp. 251–278.
- Avrutin, Eugene A and Benjamin M Russell (2009). “Dynamics and Spectra of Monolithic Mode-Locked Laser Diodes Under External Optical Feedback”. In: *IEEE Journal of Quantum Electronics* 45.11, pp. 1456–1464.
- Azouigui, S et al. (2007). “Tolerance to Optical Feedback of 10-Gb/s Quantum-Dash-Based Lasers Emitting at 1.51 μm ”. In: *IEEE Photonics Technology Letters* 19.15, pp. 1181–1183.

- Azouigui, Shéhérazade et al. (2009). “Optical Feedback Tolerance of Quantum-Dot-and Quantum-Dash-Based Semiconductor Lasers Operating at $1.55 \mu\text{m}$ ”. In: *IEEE Journal of Selected Topics in Quantum Electronics* 15.3, pp. 764–773.
- Bardella, P et al. (2018). “Mode locking in a tapered two-section quantum dot laser: design and experiment”. In: *Optics letters* 43.12, pp. 2827–2830.
- Bayer, M and Alfred Forchel (2002). “Temperature dependence of the exciton homogeneous linewidth in $\text{In}_{0.60}\text{Ga}_{0.40}\text{As}/\text{GaAs}$ self-assembled quantum dots”. In: *Physical Review B* 65.4, p. 041308.
- Becker, Annette et al. (2017). “Widely tunable narrow-linewidth $1.5 \mu\text{m}$ light source based on a monolithically integrated quantum dot laser array”. In: *Applied Physics Letters* 110.18, p. 181103.
- Beha, Katja et al. (2017). “Electronic synthesis of light”. In: *Optica* 4.4, pp. 406–411.
- Bennett, Charles H, Gilles Brassard, and N David Mermin (1992). “Quantum cryptography without Bell’s theorem”. In: *Physical review letters* 68.5, p. 557.
- Bhattacharya, Pallab et al. (2000). “High-Speed Modulation and Switching Characteristics of $\text{In}(\text{Ga})\text{As}-\text{Al}(\text{Ga})\text{As}$ Self-Organized Quantum-Dot Lasers”. In: *IEEE Journal of Selected Topics in Quantum Electronics* 6.3, pp. 426–438.
- Bhattacharyya, D et al. (1999). “Spectral and Dynamic Properties of $\text{InAs}-\text{GaAs}$ Self-Organized Quantum-Dot Lasers”. In: *IEEE Journal of selected topics in quantum electronics* 5.3, pp. 648–657.
- Bimberg, Dieter, Marius Grundmann, and Nikolai N Ledentsov (1999). *Quantum dot heterostructures*. John Wiley & Sons.
- Binder, Jann O and George D Cormack (1989). “Mode selection and stability of a semiconductor laser with weak optical feedback”. In: *IEEE Journal of Quantum Electronics* 25.11, pp. 2255–2259.
- Bockelmann, U and G Bastard (1990). “Phonon scattering and energy relaxation in two-, one-, and zero-dimensional electron gases”. In: *Physical Review B* 42.14, p. 8947.
- Borri, Paola et al. (2001). “Ultralong dephasing time in InGaAs quantum dots”. In: *Physical Review Letters* 87.15, p. 157401.
- Bouwmeester, Dik et al. (1997). “Experimental quantum teleportation”. In: *Nature* 390.6660, pp. 575–579.
- Boyd, Robert W (2020). *Nonlinear optics*. Academic press.
- Brackett, Charles A. (1990). “Dense wavelength division multiplexing networks: Principles and applications”. In: *IEEE Journal on Selected areas in Communications* 8.6, pp. 948–964.

- Brasch, Victor et al. (2016). “Photonic chip–based optical frequency comb using soliton Cherenkov radiation”. In: *Science* 351.6271, pp. 357–360.
- Braunstein, Samuel L and Peter Van Loock (2005). “Quantum information with continuous variables”. In: *Reviews of modern physics* 77.2, p. 513.
- Broom, R et al. (1970). “Microwave self-modulation of a diode laser coupled to an external cavity”. In: *IEEE Journal of Quantum Electronics* 6.6, pp. 328–334.
- Buffolo, Matteo et al. (2019). “Investigation of current-driven degradation of 1.3 μm quantum-dot lasers epitaxially grown on silicon”. In: *IEEE Journal of Selected Topics in Quantum Electronics* 26.2, pp. 1–8.
- Buus, J (1985). “Mode Selectivity in DFB Lasers with Cleaved Facets”. In: *Electronics Letters* 21.5, pp. 179–180.
- Cao, Hui et al. (2019). “Complex lasers with controllable coherence”. In: *Nature Reviews Physics* 1.2, pp. 156–168.
- Capmany, José and Dalma Novak (2007). “Microwave photonics combines two worlds”. In: *Nature Photonics* 1.6, p. 319.
- Cappelli, Francesco et al. (2015). “Intrinsic linewidth of quantum cascade laser frequency combs”. In: *Optica* 2.10, pp. 836–840.
- Capua, A et al. (2007). “Direct correlation between a highly damped modulation response and ultra low relative intensity noise in an InAs/GaAs quantum dot laser”. In: *Optics Express* 15.9, pp. 5388–5393.
- Carlson, David R et al. (2018). “Ultrafast electro-optic light with subcycle control”. In: *Science* 361.6409, pp. 1358–1363.
- Carpintero, Guillermo et al. (2009). “Low noise performance of passively mode-locked 10-GHz quantum-dot laser diode”. In: *IEEE Photonics Technology Letters* 21.6, pp. 389–391.
- Cathabard, O et al. (2010). “Quantum cascade lasers emitting near 2.6 μm ”. In: *Applied Physics Letters* 96.14, p. 141110.
- Chan, Sze-Chun, Sheng-Kwang Hwang, and Jia-Ming Liu (2006). “Radio-over-fiber AM-to-FM upconversion using an optically injected semiconductor laser”. In: *Optics Letters* 31.15, pp. 2254–2256.
- Chang, Lin et al. (2020). “Ultra-efficient frequency comb generation in AlGaAs-on-insulator microresonators”. In: *Nature communications* 11.1, pp. 1–8.
- Chang, Milton (2016). “IoT opportunities in photonics”. In: *Laser Focus World* 52.7.
- Chen, Jun-Da et al. (2021). “3D chaos lidar system with a pulsed master oscillator power amplifier scheme”. In: *Optics Express* 29.17, pp. 27871–27881.
- Chen, Tupei and Yang Liu (2016). *Semiconductor Nanocrystals and Metal Nanoparticles: Physical Properties and Device Applications*. CRC Press.

- Cheng, Qixiang et al. (2018). “Recent advances in optical technologies for data centers: a review”. In: *Optica* 5.11, pp. 1354–1370.
- Cho, Alfred Y (1971). “Film deposition by molecular-beam techniques”. In: *Journal of Vacuum Science and Technology* 8.5, S31–S38.
- Chow, Weng W and Stephan W Koch (1999). *Semiconductor-laser fundamentals: physics of the gain materials*. Springer Science & Business Media.
- (2005). “Theory of Semiconductor Quantum-Dot Laser Dynamics”. In: *IEEE Journal of Quantum Electronics* 41.4, pp. 495–505.
- Chow, Weng W, Songtao Liu, et al. (2020). “Multimode description of self-mode locking in a single-section quantum-dot laser”. In: *Optics express* 28.4, pp. 5317–5330.
- Chrostowski, Lukas et al. (2007). “40 GHz Bandwidth and 64 GHz Resonance Frequency in Injection-Locked $1.55\mu\text{m}$ VCSELs”. In: *IEEE Journal of Selected Topics in Quantum Electronics* 13.5, pp. 1200–1208.
- Cingöz, Arman et al. (2012). “Direct frequency comb spectroscopy in the extreme ultraviolet”. In: *Nature* 482.7383, pp. 68–71.
- Coldren, Larry A, Scott W Corzine, and Milan L Mashanovitch (2012). *Diode lasers and photonic integrated circuits*. Vol. 218. John Wiley & Sons.
- Collins, Matthew J et al. (2013). “Integrated spatial multiplexing of heralded single-photon sources”. In: *Nature communications* 4.1, pp. 1–7.
- Contestabile, Giampiero, Akihiro Maruta, and Ken-Ichi Kitayama (2014). “Four wave mixing in quantum dot semiconductor optical amplifiers”. In: *IEEE Journal of Quantum Electronics* 50.5, pp. 379–389.
- Cook, Gary (2011). *How dirty is your data: A look at the energy choices that power cloud computing*. Greenpeace.
- Cornet, Charles et al. (2005). “Approach to wetting-layer-assisted lateral coupling of InAs/InP quantum dots”. In: *Physical Review B* 72.3, p. 035342.
- Cox, Charles H et al. (2006). “Limits on the Performance of RF-Over-Fiber Links and Their Impact on Device Design”. In: *IEEE Transactions on Microwave Theory and Techniques* 54.2, pp. 906–920.
- Dagens, B et al. (2005). “Giant linewidth enhancement factor and purely frequency modulated emission from quantum dot laser”. In: *Electronics Letters* 41.6, pp. 323–324.
- David, Klaus et al. (1991). “Gain-coupled DFB lasers versus index-coupled and phase shifted DFB lasers: a comparison based on spatial hole burning corrected yield”. In: *IEEE Journal of Quantum Electronics* 27.6, pp. 1714–1723.
- Dery, Hanan and Gadi Eisenstein (2005). “The Impact of Energy Band Diagram and Inhomogeneous Broadening on the Optical Differential Gain in Nanostructure Lasers”. In: *IEEE Journal of Quantum Electronics* 41.1, pp. 26–35.

- Devaux, F, Y Sorel, and JF Kerdiles (1993). “Simple Measurement of Fiber Dispersion and of Chirp Parameter of Intensity Modulated Light Emitter”. In: *Journal of Lightwave Technology* 11.12, pp. 1937–1940.
- Diamanti, Eleni et al. (2016). “Practical challenges in quantum key distribution”. In: *npj Quantum Information* 2.1, pp. 1–12.
- Diddams, Scott A, Leo Hollberg, and Vela Mbele (2007). “Molecular fingerprinting with the resolved modes of a femtosecond laser frequency comb”. In: *Nature* 445.7128, pp. 627–630.
- Diddams, Scott A, Th Udem, et al. (2001). “An optical clock based on a single trapped $^{199}\text{Hg}^+$ ion”. In: *Science* 293.5531, pp. 825–828.
- Diddams, Scott A, Kerry Vahala, and Thomas Udem (2020). “Optical frequency combs: coherently uniting the electromagnetic spectrum”. In: *Science* 369.6501.
- Diez, Stefan et al. (1997). “Four-wave mixing in semiconductor optical amplifiers for frequency conversion and fast optical switching”. In: *IEEE Journal of selected topics in Quantum Electronics* 3.5, pp. 1131–1145.
- Dmitriev, Ivan A and Robert A Suris (2005). “Quantum cascade lasers based on quantum dot superlattice”. In: *physica status solidi (a)* 202.6, pp. 987–991.
- Doumbia, Yaya et al. (2021). “Tailoring frequency combs through VCSEL polarization dynamics”. In: *Optics Express* 29.21, pp. 33976–33991.
- Droste, Stefan et al. (2016). “Optical frequency comb generation based on erbium fiber lasers”. In: *Nanophotonics* 5.2, pp. 196–213.
- Duan, G, Philippe Gallion, and G Debarge (1987). “Analysis of frequency chirping of semiconductor lasers in the presence of optical feedback”. In: *Optics Letters* 12.10, pp. 800–802.
- Duan, G-H, Philippe Gallion, and Govind P Agrawal (1992). “Effective nonlinear gain in semiconductor lasers”. In: *IEEE Photonics Technology Letters* 4.3, pp. 218–220.
- Duan, J, H Huang, D Jung, et al. (2018). “Semiconductor quantum dot lasers epitaxially grown on silicon with low linewidth enhancement factor”. In: *Applied Physics Letters* 112.25, p. 251111.
- Duan, J, H Huang, ZG Lu, et al. (2018). “Narrow spectral linewidth in InAs/InP quantum dot distributed feedback lasers”. In: *Applied Physics Letters* 112.12, p. 121102.
- Duan, Jianan, Weng W Chow, et al. (2021). “Enhanced optical nonlinearities in epitaxial quantum dots lasers on silicon for future photonic integrated systems”. In: *arXiv preprint arXiv:2106.10871*.
- Duan, Jianan, Heming Huang, et al. (2019). “1.3- μm Reflection Insensitive InAs/GaAs Quantum Dot Lasers Directly Grown on Silicon”. In: *IEEE Photonics Technology Letters* 31.5, pp. 345–348.

- Duan, Jianan, Yueguang Zhou, et al. (2020). "Effect of p-doping on the intensity noise of epitaxial quantum dot lasers on silicon". In: *Optics Letters* 45.17, pp. 4887–4890.
- Ekert, Artur K (1991). "Quantum cryptography based on Bell's theorem". In: *Physical review letters* 67.6, p. 661.
- Farfad, S et al. (1995). "Phonons and radiative recombination in self-assembled quantum dots". In: *Physical Review B* 52.8, p. 5752.
- Fermann, Martin E and Ingmar Hartl (2013). "Ultrafast fibre lasers". In: *Nature photonics* 7.11, pp. 868–874.
- Fiol, G et al. (2010). "Hybrid mode-locking in a 40 GHz monolithic quantum dot laser". In: *Applied Physics Letters* 96.1, p. 011104.
- Fiore, Andrea and Alexander Markus (2007). "Differential Gain and Gain Compression in Quantum-Dot Lasers". In: *IEEE Journal of Quantum Electronics* 43.4, pp. 287–294.
- Fork, RL, BI Greene, and Charles V Shank (1981). "Generation of optical pulses shorter than 0.1 psec by colliding pulse mode locking". In: *Applied Physics Letters* 38.9, pp. 671–672.
- Freedman, Stuart J and John F Clauser (1972). "Experimental test of local hidden-variable theories". In: *Physical Review Letters* 28.14, p. 938.
- Furuya, K (1985). "Dependence of Linewidth Enhancement Factor α on Waveguide Structure in Semiconductor Lasers". In: *Electronics Letters* 21.5, pp. 200–201.
- Ghafouri-Shiraz, H (2003). *Distributed feedback laser diodes and optical tunable filters*. John Wiley & Sons.
- Gioannini, Mariangela (2006). "Analysis of the Optical Gain Characteristics of Semiconductor Quantum-Dash Materials Including the Band Structure Modifications Due to the Wetting Layer". In: *IEEE journal of quantum electronics* 42.3, pp. 331–340.
- Gisin, Nicolas et al. (2002). "Quantum cryptography". In: *Reviews of modern physics* 74.1, p. 145.
- Goldstein, L et al. (1985). "Growth by molecular beam epitaxy and characterization of InAs/GaAs strained-layer superlattices". In: *Applied Physics Letters* 47.10, pp. 1099–1101.
- Gomez, S et al. (2020). "High coherence collapse of a hybrid III–V/Si semiconductor laser with a large quality factor". In: *Journal of Physics: Photonics* 2.2, p. 025005.
- Gong, Ming et al. (2008). "Electronic structure of self-assembled InAs/InP quantum dots: Comparison with self-assembled InAs/GaAs quantum dots". In: *Physical Review B* 77.4, p. 045326.

- Gong, Zheng et al. (2018). “High-fidelity cavity soliton generation in crystalline AlN micro-ring resonators”. In: *Optics Letters* 43.18, pp. 4366–4369.
- Gosset, Christophe et al. (2006). “Subpicosecond pulse generation at 134 GHz using a quantum-dash-based Fabry-Perot laser emitting at 1.56 μm ”. In: *Applied Physics Letters* 88.24, p. 241105.
- Grangier, Philippe, Gerard Roger, and Alain Aspect (1986). “Experimental evidence for a photon anticorrelation effect on a beam splitter: a new light on single-photon interferences”. In: *EPL (Europhysics Letters)* 1.4, p. 173.
- Grillot, F, B Thedrez, O Gauthier-Lafaye, et al. (2003). “Coherence-collapse threshold of 1.3- μm semiconductor DFB lasers”. In: *IEEE Photonics Technology Letters* 15.1, pp. 9–11.
- Grillot, F, B Thedrez, J Py, et al. (2002). “2.5-Gb/s transmission characteristics of 1.3- μm DFB lasers with external optical feedback”. In: *IEEE Photonics Technology Letters* 14.1, pp. 101–103.
- Grillot, Frédéric (2009). “On the effects of an antireflection coating impairment on the sensitivity to optical feedback of AR/HR semiconductor DFB lasers”. In: *IEEE Journal of Quantum Electronics* 45.6, pp. 720–729.
- Grillot, Frederic et al. (2020). “Quantum dot lasers based photonics integrated circuits”. In: *2020 IEEE Photonics Conference (IPC)*. IEEE, pp. 1–2.
- Grillot, Frédéric, Béatrice Dagens, et al. (2008). “Gain Compression and Above-Threshold Linewidth Enhancement Factor in 1.3- μm InAs/GaAs Quantum-Dot Lasers”. In: *IEEE Journal of Quantum Electronics* 44.10, pp. 946–951.
- Grillot, Frédéric, Jianan Duan, et al. (2021). “Uncovering recent progress in nanostructured light-emitters for information and communication technologies”. In: *Light: Science & Applications* 10.1, pp. 1–17.
- Grillot, Frédéric, Justin C Norman, et al. (2020). “Physics and applications of quantum dot lasers for silicon photonics”. In: *Nanophotonics* 9.6, pp. 1271–1286.
- Grillot, Frédéric, Bruno Thedrez, and Guang-Hua Duan (2004). “Feedback sensitivity and coherence collapse threshold of semiconductor DFB lasers with complex structures”. In: *IEEE Journal of Quantum Electronics* 40.3, pp. 231–240.
- Grundmann, M et al. (1995). “Ultrannarrow luminescence lines from single quantum dots”. In: *Physical Review Letters* 74.20, p. 4043.
- Haegeman, Bart et al. (2002). “Stability and rupture of bifurcation bridges in semiconductor lasers subject to optical feedback”. In: *Physical Review E* 66.4, p. 046216.
- Hakki, Basil W and Thomas L Paoli (1973). “CW degradation at 300°K of GaAs double-heterostructure junction lasers. II. Electronic gain”. In: *Journal of Applied Physics* 44.9, pp. 4113–4119.

- Hänsel, Andreas and Martijn JR Heck (2020). “Opportunities for photonic integrated circuits in optical gas sensors”. In: *Journal of Physics: Photonics* 2.1, p. 012002.
- Hantschmann, Constanze et al. (2018). “Understanding the Bandwidth Limitations in Monolithic 1.3 μm InAs/GaAs Quantum Dot Lasers on Silicon”. In: *Journal of Lightwave Technology* 37.3, pp. 949–955.
- Harder, Christoph, Kerry Vahala, and Amnon Yariv (1983). “Measurement of the linewidth enhancement factor α of semiconductor lasers”. In: *Applied Physics Letters* 42.4, pp. 328–330.
- Hargrove, LE, Richard L Fork, and MA Pollack (1964). “Locking of He-Ne laser modes induced by synchronous intracavity modulation”. In: *Applied Physics Letters* 5.1, pp. 4–5.
- Haug, Hartmut and Stephan W Koch (2009). *Quantum theory of the optical and electronic properties of semiconductors*. World Scientific Publishing Company.
- Hayat, Ahmad et al. (2009). “Long Wavelength VCSEL-by-VCSEL Optical Injection Locking”. In: *IEEE Transactions on Microwave Theory and Techniques* 57.7, pp. 1850–1858.
- He, Yang et al. (2019). “Self-starting bi-chromatic LiNbO₃ soliton microcomb”. In: *Optica* 6.9, pp. 1138–1144.
- Hegarty, SP et al. (2005). “Free-Carrier Effect on Index Change in 1.3 μm Quantum-Dot Lasers”. In: *Electronics Letters* 41.7, pp. 416–418.
- Heil, T et al. (2001). “Dynamics of semiconductor lasers subject to delayed optical feedback: The short cavity regime”. In: *Physical Review Letters* 87.24, p. 243901.
- Helms, Jochen and K Petermann (1990). “A Simple Analytic Expression for the Stable Operation Range of Laser Diodes with Optical Feedback”. In: *IEEE Journal of Quantum Electronics* 26.5, pp. 833–836.
- Henry, C (1985). “Performance of Distributed Feedback Lasers Designed to Favor the Energy Gap Mode”. In: *IEEE Journal of Quantum Electronics* 21.12, pp. 1913–1918.
- Henry, C and R Kazarinov (1986). “Instability of Semiconductor Lasers due to Optical Feedback from Distant Reflectors”. In: *IEEE Journal of Quantum Electronics* 22.2, pp. 294–301.
- Henry, C, N Olsson, and N Dutta (1985). “Locking range and stability of injection locked 1.54 μm InGaAsP semiconductor lasers”. In: *IEEE Journal of Quantum Electronics* 21.8, pp. 1152–1156.
- Henry, Charles (1982). “Theory of the Linewidth of Semiconductor Lasers”. In: *IEEE Journal of Quantum Electronics* 18.2, pp. 259–264.

- Herrera, Daniel, Vassilios Kovanis, and Luke F Lester (2021). “Using transitional points in the optical injection locking behavior of a semiconductor laser to extract its dimensionless operating parameters”. In: *IEEE Journal of Selected Topics in Quantum Electronics*.
- Hillbrand, Johannes et al. (2018). “Tunable dispersion compensation of quantum cascade laser frequency combs”. In: *Optics Letters* 43.8, pp. 1746–1749.
- Hillmer, H, K Magari, and Y Suzuki (1993). “Chirped gratings for DFB laser diodes using bent waveguides”. In: *IEEE Photonics Technology Letters* 5.1, pp. 10–12.
- Huang, Chen-Bin, Zhi Jiang, et al. (2008). “Spectral line-by-line shaping for optical and microwave arbitrary waveform generations”. In: *Laser & Photonics Reviews* 2.4, pp. 227–248.
- Huang, Chen-Bin, Sang-Gyu Park, et al. (2008). “Nonlinearly broadened phase-modulated continuous-wave laser frequency combs characterized using DPSK decoding”. In: *Optics express* 16.4, pp. 2520–2527.
- Huang, H. et al. (2020). “Epitaxial quantum dot lasers on silicon with high thermal stability and strong resistance to optical feedback”. In: *APL Photonics* 5.1, p. 016103.
- Huang, Heming (2017). “Optical nonlinearities in quantum dot lasers for high-speed communications”. PhD thesis. Paris, ENST.
- Huang, Heming, Jianan Duan, et al. (2018). “Analysis of the optical feedback dynamics in InAs/GaAs quantum dot lasers directly grown on silicon”. In: *JOSA B* 35.11, pp. 2780–2787.
- Huang, Heming, Lyu-Chih Lin, et al. (2018). “Multimode optical feedback dynamics in InAs/GaAs quantum dot lasers emitting exclusively on ground or excited states: transition from short-to long-delay regimes”. In: *Optics Express* 26.2, pp. 1743–1751.
- Huang, Heming, Kevin Schires, et al. (2015). “Non-degenerate four-wave mixing in an optically injection-locked InAs/InP quantum dot Fabry-Perot laser”. In: *Applied Physics Letters* 106.14, p. 143501.
- Huang, Jian and Lee W Casperson (1993). “Gain and saturation in semiconductor lasers”. In: *Optical and Quantum Electronics* 25.6, pp. 369–390.
- Huber, Daniel et al. (2018). “Semiconductor quantum dots as an ideal source of polarization-entangled photon pairs on-demand: a review”. In: *Journal of Optics* 20.7, p. 073002.
- Huffaker, DL et al. (1998). “1.3 μm room-temperature GaAs-based quantum-dot laser”. In: *Applied Physics Letters* 73.18, pp. 2564–2566.
- Hugi, Andreas et al. (2012). “Mid-infrared frequency comb based on a quantum cascade laser”. In: *Nature* 492.7428, pp. 229–233.

- Hui, R et al. (1990). “Novel Measurement Technique of Alpha Factor in DFB Semiconductor Lasers by Injection Locking”. In: *Electronics Letters* 26.14, pp. 997–998.
- Inoshita, Takeshi and Hiroyuki Sakaki (1992). “Electron relaxation in a quantum dot: Significance of multiphonon processes”. In: *Physical Review B* 46.11, p. 7260.
- Inoue, Daisuke et al. (2018). “Directly modulated 1.3 μm quantum dot lasers epitaxially grown on silicon”. In: *Optics express* 26.6, pp. 7022–7033.
- Itaya, Y et al. (1985). “Phase control by coating in 1.56 μm distributed feedback lasers”. In: *IEEE Journal of Quantum Electronics* 21.6, pp. 527–533.
- Javaloyes, Julien and Salvador Balle (2010). “Mode-Locking in Semiconductor Fabry-Perot Lasers”. In: *IEEE Journal of Quantum Electronics* 46.7, pp. 1023–1030.
- Jiang, Hongtao and Jasprit Singh (1998). “Radiative and non-radiative inter-subband transition in self assembled quantum dots”. In: *Physica E: Low-dimensional Systems and Nanostructures* 2.1-4, pp. 720–724.
- Jiao, Zhejing et al. (2013). “Modeling of single-section quantum dot mode-locked lasers: Impact of group velocity dispersion and self phase modulation”. In: *IEEE Journal of Quantum Electronics* 49.12, pp. 1008–1015.
- Jin, Warren et al. (2021). “Hertz-linewidth semiconductor lasers using CMOS-ready ultra-high-Q microresonators”. In: *Nature Photonics* 15.5, pp. 346–353.
- Jones, Richard et al. (2019). “Heterogeneously Integrated InP/Silicon Photonics: Fabricating Fully Functional Transceivers”. In: *IEEE Nanotechnology Magazine* 13.2, pp. 17–26.
- Joshi, Siddharth et al. (2014). “Quantum dash based single section mode locked lasers for photonic integrated circuits”. In: *Optics Express* 22.9, pp. 11254–11266.
- Jung, Daehwan, Robert Herrick, et al. (2018). “Impact of threading dislocation density on the lifetime of InAs quantum dot lasers on Si”. In: *Applied Physics Letters* 112.15, p. 153507.
- Jung, Daehwan, Justin Norman, et al. (2017). “High efficiency low threshold current 1.3 μm InAs quantum dot lasers on on-axis (001) GaP/Si”. In: *Applied Physics Letters* 111.12, p. 122107.
- Jung, Daehwan, Zeyu Zhang, et al. (2017). “Highly reliable low-threshold InAs quantum dot lasers on on-axis (001) Si with 87% injection efficiency”. In: *ACS Photonics* 5.3, pp. 1094–1100.
- Kamath, K et al. (1996). “Room-Temperature Operation of $\text{In}_{0.4}\text{Ga}_{0.6}\text{As}/\text{GaAs}$ Self-Organised Quantum Dot Lasers”. In: *Electronics Letters* 32.15, pp. 1374–1375.
- Kane, Deborah M and K Alan Shore (2005). *Unlocking dynamical diversity: optical feedback effects on semiconductor lasers*. John Wiley & Sons.

- Katsuyama, Tsukuru (2009). “Development of semiconductor laser for optical communication”. In: *SEI Techn Rev* 69, pp. 13–20.
- Keating, T et al. (1999). “Temperature Dependence of Electrical and Optical Modulation Responses of Quantum-Well Lasers”. In: *IEEE Journal of Quantum Electronics* 35.10, pp. 1526–1534.
- Khan, Mohammed Zahed Mustafa, Tien Khee Ng, and Boon S Ooi (2014). “Self-assembled InAs/InP quantum dots and quantum dashes: Material structures and devices”. In: *Progress in Quantum Electronics* 38.6, pp. 237–313.
- Kim, Jimyung, Myoung-Taek Choi, and Peter J Delfyett (2006). “Pulse generation and compression via ground and excited states from a grating coupled passively mode-locked quantum dot two-section diode laser”. In: *Applied Physics Letters* 89.26, p. 261106.
- Kim, JK et al. (1999). “Design parameters for lateral carrier confinement in quantum-dot lasers”. In: *Applied physics letters* 74.19, pp. 2752–2754.
- Kim, Jungho et al. (2010). “Effect of Inhomogeneous Broadening on Gain and Phase Recovery of Quantum-Dot Semiconductor Optical Amplifiers”. In: *IEEE Journal of Quantum Electronics* 46.11, pp. 1670–1680.
- Kim, Kyoung Chan et al. (2010). “Gain-dependent linewidth enhancement factor in the quantum dot structures”. In: *Nanotechnology* 21.13, p. 134010.
- Kippenberg, Tobias J, Alexander L Gaeta, et al. (2018). “Dissipative Kerr solitons in optical microresonators”. In: *Science* 361.6402.
- Kippenberg, Tobias J, Ronald Holzwarth, and Scott A Diddams (2011). “Microresonator-based optical frequency combs”. In: *science* 332.6029, pp. 555–559.
- Kirstaedter, N et al. (1994). “Low Threshold, Large T_0 Injection Laser Emission from (InGa)As Quantum Dots”. In: *Electronics Letters* 30.17, pp. 1416–1417.
- Klotzkin, David J (2020). *Introduction to semiconductor lasers for optical communications*. Springer.
- Kobayashi, S and T Kimura (1980). “Coherence of injection phase-locked AlGaAs semiconductor laser”. In: *Electronics Letters* 16.17, pp. 668–670.
- Koch, Brian R et al. (2013). “Integrated silicon photonic laser sources for telecom and datacom”. In: *National Fiber Optic Engineers Conference*. Optical Society of America, PDP5C–8.
- Koch, Thomas L and John E Bowers (1984). “Nature of wavelength chirping in directly modulated semiconductor lasers”. In: *Electronics Letters* 20.25, pp. 1038–1040.
- Kogelnik, H and CV Shank (1972). “Coupled-wave theory of distributed feedback lasers”. In: *Journal of applied physics* 43.5, pp. 2327–2335.

- Koltchanov, Igor et al. (1996). “Analytical theory of terahertz four-wave mixing in semiconductor-laser amplifiers”. In: *Applied Physics Letters* 68.20, pp. 2787–2789.
- Kotaki, Y et al. (1989). “Tunable, narrow-linewidth and high-power $\lambda/4$ -shifted DFB laser”. In: *Electronics Letters* 25.15, pp. 990–992.
- Kourogi, Motonobu, Ken’ichi Nakagawa, and Motoichi Ohtsu (1993). “Wide-span optical frequency comb generator for accurate optical frequency difference measurement”. In: *IEEE Journal of Quantum Electronics* 29.10, pp. 2693–2701.
- Kreuter, Philipp, Bernd Witzigmann, and Wolfgang Fichtner (2011). “Toward Frequency-Domain Modeling of Mode Locking in Semiconductor Lasers”. In: *IEEE Journal of Selected Topics in Quantum Electronics* 17.5, pp. 1280–1291.
- Kroemer, Herbert (1963). “A Proposed Class of Hetero-Junction Injection Lasers”. In: *Proceedings of the IEEE* 51.12, pp. 1782–1783.
- Kurczveil, Geza, M Ashkan Seyedi, et al. (2017). “Error-Free Operation in a Hybrid-Silicon Quantum Dot Comb Laser”. In: *IEEE Photonics Technology Letters* 30.1, pp. 71–74.
- Kurczveil, Geza, Chong Zhang, et al. (2018). “On-Chip Hybrid Silicon Quantum Dot Comb Laser with 14 Error-Free Channels”. In: *2018 IEEE International Semiconductor Laser Conference (ISLC)*. IEEE, pp. 1–2.
- Kuroda, Takashi et al. (2013). “Symmetric quantum dots as efficient sources of highly entangled photons: Violation of Bell’s inequality without spectral and temporal filtering”. In: *Physical Review B* 88.4, p. 041306.
- Kwiat, Paul G et al. (1995). “New high-intensity source of polarization-entangled photon pairs”. In: *Physical Review Letters* 75.24, p. 4337.
- Lang, Roy (1982). “Injection locking properties of a semiconductor laser”. In: *IEEE Journal of Quantum Electronics* 18.6, pp. 976–983.
- Lang, Roy and Kohroh Kobayashi (1980). “External Optical Feedback Effects on Semiconductor Injection Laser Properties”. In: *IEEE Journal of Quantum Electronics* 16.3, pp. 347–355.
- Lau, Erwin K, Liang Jie Wong, and Ming C Wu (2009). “Enhanced modulation characteristics of optical injection-locked lasers: A tutorial”. In: *IEEE Journal of Selected Topics in Quantum Electronics* 15.3, pp. 618–633.
- Lazaridis, P, G Debarge, and P Gallion (1995). “Time-bandwidth product of chirped sech^2 pulses: application to phase–amplitude-coupling factor measurement”. In: *Optics Letters* 20.10, pp. 1160–1162.
- Lee, Ka-Lun et al. (2012). “Energy efficiency of optical transceivers in fiber access networks”. In: *Journal of Optical Communications and Networking* 4.9, A59–A68.

- Lelarge, F et al. (2005). “Room Temperature Continuous-Wave Operation of Buried Ridge Stripe Lasers Using InAs-InP (100) Quantum Dots as Active Core”. In: *IEEE Photonics Technology Letters* 17.7, pp. 1369–1371.
- Lelarge, Francois et al. (2007). “Recent Advances on InAs/InP Quantum Dash Based Semiconductor Lasers and Optical Amplifiers Operating at $1.55\mu\text{m}$ ”. In: *IEEE Journal of Selected Topics in Quantum Electronics* 13.1, pp. 111–124.
- Lenstra, Daan, Theodorus Thomas Marinus van Schaijk, and Kevin A Williams (2019). “Toward a Feedback-Insensitive Semiconductor Laser”. In: *IEEE Journal of Selected Topics in Quantum Electronics* 25.6, pp. 1–13.
- Lenstra, Daan, B Verbeek, and A. Den Boef (1985). “Coherence Collapse in Single-Mode Semiconductor Lasers due to Optical Feedback”. In: *IEEE Journal of Quantum Electronics* 21.6, pp. 674–679.
- Leonard, D et al. (1993). “Direct formation of quantum-sized dots from uniform coherent islands of InGaAs on GaAs surfaces”. In: *Applied Physics Letters* 63.23, pp. 3203–3205.
- Letal, GJ et al. (1998). “Determination of Active-Region Leakage Currents in Ridge-Waveguide Strained-Layer Quantum-Well Lasers by Varying the Ridge Width”. In: *IEEE Journal of Quantum Electronics* 34.3, pp. 512–518.
- Li, Chih-Hao et al. (2008). “A laser frequency comb that enables radial velocity measurements with a precision of 1 cm s^{-1} ”. In: *Nature* 452.7187, pp. 610–612.
- Li, Qing et al. (2017). “Stably accessing octave-spanning microresonator frequency combs in the soliton regime”. In: *Optica* 4.2, pp. 193–203.
- Li, Xiang et al. (2021). “Phase noise reduction of a $2\mu\text{m}$ passively mode-locked laser through hybrid III-V/silicon integration”. In: *Optica* 8.6, pp. 855–860.
- Li, Xin-Qi and Yasuhiko Arakawa (1997). “Ultrafast energy relaxation in quantum dots through defect states: A lattice-relaxation approach”. In: *Physical Review B* 56.16, p. 10423.
- Liang, Di et al. (2016). “Integrated finely tunable microring laser on silicon”. In: *Nature Photonics* 10.11, pp. 719–722.
- Liao, Mengya et al. (2018). “Low-noise $1.3\mu\text{m}$ InAs/GaAs quantum dot laser monolithically grown on silicon”. In: *Photonics Research* 6.11, pp. 1062–1066.
- Liao, Paul F and Paul Kelley (2012). *Quantum well lasers*. Elsevier.
- Liao, Sheng-Kai et al. (2018). “Satellite-relayed intercontinental quantum network”. In: *Physical review letters* 120.3, p. 030501.
- Lin, C-Y, Frédéric Grillot, et al. (2010). “RF linewidth reduction in a quantum dot passively mode-locked laser subject to external optical feedback”. In: *Applied Physics Letters* 96.5, p. 051118.

- Lin, C-Y, Y-C Xin, et al. (2009). “Cavity design and characteristics of monolithic long-wavelength InAs/InP quantum dash passively mode-locked lasers”. In: *Optics Express* 17.22, pp. 19739–19748.
- Lin, Chih-Hao, Hung-Hsin Lin, and Fan-Yi Lin (2012). “Four-wave mixing analysis of quantum dot semiconductor lasers for linewidth enhancement factor extraction”. In: *Optics Express* 20.1, pp. 101–110.
- Lin, Chinlon and Fin Mengel (1984). “Reduction of frequency chirping and dynamic linewidth in high-speed directly modulated semiconductor lasers by injection locking”. In: *Electronics Letters* 20.25, pp. 1073–1075.
- Lin, Fan-Yi and Jia-Ming Liu (2004). “Chaotic Lidar”. In: *IEEE Journal of Selected Topics in Quantum Electronics* 10.5, pp. 991–997.
- Lin, FY and JM Liu (2003). “Nonlinear dynamical characteristics of an optically injected semiconductor laser subject to optoelectronic feedback”. In: *Optics Communications* 221.1-3, pp. 173–180.
- Lin, Gray et al. (2011). “Analysis of relative intensity noise spectra for uniformly and chirpily stacked InAs–InGaAs–GaAs quantum dot lasers”. In: *Journal of lightwave technology* 30.3, pp. 331–336.
- Linder, KK et al. (1999). “Self-organized $\text{In}_{0.4}\text{Ga}_{0.6}\text{As}$ quantum-dot lasers grown on Si substrates”. In: *Applied physics letters* 74.10, pp. 1355–1357.
- Lingnau, Benjamin, Weng W Chow, et al. (2013). “Feedback and injection locking instabilities in quantum-dot lasers: a microscopically based bifurcation analysis”. In: *New Journal of Physics* 15.9, p. 093031.
- Lingnau, Benjamin, Kathy Lüdge, et al. (2012). “Failure of the α factor in describing dynamical instabilities and chaos in quantum-dot lasers”. In: *Physical Review E* 86.6, p. 065201.
- Liu, Alan Y and John Bowers (2018). “Photonic integration with epitaxial III–V on silicon”. In: *IEEE Journal of Selected Topics in Quantum Electronics* 24.6, pp. 1–12.
- Liu, Alan Y, Tin Komljenovic, et al. (2017). “Reflection sensitivity of $1.3\ \mu\text{m}$ quantum dot lasers epitaxially grown on silicon”. In: *Optics express* 25.9, pp. 9535–9543.
- Liu, Alan Y, Sudharsanan Srinivasan, et al. (2015). “Quantum dot lasers for silicon photonics”. In: *Photonics Research* 3.5, B1–B9.
- Liu, G, Xiaomin Jin, and Shun-Lien Chuang (2001). “Measurement of linewidth enhancement factor of semiconductor lasers using an injection-locking technique”. In: *IEEE Photonics Technology Letters* 13.5, pp. 430–432.
- Liu, G, A Stintz, et al. (1999). “Extremely Low Room-Temperature Threshold Current Density Diode Lasers Using InAs Dots in $\text{In}_{0.15}\text{Ga}_{0.85}\text{As}$ Quantum Well”. In: *Electronics Letters* 35.14, pp. 1163–1165.

- Liu, JM et al. (1997). “Modulation bandwidth, noise, and stability of a semiconductor laser subject to strong injection locking”. In: *IEEE Photonics Technology Letters* 9.10, pp. 1325–1327.
- Liu, S, D Jung, et al. (2018). “490 fs Pulse Generation from Passively Mode-Locked Single Section Quantum Dot Laser Directly Grown on On-Axis GaP/Si”. In: *Electronics Letters* 54.7, pp. 432–433.
- Liu, Songtao, Justin C Norman, et al. (2018). “Monolithic 9 GHz passively mode locked quantum dot lasers directly grown on on-axis (001) Si”. In: *Applied Physics Letters* 113.4, p. 041108.
- Liu, Songtao, Xinru Wu, et al. (2019). “High-channel-count 20 GHz passively mode-locked quantum dot laser directly grown on Si with 4.1 Tbit/s transmission capacity”. In: *Optica* 6.2, pp. 128–134.
- Lu, Hanh, Case Blaauw, and Toshihiko Makino (1996). “Single-Mode Operation over a Wide Temperature Range in 1.3 μm InGaAsP/InP Distributed Feedback Lasers”. In: *Journal of Lightwave Technology* 14.5, pp. 851–859.
- Lu, ZG, JR Liu, S Raymond, et al. (2008). “312-fs pulse generation from a passive C-band InAs/InP quantum dot mode-locked laser”. In: *Optics Express* 16.14, pp. 10835–10840.
- Lu, ZG, JR Liu, CY Song, et al. (2018). “High performance InAs/InP quantum dot 34.462-GHz C-band coherent comb laser module”. In: *Optics Express* 26.2, pp. 2160–2167.
- Lu, Zhenguo et al. (2021). “InAs/InP quantum dash semiconductor coherent comb lasers and their applications in optical networks”. In: *Journal of Lightwave Technology* 39.12, pp. 3751–3760.
- Luo, Wei et al. (2020). “Comparison of growth structures for continuous-wave electrically pumped 1.55 μm quantum dash lasers grown on (001) Si”. In: *Photonics Research* 8.12, pp. 1888–1894.
- Lvovsky, Alexander I (2015). “Squeezed light”. In: *Photonics: Scientific Foundations, Technology and Applications* 1, pp. 121–163.
- Macario, Julien et al. (2012). “Full spectrum millimeter-wave modulation”. In: *Optics Express* 20.21, pp. 23623–23629.
- Magnúsdóttir, Ingibjörg et al. (2002). “One-and two-phonon capture processes in quantum dots”. In: *Journal of Applied Physics* 92.10, pp. 5982–5990.
- Malic, Ermin et al. (2007). “Coulomb Damped Relaxation Oscillations in Semiconductor Quantum Dot Lasers”. In: *IEEE Journal of Selected Topics in Quantum Electronics* 13.5, pp. 1242–1248.
- Malins, DB et al. (2006). “Ultrafast electroabsorption dynamics in an InAs quantum dot saturable absorber at 1.3 μm ”. In: *Applied Physics Letters* 89.17, p. 171111.

- Marcinkevičius, Saulius (2008). “Dynamics of carrier transfer into In (Ga) As self-assembled quantum dots”. In: *Self-Assembled Quantum Dots*. Springer, pp. 129–163.
- Marin-Palomo, Pablo et al. (2017). “Microresonator-based solitons for massively parallel coherent optical communications”. In: *Nature* 546.7657, pp. 274–279.
- Marzin, J-Y et al. (1994). “Photoluminescence of single InAs quantum dots obtained by self-organized growth on GaAs”. In: *Physical review letters* 73.5, p. 716.
- Matsuda, K et al. (2001). “Homogeneous linewidth broadening in a $\text{In}_{0.5}\text{Ga}_{0.5}\text{As}/\text{GaAs}$ single quantum dot at room temperature investigated using a highly sensitive near-field scanning optical microscope”. In: *Physical Review B* 63.12, p. 121304.
- Matsusue, Toshio and Hiroyuki Sakaki (1987). “Radiative recombination coefficient of free carriers in GaAs-AlGaAs quantum wells and its dependence on temperature”. In: *Applied Physics Letters* 50.20, pp. 1429–1431.
- McCumber, DE (1966). “Intensity fluctuations in the output of cw laser oscillators. I”. In: *Physical Review* 141.1, p. 306.
- Meinecke, Stefan et al. (2019). “Ultra-short pulse generation in a three section tapered passively mode-locked quantum-dot semiconductor laser”. In: *Scientific Reports* 9.1, pp. 1–14.
- Meng, XJ et al. (1998). “Suppression of second harmonic distortion in directly modulated distributed feedback lasers by external light injection”. In: *Electronics Letters* 34.21, pp. 2040–2041.
- Merghem, K et al. (2009). “Low noise performance of passively mode locked quantum-dash-based lasers under external optical feedback”. In: *Applied Physics Letters* 95.13, p. 131111.
- Meuer, Christian et al. (2011). “40 Gb/s wavelength conversion via four-wave mixing in a quantum-dot semiconductor optical amplifier”. In: *Optics Express* 19.4, pp. 3788–3798.
- Mi, Z, P Bhattacharya, and S Fathpour (2005). “High-speed 1.3 μm tunnel injection quantum-dot lasers”. In: *Applied Physics Letters* 86.15, p. 153109.
- Mi, Z, P Bhattacharya, J Yang, et al. (2005). “Room-Temperature Self-Organised $\text{In}_{0.5}\text{Ga}_{0.5}\text{As}$ Quantum Dot Laser on Silicon”. In: *Electronics letters* 41.13, pp. 742–744.
- Mikhrin, SS et al. (2005). “High power temperature-insensitive 1.3 μm InAs/InGaAs/GaAs quantum dot lasers”. In: *Semiconductor science and technology* 20.5, p. 340.
- Mirin, R, A Gossard, and J Bowers (1996). “Room Temperature Lasing from InGaAs Quantum Dots”. In: *Electronics Letters* 32.18, p. 1732.
- Miyamoto, Yasuyuki et al. (1987). “Light emission from quantum-box structure by current injection”. In: *Japanese journal of applied physics* 26.4A, p. L225.

- Mogensen, Finn, Henning Olesen, and Gunnar Jacobsen (1985). “Locking conditions and stability properties for a semiconductor laser with external light injection”. In: *IEEE Journal of Quantum Electronics* 21.7, pp. 784–793.
- Moison, JM et al. (1994). “Self-organized growth of regular nanometer-scale InAs dots on GaAs”. In: *Applied Physics Letters* 64.2, pp. 196–198.
- Mols, Peter PG et al. (1989). “Yield and device characteristics of DFB lasers: Statistics and novel coating design in theory and experiment”. In: *IEEE Journal of Quantum Electronics* 25.6, pp. 1303–1313.
- Mørk, J, J Mark, and B Tromborg (1990). “Route to chaos and competition between relaxation oscillations for a semiconductor laser with optical feedback”. In: *Physical Review Letters* 65.16, p. 1999.
- Mork, Jesper, Bjarne Tromborg, and Peter Leth Christiansen (1988). “Bistability and low-frequency fluctuations in semiconductor lasers with optical feedback: a theoretical analysis”. In: *IEEE Journal of Quantum Electronics* 24.2, pp. 123–133.
- Mork, Jesper, Bjarne Tromborg, and Jannik Mark (1992). “Chaos in semiconductor lasers with optical feedback: theory and experiment”. In: *IEEE Journal of Quantum Electronics* 28.1, pp. 93–108.
- Morris, D, N Perret, and S Fafard (1999). “Carrier energy relaxation by means of Auger processes in InAs/GaAs self-assembled quantum dots”. In: *Applied Physics Letters* 75.23, pp. 3593–3595.
- Morthier, Geert, Klaus David, et al. (1990). “A new DFB-laser diode with reduced spatial hole burning”. In: *IEEE Photonics Technology Letters* 2.6, pp. 388–390.
- Morthier, Geert and Patrick Vankwikelberge (2013). *Handbook of distributed feedback laser diodes*. Artech House - 685 Canton Street, Norwood, MA 02062 USA.
- Muroya, Y et al. (1997). “Precise wavelength control for DFB laser diodes by novel corrugation delineation method”. In: *IEEE Photonics Technology Letters* 9.3, pp. 288–290.
- Nakagawa, K, M Kouroggi, and M Ohtsu (1993). “Proposal of a frequency-synthesis chain between the microwave and optical frequencies of the Ca intercombination line at 657 nm using diode lasers”. In: *Applied Physics B* 57.6, pp. 425–430.
- Nakajima, H and J-C Bouley (1991). “Observation of Power Dependent Linewidth Enhancement Factor in 1.55 μm Strained Quantum Well Lasers”. In: *Electronics Letters* 27.20, pp. 1840–1841.
- Newell, TC et al. (1999). “Gain and Linewidth Enhancement Factor in InAs Quantum-Dot Laser Diodes”. In: *IEEE Photonics Technology Letters* 11.12, pp. 1527–1529.
- Newman, Zachary L et al. (2019). “Architecture for the photonic integration of an optical atomic clock”. In: *Optica* 6.5, pp. 680–685.

- Nguyen-Van, Hoang et al. (2018). “Quantum cascade lasers grown on silicon”. In: *Scientific reports* 8.1, pp. 1–8.
- Nielsen, David and Shun Lien Chuang (2010). “Four-wave mixing and wavelength conversion in quantum dots”. In: *Physical Review B* 81.3, p. 035305.
- Nielsen, Torben Roland, Paul Gartner, and Frank Jahnke (2004). “Many-body theory of carrier capture and relaxation in semiconductor quantum-dot lasers”. In: *Physical Review B* 69.23, p. 235314.
- Nilsson, HH, J-Z Zhang, and I Galbraith (2005). “Homogeneous broadening in quantum dots due to Auger scattering with wetting layer carriers”. In: *Physical Review B* 72.20, p. 205331.
- Nishi, K et al. (2013). “Molecular beam epitaxial growths of high-optical-gain InAs quantum dots on GaAs for long-wavelength emission”. In: *Journal of Crystal Growth* 378, pp. 459–462.
- Nishi, Kenichi, Keizo Takemasa, et al. (2017). “Development of Quantum Dot Lasers for Data-Com and Silicon Photonics Applications”. In: *IEEE Journal of Selected Topics in Quantum Electronics* 23.6, pp. 1–7.
- Nishi, Kenichi, Mitsuki Yamada, et al. (1998). “Long-wavelength lasing from InAs self-assembled quantum dots on (311)B InP”. In: *Applied physics letters* 73.4, pp. 526–528.
- Norman, Justin C, Daehwan Jung, Yating Wan, et al. (2018). “Perspective: The future of quantum dot photonic integrated circuits”. In: *APL photonics* 3.3, p. 030901.
- Norman, Justin C, Daehwan Jung, Zeyu Zhang, et al. (2019). “A Review of High-Performance Quantum Dot Lasers on Silicon”. In: *IEEE Journal of Quantum Electronics* 55.2, pp. 1–11.
- Norman, Justin C, Richard P Mirin, and John E Bowers (2021). “Quantum dot lasers—History and future prospects”. In: *Journal of Vacuum Science & Technology A: Vacuum, Surfaces, and Films* 39.2, p. 020802.
- Norman, Justin C, Zeyu Zhang, et al. (2019). “The Importance of P-Doping for Quantum Dot Laser on Silicon Performance”. In: *IEEE Journal of Quantum Electronics* 55.6, pp. 1–11.
- Nozik, Arthur J (2008). “Multiple exciton generation in semiconductor quantum dots”. In: *Chemical Physics Letters* 457.1-3, pp. 3–11.
- Ohnesorge, B et al. (1996). “Rapid carrier relaxation in self-assembled $\text{In}_x\text{Ga}_{1-x}\text{As}/\text{GaAs}$ quantum dots”. In: *Physical Review B* 54.16, p. 11532.
- Ohtsubo, Junji (2012). *Semiconductor lasers: stability, instability and chaos*. Vol. 111. Springer.
- Olofsson, L and TG Brown (1992). “Frequency dependence of the chirp factor in 1.55 μm distributed feedback semiconductor lasers”. In: *IEEE Photonics Technology Letters* 4.7, pp. 688–691.

- Opačak, Nikola et al. (2021). “Spectrally resolved linewidth enhancement factor of a semiconductor frequency comb”. In: *arXiv preprint arXiv:2104.05747*.
- Osinski, Marek and Jens Buus (1987). “Linewidth Broadening Factor in Semiconductor Lasers—An Overview”. In: *IEEE Journal of Quantum Electronics* 23.1, pp. 9–29.
- Otsuka, K and S Tarucha (1981). “Theoretical studies on injection locking and injection-induced modulation of laser diodes”. In: *IEEE Journal of Quantum Electronics* 17.8, pp. 1515–1521.
- Otto, C et al. (2012). “Delay-induced dynamics and jitter reduction of passively mode-locked semiconductor lasers subject to optical feedback”. In: *New Journal of Physics* 14.11, p. 113033.
- Otto, Christian (2014). *Dynamics of Quantum Dot Lasers: Effects of Optical Feedback and External Optical Injection*. Springer Science & Business Media.
- Papp, Scott B et al. (2014). “Microresonator frequency comb optical clock”. In: *Optica* 1.1, pp. 10–14.
- Perrière, Vincent Brac de la et al. (2021). “Electrically injected parity-time symmetric distributed feedback laser diodes (DFB) for telecom applications”. In: *Nanophotonics* 10.4, pp. 1309–1317.
- Petermann, Klaus (1991). *Laser diode modulation and noise*. Vol. 3. Springer Science & Business Media.
- (1995). “External Optical Feedback Phenomena in Semiconductor Lasers”. In: *IEEE Journal of Selected Topics in Quantum Electronics* 1.2, pp. 480–489.
- Pfeiffer, Martin HP et al. (2017). “Octave-spanning dissipative Kerr soliton frequency combs in Si₃N₄ microresonators”. In: *Optica* 4.7, pp. 684–691.
- Poole, Philip J et al. (2021). “A Performance Comparison Between Quantum Dash and Quantum Well Fabry-Pérot Lasers”. In: *IEEE Journal of Quantum Electronics* 57.6, pp. 1–7.
- Preskill, John (2018). “Quantum computing in the NISQ era and beyond”. In: *Quantum* 2, p. 79.
- Prior, E et al. (2016). “Dynamics of dual-polarization VCSEL-based optical frequency combs under optical injection locking”. In: *Optics Letters* 41.17, pp. 4083–4086.
- Provost, J-G et al. (2011). “Single step measurement of optical transmitters Henry factor using sinusoidal optical phase modulations”. In: *Optics express* 19.22, pp. 21396–21403.
- Provost, Jean-Guy and Frederic Grillot (2011). “Measuring the chirp and the linewidth enhancement factor of optoelectronic devices with a Mach-Zehnder interferometer”. In: *IEEE Photonics Journal* 3.3, pp. 476–488.

- Rafailov, Edik U, Maria Ana Cataluna, and Wilson Sibbett (2007). “Mode-locked quantum-dot lasers”. In: *Nature photonics* 1.7, pp. 395–401.
- Raghunathan, Ravi et al. (2012). “Pulse Characterization of Passively Mode-Locked Quantum-Dot Lasers Using a Delay Differential Equation Model Seeded With Measured Parameters”. In: *IEEE Journal of Selected Topics in Quantum Electronics* 19.4, pp. 1100311–1100311.
- Rasmussen, Thorsten S and Jesper Mork (2021). “Theory of microscopic semiconductor lasers with external optical feedback”. In: *Optics Express* 29.10, pp. 14182–14188.
- Rebrova, Natalia et al. (2011). “Optically injected mode-locked laser”. In: *Physical Review E* 83.6, p. 066202.
- Risch, Ch and C Voumard (1977). “Self-pulsation in the output intensity and spectrum of GaAs-AlGaAs cw diode lasers coupled to a frequency-selective external optical cavity”. In: *Journal of Applied Physics* 48.5, pp. 2083–2085.
- Roelkens, Günther et al. (2010). “III-V/silicon photonics for on-chip and intra-chip optical interconnects”. In: *Laser & Photonics Reviews* 4.6, pp. 751–779.
- Roncin, Vincent (2004). “Contribution à l’étude de fonctions optiques à base d’amplificateurs optiques à semi-conducteurs pour la régénération des signaux de télécommunication à très haut débit”. PhD thesis. Université Rennes 1.
- Rontani, D et al. (2016). “Enhanced complexity of optical chaos in a laser diode with phase-conjugate feedback”. In: *Optics letters* 41.20, pp. 4637–4640.
- Rontani, Damien et al. (2016). “Compressive sensing with optical chaos”. In: *Scientific reports* 6.1, pp. 1–7.
- Rosales, Ricardo, Kamel Merghem, et al. (2011). “InAs/InP Quantum-Dot Passively Mode-Locked Lasers for 1.55- μm Applications”. In: *IEEE Journal of Selected Topics in Quantum Electronics* 17.5, pp. 1292–1301.
- Rosales, Ricardo, SG Murdoch, et al. (2012). “High performance mode locking characteristics of single section quantum dash lasers”. In: *Optics express* 20.8, pp. 8649–8657.
- Rosencher, Emmanuel and Borge Vinter (2002). *Optoelectronics*. Cambridge University Press.
- Rossetti, Mattia, Paolo Bardella, and Ivo Montrosset (2011). “Modeling Passive Mode-Locking in Quantum Dot Lasers: A Comparison Between a Finite-Difference Traveling-Wave Model and a Delayed Differential Equation Approach”. In: *IEEE Journal of Quantum Electronics* 47.5, pp. 569–576.
- Rossetti, Mattia, Tianhong Xu, et al. (2011). “Impact of Gain Saturation on Passive Mode Locking Regimes in Quantum Dot Lasers with Straight and Tapered Waveguides”. In: *IEEE Journal of Quantum Electronics* 47.11, pp. 1404–1413.

- Sadeev, Tagir et al. (2015). “Highly efficient non-degenerate four-wave mixing under dual-mode injection in InP/InAs quantum-dash and quantum-dot lasers at $1.55 \mu\text{m}$ ”. In: *Applied Physics Letters* 107.19, p. 191111.
- Sakamoto, Akira and Mitsuru Sugawara (2000). “Theoretical Calculation of Lasing Spectra of Quantum-Dot Lasers: Effect of Homogeneous Broadening of Optical Gain”. In: *IEEE Photonics Technology Letters* 12.2, pp. 107–109.
- Saldutti, Marco et al. (2020). “Impact of carrier transport on the performance of QD lasers on silicon: a drift-diffusion approach”. In: *Photonics Research* 8.8, pp. 1388–1397.
- Samara, Farid et al. (2019). “High-rate photon pairs and sequential Time-Bin entanglement with Si₃N₄ microring resonators”. In: *Optics express* 27.14, pp. 19309–19318.
- Sanaee, Maryam and Abbas Zarifkar (2015). “Theoretical Modeling of Relative Intensity Noise in P-Doped $1.3\text{-}\mu\text{m}$ InAs/GaAs Quantum Dot Lasers”. In: *Journal of Lightwave Technology* 33.1, pp. 234–243.
- Sargent III, M, MO Scully, and WE Lamb Jr (1974). “Laser Physics Addison-Wesley”. In: *Reading, Mass.*
- Schimpe, R, JE Bowers, and Thomas L Koch (1986). “Characterisation of frequency response of $1.5 \mu\text{m}$ InGaAsP DFB laser diode and InGaAs PIN photodiode by heterodyne measurement technique”. In: *Electronics Letters* 22.9, pp. 453–454.
- Schliesser, Albert, Nathalie Picqué, and Theodor W Hänsch (2012). “Mid-infrared frequency combs”. In: *Nature photonics* 6.7, pp. 440–449.
- Schnatz, H et al. (1996). “First phase-coherent frequency measurement of visible radiation”. In: *Physical Review Letters* 76.1, p. 18.
- Schneider, Hans Christian, Weng Wah Chow, and Stephan W Koch (2004). “Excitation-induced dephasing in semiconductor quantum dots”. In: *Physical Review B* 70.23, p. 235308.
- Schunk, N and K Petermann (1989). “Stability Analysis for Laser Diodes with Short External Cavities”. In: *IEEE Photonics Technology Letters* 1.3, pp. 49–51.
- Schunk, Nikolaus and KLAUS Petermann (1986). “Noise analysis of injection-locked semiconductor injection lasers”. In: *IEEE Journal of Quantum Electronics* 22.5, pp. 642–650.
- Schunk, Nikolaus and Klaus Petermann (1988). “Numerical analysis of the feedback regimes for a single-mode semiconductor laser with external feedback”. In: *IEEE Journal of Quantum Electronics* 24.7, pp. 1242–1247.
- Sciamanna, Marc and K Alan Shore (2015). “Physics and applications of laser diode chaos”. In: *Nature photonics* 9.3, pp. 151–162.

- Seebeck, Jan et al. (2005). “Polarons in semiconductor quantum dots and their role in the quantum kinetics of carrier relaxation”. In: *Physical Review B* 71.12, p. 125327.
- Senellart, Pascale, Glenn Solomon, and Andrew White (2017). “High-performance semiconductor quantum-dot single-photon sources”. In: *Nature nanotechnology* 12.11, pp. 1026–1039.
- Seok, Tae Joon et al. (2019). “Wafer-scale silicon photonic switches beyond die size limit”. In: *Optica* 6.4, pp. 490–494.
- Septon, Tali et al. (2019). “Large linewidth reduction in semiconductor lasers based on atom-like gain material”. In: *Optica* 6.8, pp. 1071–1077.
- Sercel, Peter C, Al L Efron, and M Rosen (1999). “Intrinsic gap states in semiconductor nanocrystals”. In: *Physical Review Letters* 83.12, p. 2394.
- Shalm, Lynden K et al. (2015). “Strong loophole-free test of local realism”. In: *Physical review letters* 115.25, p. 250402.
- Shang, Chen et al. (2021). “High-temperature reliable quantum-dot lasers on Si with misfit and threading dislocation filters”. In: *Optica* 8.5, pp. 749–754.
- Shoji, H et al. (1996). “Room Temperature CW Operation at the Ground State of Self-Formed Quantum Dot Lasers with Multi-Stacked Dot Layer”. In: *Electronics Letters* 32.21, pp. 2023–2024.
- Siegert, Jörg, Saulius Marcinkevičius, and Qing Xiang Zhao (2005). “Carrier dynamics in modulation-doped InAs/GaAs quantum dots”. In: *Physical Review B* 72.8, p. 085316.
- Simpson, TB, JM Liu, and A Gavrielides (1995). “Bandwidth enhancement and broadband noise reduction in injection-locked semiconductor lasers”. In: *IEEE Photonics Technology Letters* 7.7, pp. 709–711.
- Sinclair, Laura C et al. (2015). “Invited Article: A compact optically coherent fiber frequency comb”. In: *Review of scientific instruments* 86.8, p. 081301.
- Soda, Haruhisa et al. (1987). “Stability in Single Longitudinal Mode Operation in GaInAsP/InP Phase-Adjusted DFB Lasers”. In: *IEEE Journal of Quantum Electronics* 23.6, pp. 804–814.
- Solgaard, Olav and Kam Y Lau (1993). “Optical feedback stabilization of the intensity oscillations in ultrahigh-frequency passively modelocked monolithic quantum-well lasers”. In: *IEEE Photonics Technology Letters* 5.11, pp. 1264–1267.
- Sooudi, Ehsan et al. (2013). “A novel scheme for two-level stabilization of semiconductor mode-locked lasers using simultaneous optical injection and optical feedback”. In: *IEEE Journal of Selected Topics in Quantum Electronics* 19.4, pp. 1101208–1101208.

- Spence, David E, P Np Kean, and Wilson Sibbett (1991). “60-fsec pulse generation from a self-mode-locked Ti: sapphire laser”. In: *Optics Letters* 16.1, pp. 42–44.
- Spencer, Daryl T et al. (2018). “An optical-frequency synthesizer using integrated photonics”. In: *Nature* 557.7703, pp. 81–85.
- Spitz, Olivier et al. (2021). “Private communication with quantum cascade laser photonic chaos”. In: *Nature communications* 12.1, pp. 1–8.
- Spott, Alexander et al. (2018). “Interband cascade laser on silicon”. In: *Optica* 5.8, pp. 996–1005.
- Sprengers, JP et al. (2011). “Waveguide superconducting single-photon detectors for integrated quantum photonic circuits”. In: *Applied Physics Letters* 99.18, p. 181110.
- Spring, Justin B et al. (2013). “On-chip low loss heralded source of pure single photons”. In: *Optics express* 21.11, pp. 13522–13532.
- Steane, Andrew (1998). “Quantum computing”. In: *Reports on Progress in Physics* 61.2, p. 117.
- Su, H et al. (2005). “Nondegenerate four-wave mixing in quantum dot distributed feedback lasers”. In: *IEEE Photonics Technology Letters* 17.8, pp. 1686–1688.
- Sudoh, TK et al. (1993). “Self-suppression effect of longitudinal spatial hole burning in absorptive-grating gain-coupled DFB lasers”. In: *IEEE Photonics Technology Letters* 5.11, pp. 1276–1278.
- Sugawara, Mitsuru et al. (2000). “Effect of homogeneous broadening of optical gain on lasing spectra in self-assembled $\text{In}_x\text{Ga}_{1-x}\text{As}/\text{GaAs}$ quantum dot lasers”. In: *Physical Review B* 61.11, p. 7595.
- Suh, Myoung-Gyun, Qi-Fan Yang, et al. (2016). “Microresonator soliton dual-comb spectroscopy”. In: *Science* 354.6312, pp. 600–603.
- Suh, Myoung-Gyun, Xu Yi, et al. (2019). “Searching for exoplanets using a microresonator astrocomb”. In: *Nature photonics* 13.1, pp. 25–30.
- Supradeepa, VR and Andrew M Weiner (2012). “Bandwidth scaling and spectral flatness enhancement of optical frequency combs from phase-modulated continuous-wave lasers using cascaded four-wave mixing”. In: *Optics Letters* 37.15, pp. 3066–3068.
- Tager, AA and BB Elenkrig (1993). “Stability regimes and high-frequency modulation of laser diodes with short external cavity”. In: *IEEE Journal of Quantum Electronics* 29.12, pp. 2886–2890.
- Tan, F et al. (2012). “Relative intensity noise of a quantum well transistor laser”. In: *Applied Physics Letters* 101.15, p. 151118.
- Tanabe, Katsuaki, Katsuyuki Watanabe, and Yasuhiko Arakawa (2012). “III-V/Si hybrid photonic devices by direct fusion bonding”. In: *Scientific reports* 2.1, pp. 1–6.

- Taylor, Michael A et al. (2013). “Biological measurement beyond the quantum limit”. In: *Nature Photonics* 7.3, pp. 229–233.
- Temkin, Henryk et al. (1986). “Reflection noise in index-guided InGaAsP lasers”. In: *IEEE Journal of Quantum Electronics* 22.2, pp. 286–293.
- Thompson, Mark G et al. (2009). “InGaAs Quantum-Dot Mode-Locked Laser Diodes”. In: *IEEE Journal of Selected Topics in Quantum Electronics* 15.3, pp. 661–672.
- Tkach, R and AR1986JLwT Chraplyvy (1986). “Regimes of Feedback Effects in 1.5- μm Distributed Feedback Lasers”. In: *Journal of Lightwave technology* 4.11, pp. 1655–1661.
- Torres-Company, Victor and Andrew M Weiner (2014). “Optical frequency comb technology for ultra-broadband radio-frequency photonics”. In: *Laser & Photonics Reviews* 8.3, pp. 368–393.
- Trocha, Philipp et al. (2018). “Ultrafast optical ranging using microresonator soliton frequency combs”. In: *Science* 359.6378, pp. 887–891.
- Tromborg, Bjarne, J Osmundsen, and Henning Olesen (1984). “Stability analysis for a semiconductor laser in an external cavity”. In: *IEEE journal of quantum electronics* 20.9, pp. 1023–1032.
- Tuan, Tong Hoang et al. (2013). “Optical parametric gain and bandwidth in highly nonlinear tellurite hybrid microstructured optical fiber with four zero-dispersion wavelengths”. In: *Optics Express* 21.17, pp. 20303–20312.
- Uchida, Atsushi (2012). *Optical communication with chaotic lasers: applications of nonlinear dynamics and synchronization*. John Wiley & Sons.
- Udem, Th et al. (1999). “Accurate measurement of large optical frequency differences with a mode-locked laser”. In: *Optics letters* 24.13, pp. 881–883.
- Ukhanov, AA et al. (2002). “Orientation dependence of the optical properties in InAs quantum-dash lasers on InP”. In: *Applied physics letters* 81.6, pp. 981–983.
- Urayama, Junji et al. (2001). “Observation of phonon bottleneck in quantum dot electronic relaxation”. In: *Physical Review Letters* 86.21, p. 4930.
- Usami, Masashi, Shigeyuki Akiba, and Katsuyuki Utaka (1987). “Asymmetric $\lambda/4$ -shifted InGaAsP/InP DFB Lasers”. In: *IEEE Journal of Quantum Electronics* 23.6, pp. 815–821.
- Uskov, Alexander V et al. (2004). “Carrier-induced refractive index in quantum dot structures due to transitions from discrete quantum dot levels to continuum states”. In: *Applied physics letters* 84.2, pp. 272–274.
- Ustinov, VM et al. (1998). “Low-threshold quantum-dot injection heterolaser emitting at 1.84 μm ”. In: *Technical Physics Letters* 24.1, pp. 22–23.

- Vahala, Kerry and Amnon Yariv (1983). “Semiclassical theory of noise in semiconductor lasers-Part II”. In: *IEEE Journal of Quantum Electronics* 19.6, pp. 1102–1109.
- Van der Ziel, JP et al. (1975). “Laser oscillation from quantum states in very thin GaAs- Al_{0.2}Ga_{0.8}As multilayer structures”. In: *Applied Physics Letters* 26.8, pp. 463–465.
- Verolet, Théo et al. (2020). “Mode Locked Laser Phase Noise Reduction under Optical Feedback for Coherent DWDM Communication”. In: *Journal of Lightwave Technology* 38.20, pp. 5708–5715.
- Veselinov, Kiril et al. (2007). “Analysis of the Double Laser Emission Occurring in 1.55- μm InAs/InP (113) B Quantum-Dot Lasers”. In: *IEEE Journal of Quantum Electronics* 43.9, pp. 810–816.
- Vijayakumar, Deepak et al. (2011). “Narrow line width operation of a 980 nm gain guided tapered diode laser bar”. In: *Optics Express* 19.2, pp. 1131–1137.
- Virte, Martin (2014). “Two-mode dynamics and switching in quantum dot lasers.” PhD thesis. Supélec.
- Virte, Martin et al. (2013). “Deterministic polarization chaos from a laser diode”. In: *Nature Photonics* 7.1, pp. 60–65.
- Vivien, Laurent and Lorenzo Pavesi (2016). *Handbook of silicon photonics*. Taylor & Francis.
- Vladimirov, Andrei G, Uwe Bandelow, et al. (2010). “Dynamical regimes in a monolithic passively mode-locked quantum dot laser”. In: *JOSA B* 27.10, pp. 2102–2109.
- Vladimirov, Andrei G and Dmitry Turaev (2005). “Model for passive mode locking in semiconductor lasers”. In: *Physical Review A* 72.3, p. 033808.
- Vurgaftman, I et al. (2015). “Interband cascade lasers”. In: *Journal of Physics D: Applied Physics* 48.12, p. 123001.
- Waldmueller, Inès et al. (2006). “Nonequilibrium Many-Body Theory of Intersubband Lasers”. In: *IEEE Journal of Quantum Electronics* 42.3, pp. 292–301.
- Walker, RG, I Bennion, and AC Carter (1989). “Low-voltage, 50 Ω , GaAs/AlGaAs travelling-wave modulator with bandwidth exceeding 25 GHz”. In: *Electronics Letters* 25.23, pp. 1549–1550.
- Wan, Yating et al. (2020). “Directly modulated single-mode tunable quantum dot lasers at 1.3 μm ”. In: *Laser & Photonics Reviews* 14.3, p. 1900348.
- Wang, Cheng, Frédéric Grillot, et al. (2013). “Nondegenerate four-wave mixing in a dual-mode injection-locked InAs/InP (100) nanostructure laser”. In: *IEEE Photonics Journal* 6.1, pp. 1–8.

- Wang, Cheng, Kevin Schires, et al. (2016). “Thermally insensitive determination of the linewidth broadening factor in nanostructured semiconductor lasers using optical injection locking”. In: *Scientific reports* 6.1, pp. 1–8.
- Wang, Cheng, Jun-Ping Zhuang, et al. (2016). “Contribution of off-resonant states to the phase noise of quantum dot lasers”. In: *Optics express* 24.26, pp. 29872–29881.
- Wang, Jianwei et al. (2020). “Integrated photonic quantum technologies”. In: *Nature Photonics* 14.5, pp. 273–284.
- Wang, Ruijun et al. (2020). “Mid-infrared quantum cascade laser frequency combs based on multi-section waveguides”. In: *Optics Letters* 45.23, pp. 6462–6465.
- Wang, Ting et al. (2011). “1.3- μm InAs/GaAs quantum-dot lasers monolithically grown on Si substrates”. In: *Optics express* 19.12, pp. 11381–11386.
- Wang, Xing-Guang et al. (2021). “Nonlinear dynamics of a quantum cascade laser with tilted optical feedback”. In: *Physical Review A* 103.2, p. 023528.
- Wang, Yi et al. (2018). “Monolithic quantum-dot distributed feedback laser array on silicon”. In: *Optica* 5.5, pp. 528–533.
- Weber, Christoph et al. (2015). “Picosecond pulse amplification up to a peak power of 42 W by a quantum-dot tapered optical amplifier and a mode-locked laser emitting at 1.26 μm ”. In: *Optics letters* 40.3, pp. 395–398.
- Weiss, CO, A Godone, and A Olafsson (1983). “Routes to chaotic emission in a cw He-Ne laser”. In: *Physical Review A* 28.2, p. 892.
- Weiss, CO, W Klische, et al. (1985). “Instabilities and chaos of a single mode NH₃ ring laser”. In: *Optics communications* 52.6, pp. 405–408.
- Westbrook, LD (1985). “Dispersion of Linewidth-Broadening Factor in 1.5 μm Laser Diodes”. In: *Electronics Letters* 21.22, pp. 1018–1019.
- Wieczorek, Sebastian, Bernd Krauskopf, and Daan Lenstra (2002). “Multipulse excitability in a semiconductor laser with optical injection”. In: *Physical Review Letters* 88.6, p. 063901.
- Willatzen, Morten et al. (1991). “Nonlinear Gain Suppression in Semiconductor Lasers Due to Carrier Heating”. In: *IEEE Photonics Technology Letters* 3.7, pp. 606–609.
- Wirths, Stephan et al. (2018). “Room-temperature lasing from monolithically integrated GaAs microdisks on silicon”. In: *ACS nano* 12.3, pp. 2169–2175.
- Wu, Ling-An et al. (1986). “Generation of squeezed states by parametric down conversion”. In: *Physical review letters* 57.20, p. 2520.
- Xiang, Chao et al. (2021). “Laser soliton microcombs heterogeneously integrated on silicon”. In: *Science* 373.6550, pp. 99–103.

- Xin, Y-C et al. (2007). “Reconfigurable quantum dot monolithic multi-section passive mode-locked lasers”. In: *Optics Express* 15.12, pp. 7623–7633.
- Xue, Ying et al. (2020). “1.55 μm electrically pumped continuous wave lasing of quantum dash lasers grown on silicon”. In: *Optics Express* 28.12, pp. 18172–18179.
- YAMADA, Minoru and Michihiko SUHARA (1990). “Analysis of Excess Noise Induced by Optical Feedback in Semiconductor Laser Based on Mode Competition Theory”. In: *IEICE TRANSACTIONS (1976-1990)* 73.1, pp. 77–82.
- Yamamoto, Yoshihisa (1980). “Receiver performance evaluation of various digital optical modulation-demodulation systems in the 0.5-10 μm wavelength region”. In: *IEEE Journal of Quantum Electronics* 16.11, pp. 1251–1259.
- Yamaoka, Suguru et al. (2021). “Directly modulated membrane lasers with 108 GHz bandwidth on a high-thermal-conductivity silicon carbide substrate”. In: *Nature Photonics* 15.1, pp. 28–35.
- Yariv, A (1989). *Quantum Electronics*. John Wiley, New York.
- Yin, Juan et al. (2017). “Satellite-to-ground entanglement-based quantum key distribution”. In: *Physical review letters* 119.20, p. 200501.
- Yoo, SJ Ben (1996). “Wavelength conversion technologies for WDM network applications”. In: *Journal of Lightwave Technology* 14.6, pp. 955–966.
- Yousefi, Mirvais and Daan Lenstra (1999). “Dynamical behavior of a semiconductor laser with filtered external optical feedback”. In: *IEEE Journal of Quantum Electronics* 35.6, pp. 970–976.
- Yu, Yanguang, Guido Giuliani, and Silvano Donati (2004). “Measurement of the linewidth enhancement factor of semiconductor lasers based on the optical feedback self-mixing effect”. In: *IEEE Photonics Technology Letters* 16.4, pp. 990–992.
- Yvind, Kresten et al. (2008). “Low-noise monolithic mode-locked semiconductor lasers through low-dimensional structures”. In: *Novel In-Plane Semiconductor Lasers VII*. Vol. 6909. International Society for Optics and Photonics, 69090A.
- Zhang, Y et al. (2021). “Squeezed light from a nanophotonic molecule”. In: *Nature communications* 12.1, pp. 1–6.
- Zhang, Zeyu et al. (2018). “Effects of modulation p doping in InAs quantum dot lasers on silicon”. In: *Applied Physics Letters* 113.6, p. 061105.
- Zhao, Shiyuan and Frédéric Grillot (2021). “Effect of Shockley-Read-Hall recombination on the static and dynamical characteristics of epitaxial quantum-dot lasers on silicon”. In: *Physical Review A* 103.6, p. 063521.
- Zhao, Yun et al. (2020). “Near-degenerate quadrature-squeezed vacuum generation on a silicon-nitride chip”. In: *Physical Review Letters* 124.19, p. 193601.

- Zhou, Yue-Guang et al. (2017). “Relative intensity noise of InAs quantum dot lasers epitaxially grown on Ge”. In: *Optics Express* 25.23, pp. 28817–28824.
- Zhu, Si et al. (2018). “1.5 μ m quantum-dot diode lasers directly grown on CMOS-standard (001) silicon”. In: *Applied Physics Letters* 113.22, p. 221103.
- Zilkie, Aaron J et al. (2008). “Time-Resolved Linewidth Enhancement Factors in Quantum Dot and Higher-Dimensional Semiconductor Amplifiers Operating at 1.55 μ m”. In: *Journal of Lightwave Technology* 26.11, pp. 1498–1509.

Appendix A

PUBLISHED CONTENTS

Journal papers

1. **B. Dong**, J. Duan, H. Huang, J. C. Norman, K. Nishi, K. Takemasa, M. Sugawara, J. E. Bowers, and F. Grillot (2021). "Dynamic performance and reflection sensitivity of quantum dot distributed feedback lasers with large optical mismatch." In: *Photonics Research*, 9.8, pp. 1550-1558.
2. **B. Dong**, J. -D. Chen, F. -Y. Lin, J. C. Norman, J. E. Bowers, and F. Grillot (2021). "Dynamic and nonlinear properties of epitaxial quantum-dot lasers on silicon operating under long-and short-cavity feedback conditions for photonic integrated circuits." In: *Physical Review A*, 103.3, pp. 033509.
3. **B. Dong**, X. Champagne de Labriolle, S. Liu, M. Dumont, H. Huang, J. Duan, J. C. Norman, J. E Bowers, and F. Grillot (2020). "1.3- μm passively mode-locked quantum dot lasers epitaxially grown on silicon: gain properties and optical feedback stabilization." In: *Journal of Physics: Photonics*, 2, pp. 045006.
4. **B. Dong**, H. Huang, J. Duan, G. Kurczveil, D. Liang, R. G. Beausoleil, and F. Grillot (2019). "Frequency comb dynamics of a 1.3 μm hybrid-silicon quantum dot semiconductor laser with optical injection." In: *Optics Letters*, 44.23, pp. 5755-5758.
5. **B. Dong**, J. Duan, C. Shang, H. Huang, A. B. Sawadogo, D. Jung, Y. Wan, J. E. Bowers, and F. Grillot (2019). "Influence of the polarization anisotropy on the linewidth enhancement factor and reflection sensitivity of 1.55- μm InP-based InAs quantum dash lasers." In: *Applied Physics Letters*, 115.9, pp. 091101.
6. F. Grillot, J. Duan, **B. Dong**, H. Huang (2021). "Uncovering recent progress in nanostructured light-emitters for information and communication technologies." In: *Light: Science & Applications*, 10.1, pp. 1-17.
7. J. Duan, Y. Zhou, **B. Dong**, H. Huang, J. C. Norman, D. Jung, Z. Zhang, C. Wang, J. E. Bowers, and F. Grillot (2020). "Effect of p-doping on the intensity

- noise of epitaxial quantum dot lasers on silicon." In: *Optics Letters*, 45.17, pp. 4887-4890.
8. F. Grillot, J. C. Norman, J. Duan, Z. Zhang, **B. Dong**, H. Huang, W. W. Chow, and J. E. Bowers (2020). "Physics and applications of quantum dot lasers for silicon photonics." In: *Nanophotonics*, 9.6, pp. 20190570.
 9. F. Köster, J. Duan, **B. Dong**, H. Huang, F. Grillot, and K. Lüdge (2020). "Temperature dependent linewidth rebroadening in quantum dot semiconductor lasers." In: *Journal of Physics D: Applied Physics*, 53.23, pp. 235106.
 10. H. Huang, J. Duan, **B. Dong**, J. C. Norman, D. Jung, J. E. Bowers, and F. Grillot (2020). "Epitaxial quantum dot lasers on silicon with high thermal stability and strong resistance to optical feedback." In: *APL Photonics*, 5.1, pp. 016103.
 11. J. Duan, H. Huang, **B. Dong**, J. C. Norman, Z. Zhang, J. E. Bowers, and F. Grillot (2019). "Dynamic and nonlinear properties of epitaxial quantum dot lasers on silicon for isolator-free integration." In: *Photonics Research*, 7.11, pp. 1222-1228.
 12. J. Duan, H. Huang, **B. Dong**, D. Jung, J. C. Norman, J. E. Bowers, and F. Grillot (2019). "1.3- μm Reflection Insensitive InAs/GaAs Quantum Dot Lasers Directly Grown on Silicon." In: *IEEE Photonics Technology Letters*, 31.5, pp. 345-348.

Conference papers

1. **B. Dong**, S. Zhao, H. Huang, J. Duan, S. Liu, J. E. Bowers, and F. Grillot (2021). "Nonlinear properties and stabilization of epitaxial mode-locked quantum-dot lasers on silicon (poster)." In: *International Symposium on Physics and Applications of Laser Dynamics (IS-PALD)*, Virtual Event.
2. **B. Dong**, J.-D. Chen, J. C. Norman, J. E. Bowers, F.-Y. Lin, and F. Grillot (2021). "Dynamics of epitaxial quantum dot laser on silicon subject to chip-scale back-reflection for isolator-free photonics integrated circuits (oral presentation)." In: *Conference on Lasers and Electro-Optics Europe & European Quantum Electronics Conference (CLEO/Europe-EQEC)*, Virtual Event.

3. **B. Dong**, S. Zhao, H. Huang, F. Grillot, S. Liu, and J. E. Bowers (2021). "Performance improvement of epitaxial 20 GHz passively mode-locked quantum-dot lasers on silicon (oral presentation)." In: *Photonics North*, Virtual Event.
4. **B. Dong**, J. Duan, H. Huang, G. Kurczveil, D. Liang, and F. Grillot (2020). "Study of hybrid silicon quantum dot frequency comb laser dynamic for 5G and datacom applications (oral presentation)." In: *European conference on integrated optics (ECIO)*, Virtual Event.
5. **B. Dong**, X. Champagne de Labriolle, H. Huang, J. Duan, S. Liu, J. C. Norman, J. E. Bowers, and F. Grillot (2020). "Resonant optical feedback in epitaxial 1.3 micron passively mode-locked quantum dot lasers on silicon (oral presentation)." In: *Photonics North*, Virtual Event.
6. **B. Dong**, J.-D. Chen, H.-L. Tsay, H. Huang, J. Duan, J. C. Norman, J. E. Bowers, F.-Y. Lin, and F. Grillot (2020). "P-doping effect on external optical feedback dynamics in 1.3-microns InAs/GaAs quantum dot laser epitaxially grown on silicon (oral presentation)." In: *SPIE Photonics Europe*, Virtual Event.
7. **B. Dong**, A. Sawadogo, J. Duan, H. Huang, G. Kurczveil, D. Liang, and F. Grillot (2019). "Linewidth enhancement factor and optical injection in a hybrid-silicon quantum dot comb laser (poster)." In: *IEEE Group IV photonics (GFP)*, Singapore.
8. F. Grillot, **B. Dong**, J. Liu, H. Huang, K. Nishi, K. Takemasa, M. Sugawara, and J. E. Bowers (2021). "Recent progress in quantum dot distributed feedback lasers with large wavelength detuning for uncooled and isolation-free applications." In: *Optoelectronics and Communications Conference*, Virtual Event
9. S. Ding, **B. Dong**, H. Huang, J. E. Bowers, and F. Grillot (2021). "Linewidth enhancement factor measurement by using phase modulation method for epitaxial quantum dot laser on silicon." In: *34th Semiconductor and Integrated Optoelectronics (SIOE)*, Virtual Event.
10. F. Grillot, J. Duan, S. Zhao, **B. Dong**, H. Huang, J. C. Norman, and J. E. Bowers (2021). "Intensity noise and modulation dynamic of epitaxial quantum dot semiconductor lasers on silicon." In: *SPIE Photonics West*, Virtual Event.

11. S. Zhao, J. Duan, **B. Dong**, and F. Grillot (2021). "Effects of Shockley-Read-Hall recombination on the reflection sensitivity of quantum dot lasers directly grown on silicon." *SPIE Photonics West*, Virtual Event.
12. J. Duan, Y. Zhou, H. Huang, **B. Dong**, C. Wang, and F. Grillot (2020). "Dynamic properties of two-state lasing quantum dot laser for external optical feedback resistant applications." In: *International Conference on Numerical Simulation of Optoelectronic Devices (NUSOD)*, Virtual Event.
13. F. Grillot, J. Duan, **B. Dong**, H. Huang, S. Liu, W. W. Chow, J. C. Norman, and J. E. Bowers (2020). "Quantum dot lasers based photonics integrated circuits." In: *IEEE Photonics Conference (IPC)*, Virtual Event.
14. S. Liu, X. Wu, J. C. Norman, D. Jung, M. Dumont, C. Shang, Y. Wan, M. J. Kennedy, **B. Dong**, D. Auth, S. Breuer, F. Grillot, W. Chow, A. Gossard, and J. Bowers (2020). "High-performance mode-locked lasers on silicon (invited)." In: *SPIE Photonics West*, San Francisco, USA.
15. J. Duan, H. Huang, **B. Dong**, D. Jung, Z. Zhang, J. C. Norman, J. E. Bowers, and F. Grillot (2019). "Thermally insensitive determination of the chirp parameter of InAs/GaAs quantum dot lasers epitaxially grown onto silicon (oral presentation)." In: *SPIE Photonics West*, San Francisco, USA.
16. J. Duan, **B. Dong**, H. Huang, Z. G. Lu, P. J. Poole, and F. Grillot (2019). "Thermal dependence of the emission linewidth of 1.52- μm single mode InAs/InP quantum dot lasers (oral presentation)." In: *Compound Semiconductor Week*, Nara, Japan.
17. F. Grillot, J. Duan, H. Huang, **B. Dong**, D. Jung, Z. Zhang, J. C. Norman, and J. E. Bowers (2019). "Linewidth broadening factor and optical feedback sensitivity of silicon based quantum dot lasers (invited)." In: *SPIE Photonics West*, San Francisco, USA.

Appendix B

RÉSUMÉ DE THÈSE EN FRANÇAIS

La photonique sur silicium est prometteuse pour les communications optiques à haut débit, les interconnexions optiques à courte portée et les technologies quantiques. Au cours des deux dernières décennies, la croissance de matériaux III-V sur silicium constitue également une solution idéale pour la prochaine génération de circuits photoniques intégrés (PIC). En utilisant la ligne de production de tranches de silicium standard de 300 mm offerte par la fonderie mature à semi-conducteurs à oxyde de métal complémentaire (CMOS), le PIC en silicium permet d'augmenter considérablement le nombre de composants optoélectroniques sur puce et de réduire le coût. En 2019, le nombre de composants sur un PIC en silicium a largement dépassé celui sur un PIC natif basé sur InP, qui approchait les cent mille par puce. De nos jours, les technologies d'intégration photonique sur silicium sont poursuivies à la fois dans l'académie et commercialement par Juniper Networks (États-Unis), Hewlett Packard Enterprise (États-Unis), Intel (États-Unis), AIM photonics (États-Unis), IMEC (Europe), IBM (Europe), NTT (Japon) et AMF (Singapour). Il convient de souligner que les riches non-linéarités optiques de la plate-forme de silicium joueraient un rôle important dans les techniques quantiques intégrées au futur.

À cause de la bande interdite indirecte du silicium, la fabrication de sources laser à haut rendement sur silicium était un défi. Pour surmonter ce problème, l'une des solutions les plus fiables consiste à faire croître des lasers à semi-conducteur III-V sur un substrat de silicium. Pour ce faire, les îlots quantiques (QD) avec une densité d'états du type atomique présentent un avantage unique pour servir de matériau de milieu de gain du laser sur Si, en raison de leur compacité et d'une tolérance accrue aux défauts structuraux. Par rapport aux lasers massifs ou à puits quantiques sur silicium, les lasers QD sur silicium ont montré des performances supérieures. Des exemples comme un faible courant de seuil, un gain de matériau élevé, et une grande stabilité thermique ont été montrés récemment.

Malgré les énormes progrès réalisés dans le développement du PIC en silicium, il reste encore des défis à relever. Certains d'entre eux proviennent des lasers. L'objectif de cette thèse est d'étudier les propriétés non linéaires et les dynamiques des lasers QD sur silicium afin de développer les lasers de haute performance pour

PIC. Cette thèse est organisée en suivant:

1. Chapitre I comprend une introduction générale présentant un contexte de la recherche et les motivations.
2. Chapitre II examine les propriétés fondamentales des lasers QD, y compris la structure électronique, les mécanismes d'élargissement du gain, les oscillations de relaxation, le facteur d'élargissement spectral, le bruit, et enfin la susceptibilité non linéaire. Ce chapitre prépare bien le lecteur à comprendre les recherches, les résultats et les conclusions dans les chapitres suivants.
3. Chapitre III se polarise sur les lasers QD directement épitaxiés sur Si en présence de contre-réaction optique (EOF). Dans le régime de cavité courte, les résultats rapportent des tolérances élevées aux réflexions parasites ce qui rend possible l'intégration de ces sources sur des PIC dépourvus d'isolateur optique. Par ailleurs, la réduction du facteur d'élargissement spectral est un déterminant fondamental permettant d'atteindre cet objectif.
4. Chapitre IV analyse les propriétés statiques et dynamiques d'un laser QD à rétroaction optique distribuée (DFB) pour des applications sans isolateur et sans Peltier. Pour ce faire, la conception du laser intègre un désaccord entre le pic de gain et le pic d'émission DFB contrôlable par la variation de température. Par conséquent, les performances du laser sont substantiellement améliorées avec l'augmentation de la température.
5. Chapitre V du manuscrit aborde les lasers QD sur Si pour la génération de peignes de fréquences optiques (OFC). Les techniques de contrôle externe comme la contre-réaction et l'injection optique sont utilisées pour régénérer les performances notamment le bruit de phase, la gigue temporelle et la bande passante d'émission du peigne.
6. Chapitre VI s'articule autour des non-linéarités optiques dans les lasers QD sur Si notamment sous l'angle du mélange à quatre ondes (FWM). L'étude montre que l'efficacité FWM du laser QD est supérieure de plus d'un ordre de grandeur à celle d'un laser à puits quantiques prouvant ainsi que les milieux QD sont très efficaces pour obtenir des peignes de fréquence de grande qualité et de l'auto blocage de mode.
7. Chapitre VII présent les conclusions générales de la recherche et les perspectives d'exploitation des résultats dans cette thèse.

Ce travail démontre l'importance des solutions lasers QD en particulier pour les technologies photoniques intégrées sur silicium.

Titre : Lasers à îlots quantiques sur silicium : propriétés non-linéaires, dynamique et applications

Mots clés : Lasers à îlot quantiques, photonique sur silicium, circuits intégrés photoniques, peigne de fréquences optiques, dynamique non-linéaire, mélange à quatre ondes

Résumé : La photonique sur silicium est une technologie prometteuse pour les systèmes de communication à haut débit, les interconnexions optiques à courte portée et pour le déploiement des technologies quantiques. La croissance de matériaux III-V sur silicium constitue également une solution idéale pour la prochaine génération de circuits photoniques intégrés (PIC). Dans ce contexte, les lasers à îlots quantiques (QD) utilisant des atomes semi-conducteurs comme milieu de gain sont des candidats très prometteurs en raison de leur compacité, de leur grande stabilité thermique et d'une tolérance accrue aux défauts structuraux. L'objectif de cette thèse est d'étudier les propriétés non-linéaires et les dynamiques des lasers QD sur Si en vue des applications susmentionnées. La première partie se polarise sur les lasers QD directement épitaxiés sur Si en présence de contre-réaction optique (EOF). Dans le régime de cavité courte, les résultats rapportent des tolérances élevées aux réflexions parasites ce qui rend possible l'intégration de ces sources sur des PIC dépourvus d'isolateur optique. Par ailleurs, la réduction du facteur d'élargissement spectral est un déterminant fondamental permettant d'atteindre cet objectif. La deuxième partie analyse les propriétés statiques et dynamiques d'un laser QD à rétroaction op-

tique distribuée (DFB) pour des applications sans isolateur et sans Peltier. Pour ce faire, la conception du laser intègre un désaccord entre le pic de gain et le pic d'émission DFB contrôlable par la variation de température. Par conséquent, les performances du laser sont substantiellement améliorées avec l'augmentation de la température. La troisième partie du manuscrit aborde les lasers QD sur Si pour la génération de peigne de fréquences optiques (OFC). Les techniques de contrôles externes comme la contre-réaction et l'injection optique sont utilisées pour régénérer les performances notamment le bruit de phase, la gigue temporelle et la bande passante d'émission du peigne. La dernière partie s'articule autour des non-linéarités optiques dans les lasers QD sur Si notamment sous l'angle du mélange à quatre ondes (FWM). L'étude montre que l'efficacité FWM du laser QD est supérieure de plus d'un ordre de grandeur à celle d'un laser à puits quantiques prouvant ainsi que les milieux QD sont très efficaces pour obtenir des peignes de fréquence de grande qualité et de l'auto blocage de mode. Ce travail démontre l'importance des solutions lasers QD en particulier pour les technologies photoniques intégrées sur Si.

Title : Quantum-dot lasers on silicon: nonlinear properties, dynamics and applications

Keywords : Quantum-dot lasers, silicon photonics, photonic integrated circuits, optical frequency combs, nonlinear dynamics, four-wave mixing

Abstract : Silicon photonics is promising for high-speed communication systems, short-reach optical interconnects, and quantum technologies. Direct epitaxial growth of III-V materials on silicon is also an ideal solution for the next generation of photonic integrated circuits (PICs). In this context, quantum-dots (QD) lasers with atom-like density of states are promising to serve as the on-chip laser sources, owing to their high thermal stability and strong tolerance for the defects that arise during the epitaxial growth. The purpose of this dissertation is to investigate the nonlinear properties and dynamics of QD lasers on Si for PIC applications. The first part of this thesis investigates the dynamics of epitaxial QD lasers on Si subject to external optical feedback (EOF). In the short-cavity regime, the QD laser exhibits a strong robustness against parasitic reflections hence giving further insights for developing isolator-free PICs. In particular, a near-zero linewidth enhancement factor is crucial to achieve this goal. The second part is devoted to studying the static properties and dynamics of

a single-frequency QD distributed feedback (DFB) laser for uncooled and isolator-free applications. The design of a temperature-controlled mismatch between the optical gain peak and the DFB wavelength contributes to improving the laser performance with the increase of temperature. The third part of this dissertation investigates the QD-based optical frequency comb (OFC). External control techniques including EOF and optical injection are used to improve the phase noise, the timing-jitter, and the frequency comb bandwidth. In the last part, an investigation of the optical nonlinearities of the QD laser on Si is carried out by the four-wave mixing (FWM). This study demonstrates that the FWM efficiency of QD laser is more than one order of magnitude higher than that of a commercial quantum-well laser, which gives insights for developing self-mode-locked OFCs based on QD. All these results allow for a better understanding of the nonlinear dynamics of QD lasers and pave the way for developing high-performance classical and quantum PICs on Si.